Macon CarbonSAFE

Report of Geology from the T.R. McMillen #2 Well Drilled for CarbonSAFE Illinois - Macon County

Task 6

Technical Report

April 1, 2017 through March 31, 2022

Jared Freiburg

Prairie Research Institute
University of Illinois
Urbana-Champaign, IL 61820

Report Issued: March 31, 2022

Report Number: DOE- FE0029381-6
U.S. DOE Cooperative Agreement Number: DE- FE0029381

Principal Investigator: Dr. Steve Whittaker
Business Contact: Illinois State Geological Survey
615 E Peabody Drive
Champaign, IL 61820-7406

ILLINOIS
Illinois State Geological Survey
PRAIRIE RESEARCH INSTITUTE

DISCLAIMER

AKNOWLEDGEMENT

This material is based on work supported by the Department of Energy under Award Number DE-FE0029381.

CONTENTS

Chapter 1
Sedimentology and Sequence Stratigraphy of the Mt. Simon Sandstone

By: Dr. Franck Delpomdor
Illinois State Geological Survey

Introduction

The Illinois Basin is one of the most important explored basins for the geological storage of carbon dioxide (CO_2) in the United States (Finley, 2014). Exploration and evaluation of the Illinois Basin began in the late 2000s with the Illinois Basin - Decatur Project (IBDP), which targeted the Cambrian Mt. Simon Sandstone as the commercial-scale deep reservoir for storage performance for CO_2 in Illinois and other locations throughout Indiana and Kentucky (Leetaru et al., 2008; Leetaru and McBride, 2009). In early 2017, nearly 1 million metric tons of CO_2 were injected over a period of three years from the ethanol production facility at Archer Daniels Midland Company at Decatur in Macon County, Illinois (Bauer et al., 2016). Extensive monitoring including seismic reflection, geophysical technology, and core and borehole data took place during and after injection to confirm the position of the CO_2 underground (Leetaru et al., 2008).

Other sites were recently targeted in Illinois that were identified as potential sites for geological storage of CO_2 in the Cambrian Lower Mt. Simon Sandstone. One of the sites was located a few miles east of the Mount Auburn village in Christian County, nearly 18 miles SW of Decatur (Figure 1). The Illinois State Geological Survey in collaboration with well permit holder Podolsky Oil drilled the T.R. McMillen #2 well at the Mt. Auburn Oil Field in Christian County, Illinois. Originally, the well site was planned for the Forsyth Field in Macon County (hence the CarbonSAFE Macon Co. project name). However, after careful consideration, the Mt. Auburn Field was selected as a better location to provide more regional geologic context to the distribution of the high-reservoir-quality Lower Mt. Simon Sandstone, as the previous site was approximately one mile north from the IBDP, which already has four wells through the Mt. Simon Sandstone and into the Precambrian basement providing limited geologic context to the prior knowledge.

The T.R. McMillen #2 well was drilled to a depth of 6,478 ft through Pennsylvanian to Cambrian units and into the Precambrian crystalline basement (Figure 1). Seismic reflection data showed that the Precambrian crystalline basement had distinct topographic features with a thick (up to 400 ft) paleo-high—in this report interpreted as a monadnock—bordered by an incised river valley and channels (Figure 1). A full suite of standard geophysical logs were run, including Fullbore Microimaging (FMI; from total depth to top of New Albany). Approximately 60 ft of 4 in core was cut in the base of the New Albany Shale seal and into the Racine dolomite, 30 ft in the Eau Claire and into the Upper Mt. Simon Sandstone, 60 ft in the Lower Mt. Simon and into the Argenta Sandstone, 17 ft in the Precambrian basement, and 100 of 1 in diameter rotary sidewall cores from the Eau Claire, Mt. Simon, and Precambrian units. A 30-mile, conventional, two-dimensional seismic reflection east-west line was acquired through Sangamon, Christian, and Macon Counties (Figure 1). The line traverses just north of the well site and was tied into the well with a north-south line recorded as a 10,000 ft vertical offset profile.

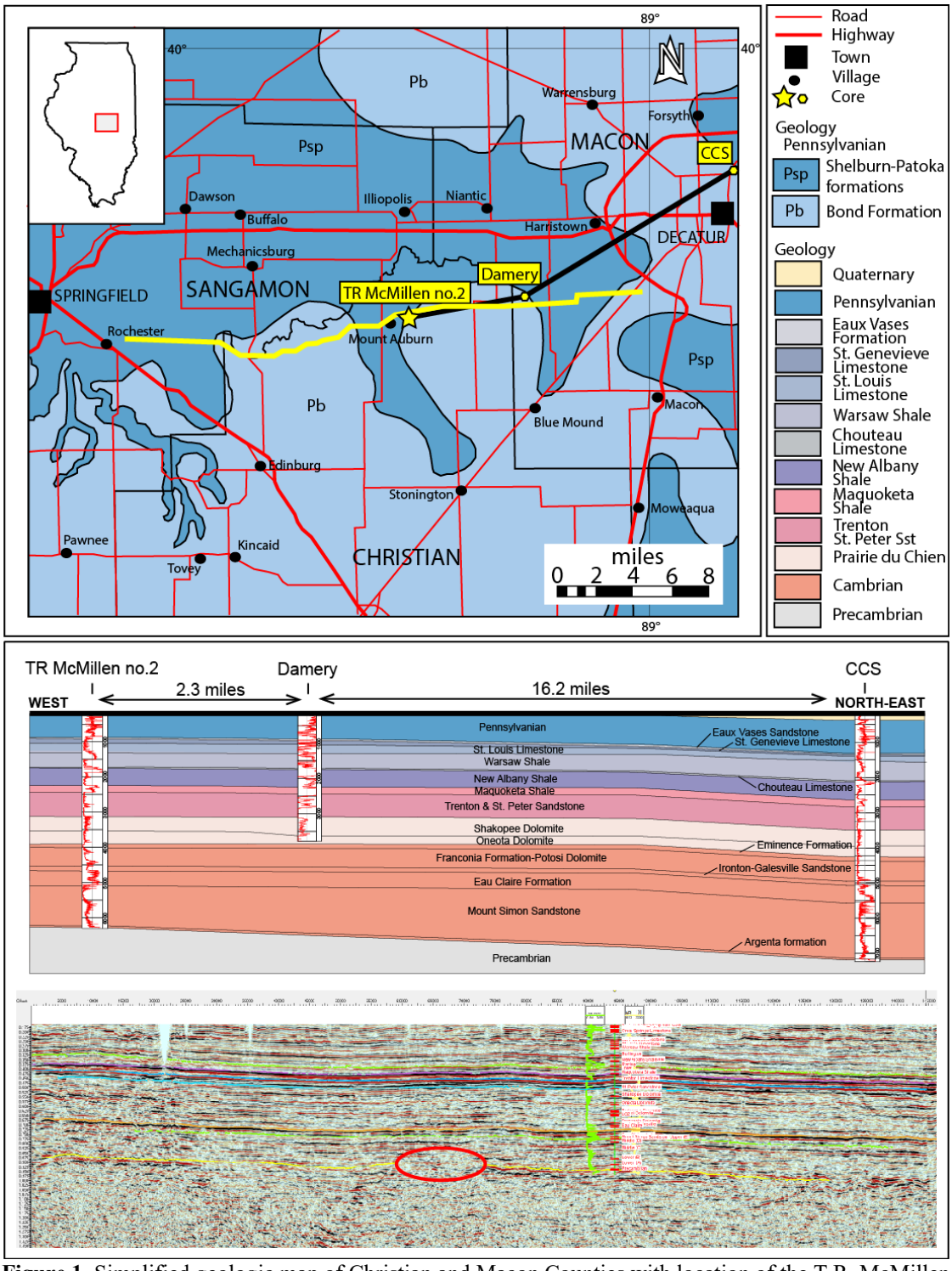

Figure 1. Simplified geologic map of Christian and Macon Counties with location of the T.R. McMillen #2 well and cited boreholes in this report (geologic map modified from Kolata, 2005). Geologic cross-section (dark line) represents nearly 19 miles of profiles. Each borehole contains gamma-ray log, and the stratigraphic units are noted. Seismic reflection profile (yellow line) with location of the T.R. McMillen #2 well and gamma-ray log. The seismic reflection shows an onlap pattern of reflections, which suggests there is a Precambrian paleotopographic 400 ft high about 3 miles west of the drilled borehole.

Site Geological Setting

Located in the midwestern regions of the United States, the Illinois Basin is a NNW-SSE-oriented, spoon-shaped structure covering an area of approximately 110,039 mi^2 extending westward to eastward from Illinois to eastern Indiana and from northward to southward from southern Wisconsin to northwestern Kentucky and northern Tennessee (Kolata and Nelson, 2010). The Paleozoic sedimentary fill of this basin was conditioned by at least four tectonic-eustatic cycles linked to the Precambrian and Paleozoic tectonic evolution of Laurentia continent (McBride et al., 2003). These cycles or supersequences include, from oldest to youngest, Sauk (Cambrian to Early Ordovician), Tippecanoe (Early Ordovician to Early Devonian), Kaskaskia (Early Devonian to Late Mississippian), and Absaroka (Early Pennsylvanian to Early Permian) (Willman et al., 1975).

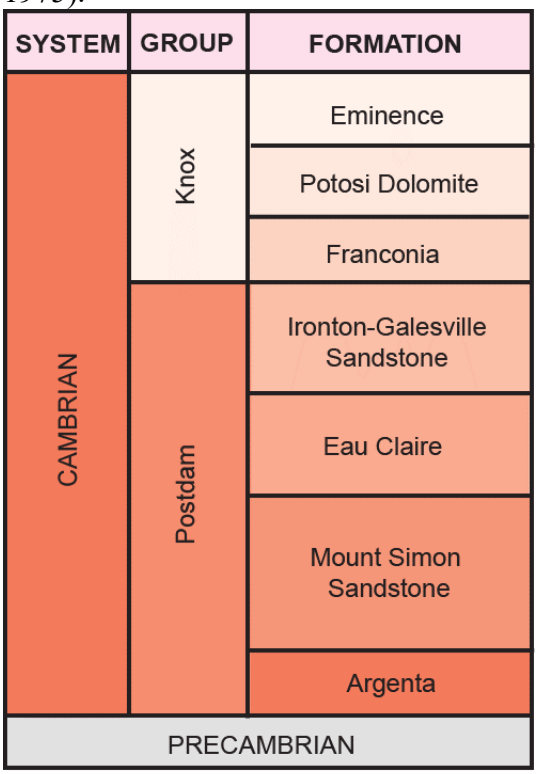

Figure 2. Stratigraphic column of the Cambrian

Three major tectonic structures crosscut the Illinois Basin and have controlled the deposition within the basin. They include the LaSalle Anticlinal Belt in east-central Illinois, the DuQuoin-Louden Anticlinal Belt in south-central Illinois, and the Rough Creek-Shawneetown Fault Zone in extreme southwest Illinois (Willman et al., 1975; Treworgy et al., 1991). Other minor tectonic structures have regionally contributed to sedimentation within the basin (e.g., Sandwich Fault Zone, etc.). The entire stratigraphic record of the Illinois Basin is up to 15,000 ft in thickness that thickens southward into the deepest part located near the mouth of the Wabash River at the tri-state borders between Illinois, Indiana, and Kentucky (Willman et al., 1975). The Paleozoic system was deposited based on biostratigraphy, mainly trilobites and conodonts, and geochronology in a time interval between the Early or Middle Cambrian to Early Permian (Collinson et al., 1988; Norby, 1991; Thomas et al., 2020). Local consolidated sediments of the Cretaceous age are found only in relatively small areas in southern and western Illinois (Willman

et al., 1975). The bedrock is covered by Late Cenozoic and Quaternary sediments that directly underlie the surface of almost the entire state (Willman et al., 1975).

The initial stage of pre-rifting has occurred in east-central Illinois and west-central Indiana by the strike-slip faulting of the 1.4–1.1 Ga Eastern Granite-Rhyolite Province (EGRP) (ages based on U-Pb geochronology; Heidlauf et al., 1986; Denison et al., 1987; Leighton and Kolata, 1991; Kolata and Nelson, 1991, 2010; Van der Pluijm and Catacosinos, 1996; Van Schmus et al., 1996, 2007) that have built the initial structural framework of the proto-Illinois Basin. The crystalline basement is intruded by 1073 ± 12 Ma Gabbro dikes that have recorded the far-field effect of the Grenville-age extension in the proto-basin (U-Pb zircon ages; Freiburg et al., 2020). Recent core and well data from the CarbonSAFE Wabash project Wabash #1 well, Vigo County, Indiana, have shown the deposition of sandstone with volcanic intrusions that overlies the Precambrian crystalline basement and underlies the Paleozoic system of the Illinois Basin. This new unit may correlate with the pre-rifting Precambrian lacustrine-fluvial Late Middle Run Formation (Keweenawan in age) in Indiana and Ohio. Early Cambrian zircons identified in the Argenta and Lower Mt. Simon indicate Early Cambrian-age volcanics and imply a culminating date of rifting in the basin (Chapter 2; Freiburg et al., 2020). Seismic reflection data have revealed the occurrence of a layered sequence, called the Centralia Sequence, that appears to thicken from east-central Illinois toward a northeast depocenter (Pratt et al. 1992; McBride and Kolata, 1999; McBride et al., 2003). Freiburg et al. (2014) have discussed the possible correlation of the Centralia sequence with the Argenta Formation. Overlying the Argenta Formation, the Mt. Simon Sandstone appears to be part of the pre-rifting stage initiated with the deposition of the Argenta Formation. It thickens from east-central Illinois to a northern depocenter with a maximum deposition up to 2,500 ft (Freiburg et al., 2014). The Mt. Simon Sandstone is included in the Potsdam Supergroup that is overlain by the Knox Dolomite Supergroup, itself composed, from oldest to youngest, by the Eau Claire Formation, Ironton-Galesville Sandstone, Franconia Formation, Potosi Dolomite, and Eminence Formation on its lower part (Figure 2). Both supergroups are grouped in the Sauk supersequence in the Illinois Basin (Sloss, 1963). The Mt. Simon Sandstone is overlain by the Upper Cambrian Eau Claire Formation (Becker et al., 1978).

Methodology

In this report, data from Argenta Formation and Mt. Simon Sandstone were acquired through detailed log analysis, description of cores, high-resolution Fullbore Formation Micro-Imager (FMI), gamma-ray log of the T.R. McMillen #2 well, Christian County (Illinois), and regional seismic acquisition. All cores are stored at the Sample and Core Library of the Illinois State Geological Survey at Champaign, Illinois. Petrographic analysis was completed on 123 thin sections prepared from all rotary side wall cores and select samples taken from the full diameter core. Mineralogical data was obtained through petrographic point counts, X-ray diffraction (XRD), and scanning electron microscopy with energy dispersive spectroscopy (SEM-EDS).

Only the Lower Mt. Simon Sandstone (Arkose unit) was cored between 6,240 and 6,301 ft in depth. Other units were logged based on FMI that provides a high-resolution visualisation of the sedimentary structures in the borehole. FMI is an electric tool that measures the microresistivity of the rocks. The produced images have a vertical resolution of 5 mm and cover up more than 80% of the borehole wall. The variation of brightness depends on the porosity. When the porosity is low (<1%), the FMI images are clear or white. Core and FMI logs are drawn based on descriptive observations and recognition of lithofacies codes from individual core segments, mosaics of core photographs, and FMI imaging that is digitally enhanced. Sedimentary facies are classified based

on grain-size and sedimentary structures, following the methodology and lithofacies codes adapted from Miall (2006) for the fluvial deposits and Kocurek (1996) for the Aeolian dune deposits. Recognition and direction of sedimentary structures of cross-strata are measured on the north-oriented FMI log (Glover and Bormann, 2007). Lithofacies are grouped into four distinct lithofacies associations (LFA): alluvial-fluvial system, fluvial system, aeolian-fluvial system, and delta front-lagoon/lake system. A block diagram representing the paleoenvironmental evolution stages is proposed in this report for the deposition of the Argenta Formation and Mt. Simon Sandstone. Grain size analysis is an analytical technique to determine the size of the different particles and their distribution within sedimentary rocks. The grain size analysis was performed using microscopy by point counting on thin section samples. Weight percentage frequencies and cumulative weight percentage frequencies were calculated with the formulae of Folk and Ward (1957). The grain size parameters like graphic mean (Mz), inclusive graphic standard deviation (SD), inclusive graphic skewness (Sk), and graphic kurtosis (KG) were presented in a graphical or statistical form. The stratigraphic framework was developed based on the assumptions of the sequence stratigraphy sensu Catuneanu (2006) and Catuneanu et al. (2009). A correlation section between the T.R. McMillen #2 well and Verification Well (VW) #1 and VW #2 boreholes was constructed for the identification of key stratigraphic surfaces and system tracts.

Select samples from the Argenta, Lower Mt. Simon, and Precambrian basement from the T.R. McMillen #2 well samples and the FutureGen Alliance 2.0 well in Morgan County, Illinois, were selected for U-Pb geochronological age-dating to understand detrital source of reservoir sediments as well as regional and local controls of the Precambrian basement on the sedimentology.

Results

Core Description

The T.R. McMillen #2 well crosses a total of 6,469 ft through Palaeozoic rocks. The upper part of the Pennsylvanian and Permian systems is missing. Twelve stratigraphic units were identified and they consist of, from youngest to oldest: (1) the undifferentiated Pennsylvanian System (0-864 ft in depth), (2) the Aux Vases Formation (864-907 ft in depth), (3) the St. Genevieve Limestone (907-1,035 ft in depth), (4) the St. Louis Limestone and Salem Limestone (1,035-1,252 ft in depth), (5) the Warsaw Shale (1,252-1,502 ft in depth), (6) the Burlington Limestone and Chouteau Limestone (1,502-1,726 ft in depth), (7) the New Albany Shale (1,726-1,874 ft in depth), (8) the Maquoketa Shale including the Racine Formation and Joliet Formation (1,874-2,434 ft in depth), (9) the Trenton Dolomite and St. Peter Sandstone (2,434-3,121 ft in depth), (10) the Prairie du Chien Group (3,121-3,888 ft in depth), (11) the Cambrian System (3,888-6,386 ft in depth), and (12) the Precambrian crystalline basement (6,386-6,469 ft in depth) (Figure 1). The Argenta Formation and the Mt. Simon Sandstone are identified respectively at 6,299-6,386 ft and 5,130-6,299 ft in depths. The Precambrian crystalline basement consists of light- to dark-maroon to dark-gray to pink granite and rhyolite with quartz, feldspar, pyroxene, amphibole, and magnetite. Locally, the crystalline rocks are altered in a maroon-orange clay. The contact with the Argenta Formation appears to be sharp and unconformable as shown by the differential resistivity intensities in the FMI log.

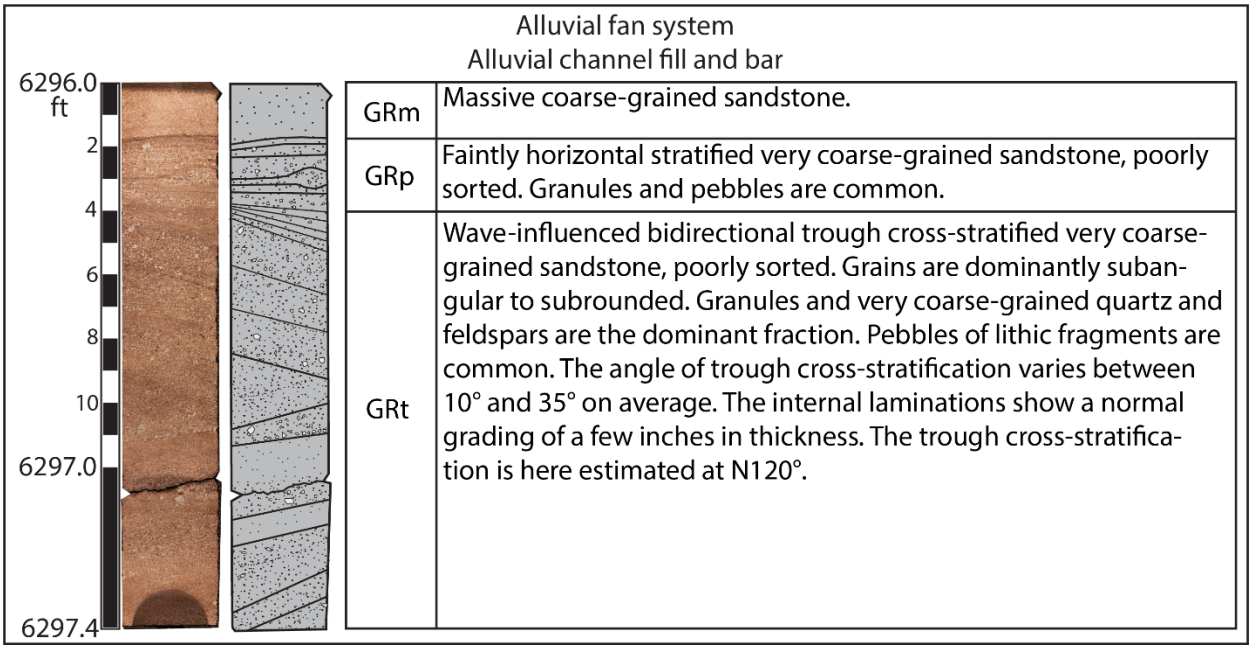

Figure 3. Cores from the T.R. McMillen #2 well showing coarse-grained, pebbly sandstone with massive structure, planar, and crossed-stratification in the unit A (Arkose) of the Lower Mt. Simon Sandstone. The sandstone is interpreted as a channel fill and bar in an alluvial-fluvial river system.

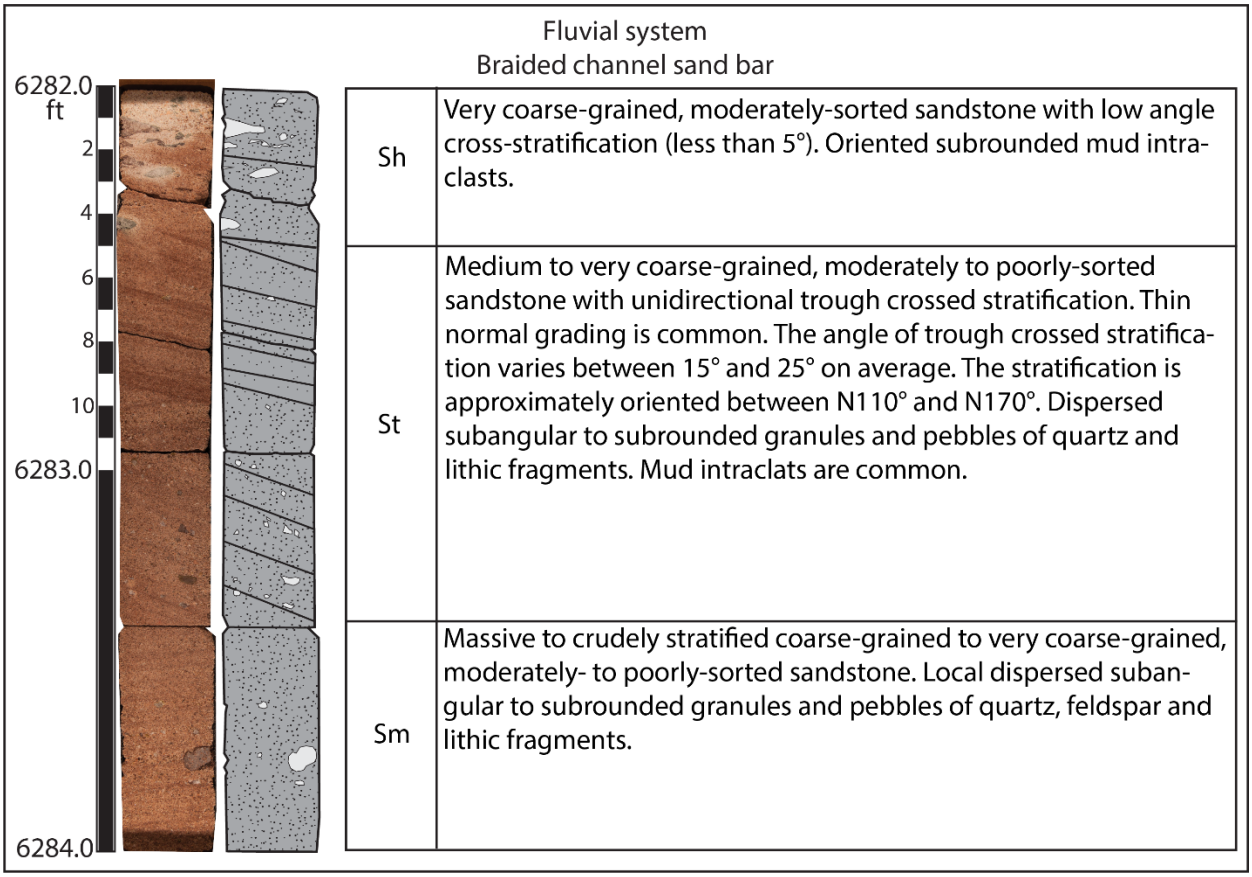

Figure 4. Cores from the T.R. McMillen #2 well showing coarse-grained sandstone with massive structure, faintly horizontal, low-angle, and crossed-stratification in the unit A (Arkose) of the Lower Mt. Simon Sandstone. The sandstone is interpreted as a braided sand channel fill and bar in a fluvial river system.

The lithology of the Argenta Formation is defined using the FMI log and plugs. It consists dominantly of dark-maroon to dark-brown (light-orange to light-tan when altered), medium- to very coarse-grained, moderately sorted sandstone, locally pebbly, with thin, dark-maroon mudstone partings. Layers of conglomerate rich in quartz pebbles are common. Matrix is hematitic or composed of fine materials. Grains are subangular to subrounded and are dominantly composed of quartz, altered feldspars, and lithic fragments. Planar, low-angle, and crossed-stratifications are common. The lower part of this formation is dominantly composed of fine- to medium-grained sandstone (6,325-6,386 ft in depth), while the upper part is dominantly composed of medium- to pebbly-grained sandstone and conglomerate (6,299-6,325 ft in depth). The FMI images have identified possible vertical bioturbation in the depth interval of 6,325-5,327 ft.

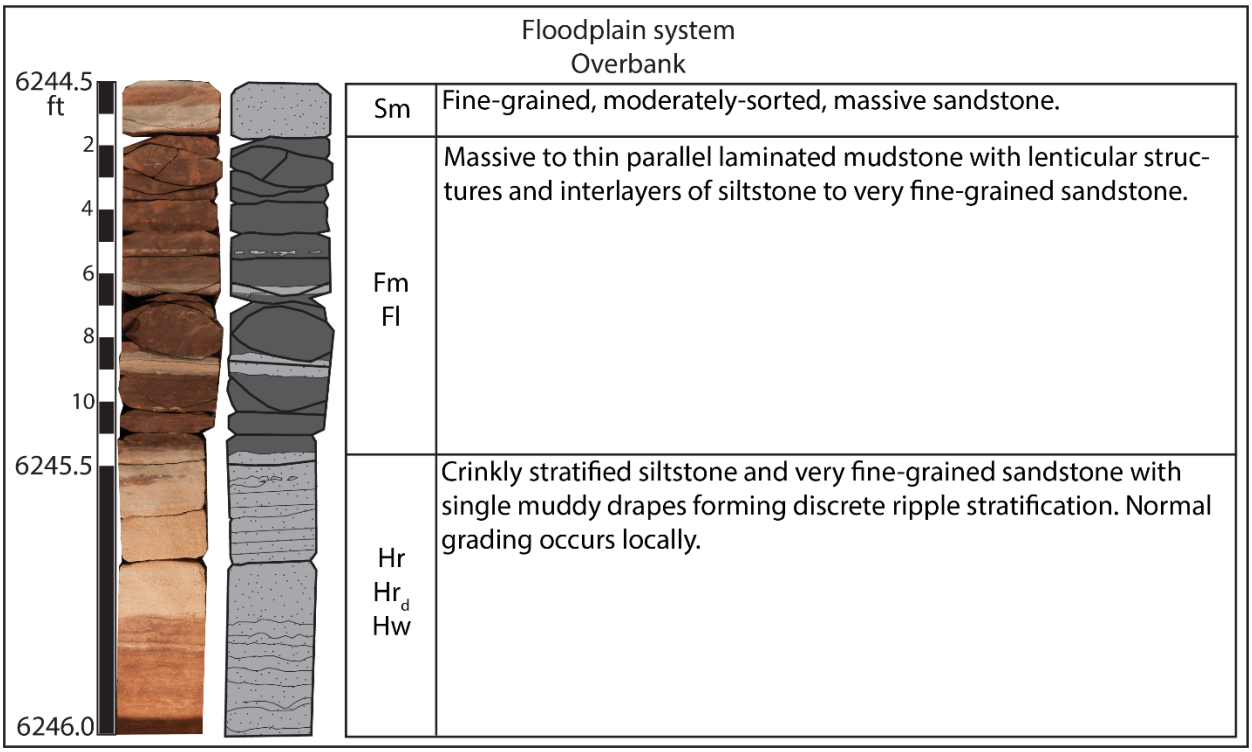

Figure 5. Cores from the T.R. McMillen #2 well showing heterolytic sandstone and mudstone in the unit A (Arkose) of the Lower Mt. Simon Sandstone. The sandstone is interpreted as floodplain in a fluvial river system.

The Mt. Simon Sandstone comprises from oldest to youngest: (1) the Lower Mt. Simon Sandstone that includes the units A and B, (2) the Middle Mt. Simon Sandstone that includes the units C and D, and (3) the Upper Mt. Simon Sandstone that includes only the unit E.

The unit A is identified between 6,129 and 6,299 ft in depth. Cores, FMI and gamma-ray logs, and plugs were used to describe this unit. The unit A consists of dark- to light-maroon to brown (light-tan to gray when altered), fine- to coarse-grained, moderately to well sorted sandstone with thin, dark maroon mudstone partings (Figures 4-7). Layers of pebbly sandstone were identified using the FMI log in the lower part of the unit. Sandstone is sandier in the middle part of the unit. Subangular to subrounded sand-sized grains of quartz and feldspar are the dominant fraction. Lithic fragments are also recognized. The grains are consolidated with a maroon to brown, hematitic clay matrix. Sedimentary features such as planar, low-angle, and crossed-stratifications are common.

The unit B is identified between 5,955 and 6,129 ft in depth (Figure 10). Only the FMI and gamma-ray logs and plugs were used to describe this unit. The unit B consists of dark- to light-maroon to red, fine- to coarse-grained, moderately to well sorted sandstone. In the FMI log, the lower and upper parts of the unit appear to be finer than the middle part of the unit, which appears coarser. Quartz is major in the unit, but minor feldspar and lithic fragments are present. Grains are dominantly subrounded. A maroon to brown, locally red clay matrix fills the interparticular spaces. Cross-stratification is common in the lower part of the unit (6,074-6,129 ft in depth), while the middle and upper parts of the unit are laminar.

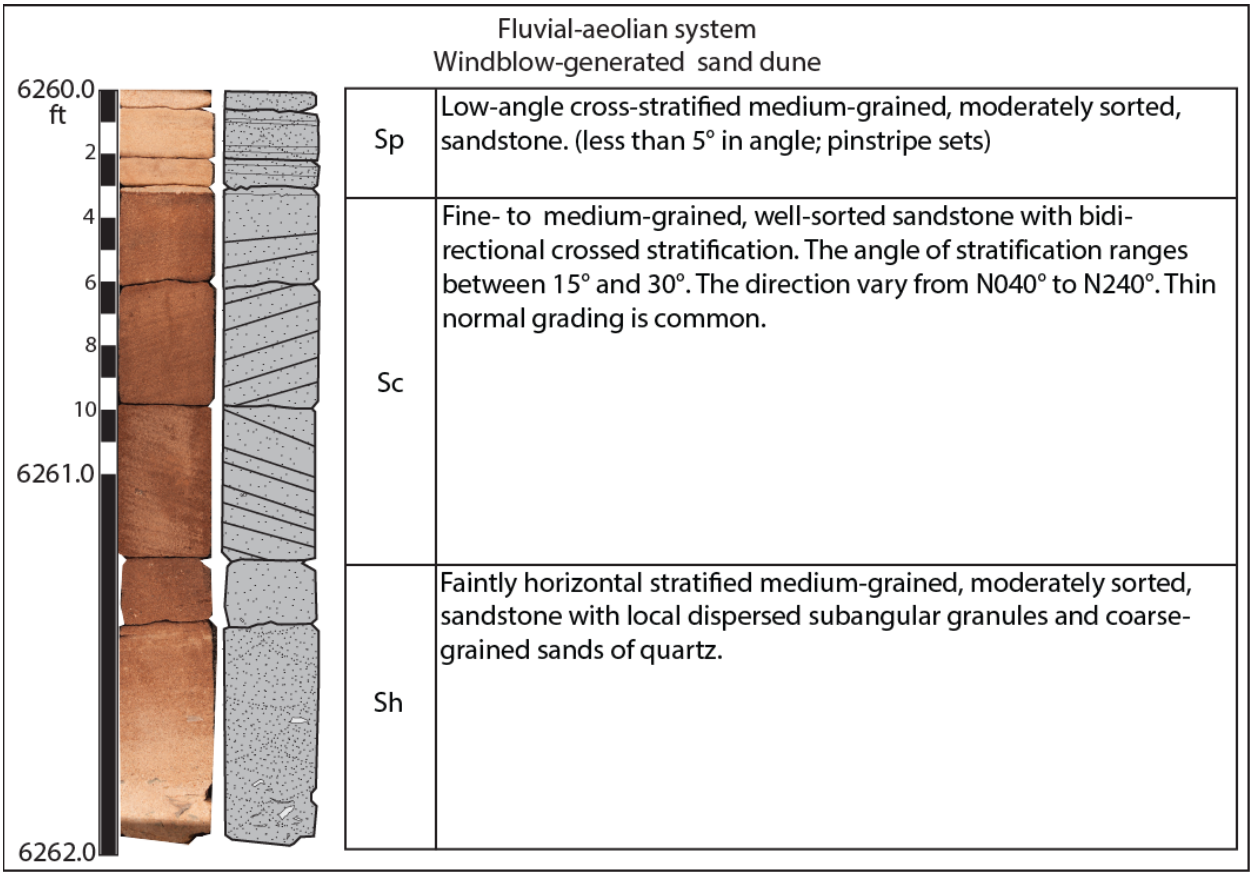

Figure 6. Cores from the T.R. McMillen #2 well showing medium- to fine-grained sandstone with large-scale trough crossed-stratification in the unit A (Arkose) of the Lower Mt. Simon Sandstone. The sandstone is interpreted as a sand dune in an aeolian plain system.

The unit C is identified between 5,541 and 5,955 ft in depth (Figure 12). Only the FMI and gamma-ray logs and plugs were used to describe this unit. The unit consists of dark- to light-maroon to red (light-tan to pink when altered), fine- to coarse-grained, moderately sorted, sandstone. Thin, dark-maroon to dark-red mudstone partings are common in the upper part of the unit. Quartz is major in the unit, but feldspar is locally abundant. Grains are dominantly subrounded to well rounded. Grains float in a maroon to brown, locally red clay matrix. Planar to cross-stratifications are identified in the FMI log. The top of the unit C (5,541-5,570 ft in depth) appears finer in the FMI log.

The unit D is identified between 5,270 and 5,541 ft in depth (Figure 13). Only the FMI and gamma-ray logs and plugs were used to describe this unit. The unit consists of light-maroon to red

(light-tan to pink when altered), fine- to medium-grained, moderately sorted sandstone. Massive and planar stratification are the dominant sedimentary features as recognized in the FMI log. Quartz is dominant and subrounded to well-rounded and is consolidated in a dark-maroon clay matrix. The bedding appears thicker in the lower part of the unit, while the top of the unit is thinner in the FMI log. Possible vertical bioturbation is recognized in 5,280 ft in depth.

The unit E is identified between 5,130 and 5,270 ft in depth (Figure 14). Only the FMI and gamma-ray logs and plugs were used to describe this unit. The unit consists of light-maroon to red (light-tan to pink when altered), fine- to medium-grained, moderately to very well sorted sandstone. In the FMI log, cross-stratification is common on the lower $^2/_3$ part of the unit, while the upper part is laminar and muddy. Quartz is dominant and is sub-rounded to well-rounded and is consolidated in a dark-maroon clay matrix. Mudstone and fine-grained sandstone are abundant between 5,130 and 5,172 ft in depth. Bleaching appears to be randomly distributed in the cores and plugs.

Composition and grain size analysis

Composition and grain size analysis are summarized in Table 1. The composition of the Argenta Formation displays relatively high contents of quartz (mono- and polycrystalline) and feldspar (anorthite, orthoclase, plagioclase) that range between 9.50% and 72.50% (average = 49.60%, n = 13) and between 1.00% and 29.50% (average = 7.54%, n = 13), respectively. The content of lithic materials is strongly variable and has a maximum of 18% (n = 13). The composition of the Lower Mt. Simon Sandstone is marked by a compositional differentiation between the units A and B. The unit A is more felspathic than the unit B. The content of feldspar varies from 3.00% to 17.75% (average = 10.39%, n = 10) in the unit A, while the content of feldspar ranges from 0.25% to 14.50% (average = 5.40%, n = 25) in the unit B. The content of quartz is similar with averages of 51.48% (n = 10) and 58.29% (n = 25), respectively. The lithic compositions of both units have averages of 5.88% (n = 10) and 3.56% (n = 25), respectively. The Middle and Upper Mt. Simon Sandstone units have similar compositions with high contents of quartz and very low contents of feldspar (less than 3.00%) and lithic materials (less than 3.00%). The contents of quartz range from 66.25% to 82.00% (average = 71.45%, n = 8) in the unit C, from 62.25% to 88.50% (average = 74.14%, n = 9) in the unit D, and from 64.25% to 87.25% (average = 76.32%, n = 7) in the unit E. Illite is the major authigenic mineral, but kaolinite traces are present in the Argenta Formation and the unit A of the Mt. Simon Sandstone.

The cross-plot Sorting (σ) vs Mean (φ) shows that the rock samples of the Argenta Formation and Mt. Simon Sandstone are dominantly medium- to fine-sized and poorly to moderately sorted (Figure 7). The Argenta Formation ranges from very coarse- to fine-grained sandstone, with an average of medium sand. The Argenta Formation is largely moderately sorted. The Lower Mt. Simon Sandstone (units A and B) covers a large area of clustering from very coarse silt to very coarse sand, but the average grain size is dominantly medium sand. The sorting ranges from very poorly sorted to moderately sorted with an average in moderately sorted for the Lower Mt. Simon Sandstone (unit A). Unit B of the Lower Mt. Simon Sandstone is finer than unit A of the Lower Mt. Simon Sandstone, which displays a distinct shift to fine materials. The Middle Mt. Simon Sandstone (units C and D) is centered in an area of medium- and fine-sized sands and is poorly to moderately sorted. The Upper Mt. Simon Sandstone (unit E) contains fine-grained sands and is poorly to moderately sorted.

The cross-plot Skewness (Ski) vs Sorting (σ) shows that the rock samples range from moderately well sorted to very poorly sorted and coarse-skewed to fine-skewed (Figure 7). The

Argenta Formation is near-symmetrical to fine-skewed towards medium- and fine-sand fractions. The coarser fraction ranges from coarse-skewed to fine-skewed. The Lower Mt. Simon Sandstone (units A and B) displays a skewness (Ski) that ranges from coarse-skewed to fine-skewed in all grain fractions. The Middle Mt. Simon Sandstone (units C and D) are dominantly fine-skewed in medium-sand fractions. The Upper Mt. Simon Sandstone (unit E) ranges from coarse-skewed to fine-skewed in fine-sand fractions. The variation of skewness shows a significant shift from positive to negative skewness, respectively, from the Argenta Formation to Lower Mt. Simon Sandstone (units A and B). Plotting of skewness (Ski) against kurtosis (KG) of the Argenta Formation and Mt. Simon Sandstone lie within the very platykurtic range (Figure 7).

Table 1: Descriptive statistical analysis for the grain size parameters from the Argenta Formation and the Mount Simon Sandstone.

Grain size parameters					
Formation/Member		Mean (Φ)	Sorting (σ)	Skewness (Ski)	Kurtosis (KG)
Argenta Formation	Max.	2.65	1.61	0.32	0.72
	Min.	-0.33	0.51	-0.32	0.50
	Ave.	1.51	0.84	0.04	0.63
Mount Simon Sandstone					
Lower					
Unit A (Arkose)	Max.	4.27	1.27	0.31	0.81
	Min.	-0.11	0.44	-0.42	0.50
	Ave.	2.29	0.72	0.00	0.63
Unit B	Max.	4.40	1.49	0.26	1.11
	Min.	0.46	0.50	-0.29	0.53
	Ave.	1.94	0.84	-0.02	0.67
Middle					
Unit C	Max.	2.43	0.90	0.49	0.77
	Min.	1.04	0.39	-0.11	0.56
	Ave.	1.61	0.69	0.21	0.65
Unit D	Max.	2.84	0.97	0.19	0.80
	Min.	0.98	0.44	-0.23	0.56
	Ave.	2.17	0.66	0.03	0.67
Upper					
Unit E	Max.	2.73	0.97	0.18	0.79
	Min.	0.66	0.45	-0.42	0.56
	Ave.	2.35	0.67	-0.02	0.66

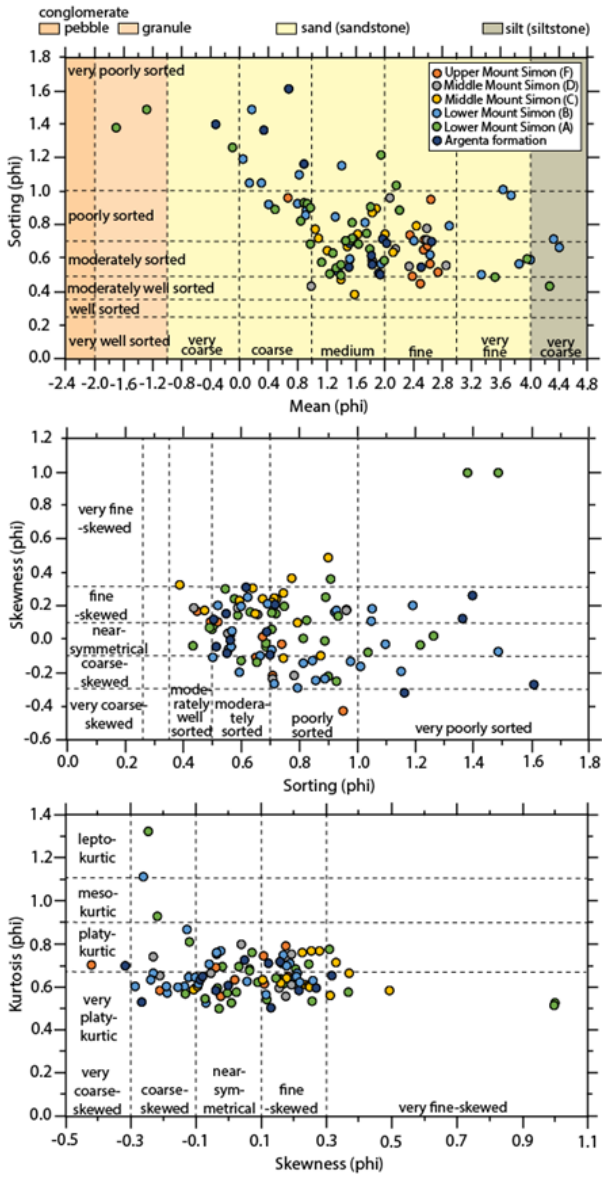

Figure 7. Bivariate plots showing the grain size versus sorting, the sorting versus skewness, and the skewness versus kurtosis. The dashed lines show the descriptions of the grain size parameters.

Sedimentology

Lithofacies associations

Four LFAs were identified in the Argenta Formation and Mt. Simon Sandstone intervals of the T.R. McMillen #2 well: (1) gravely braided river in alluvial-fluvial deposits within incised valleys, (2) sandy braided river in a fluvial plain, (3) aeolian dunes in a fluvial plain, and (4) sandy braided river delta deposits to lagoon or lacustrine fine-grained deposits. In total, twelve lithofacies are identified and summarized in Tables 2 and 3. Detailed descriptions and interpretations are presented below.

Lithofacies association LFA-A: waterlain alluvial fan

Description: LFA-A contains the lithofacies A1 and A2. Lithofacies A1 is the coarsest facies of the alluvial-fluvial plain. It comprises 1 to 5 inches-thick, fining-upward sequences that are composed of massive (Gcm) or crudely stratified (Gh), clast-supported to sandy matrix-supported conglomerates in a dark-maroon to dark-brown, coarse-grained arkose sandstone matrix. Size fraction varies from very coarse-grained sand to small pebble. Grains are dominantly subangular to subrounded, poorly sorted, and show a normal grading. The grains are dominantly smooth and matte. Conglomerates are polymictic and comprise quartz, lithic arkose, arkose, siltstone, mudstone, and rhyolite clasts. Basal scours are common. In the FMI log, the difference of resistivity appears massive and irregular with the recognition of coarse-grained sands, granules, and pebbles.

Lithofacies A2 is a faintly horizontal (GRm), low-angle (GRp) to trough (GRt) cross-stratified, pebbly-supported sandstone (Figure 3). The matrix is composed of a dark-maroon to dark-brown, fine- to coarse-grained arkose sandstone. The lithology of granules and pebbles is similar to lithofacies A1. Individual beds eroded at the top and base contacts are 1 to 3 inches thick, locally thicker. A normal grading at the bottom of beds is common. In the FMI log, the difference of resistivity appears planar parallel and trough cross-stratified with the recognition of coarse-grained sands, granules, and pebbles.

Interpretation: LFA-A represents the transition between distal section of waterlain alluvial fans (lithofacies A1) and a proximal section of fluvial braided river plain (lithofacies A2) bordered by a floodplain (see LFA-B for description and interpretation). The lithofacies A1 records channel-fill deposits in a waterlain alluvial fan system, commonly characterized by well sorted, sandy to gravelly lenses and sheets that were formed in high-energy water flow conditions in the absence of fine-grained suspension materials (Miall, 1977; Moscariello, 2018). The massive structure was developed in high-energy and persistent stream flows by traction currents and low-sinuosity channel systems (Miall, 2010). The lithofacies A2 represents fluvial channel bars formed by bedload-related traction currents by transport and saltation of grains (Maciaszek et al., 2019). The normal grading, forming locally gravel-sand couplets, was formed by unsteady sediment dumping under supercritical bedload currents (Blair, 1987; Moscariello, 1998). Proximal alluvial fan facies are associated with turbulent and supercritical flows of debris flow deposits. In the T.R. McMillen #2 well, none of these alluvial fan facies have been identified.

Lithofacies association LFA-B: fluvial braided river

Description: LFA-B includes five distinct lithofacies: (1) massive sandstone (lithofacies B1); (2) horizontal to low-angle cross-stratified sandstone (lithofacies B2); (3) trough cross-stratified sandstone (lithofacies B3); (4) heterolytic sandstone, siltstone, and mudstone (lithofacies B4); and (5) mudstone (lithofacies B5). Lithofacies B1 is characterized by 1 to 3 inches-thick, fining-upward sequences that are commonly composed of massive coarse- to pebble-grained, poorly to moderately sorted sandstone (Sm) at the bottom, overlain by fine- to medium-grained, moderately sorted sandstone (Figure 4). Dispersed coarse-grained, sand- to pebble-sized grain fraction of quartz, feldspar, lithic fragments, and rare mud intraclasts are locally present in this lithofacies. Erosive surface contacts are common. In the FMI log, the difference of resistivity appears massive. The lithofacies B1 vertically grades, fine- to very coarse-grained, faintly

horizontal, crinkly or low-angle cross-stratified sandstone (Sh), here attributed to the lithofacies B2. The angle of distinct stratification is lower than 5°. Rare scour surfaces are observed at the bottom of individual beds. In the FMI log, the difference of resistivity shows an appearance of planar parallel, straight, and irregular sets.

Lithofacies B3 is marked by fine- to coarse-grained, moderately to poorly sorted, trough cross-stratified sandstone (St) (Figure 4). The angle of distinct stratification is lower than 20°. Like lithofacies B2, dispersed coarse-grained, sand- to pebble-sized grains are locally observed. Local ripples are also observed. The individual beds vary from a few inches to 3 ft in thickness. Additionally, they can be marked by a scour surface at the bottom that is draped by regular to irregular single mud partings or layers (St_d; $^1/_{10}$ - $^1/_2$ in thick). In the FMI log, the difference of resistivity shows unidirectional sets of trough cross-stratification.

Lithofacies B4 consists of very fine- to fine-grained, rarely coarse- to medium-grained, moderately to well sorted sandstone with flaser-type and wavy-type laminations. Flaser laminations (Hr) show small lenses of mud or silt within coarsely grained sands. They are concave upwards and fill the depressions between poorly visible ripples. The wavy laminations (Hw) form alternating continuous thick, sandy and thin, muddy layers within the channel-fill deposits. Locally, the depressions of wavy laminations (Hr_d) are filled by single mud drapes ($^1/_{10}$ - $^1/_2$ in thick). When the amount of mud increases, lenticular laminations (Hr) are common in this lithofacies. These sedimentary structures are near-symmetrical, convex both upwards and downwards, lens-like coarser-grained sands (e.g., muddy sand) in a matrix of finer-grained materials (e.g., mudstone). Their maximum thickness and length are ½ in and $^1/_4$ to more than 5 in, respectively. No grading is observed. The individual beds range from 1 to 5 in thick, and the bottom contact can be marked by an erosive surface. In the FMI log, the difference of resistivity shows thin, alternating dark and light colors with planar parallel to wavy irregular appearance.

Lithofacies B5 is characterized by thin, individual beds, ranging from ¼ to 2 inches, locally thicker, of pure mudstone (Fm) and finely planar, locally crinkly, laminated mudstone (Fl) (Figure 5). Rare, small-scale, vertical to oblique bioturbation is preserved locally. In the FMI log, the difference of resistivity shows light-colored massive or planar appearance.

Interpretation: LFA-B represents low-energy channel and floodplain deposits in a fluvial system. The finer materials than in LFA-A indicate less kinetic energy. Lithofacies B1 to B3 may represent small-scale fluvial channels formed by low-energy traction flows. Thin mudstone layers within sandstones, which show a vertically normal grading, can be interpreted as crevasse splay channels on levee breaching or overbanking along channel bars or floodplains (Miall, 1996; Cain and Mountney, 2009). When the bedload-related transport is higher than the suspended-load transport, ripples can be formed on the top foreset of channel bars. Heterolithic structures were principally formed when low-energy water flow currents changed alternatively. Sandy materials were deposited under the highest flow regime (i.e., <0.5 m/s), while fine-grained materials were formed atop the ripples in intervals of slack to almost stagnant water. Erosive surfaces recorded the changes of flow regime (Maciaszek et al., 2019). The finest materials of the braided river system were deposited by suspension in a floodplain environment (Miall, 1996).

Lithofacies association	Lithology	Code	Sedimentology	Characteristics in FMI		Interpretation
LFA-A Alluvial-fluvial system	A1: Massive sandy conglomerate	Gcm Gh	Massive or crudely stratified clast-supported to sandy matrix -supported conglomerates with a coarse-grained sandstone, composed of subangular to subrounded granules and pebbles of polymitic fragments (quartz, feldspar and lithic). Beds range from 1 to 5 inches in thickness. Local scour surfaces at the base.	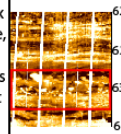	Massive, irregular appearance with granules and gravels.	Reworking of sediments in high hydrodynamic conditions by strong subaqueous tractive current forming channel deposits.
	A2: Cross-stratified sandy conglomerate	GRm GRp GRt	Faintly horizontal stratified, low-angle to through cross-stratified clast-supported conglomerate to very coarse-grained sandstone, poorly sorted, composed of subangular to subrounded granules and pebbles of quartz, feldspar and lithic fragments. Beds range a few inches to 1-3 feet in thickness. Sharp erosive surfaces atop base and top.	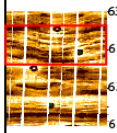	Planar parallel to through cross-stratified appearance with granules and gravels.	Reworking and transport of sediments in hyperconcentrated conditions by to tractional flows forming possible channel bars or channel deposits.
LFA-B Fluvial system	B1: Massive sandstone	Sm	Fine- to very coarse-grained, moderately to poorly-sorted massive sandstone, locally normal grading. Absence of sedimentary structures. Local dispersed subangular granules and pebbles of quartz, feldspar and lithic fragments, and mud intraclasts (< 1/2 to 3 inches). Beds range a few inches to 1-3 feet in thickness. Local erosive surfaces at the base.	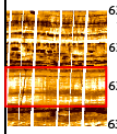	Massive appearance.	Rapid deposition of hyperconcentrated to tractional flows in crevasse splay channels or channel deposits.
	B2: Horizontal to low-angle cross-stratified sandstone	Sh	Fine- to very coarse-grained, moderately to poorly-sorted sandstone with horizontal to low angle cross-stratification (less than 5°). Local dispersed subangular granules and pebbles of quartz, feldspar and lithic fragments. Beds range a few inches to 1-3 feet in thickness. Rare scour surfaces at the base.	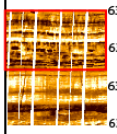	Sets of planar, straight or irregular appearance.	Predominantly tractional deposition from bedload transport in transition between lower and upper flow regime forming crevasse splay channels or channel deposits.
	B3: Trough cross-stratified sandstone	St St_d	Fine- to very coarse-grained, moderately to poorly-sorted sandstone with unidirectional trough crossed stratification (less than 20°). Local thin normal grading. Regular to irregular thin single mud drapes (1/10 to 1/2 inches in thickness). Local dispersed subangular granules and pebbles of quartz and lithic fragments. Beds range a few inches to 1-3 feet in thickness.	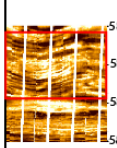	Unidirectional sets of trough cross-stratified appearance.	Migration of subaqueous sandy dunes in unidirectional lower flow regime, and deposition by settling down of suspensed load in standing water.
	B4: Heterolitic sandstone and siltstone	Hr Hr_d Hw	Heterolithic structures composed of very fine- to fine-grained, rarely coarse- to medium-grained, sandstone, fine to coarse-grained siltstone and mudstone with wavy, lenticular or flaser laminations. Locally thin parallel to wavy laminations of single muddy drapes (1/10 to 1/2 inches in thickness). Non- to weak normal grading occurs locally. Sharp or erosive surfaces at the base. Beds range from 1 to 5 inches in thickness.	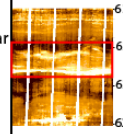	Planar parallel to wavy irregular appearance.	Alternating traction process with subaqueous ripples in unidirectional lower flow regime and deposition by decantation of suspended load deposited in a levee overbank (flood plain)
	B5: Mudstone	Fm Fl	Brick red to greeen mudstone, massive to thin parallel lamination. Beds range from 1/4 inches to 1-2 feet in thickness.	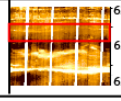	Massive or planar appearance.	Floculation of clay, suspension settling deposited in a levee overbank (flood plain).

Table 2: Description and interpretation of lithofacies and lithofacies associations based on high-resolution Fullbore Formation Micro-Imager (FMI) and gamma-ray logs of the T.R. McMillen#2 borehole, Christian County (Illinois).

Lithofacies association	Lithology	Code	Sedimentology	Characteristics in FMI		Interpretation
LFA-C Aeolian-fluvial system	C1: Planar stratified sandstone	Sm Sh	Massive to faintly horizontal stratified medium-grained, moderately sorted, sandstone with local horizontaly stratified dispersed subangular granules and coarse-grained sands of quartz (lag deposit). Beds range a few feet in thickness.	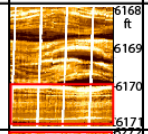	Planar, straight appearance.	High windblow velocities or grainfall deposition related to the zones of flow separation on horizontal surfaces (accretion stage).
	C2: Large cross-stratified sandstone	Sc Sc_d Sp Scr	Fine- to medium-grained, well-sorted sandstone with bidirectional crossed stratification (15-30° in angle) and low-angle cross-stratification (5-15° in angle; pinstripe sets). Rare climbing ripples and mud drapes. Contacts are locally erosional and planar. Beds range a few feet in thickness.	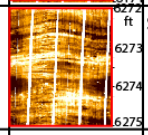	Sets of crossed stratification in appearance.	Migration of aeolian sandy dunes in bimodal upper windblow regime by saltation and sand avalanche if slip face exceeds 34°.
LFA-D Braided river delta-lacustrine/ lagoon system	D1: Bioturbated cross-stratified sandstone	St Sc Sc_i	Fine- to medium-grained, moderately to poorly-sorted small-scale through cross-stratified sandstone, locally normal gradded and accumulation of siltstone and mudstone at the top. Bioturbation in muddy sandstone composed of fine sandstone and fine materials. Local layers of granules and pebbles. Beds range from a few inches to 1-2 feet in thickness.	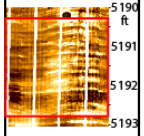	Bidirectional sets of crossed stratification in appearance. Vertical bioturbation.	Low flow regime and low current velocities caused by the interaction of river outflows and lacustrine/lagoon wave currents in a deltaic front environment forming mouth sand bars.
	D2: Bioturbated horizontal to planar stratified muddy sandstone and mudstone	Hr Hr_d Hw	Heterolithic structures composed of thin bedded of very fine- to medium-grained, medium-grained, sandstone and mudstone with wavy, lenticular or flaser laminations. Abundance of bioturbation. Beds range from 1 inches to 1 foot in thickness.	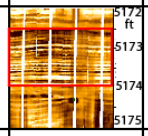	Sets of planar to wavy stratified in appearance. Vertical bioturbation.	Fall out and small-scale ripple migration in relative high energy flow regime and large input of braided river delta.
	D3: Bioturbated mudstone	Fm Fl	Massive and finely stratified mudstone, strongly biotubated. Local thin layers of very fine- to medium-grained, moderately sorted sandstone. Rare deformation structures. Beds range from a few inches to 1-2 feet in thickness.	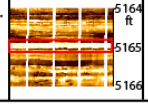	Massive appearance. Vertically crossed by bioturbation.	Floculation of clay by suspension settling. Possible turbidity currents formed in a delta-front slope of a lacustrine/lagoon environment.

Table 3: Description and interpretation of lithofacies and lithofacies associations based on high-resolution Fullbore Formation Micro-Imager (FMI) and gamma-ray logs of the T.R. McMillen#2 borehole, Christian County (Illinois).

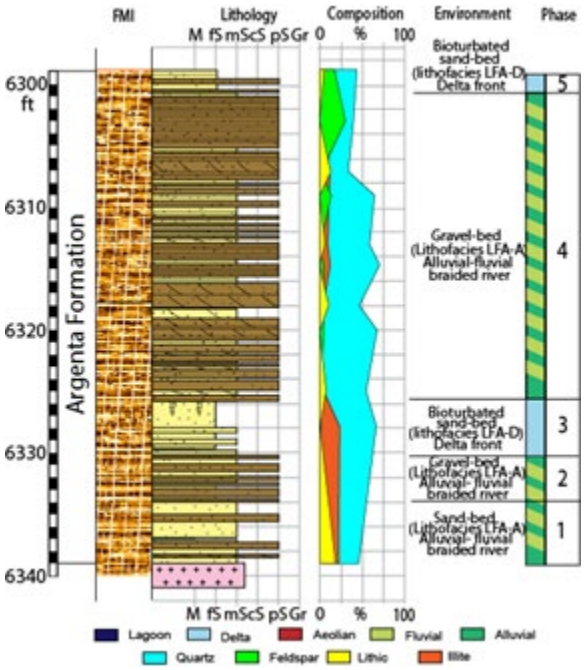

Figure 8. Lithostratigraphic column, FMI log and composition of the Argenta Formation showing lithofacies associations and paleoenvironmental interpretation.

Lithofacies association LFA-C: aeolian dunes

Description: LFA-C includes two lithofacies: (1) planar stratified sandstone (lithofacies C1) and (2) large cross-stratified sandstone (lithofacies C2). Lithofacies C1 comprises massive (Sm), faintly horizontal stratified (Sh), medium-grained, moderately sorted sandstone (Figure 6). Horizontally dispersed, subangular, coarse-grained sands and granules of quartz, which appear locally as pocket structures, are common in this lithofacies. The individual beds have a maximum thickness of a few feet. In the FMI log, the difference of resistivity appears planar or straight.

Lithofacies C1 normally grades to lithofacies C2, which is characterized by single to multiple bedsets of fine- to medium-grained, moderately to well sorted sandstone with bidirectional, low-angle (Sp), and crossed (Sc) stratifications (Figure 6). Their angle is comprised respectively between 5° and 15° and between 15° and 30°. In the FMI log, the difference of resistivity appears planar or straight. The cross-stratified bedsets are often eroded by an overlying single bedset. Rare climbing ripples (Src), in which muddy materials can fill the depressions (Src_d), are observed. The individual beds are marked by an erosive surface at the bottom, and they range a few feet in thickness. In the FMI log, sets of crossed-stratification is visible by the difference of resistivity.

Interpretation: LFA-C represents the migration of aeolian sandy dunes mainly by saltation transport on exposed channel bars, splay crevasses, or overbanks on floodplains (Lovell and Bowen, 2013). High windblown velocity caused sand deflation and accretion surfaces on the flat-related sand dunes. The deflation pattern is marked by the removal of finer sediments by wind

activity, leaving coarse-grained sediments, such as coarse-grained sand, granules, and pebbles, which cannot be moved in suspension or saltation (Reineck and Singh, 1986). The accretion surface is marked by the deposition of fine-grained sediments by migration of sand sheets forming a sand ridge or by sand avalanche if the slip face exceeded at least 34°. Normal grading is characterized by planar stratified sandstone at the base and small- to large-scale cross-stratified sandstone at the top.

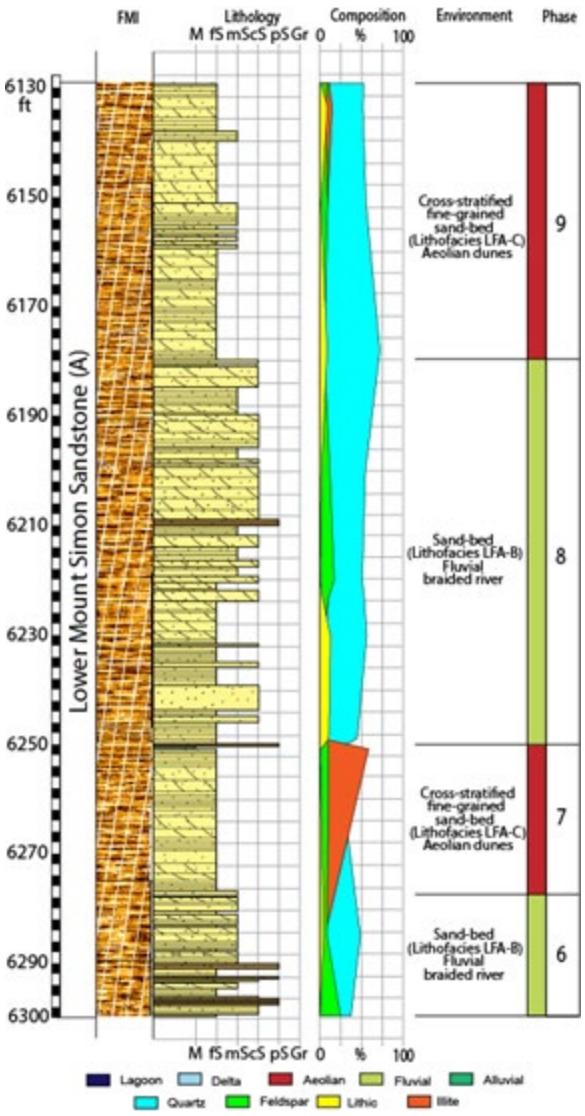

Figure 9. Lithostratigraphic column, FMI log and composition of the Unit A (Arkose) of the Lower Mt. Simon Sandstone showing lithofacies associations and paleoenvironmental interpretation.

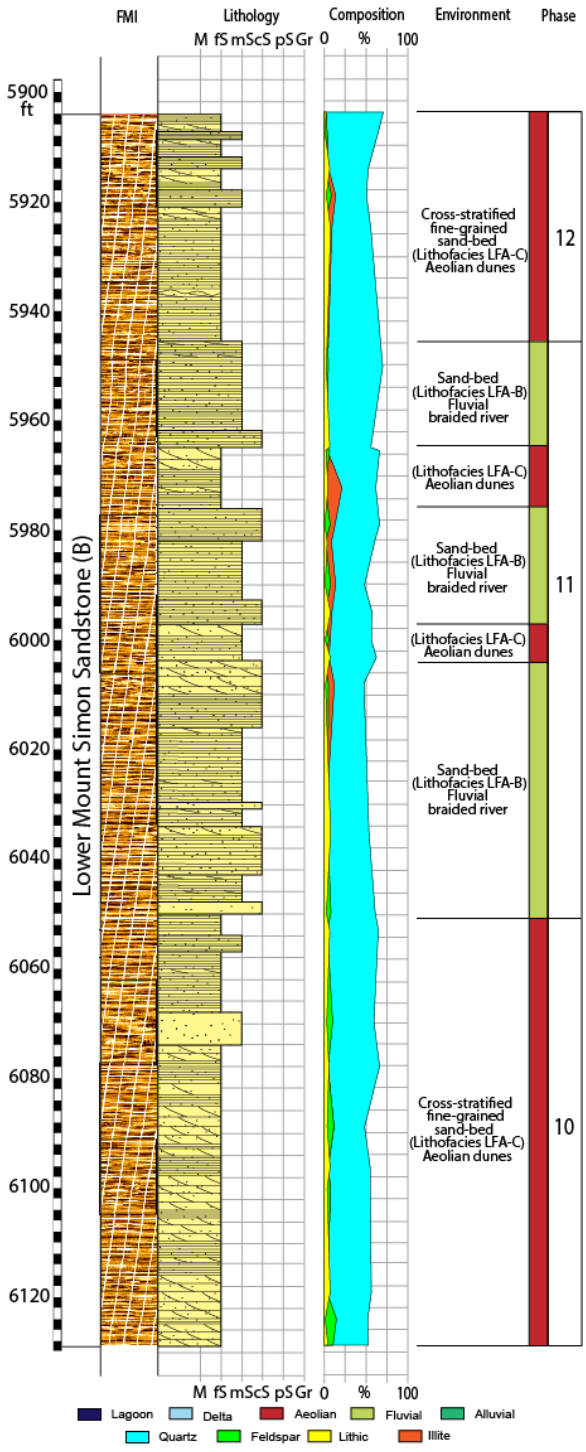

Figure 10. Lithostratigraphic column, FMI log and composition of the Unit B of the Lower Mt. Simon Sandstone showing lithofacies associations and paleoenvironmental interpretation.

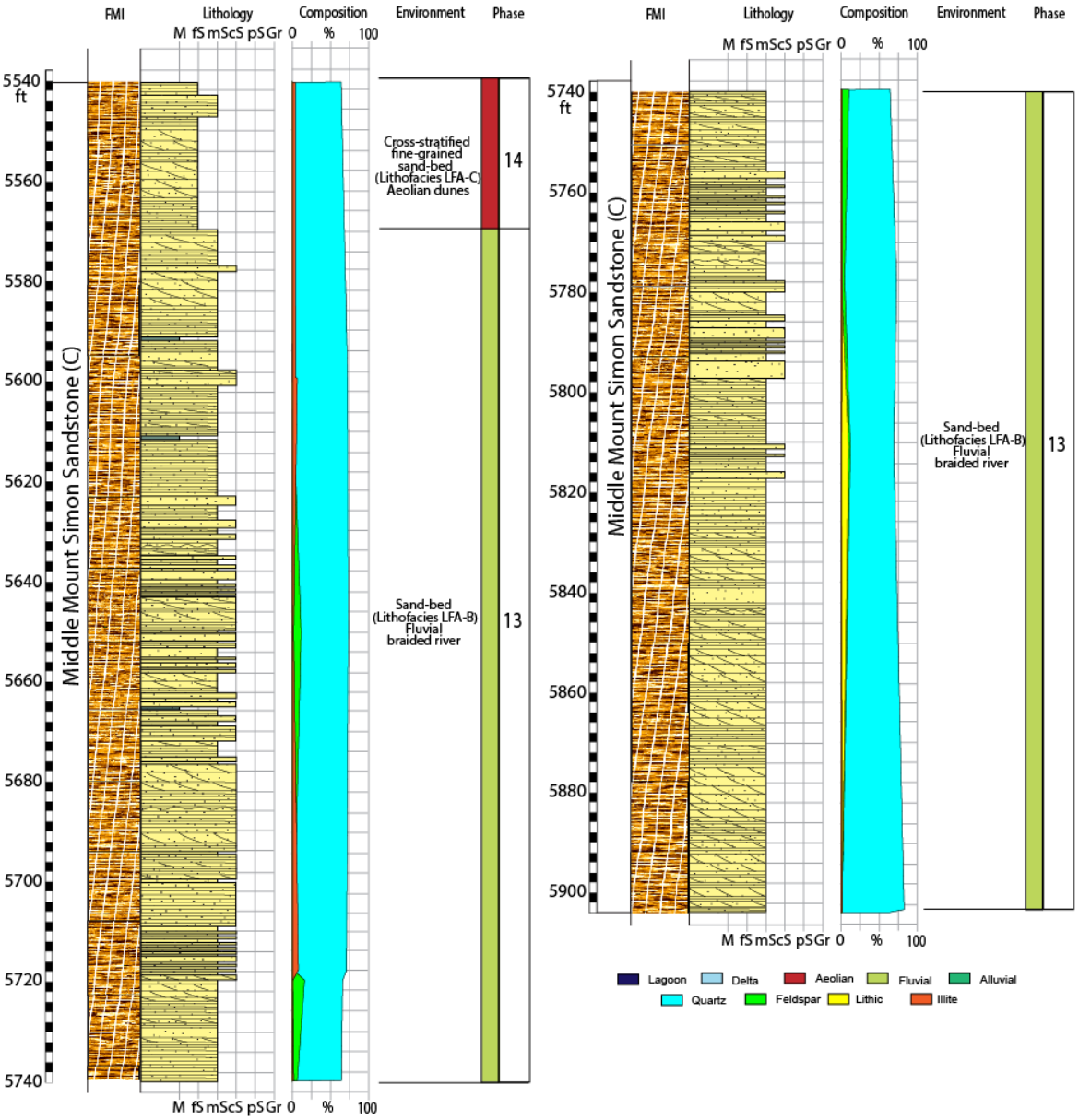

Figure 11. Lithostratigraphic column, FMI log and composition of the Unit C of the Middle Mt. Simon Sandstone showing lithofacies associations and paleoenvironmental interpretation.

Lithofacies association LFA-D: braided river delta

Description: LFA-D includes three distinct lithofacies: (1) bioturbated cross-stratified sandstone (lithofacies D1), (2) bioturbated horizontal to planar stratified muddy sandstone and mudstone (lithofacies D2), and (3) bioturbated mudstone (lithofacies D3). Lithofacies D1 is characterized by fine- to medium-grained, poorly to moderately sorted sandstone with massive structure (Sm), planar parallel (Sh) to trough crossed-stratification (St). Additionally, graded bedding, erosional bases, and bottom mud drapes (St_d) can be observed locally. Interlayers of granules and pebbles are common. Vertical to oblique bioturbation can be identified in the FMI log. The individual beds range from a few inches to 2 ft thick. In the FMI log, the difference of resistivity shows bidirectional sets of crossed-stratification.

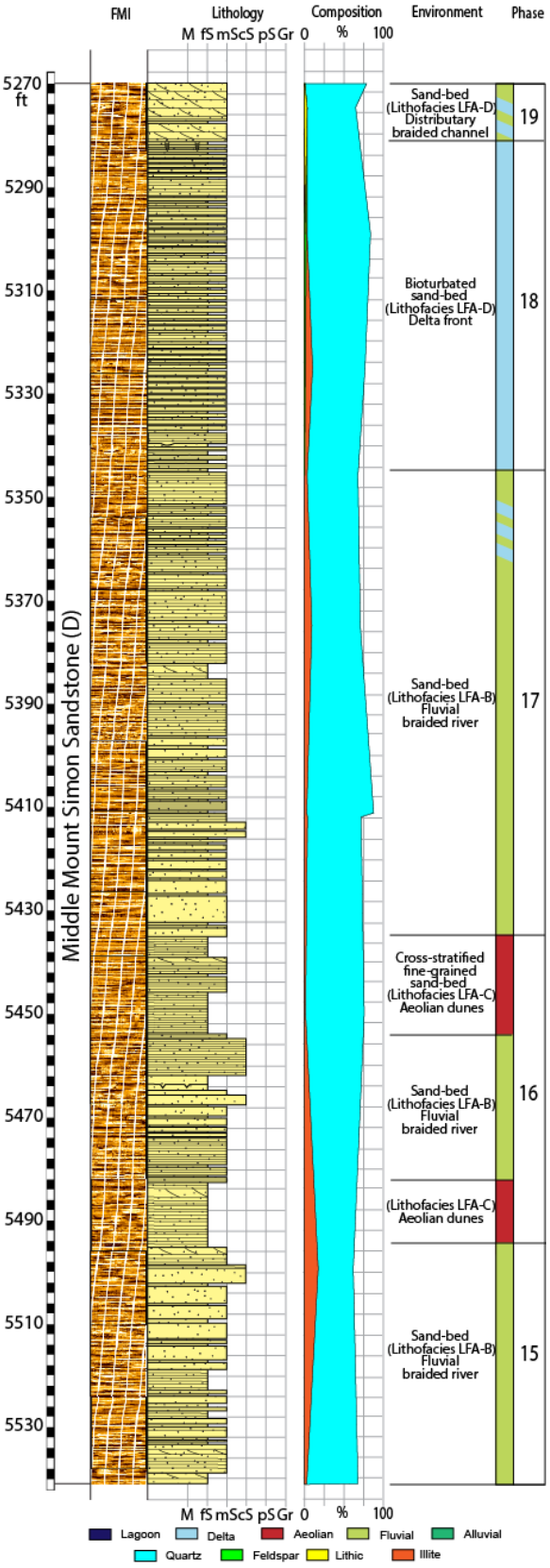

Figure 12. Lithostratigraphic column, FMI log and composition of the Unit D of the Middle Mt. Simon Sandstone showing lithofacies associations and paleoenvironmental interpretation.

Lithofacies D2 consists of thin-bedded, alternating mudstone and fine- to medium-grained, moderately sorted sandstone with heterolytic structures (i.e., flaser, wavy, and lenticular structures). Occasionally, small-scale vertical and oblique bioturbation can be identified in the FMI log. The individual beds range from 1 in to 1 ft thick. In the FMI log, the difference of resistivity shows alternating sets of light and dark, planar to wavy stratification.

Lithofacies D3 comprises strongly bioturbated mudstone with massive (Fm) or finely stratified (Fl) structures. Lithofacies D3 is often associated with the lithofacies D2. Local, thin layers of very fine- to medium-grained, moderately sorted sandstone are present. Rare deformation structures can be identified in the FMI log. The individual beds range from 1 in to 2 ft thick. In the FMI log, the difference of resistivity appears massive.

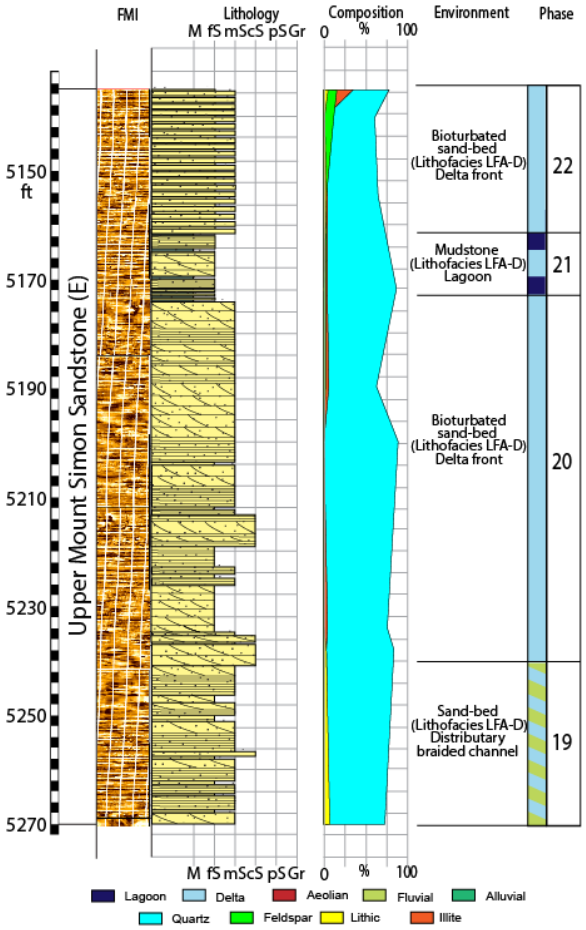

Figure 13. Lithostratigraphic column, FMI log and composition of the Unit E of the Upper Mt. Simon Sandstone showing lithofacies associations and paleoenvironmental interpretation.

Interpretation: LFA-D represents a braider river delta fan system. The lithofacies D1 can be interpreted as distributary braided channels on delta-front lobes that are commonly characterized by clast debris, basal scour surfaces, and their thin bedding (Bhattacharya and Walker, 1991). The bidirectional trough crossed-stratification was produced by reversal currents and the direction of migration of the sand-sized sediments, which indicates a tidally influenced environment. The lithofacies D2 represents mouth bars deposited by alternating oscillatory and traction regimes, forming subaqueous ripples under low flow regime and deposition of fine-

grained suspended load (Dalrymple, 2010). The finer-grained materials of the lithofacies D3 were deposited in lagoon or lacustrine environments under flocculation of clay suspension or suspension settling from standing water (Rogers and Astin, 1991; Miall, 2006). LFA-D is marked by an intensive bioturbation.

Depositional sequence

A framework of depositional sequences for the Argenta Formation and Mt. Simon Sandstone is proposed in this report. The sequences are based on the variation of LFAs that were defined by the variation of resistivity in the FMI log. The Argenta Formation comprises five distinct depositional sequences (DS1 to DS5) (Figure 9). The first depositional sequence (DS1) comprises 13-ft-thick sandy deposits (lithofacies A2) that are overlain by 6-ft-thick gravelly sandstones and sandy conglomerates (lithofacies A1) deposited (DS2) in a distal alluvial waterlain fan system. The alluvial deposits vertically progress to braided river delta facies (lithofacies association LFA-D). This depositional sequence (DS3) contains approximately 8-ft-thick distinct facies that were deposited successively in braided channels and distributary braided rivers (lithofacies D1). No delta front facies (lithofacies D2 and D3) were identified. Prior to overlying the depositional sequences, DS4 is thicker and it comprises 19-ft-thick gravelly sandstones and sandy conglomerates (lithofacies A1). The top of the Argenta Formation shows a 3-ft-thick, fining-upwards, coarse- to fine-grained sandstone, locally bioturbated (lithofacies D1).

The Mt. Simon Sandstone contains sixteen distinct depositional sequences (DS6 to DS22). The Lower Mt. Simon Sandstone contains six depositional sequences (DS6 to DS12). The unit A (Arkose) comprises, from the base to the top: (1) DS6, including 22-ft-thick fluvial sandstone (LFA-B that comprises the lithofacies B1 to B5); (2) DS7, including 27-ft-thick, cross-stratified, medium- to fine-grained sandstone (LFA-C, with mainly the lithofacies C2); (3) DS8, including 71-ft-thick fluvial sandstone (LFA-B) and local aeolian materials; (4) DS9, including 50-ft-thick, cross-stratified, medium- to fine-grained sandstone (LFA-C) (Figure 10).

The unit B starts with 80-ft-thick of DS10 that comprises a cross-stratified, medium- to fine-grained sandstone (lithofacies C2 of LFA-C), vertically evolving to faintly horizontal or low-angle, cross-stratified, coarser-grained sandstone at the top (lithofacies C1 of LFA-C) (Figure 11). A fluvial interval with ephemeral aeolian sand deposits is identified. This depositional sequence (DS11) comprises successively 43-ft-thick fluvial sandstone (LFA-B), 6-ft-thick aeolian sandstone (LFA-C), 22-ft-thick fluvial sandstone (LFA-B), 11-ft-thick aeolian sandstone (LFA-C), and 20-ft-thick fluvial sandstone (LFA-B) (Figure 11). The unit B ends with DS12 that comprises 40-ft-thick aeolian, faintly horizontal to low-angle, cross-stratified sandstone (lithofacies C1 of LFA-C) (Figure 11).

The Middle Mt. Simon Sandstone contains seven distinct depositional sequences (DS13 to DS19) (Figures 12 and 13). The facies of the unit C are dominantly fluvial (lithofacies LFA-B). A depositional sequence (DS13) comprises approximately 335-ft-thick, fining-upward cycle of massive sandstone (lithofacies B1), horizontal to low-angle cross-stratified sandstone (lithofacies B2), and trough cross-stratified sandstone (lithofacies B3) at the base, which evolve to massive sandstone (lithofacies B1), horizontal to low-angle cross-stratified sandstone (lithofacies B2), heterolytic sandstone, siltstone, and mudstone (lithofacies B4), and mudstone (lithofacies B5) at the top. The top of the unit C is marked by 28-ft-thick aeolian sandstone (LFA-C) that comprises planar stratified sandstone (lithofacies C1) and large cross-stratified sandstone (lithofacies C2).

The lowermost part of the unit D shows similar fluvial facies than previously. Fluvial sandstones (LFA-A–B) are the dominant facies. DS15 is a 47-ft-thick, massive, horizontal and

low-angle cross-stratified sandstone facies (lithofacies B1 and B2) that is overlain by a 61-ft-thick deposition sequence DS16 and marked by aeolian-dominated sandstones (LFA-C). A fluvial interval (LFA-B that here is represented dominantly by lithofacies B1 and B2) between 5,453 and 5,481 ft deep has been identified. DS17 shows 87-ft-thick, fluvial, massive sandstone (lithofacies B1) and horizontal to low-angle cross-stratified sandstone (lithofacies B2). At 5,360 ft deep, a transition between fluvial and delta facies is recognized. DS18 is marked by 66-ft-thick, thin bedded, delta front facies that show alternating bioturbated massive to planar-stratified sandstone (lithofacies D1) and bioturbated horizontal to planar stratified muddy sandstone (lithofacies D2), locally overlain by bioturbated mudstone (lithofacies D3). The top of the unit D shows a short fluvio-deltaic sandstone facies (10 ft thick) that are mainly formed by cross-stratified sandstones (LFA-B and LFA-D).

The Upper Mt. Simon Sandstone (unit E) is dominantly deltaic (Figure 14). The base of the unit E is marked by a transitional zone between fluvial and deltaic deposits. DS19 comprises 30-ft-thick braided channel (lithofacies B1 to B3 of LFA-A) and distributary braided channel (lithofacies D1 of LFA-D) facies. DS20 shows 69-ft-thick, massive, planar parallel to trough crossed-stratified sandstones (lithofacies D1 of LFA-D). A short lagoonal interval (LFA-D) is recognized in DS21. This sequence comprises 9-ft-thick, thin-bedded alternating heterolytic sandstones (lithofacies D2) and mudstones (lithofacies D3) with local interbeds of trough cross-stratified sandstones (lithofacies D1). The top of the unit E shows 30-ft-thick, thin-bedded delta front facies that show alternating bioturbated massive to planar-stratified sandstone (lithofacies D1) and bioturbated horizontal to planar stratified muddy sandstone (lithofacies D2), locally overlain by bioturbated mudstone (lithofacies D3).

Interpretation

Composition and grain size interpretation

Grain-size parameters, such as mean (φ), sorting (σ), skewness (Ski) and kurtosis (KG), are powerful tools used to reconstruct the depositional environment of sediments. This concept assumes that these parameters' reliability reflects differences in the fluid-flow mechanisms of sediment transportation and deposition (Sutherland and Lee, 1994). Variation of skewness displays a significant shift from positive to negative skewness, respectively, from the Argenta formation to Lower Mt. Simon Sandstone (units A and B). This suggests that, with selective erosion from crystalline basement paleo-highs (e.g., monadnocks), the transported sediment will be finer (from granule to sand in size), better sorted, and more negatively skewed than the source. Most fluvial sediments, producing sand dunes, display slightly positively skewed due to a high proportion of coarse grains (Folk, 1966) and because it is undergoing winnowing at the same time (Flemming, 2007). In some cases, the skewness can increase in the positive skew due to the decrease in the number of fines that can be removed as the grain size increases (Flemming, 2007). Variation of skewness in sand-sized population suggests a dominance of medium-grain-size population and a subordination of coarse and fine grain sizes, which gives either slight positive or negative skewness.

Skewness (Ski) associated with kurtosis (KG) can interpret the genesis of sediment by quantifying the degree of normality of its size distribution (Folk, 1966). The cross-plot Skewness (Ski) vs kurtosis (KG) shows that all rock samples of the Argenta Formation and Mt. Simon Sandstone lie within the very platykurtic to platykurtic range (Figure 7). Variation in the kurtosis

(KG) values reflects the flow characteristic of the depositing medium grain size population, and the finer size of platykurtic nature of sediments reflects the maturity of the sand. Generally, dune sands have positive skewness and are mesokurtic, while aeolian sands have positive skewness and are leptokurtic (Martins, 1965). Beach sands are normal or negative skew and leptokurtic (Martins, 1965). The grain size distribution shows that when sediment is removed by a unidirectional river or wind, the grains that can be transported in suspension or by saltation vary with the competency of the transport of medium-sized materials, without changes in fine materials, which can explain the positive skewness. In beach environments, transported material is submitted to bidirectional tidal currents, which means coarser materials may be carried inward and deposited on the beach and fine material may be carried out to the deeper water.

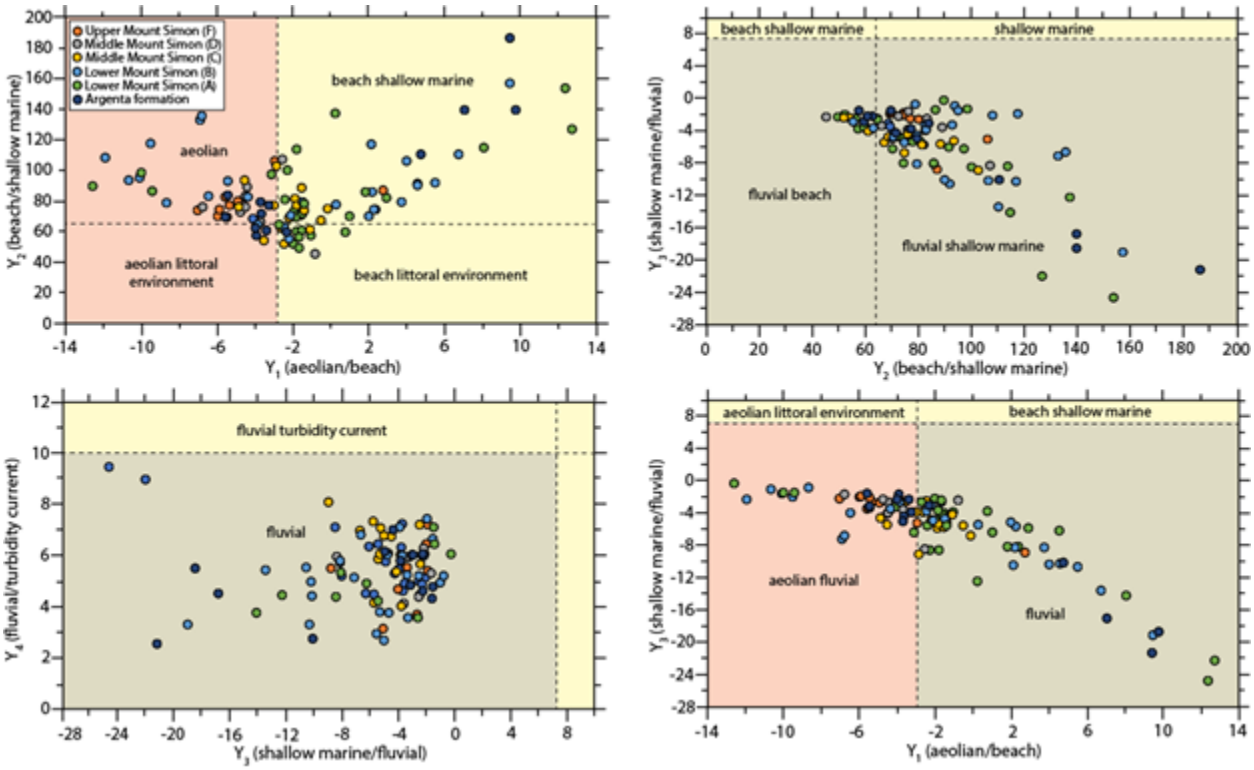

Figure 14. Plots of statistical method of linear discriminate function analysis from the formulae of Sahu (1964). The plots show the discrimination of paleoenvironments for the Argenta Formation and Mt. Simon Sandstone. Most of the samples have fluvial and aeolian origins.

The paleoenvironments can be determined using grain-size parameters' mean (M), sorting (SD), skewness (SK) and kurtosis (KG). The statistical method of linear discriminate function (LDF) analysis developed by Sahu (1964) can distinguish the nature of deposition of sediments. It was performed using the following equations:

(1) Aeolian/beach: $Y_1 = -3.5688\ \varphi + 3.7016\ \sigma^2 - 2.0766\ \text{Ski} + 3.1135\ \text{KG}$. If $Y > -2.7411$, the environment is "Beach", but if $Y < -2.7411$, the environment is "Aeolian".

(2) Beach/shallow agitated water: $Y_2 = 15.6534\ \varphi + 65.7091\ \sigma^2 + 18.1071\ \text{Ski} + 18.5043\ \text{KG}$. If $Y < 63.3650$, the environment is "Beach", but if $Y > 63.3650$, the environment is "Shallow marine".

(3) Shallow marine/fluvial environment: $Y_3 = 0.2852\ \varphi - 8.7604\ \sigma^2 - 4.8932\ Ski + 0.0482\ KG$. If $Y > -7.4190$, the environment is "Shallow marine", but if $Y < -7.4190$, the environment is "Fluvial".
(4) Fluvial/turbidity: $Y_4 = 0.7215\ \varphi + 0.403\ \sigma^2 + 6.7322\ Ski + 5.2927\ KG$. If $Y > 10.000$, the environment is "Turbidity", but if $Y < 10.000$, the environment is "Fluvial".

Plotting Y_1 against Y_2 displays a significant amount of aeolian sediments through the uppermost Argenta Formation and Mt. Simon Sandstone (Figure 14). The grains from a source of shallow marine/beach environments are dissociated in the cross-plots Y_2 vs Y_3 and Y_3 vs Y_4, from which all the samples fall (100%) in the fluvial process. Plotting Y_1 against Y_3 differentiates the fluvial process from aeolian sediments (Figure 14). The lowermost Argenta Formation is dominantly fluvial, while the uppermost is aeolian-fluvial. The linear discriminate function cross-plots do not show any marine conditions. In conclusion, the Argenta Formation and Mt. Simon Sandstone have been deposited in a dominant fluvial system with periodic deposition of aeolian dunes.

Depositional model and paleoenvironmental evolution

Argenta Formation

The Argenta Formation overlies a boundary surface (SU) at the contact with the Precambrian crystalline basement. SU represents erosion or a depositional hiatus in the sedimentary register. Depositional sequences DS1 to DS5 were deposited during a lowstand system tract (LST) stage (Figures 15 and 18). This stage is delimited at the base by SU and at the top by a transgressive surface (TS-1). This normal regression, developed in the Argenta Formation, forms a coarsening-up succession that is divided into two cycles composed of sandy conglomerates and pebbly sandstones (lithofacies LFA-A) separated by a distinctive muddy sandstone unit (lithofacies LFA-D). The lithofacies are interpreted as the vertical evolution from alluvial waterlain fan deposits to delta distributary channel rivers at the transition between a fluvial plain and a possible ephemeral lake (Figure 15). The variation of lithology at the base of the formation indicates rapid and prolonged changes in the ratio between sediment supply and the rate of accommodation space. The finer-grained sandy materials (lithofacies A2) at the base of the formation can be interpreted as the activation of the depositional system, which the coarser-grained materials were delayed from the source. Sandy sediments were driven by high-energy traction flow regime. This flow regime developed the migration of a low-relief sheet or dune elongated downstream as interpreted by the deposition of longitudinal channel fills and bars (Miall, 2006).

With the increase of sediment supply, (i.e., coarser materials composed of very coarse-grained sands, granules, and pebbles) the accommodation space progressively decreased, causing initial alluvial fan surface incision during the expansion of the drainage basin (Figure 15). Channel-lag pebble fill deposits (lithofacies A1) were accumulated under high-energy subaqueous traction regime in a waterlain alluvial-fluvial fan system complex. Due to widening of the flow into a braided river, the flood spreads out from the channels. This flow deposited sheet flood sediments such as gravel- to sand-sized dunes and antidunes (Reinech and Singh, 1986). Multiple waterlain flows occurred in the alluvial fan system that produced the truncation (e.g., scour- and fill-structures) of dunes and antidunes. The waterlain alluvial fan corresponds to base and midfan parts of an alluvial fan system complex. The fanhead part of the alluvial fan system accumulates debris flow deposits able to form fan-shaped bodies deposited on the slope toe of paleo-highs (e.g., monadnocks) or mountainous regions (Blissenbach, 1954; Reineck and Singh, 1986). The top of

this coarser material unit is inferred to be a minor maximum regressive surface (mrs-1) that marked a phase of retrogradation before the progradation of the overlapping of a fluvio-deltaic system complex (LFA-D) (Figure 18).

A rapid differential subsidence occurred through the basin with the progradation of delta front facies (LFA-D), which eastward evolved into lacustrine sediments. Wave-related reversal currents created bidirectional trough crossed-stratification by the migration of distributary channel dunes (lithofacies D1) in a transition between fluvial and delta-front lobe system complexes. The distributary channel dunes vertically graded to mouth bar deposits. The top of this sequence is inferred to be a local or regional minor erosion surface (SU) that marked the beginning of the second depositional sequence (D4 to D5) (Figure 18).

Because the drainage of the basin became dominant, a probable proximal source of sediments (e.g., monadnocks) nourished the alluvial plain system by the deposition of the second coarsening-up cycle (LFA-A). This phase is inferred to be a minor retrogradation that is marked by a minor maximum regressive surface (mrs-2) at the top of D4 (Figure 18). The source area denudation significantly decreases with the decrease of coarse-grained material supply and the transition with a new episode of progradation of fluvial-delta front sediments (LFA-D). The top of D5 is inferred to be a transgressive surface (TS).

Mt. Simon Sandstone

The transition between alluvial fan and braided river sedimentation is encountered at the base of the Lower Mt. Simon (Figures 15 and 16). This transition marked an early stage of transgressive system tract (TST) though the basin (Figure 17). This change can be explained by the increase of fluvial style sedimentation, when the rate of sediment supply exceeds that of accommodation space creation (Soegaard, 1990). Periodic reactivation of proximal source area denudation increased coarser-grained lithic sediment supply in the fluvial braided river system, as shown by the deposition of horizontally layered or dispersed granules and pebbles of quartz, feldspar, and lithic rocks. The unit A (Arkose) was dominated by extensive vertically and laterally amalgamated channel-fill and channel bar complexes (LFA-C) that were formed by the bedload-related migration of sand dunes under high-energy flow regime (Figure 15). During the deposition of the units A and B, the fluvial braided river system spread vertically and laterally with the deposition of aeolian dunes (LFA-C) (Figure 15). These dunes developed on the overbanks of a floodplain that was able to be reduced. The absence of preserved floodplain deposits (lithofacies B4 and B5) was the result of the highly mobile and cannibalistic nature of the braided channels (Cain and Mountney, 2009; Gao et al., 2017). With the absence of core samples and the lack of surface recognition in the FMI log, the transition between the units B and C is informally inferred to be a minor TS that is the base of a second stage of TST (Figure 17).

The fluvial stream sedimentation was optimal during the deposition of the Middle Mt. Simon Sandstone (units C and D) (Figures 15 and 16). The paleo-topography of the Precambrian crystalline basement was mostly flat, which decreases the supply of course-grained materials. Consequently, composition of the units C and D decreased in feldspars and lithic materials through the basin. Because the rate of sediment supply exceeded the accommodation space, the fluvial river sediments developed a wide area of fluvial plain system during a moderate to rapid subsidence. Up to 683-ft-thick braided river sandstones (LFA-B) and aeolian dune sandstones (LFA-C) of the units C and D were deposited in newly created accommodation spaces by the differential subsidence movements. The unit C dominantly deposited braided river system, while the unit D was marked by the development of aeolian dunes in a fluvial plain environment. The sediments of the unit C pinched out the paleo-highs (e.g., monadnocks, hills, mountains), while

the unit D vertically overlapped the previously unit C. Both units can be inferred to be the early phase of the late TST stage (Figure 17).

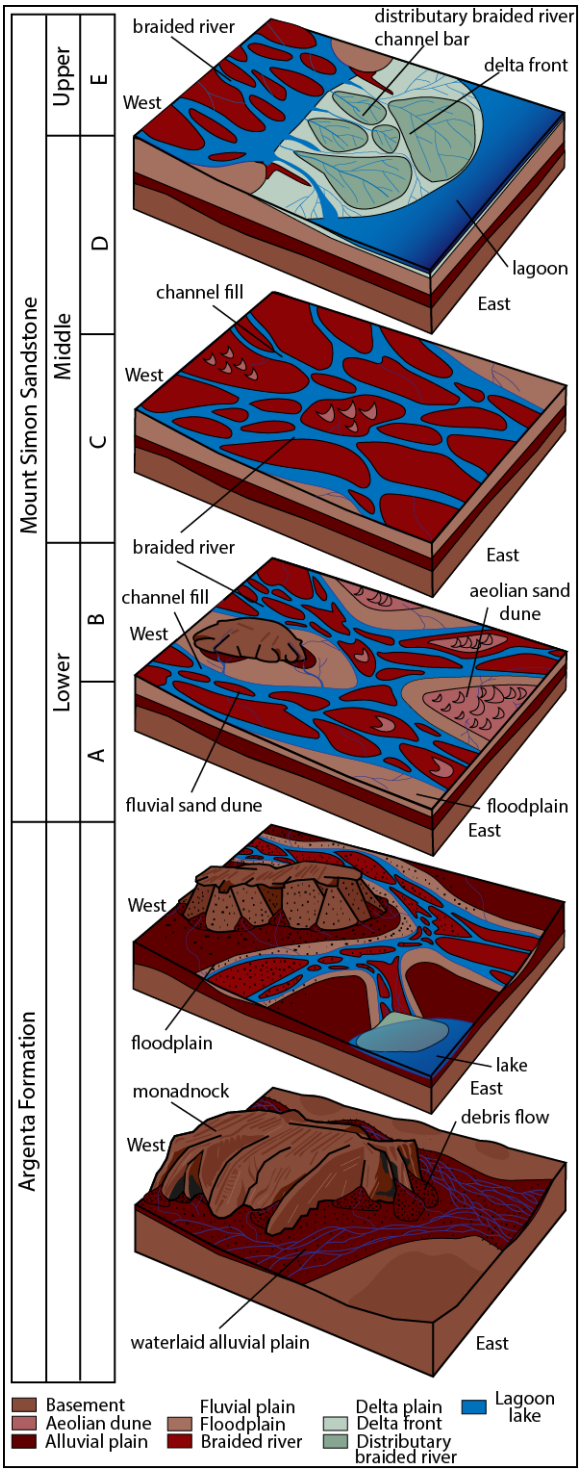

Figure 15. 3D depositional models for the T.R. McMillen #2 well showing the paleoenvironmental evolution of the Argenta Formation and Mt. Simon Sandstone.
Argenta Formation: (1) Waterlain alluvial fan deposits were accumulated around a Precambrian crystalline paleo-high, here interpreted as a monadnock, in an incised valley. (2) An alluvial-fluvial stream sedimentation developed with local deposition of proximal delta distributary braided channels. Coarser-grained materials were transported from the near source area.
Mt. Simon Sandstone: (1) The units A and B of the Lower Mt. Simon Sandstone: The drainage basin expanded, increasing the volume of sediment supply in the fluvial braided river. Aeolian dunes were deposited in the overbanks of the floodplain. The paleo-high was one of the source areas of coarser-grained materials. (2) The units C and D of the Middle Mt. Simon Sandstone: The rate of subsidence decreases through the basin that laterally increased the fluvial plain system. Locally aeolian dunes were deposited in the overbanks of the floodplain. The paleo-high was denudated and flat. (3) The unit E of the Upper Mt. Simon Sandstone: Delta fan prograded through the basin with the deposition of distributary braided channels and mouth bars in a relatively high-energy, wave-generated flow regime.

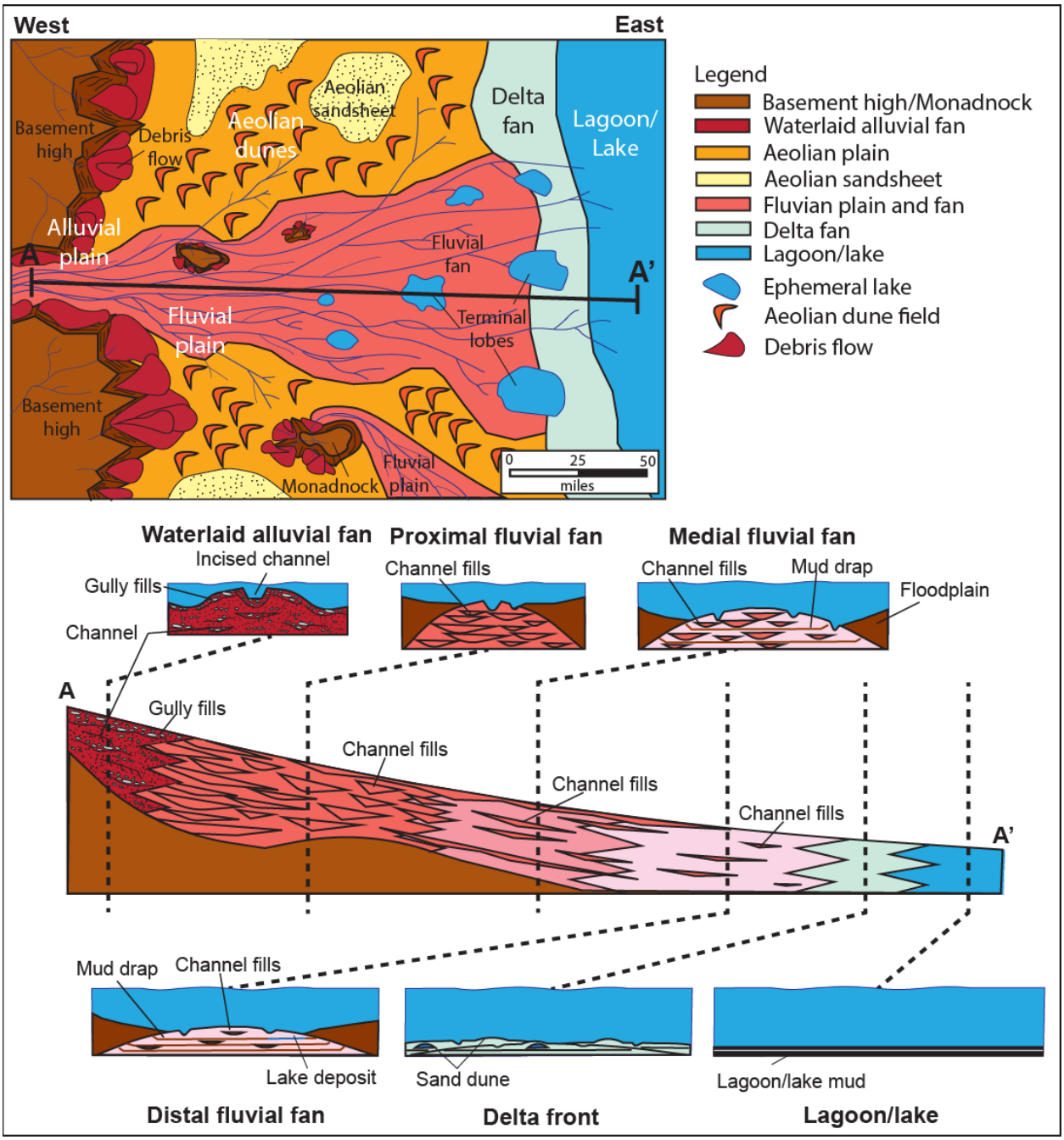

Figure 16. Large-scale depositional model for the Argenta Formation and Mt. Simon Sandstone showing the interaction from alluvial fan to delta front environments. Fluvial plain is bordered by a floodplain that accumulated aeolian dune field. Cross-sections of the alluvial and fluvial plains with details of the waterlain alluvial fan, fluvial plain, and delta fan (modified from Moscariello, 2018).

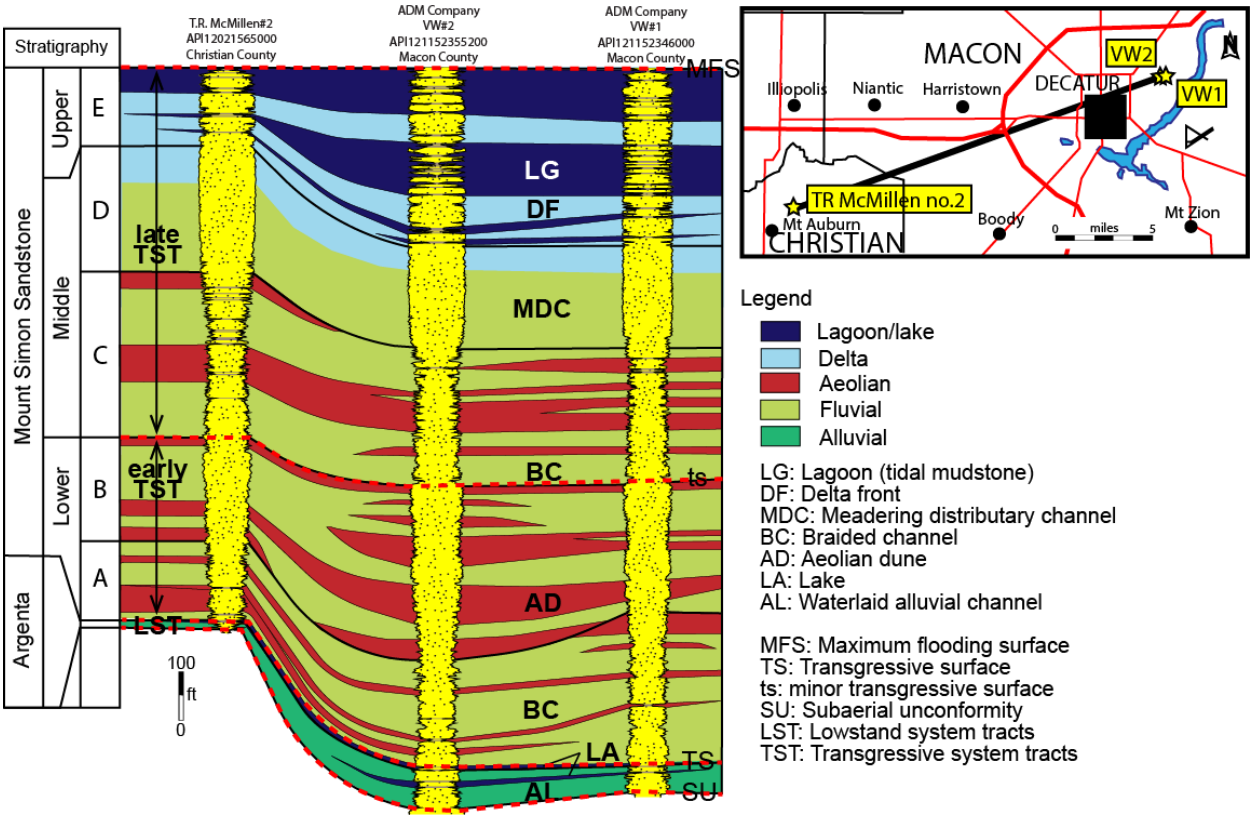

Figure 17. Profile of lithostratigraphic correlation between the T.R. McMillen #2 well, Christian County, and VW #1 and VW #2 boreholes, Macon County. Sequence stratigraphy shows that the sedimentary succession of the Argenta Formation and Mt. Simon Sandstone begins by a lowstand system tract (LST) stage over a subaerial unconformity (SU) over the Precambrian crystalline basement. LST is bounded by a transgressive surface (TS) that marked the progradation of the fluvial system through the basin. Two phases produced a fluvial-dominated and delta-dominated deposition for the Lower-Middle and Middle-Upper Mt. Simon Sandstone, respectively. The boundary with the Eau Claire Formation is marked by a maximum flooding surface (MFS).

At the end of the late TST stage, a major change occurred at the transition between the unit D and the unit E of the Upper Mt. Simon Sandstone that was marked by the progradation of braided river delta system through the basin (Figures 15 and 16). This event recorded the transition between fluvial-dominated to delta front-dominated systems (LFA-D). Amalgamated distributary braided channels (lithofacies D1) and the low content of mouth bar deposits (lithofacies D2) indicate a high discharge of river supply in a high-energy delta fan system. Microtidal structures, here represented by heterolytic sandstones (lithofacies D2), were formed by wave ripples in alternating oscillatory and traction regimes (Dalrymple, 2010). The progradation of the delta fan system gradually progressed with pure mudstones (lithofacies D3), here interpreted to be of lagoonal origin, that covered a large area across the proto-Illinois Basin. The transition from mouth bar to lagoon deposits can be inferred to be a maximum flooding surface (MFS) at the base of the Eau Claire Formation as published by Ostrom (1970) and Runkel et al. (2007) (Figure 17).

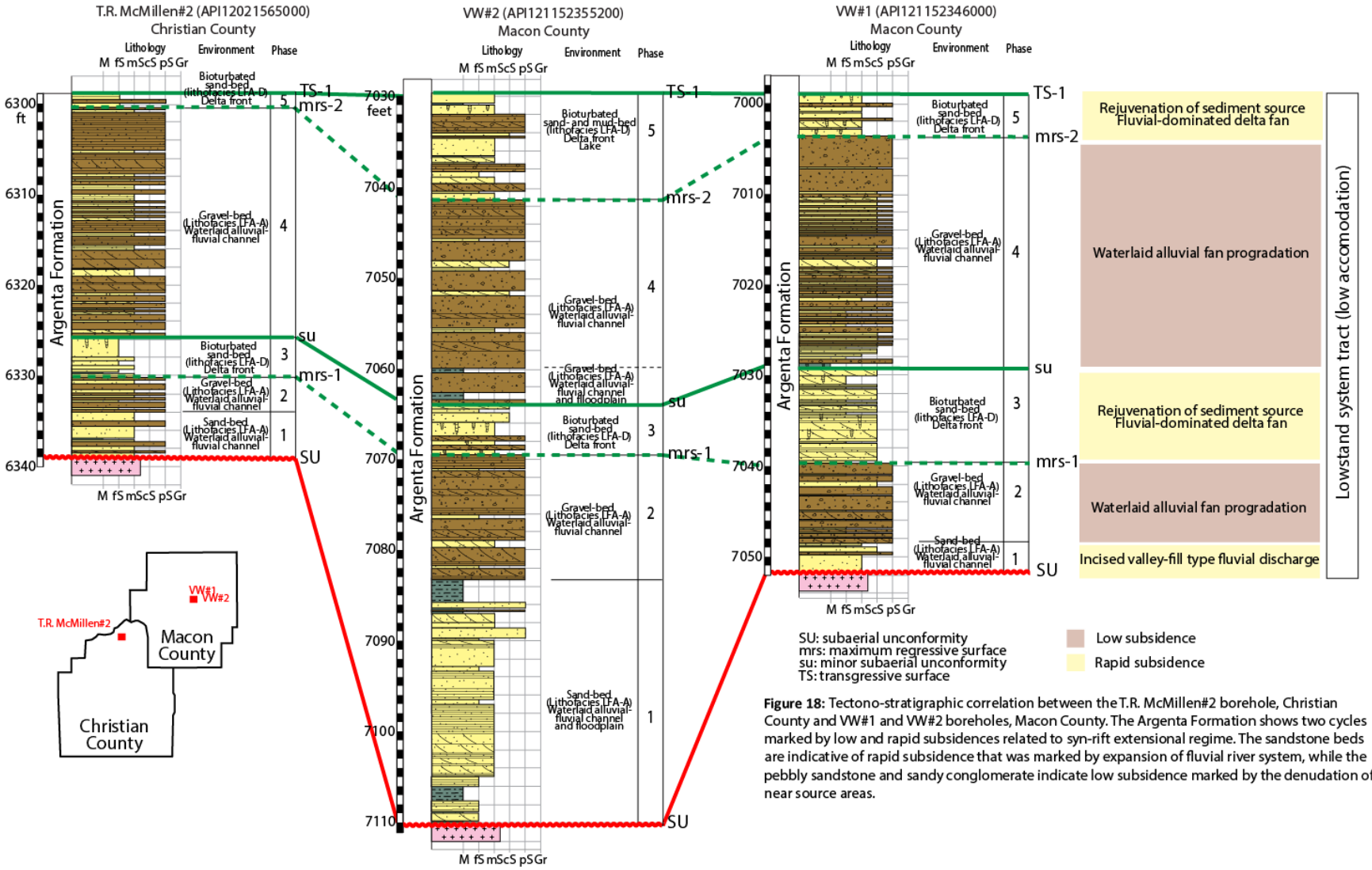

Figure 18: Tectono-stratigraphic correlation between the T.R. McMillen#2 borehole, Christian County and VW#1 and VW#2 boreholes, Macon County. The Argenta Formation shows two cycles marked by low and rapid subsidences related to syn-rift extensional regime. The sandstone beds are indicative of rapid subsidence that was marked by expansion of fluvial river system, while the pebbly sandstone and sandy conglomerate indicate low subsidence marked by the denudation of near source areas.

Discussion

Sequence stratigraphy of the Paleozoic sedimentary strata of the North American cratonic interior basins have been discussed for several decades (Sloss et al., 1949; Wheeler, 1958; Sloss, 1963; Ostrom, 1970; Runkel et al., 2007). During the Middle to Late Cambrian Periods, the strata of the North American cratonic interior basins have been relatively stable with an estimated average rate of basin subsidence of < 32 ft per million years (Sloss, 1988). Most of the subsidence occurred in the Illinois Basin due to isostatic or thermal adjustments along the Mississippi Valley–Reelfoot Rift system, which opened southward to the Ouachita passive margin and the Iapetus Ocean (Sloss, 1988; Mossler, 1992). Although the Middle to Late Cambrian strata are well documented, the Argenta Formation, recognized as the oldest sedimentary stratigraphic unit of the Illinois Basin, is not debated on the context of the tectono-sedimentary evolution through the continental-scale rifting of the North American cratonic interior basins. In Ohio and Indiana, Late Precambrian or early Late Cambrian sandstones of the Middle Run Formation beneath the Middle to Late Cambrian Mt. Simon Sandstone have been identified (Shrake et al., 1991). The oldest sedimentary strata have been interpreted as rift-related clastic materials recycled from the Grenville orogenic belt to the east and from the erosion of the Eastern Granite-Rhyolite Province to the west (Shrake et al., 1991). This formation has been recently constrained using U-Pb dating on detrital zircon grains that gave a depositional age between 1.2 and 0.9 Ga (Santos et al., 2002). Although the time interval of the Middle Run Formation is in the range of recently dated gabbro dikes intruding the Precambrian crystalline basement (i.e., 1,073 ± 12 Ma by U-Pb zircon ages; Freiburg et al., 2020), there is no evidence that these strata were deposited in the early phase of the proto-Illinois Basin. Analogy with the stratigraphic-equivalent Centralia sequence beneath the Mt. Simon Sandstone can be discussed for the Argenta Formation that has been interpreted on seismic reflection (Freiburg et al., 2014). Consequently, the Argenta Formation appears as the result of the denudation of Precambrian paleo-highs that were uplifted during the rifting of the proto-Illinois Basin.

The regional sequence stratigraphic framework for the Argenta Formation and Mt. Simon Sandstone strata is based on the multidisciplinary tools that combine lithofacies analysis, sequence stratigraphic approach, and gamma-ray and FMI log interpretation. Stratigraphic correlation, based on the recognition of lithofacies framework in cores and FMI logs, shows significant variations of deposition that thickens north-northeastwards from the T.R. McMillen #2 well to the VW #1 and VW #2 boreholes of the Decatur site (Figures 17 and 18). Two distinct coarsening-up cycles, similar with the cycles identified in the T.R. McMillen #2 well, are recognized in the VW #1 and VW #2 boreholes. Both coarsening-up cycles recorded periods of increasing sediment flux to subsidence rate ratios that developed in basinward growth of the alluvial fan system complex. The high feldspars, volcanic, and lithic fragments are typical sediment properties derived from juvenile basement in valley subsidence in extensional regimes or source uplift in compressional regimes (Dickinson, 1985; Piper et al., 1996). The lateral variation of thickness within the Argenta Formation provides evidence of local tilting of the alluvial fan surface in deeply incised valleys. The newly formed strata were intensely incised by hyperconcentrated water flows that marked minor regression surfaces (mrs). The transition with the finer-grained sediments reflected the progradation of delta lobe systems (LFA-D) through the basin that resulted from the rapid subsidence during a relative tectonic quietness. A second tectonic pulse generated a new phase of sediment supply from local source areas (e.g., monadnocks). The differential vertical movements caused a minor subaerial unconformity (su) that initiated the erosion of the Precambrian palaeo-

highs and the increases of alluvial fan supply (LFA-A) (Figure 16). A decrease of this supply turned on the progradation of delta lobe system complex (LFA-D) that was predominant in the north-northeastern part of the proto-Illinois Basin. The bottom of the proto-Illinois Basin deepened north-northeastwards, which is confirmed with the location of the depocenter in the eastern central part of the Illinois Basin.

The switch from alluvial fan to braided river (LFA-B) sedimentation began at the base of the unit A (Arkose) of the Mt. Simon Sandstone. These sediments recorded a passive tectonic phase, where the hinterland erosion was weak, and the drainage basin expanded (Figure 16). The high contents of feldspars and lithic materials reveal that the paleo-highs were periodically reactivated, increasing the coarser-grained lithic sediment supply in the fluvial braided river system. Seismic reflection in the T.R. McMillen #2 well area shows that the near paleo-high was totally denudated after the accumulation of the units A and B of the Mt. Simon Sandstone (Figures 15 and 16). This time interval probably recorded a late extensional regime of the rifting of the proto-Illinois Basin. Due to the expansion of basin drainage and a large sediment supply, the accommodation space creation was able to exceed the subsidence for the Middle Mt. Simon Sandstone, where the strata were marked by subaerial unconformities (e.g., scour and erosive surfaces) and the accumulation of aeolian sand dunes (LFA-C) (Figure 16). Aeolian sand dunes were accumulated in local areas, and it is difficult to use them as tools for stratigraphic correlation. The switch from braided stream to delta front (LFA-D) sedimentation was the result of a continental-scale marine transgression through the North American cratonic interior basins. The low rate of subsidence, the tectonic quietness, and the high rate of accommodation space facilitated the accumulation of prograding delta front deposits through the proto-Illinois Basin.

Lagoonal mudstones westward pinched out with mouth bar and distributary braided channel deposits as shown by the lithological correlation between the T. R. McMillen #2 well and the VW #1 and VW #2 boreholes (Figure 17). This suggests that a lagoon system preferentially accumulated eastward. The maximum marine flooding occurred at the boundary between the Upper Mt. Simon Sandstone and Eau Claire Formation.

Conclusion

The core and borehole data from the T.R. McMillen #2 well provide new overview on the depositional processes that occurred in the Middle to Late Cambrian Argenta Formation and Mt. Simon Sandstone at the Mount Auburn area, Christian County, Illinois. The sedimentology was performed based on cores and gamma-ray and FMI logs. The borehole data, such as seismic reflection, gave a large-scale highlight of the distribution of stratigraphic strata that were controlled by the incised valley-monadnock paleo-geomorphology.

The Argenta Formation, the oldest sedimentary stratigraphic unit in Illinois, is dominantly alluvial-fluvial succession that was bounded by an unconformable Precambrian crystalline basement at the bottom and a transgressive surface at the transition with the Lower Mt. Simon Sandstone. This succession was accumulated during a lowstand system tract (low accommodation) stage that recorded two coarsening-up cycles composed of fining-upward waterlain alluvial fan to fluvial-delta fan deposits. The deposition systems evolved with the development of the Mt. Simon Sandstone that caused fluvial stream sedimentation, mainly composed of fluvial braided channels and bars and floodplain muds, during an early phase of the TST stage. An aeolian sand field accumulated on the overbank of the floodplain. Finally, a lagoonal setting associated with fluvio-deltaic sediments was deposited during the latest phase of the TST stage.

The sedimentary sequence evolution model shows that the depositional processes were likely controlled by eroded paleo-uplift of the Precambrian crystalline basement, which generated differential tectonic movements through the proto-Illinois Basin. An active tectonic subsidence enhanced the deposition of the Argenta Formation by the coarser-grained sediment supply that gradually filled the incised valley and paleo-high (e.g., monadnock) paleogeomorphology. With the decrease of the tectonic subsidence and the expansion of the drainage basin, the paleo-uplift areas began to flatten in the Lower Mt. Simon Sandstone, and the paleo-highs were totally drowned by fluvio-deltaic sediments in the Middle and Upper Mt. Simon Sandstone.

The sedimentology features and sequence stratigraphy reported for the T.R. McMillen #2 well show similar tectono-stratigraphic and paleoenvironmental evolutions with the borehole data from the Decatur site, Macon County, Illinois. Other data must be pursued at the basin scale to understand the deposition mechanisms and the controls that applied in the proto-Illinois Basin in a probable syn-rift extensional regime.

References

Becker, L.E., Hreha, A.J., Dawson, T.A., 1978. Pre-Knox (Cambrian) stratigraphy in Indiana. State of Indiana Department of Natural Resources Geological Survey, 72 p.

Bhattacharya, J., Walker, R.G., 1991. River- and wave-dominated depositional systems of the Upper Cretaceous Dunvegan Formation, northwestern Alberta. Bulletin of Canadian Petroleum Geology, 39 (2), 165-191.

Blair, T.C., 1987. Sedimentary processes, vertical stratification sequences, and geomorphology of the Roaring River alluvial fan, Rocky Mountain National Park, Colorado. Journal of Sedimentary Petrology, 57, 1–18.

Blissenbach, E., 1954. Geology of alluvial fans in semiarid regions: Geological Society of America Bulletin, 65, 175-190.

Cain, S.A., Mountney, N.P., 2009. Spatial and temporal evolution of a terminal fluvial fan system: the Permian Organ Rock Formation, South-east Utah, USA. Sedimentology, 56 (6), 1774-1800.

Catuneanu, O., 2006. Principles of Sequence Stratigraphy. Elsevier, 374 p.

Catuneanu, O., Abreu, V., Bhattacharya, J.P., Blum, M.D., Dalrymple, R.W., Eriksson, P.G., Fielding, C.R., Fisher, W.L., Galloway, W.E., Gibling, M.R., Giles, K.A., Holbrook, J.M., Jordan, R., Kendall, C.G.St.C., Macurda, B., Martinsen, O.J., Miall, A.D., Neal, J.E., Nummedal, D., Pomar, L., Posamentier, H.W., Pratt, B.R., Sarg, J.F., Shanley, K.W., Steel, R.J., Strasser, A., Tucker, M.E., Winker,C., 2009. Towards the standardization of sequence stratigraphy. Earth-Science Reviews, 92, 1-33.

Collinson, C., Sargent, M.L., Jennings, J.R., 1988. Illinois basin region. Sedimentary Cover—North American Craton, US: Geological Society of America, The Geology of North America, 2, 383-426.

Dalrymple, R.W., 2010. Tidal depositional systems. In: James, N.P., Dalrymple, R.W., Eds., Facies Models 4. Geological Association of Canada, St. John′s, 201–232.

Denison, R.E., Bickford, M.E., Lidiak, E.G., Kisvarsanyi, E.B., 1987. Geology and Geochronology of Precambrian Rocks in the Central Interior Region of the United States. U.S. Geological Survey, Reston, Virginia, Professional Paper 1241-C.

Dickinson, W.R., 1985. Interpreting provenance relations from detrital modes of sandstones. In: Zuffa, G.G., ed., Provenance of Arenites. D. Reidel, The Netherlands, 333–361.

Finley, R.J., 2014. An overview of the Illinois Basin - Decatur Project. Greenhouse Gases: Science and Technology, 4, 571-579

Flemming, B.W., 2007. The influence of grain-size analysis methods and sediment mixing on curve shapes and textural parameters: implications for sediment trend analysis. Sedimentary Geology, 202, 425–435.
Folk, R.L ., 1966. A review of the grain size parameters. Sedimentology, 6, 73–93.
Folk, R.L., Ward, M.C., 1957. Brazos River bars: a study in the significance of grain size parameters. Journal of Sedimentary Petrology, 27, 3–27.
Freiburg, J.T., Morse, D.G., Leetaru, H.E., Hoss, R.P., Yan, Q., 2014. A Depositional and Diagenetic Characterization of the Mt. Simon Sandstone at the Illinois Basin–Decatur Project Carbon Capture and Storage Site, Decatur, Illinois, USA. Circular 583, Illinois State Geol. Survey, Champaign, 42 p.
Freiberg, J.T., McBride, J.H., Malone, D.H., Leetaru, H.E., 2020. Petrology, geochronology, and geophysical characterization of Mesoproterozoic rocks in central Illinois, USA. Geoscience Frontiers, 11 (2), 581-596.
Gao, C., Ji, Y., Ren, Y., Zhou, Y., Jin, J., Zhang, L., Li, Z., Zhou, Y., Wu, H., 2017. Geomorphology and sedimentary sequence evolution during the buried stage of paleo-uplift in the Lower Creataceous Qingshuihe Formation, Jungar Basin, northwestern China: Implications for reservoir lithofacies and hydrocarbon distribution. Marine and Petroleum Geology, 86, 1224-1251.
Heidlauf, D.T., Hsui, A.T., Klein, G.W., 1986. Tectonic subsidence analysis of the Illinois basin. Journal of Geology, 94, 779-794.
Kocurek, G., 1996. Desert Aeolian systems. In: Reading, H.G., ed., Sedimentary environments processes facies and stratigraphy, 3rd edn. Blackwell Science, Oxford, pp. 125-153.
Kolata, D.R., Nelson, W.J., 1991.Tectonic history of the Illinois basin. In: Leighton, M.W., Kolata, D.R., Oltz, D.E, Eidel, J.J., eds., Interior Cratonic Basins. American Association of Petroleum Geologists, Memoir 51, pp. 263-285.
Kolata, D.R., Nelson, W.J., 2010. Tectonic history. In: Kolata, D.R., Nimz, C.K., eds., Geology of Illinois. Illinois State Geological Survey, University of Illinois, Champaign, pp. 77– 89.
Kolata, D.R. (compiler), 2005, Bedrock Geology of Illinois: Illinois State Geological Survey, Illinois Map 14, 1:500,000 scale.
Leetaru, H.E., McBride, J.H., 2009. Reservoir uncertainty, Precambrian topography, and carbon sequestration in the Mt. Simon Sandstone, Illinois Basin. Environmental Geosciences, 16(4), 235-243.
Leetaru, H.E., Frailey, S., Morse, D., Finley, R.J., Rupp, J., Drahozval, J.A., McBride, J.H., 2008. Carbon sequestration in the Mt. Simon Sandstone saline reservoir. In: Grobe, M., Pashin, J.C., Dodge, R.L., eds., Carbon dioxide sequestration in geological media: State of the science. Tulsa, Oklahoma, American Association of Petroleum Geologists, AAPG Studies 59, pp. 1–17.
Leighton, M.W., Kolata, D.R., 1991. Selected Interior Cratonic Basins and Their Place in the Scheme of Global Tectonics. In: Leighton, M.W., Kolata, D.R., Oltz, D.E, Eidel, J.J., eds., Interior Cratonic Basins. American Association of Petroleum Geologists, Memoir 51, pp. 729-797.
Lovell, T.R., Bowen, B.B., 2013. Fluctuations in Sedimentary Provenance of the Upper Cambrian Mt. Simon Sandstone, Illinois Basin, United States. Journal of Geology, 121, 129-154.
Maciaszek, P., Chomiak, L., Wachocki, R., Widera, M., 2019. The interpretative significance of ripple-derived sedimentary structures within an upper Neogene fluvial succession of central Poland. Geologos, 25 (1), 1-13.

Martins, L.R., 1965, Significance of Skewness and Kutosis in environmental interpretation. Journal of Sedimentary Petrology, 35(3), 768–770.
McBride, J.H., Kolata, D.R., 1999. Upper crust beneath the central Illinois Basin, United States: Geological Society of America Bulletin, 111, 375–394.
McBride, J.H., Kolata, D.R., Hildenbrand, T.G., 2003. Geophysical constraints on understanding the origin of the Illinois basin and its underlying crust. Tectonophysics, 363, 45-78.
Miall, A.D., 1977. A review of the braided-river depositional environment. Earth-Science Reviews 13, 1–62.
Miall, A.D. 1996. The Geology of Fluvial Deposits. Springer, New York.
Miall, A.D., 2006. The Geology of Fluvial Deposits: Sedimentary Facies, Basin Analysis, and Petroleum Geology. Springer-Verlag, Berlin, New York, 582 p.
Miall, A.D., 2010. Alluvial deposits. In: James, N.P., Dalrymple, R.W., eds., Facies Model Revisited. SEPM, Special Publication 90, pp. 105-137.
Moscariello, A. 1998. Continental Sedimentary Record of Climate Change and Catastrophic Flood Events: Processes, Forms and Facies of Alluvial Fans in the Western U.S.A., Post-Doctoral Research Report Fellowship of the Swiss National Science Foundation, 81GE-048184.
Moscariello, A., 2018. Alluvial fans and fluvial fans at the margins of continental sedimentary basins: geomorphic and sedimentological distinction for geo-energy exploration and development. In: Ventra, D., Clarke, L.E., eds., Geology and Geomorphology of Alluvial and Fluvial Fans: Terrestrial and Planetary Perspectives. Geological Society, London, Special Publications, 440, pp. 215–243.
Mossler, J.H., 1992, Sedimentary rocks of Dresbachian age (Late Cambrian), Hollandale Embayment, southeastern Minnesota: Minnesota Geological Survey Report of Investigations 40, 71 p.
Norby, R.D., 1991. Biostratigraphy Zones in the Illinois Basin. In: Leighton, M.W., Kolata, D.R., Oltz, D.F., Eidel, J.J., eds., Interior cratonic basins, American Association of Petroleum Geologists Memoir 51, pp. 179-194.
Ostrom, M.E., 1970, Sedimentation cycles in the Lower Paleozoic rocks of western Wisconsin, in Field Trip Guidebook for Cambrian-Ordovician geology of western Wisconsin: Wisconsin Geological and Natural History Survey, Information Circular 11, p. 10-34.
Piper, J.D.A., Elliot, M.T., Kneller, B.C., 1996. Anisotropy of magnetic susceptibility in a Palaeozoic flysch basin: the Windermere Supergroup, northern England. Sedimentary Geology, 106, 235–258.
Pratt, T.L., Hauser, E.C., Nelson, K.D., 1992. Widespread buried Precambrian layered sequences in the US Mid-Continent: evidence for large Proterozoic depositional basins. AAPG Am. Assoc. Pet. Geol. Bull., 76, 1384-1401.
Reineck, H.-E., Singh, I.B., 1986. Depositional Sedimentary Envirinments (2nd. Ed.). Springer-Verlag, Berlin, Heidelberg, New York, 551 p.
Rogers D.A., Astin T.R. 1991. Ephemeral lakes, mud pellets and windblown sand and silt: reinterpretations of Devonian lacustrine cycles in north Scotland. In: Anadon, P., Cabrera, L.L., Kelts, K., eds., Lacustrine Facies Analysis. Special Publication 13, IAS, pp. 199-222.
Runkel, A.C., Miller, J.F., McKay, R.M., Palmer, A.R., Taylor, J.F., 2007. High-resolution sequence stratigraphy of lower Paleozoic sheet sandstones in central North America: The role of special conditions of cratonic interiors in development of stratal architecture: Geological Society of America Bulletin, 119 (7–8), 860–881.

Sahu, B.K., 1964. Depositional mechanisms from the size analysis of clastic sediments. Journal of Sedimentary Petrology, 34, 73–83.
Santos, J.O.S., Hartmann, L.A., McNaughton, N. J.,Easton, R.M., Rea, R.G., Potter, P.E., 2002. Sensitive high resolution ion microprobe (SHRIMP) detrital zircon geochronology provides new evidence for a hidden Neoproterozoic foreland basin to the Grenville Orogen in the eastern Midwest U.S.A. Canadian Journal of Earth Sciences, 39, 1505–1515.
Shrake, D.L., Carlton, R.W., Wickstrom, L.H. Potter, P.E., Richard, B.H., Wolfe, P.J., Sitler, G.W., 1991. Pre-Mt. Simon Basin under the Cincinnati Arch. Geology, 19, 139-142.
Sloss, L.L., 1963. Sequences in the cratonic interior of North America. Geological Society of America Bulletin, 74(2), 93-114.
Sloss, L.L., ed., 1988. Sedimentary Cover—North American Craton: US. Geological Society of America.
Sloss, L.L., Krumbein, W.C., Dapples, E.C., 1949. Integrated facies analysis. In: Longwell, C.R., ed., Sedimentary facies in geologic history: Geological Society of America Memoir 39, pp. 91–124
Soegaard, K., 1990. Fan-delta and braid-delta systems in Pennsylvanian Sandia Formation, Taos Trough, Northern New Mexico: depositional and tectonic implications. Bulletin of the Geological Society of America, 102, 1325–1343.
Sutherland, R.A., Lee, C.T., 1994. Discrimination between coastal sub environments using textural characteristics. Sedimentalogy, 41, 1133–1143.
Thomas, W.A., Gehrels, G.E., Sundell, K.E., Greb, S.F., Finzel, E.S., Clark, R.J., Malone, D.H., Hampton, B.R., Romero, M.C., 2020. Detrital zircons and sediment dispersal in the eastern Midcontinent of North America. Geosphere, 16 (3), 817-843.
Treworgy, J.D., Sargent, M.L., Kolata, D.R., 1991. Tectonic subsidence history of the Illinois Basin (extended abstract). In: Program with Abstracts for the Louis Unfer, Jr. Conference on the Geology of the Mid-Mississippi Valley, Cape Girardeau, MO.
Van der Pluijm, B.A., Catacosinos, P.A., 1996. Basement and basins of eastern North America. Geological Society of America, Special Paper 308, p. 14.
Van Schmus, W.R., Schneider, D.A., Holm, D.K., Dodson, S., Nelson, B.K., 2007. New insights into the southern margin of the Archean–Proterozoic boundary in the north-central United States based on U-Pb, Sm-Nd, and Ar-Ar geochronology. Precambrian Research, 157, 80–105.
Van Schmus, W.R., Bickford, M.E., Turek, A., 1996. Proterozoic geology of the east-central midcontinent basement. In: van der Pluijm, B.A., Catacosinos, P.A., eds., Basement and basins of eastern North America: Geological Society of America Special Paper 308, pp. 7–32.
Wheeler, H.E., 1958, Time-stratigraphy: American Association of Petroleum Geologists Bulletin, 42, 1047–2063.
Willman, H.B., Atherton, E., Buschbach, T.C., Collinson, C., Frye, J.C., 1975. Handbook of Illinois stratigraphy. Illinois State Geological Survey Bulletin 95, 1-261.

Chapter 2
Seismic Reflection

By: Dr. John McBride
Brigham Young University

Summary

The Illinois Basin is one of the premier sites for evaluating technologies for Carbon Capture and Storage (CCS). As a result, a wealth of new geophysical and geological subsurface data has been acquired, including long-record, high-resolution common depth-point (CDP) seismic reflection profiles. These profiles provide the clearest-yet images of the Precambrian basement beneath the Illinois Basin. The purpose of our study is to present and describe the basement structure from a subset of these profiles with reference to how they constrain the interpretation of previously proposed Precambrian terranes beneath the basin. Note that this section of the report refers to results from other studies, including those funded by the United States Department of Energy, under contract to the Illinois State Geological Survey, University of Illinois at Urbana-Champaign. References to these other studies are relevant to the Illinois Basin and aid in understanding results from the Macon County Contract.

Introduction

High-resolution imaging of the Precambrian basement beneath the USA Midcontinent provides a context for understanding overlying lower Paleozoic CCS reservoirs. Although many subsurface Precambrian terranes appear to be poorly reflective, or seismically transparent, the Precambrian beneath the Illinois Basin displays a strong and highly coherent reflectivity. The focus of this study is to introduce two new, not previously published seismic reflection CDP profiles that further our knowledge of the Precambrian beneath the Illinois Basin. The profiles were acquired as part of an ongoing program of evaluation of potential reservoirs for CCS (Greenberg, 2013) by the Illinois State Geological Survey as supported by the United States Department of Energy (U.S. DOE) through their CarbonSAFE program. The profiles, which were purposefully recorded to upper crustal traveltimes (5 s), lie on opposite sides of a major Precambrian terrane boundary that cuts diagonally across the central Illinois Basin (Figure 1). The boundary (or suture) divides the Mazatzal Province (1.69-1.65 Ga old) to the north from the Granite-Rhyolite Province (1.55-1.35 Ga old) to the south (Whitmeyer and Karlstrom, 2007), as defined by neodymium isotopic data (Van Schmus et al., 1996). Such a suture may represent the convergence of a juvenile crustal block (younger than 1.55 Ga) against the older, southeast-facing Laurentian continental margin (southeastern edge of the Mazatzal Province) (Whitmeyer and Karlstrom, 2007). The pair of new seismic profiles provides a fortuitous opportunity to reveal reflectivity signatures across this proposed terrane boundary beneath the Illinois Basin.

New Seismic Reflection Profiles

Locations

The northern seismic profile (Figure 2) is in northern Christian County, Illinois (and adjacent counties to the east and west), just north of the terrane boundary (Figure 1). This profile,

which trends approximately east-west and is about 45 km long, was surveyed over the northwestern flank of the Illinois Basin, as defined by Paleozoic isopach maps (Buschbach and Kolata, 1991) (Figure 1). The southern profile (Figure 3), located south of the terrane boundary, is about 25 km long and trends north-south through Richland County, Illinois, crossing the northern flank of the Paleozoic depocenter of the basin (Buschbach and Kolata, 1991).

Acquisition and Processing Parameters

The acquisition parameters for both profiles, acquired in 2019, were mostly identical. Both used a Vibroseis source, a geophone group and source interval of 110 ft (33.5 m) with a CDP bin size half of that, and a recording sample rate of 1 ms. An 8-s source sweep produced a correlated record of 5 s. The sweep frequency range for the Christian County profile was 6-100 Hz; for the Richland County profile, 2-100 Hz. Both surveys used 220 recording channels. The Christian County profile was shot with a split spread using 55-12,045 ft (18-3,671 m) offsets, which yielded a maximum CDP fold of cover of 45-54. The Richland County profile was shot with offsets of 0-12,100 ft (0-2,688 m), giving a maximum fold of 86-121. Both profiles are displayed unmigrated to preserve diffraction patterns that are useful for the interpretation of structural discontinuities and thus for characterizing heterogeneity. The profiles are shown as travel-time sections since the seismic velocity for Precambrian rocks is mostly unknown. All reported traveltimes are considered two-way unless otherwise noted.

Results and Observations

Christian County Profile

The Paleozoic strata of the Christian County section are very reflective (Figure 2). The top of the Precambrian basement arrives at ~870-1,000 ms. Relative to Paleozoic markers, the top of the basement is less coherent, somewhat discontinuous, and mostly single cycle, implying a more complex surface. In places, the surface is gently undulating or disappears. The top of the basement is occasionally underlain by a thin, layered sequence, about 100 ms in duration. Further below the top of the basement, only a few short reflector segments and/or diffractions occur. At about 1,800 ms (below CDP 2,800), a prominent reflection arrives and extends over much of the section, before being cut off by the eastern end of the profile at 2,670 ms. The length of this reflector is over 30 km and has an apparent, unmigrated dip to the east (in the plane of the section) of 4.8°-5.2°, assuming a likely basement velocity of 6.0-6.5 km/s. The relative amplitude is strong, compared to Paleozoic markers. It shows multiple cycles (at least three) and is segmented, with edge diffractions in places. Below it are numerous, less-coherent reflector segments and diffractions, some of which are as much as 10 km in length, dipping opposite to the overlying east-dipping Precambrian reflector. The western portion of the section is relatively reflection-poor in the Precambrian—it is not clear if this is related to the acquisition conditions, change in attenuation levels, or an actual change in the Precambrian geology (i.e., less acoustic impedance contrasts).

Richland County Profile

The Richland County profile is located about 150 km southeast of the center of the Christian County profile (Figure 3). The Paleozoic stratigraphy is basically similar but with thicker intervals, owing to the profile being in a deeper part of the Illinois Basin. Below the center of the profile, the top of the Precambrian arrives at about 1,625 ms (much deeper than on the Christian County profile), is one to two cycles, and is similar to the Paleozoic markers above it. The top-Precambrian reflector is more coherent, compared to the Christian County profile. A unique feature

of this surface is the appearance of prominent zones of diffractors along it, especially on the northern portion of the profile, indicating disruption of what is mostly a smooth reflector. A relatively thin interval appears further down the section (60-200 ms thick, one-way time), characterized by segmented reflections and abundant diffractions at its base, quite different from the overlying top-Precambrian reflection. Deeper, a well-developed series of flat-lying and north-dipping (apparent) reflections appears at the southern end of the profile, one at 2,370 ms, a second at 2,680 ms, and a third at 3,170 ms. None of these events mimics overlying reflections and is unlikely to be multiples. The lowermost reflection of this series is the most continuous and coherent with the highest relative amplitude. Its north-dip increases abruptly across a hinge (CDP 2,500), beyond which it dips more steeply (note that no such dip changes appear in the overlying Paleozoic section). The general unmigrated, apparent dip of the base of the series is 5.8°-6.3°, using a range of basement velocities, 6.0-6.5 km/s. Further down, reflectivity is sporadic with occasional short reflector segments and diffractions, although not as prominent as below the main dipping Precambrian reflection on the Christian County profile (cf. Figures 2 and 3).

Interpretation

On both sides of the Precambrian terrane boundary (Figure 1), two new seismic profiles show an extraordinarily bright and continuous Precambrian reflector that dips east on the north side of the boundary and dips north on the south side of it. For both seismic profiles, a distinct fabric of diffractions and short reflector segments marks the deeper basement below this reflector. However, the shallow Precambrian basement (1-2 s directly below the base of the Paleozoic) looks very different on opposite sides of the boundary. On the south side, the shallow basement shows a highly reflective and layered series resting over the bright, dipping reflector. This contrasts with the shallow basement observed north of the boundary, which is transparent or only sparsely reflective above an east-dipping reflector. This general pattern for basement reflectivity is supported by previously acquired seismic profiles over the Illinois Basin (Figure 1).

Shallow basement reflectivity on the Richland County profile can be interpreted as part of the Centralia sequence, as first recognized by Pratt et al. (1992) from older, regional, deep seismic profiles. These and other workers (e.g., McBride et al., 2003; Freiburg et al., 2020) have suggested a range of geological interpretations, including Precambrian sedimentary strata and layered felsic igneous rocks along with mafic igneous sills, which are exposed in the St. Francois mountains in southeastern Missouri (Kisvarsanyi and Kisvarsanyi, 1990). In contrast, the Christian County profile does not show a Centralia-like uppermost basement, but only the single, strong-dipping reflector and underlying diffractive zone. Other profiles north of the terrane boundary and east of the current profile show the same pattern (McBride et al., 2016). The lack of shallow basement layered reflectivity north of the boundary suggests either a more uniform composition or rock that is too heterogeneous to produce coherent acoustic impedance contrasts.

Discussion and Conclusion

Our study provides an opportunity to compare two high-quality CDP seismic profiles, collected and processed similarly, but located on opposite sides of a major North American Precambrian terrane boundary beneath the Illinois Basin Paleozoic. This boundary separates the Mazatzal Province from the Granite-Rhyolite Province, which have different isotopic ages and tectono-magmatic origins (Whitmeyer and Karlstrom, 2007). The uppermost basement north of the terrane boundary is mostly transparent above a prominent, east-dipping reflector with diffractive zones beneath it. South of the boundary, a similar, north-dipping reflector is observed,

with diffractive zones beneath it but a well-layered sequence above it. This variation in basement reflectivity observed from the new profiles is supported by older, lower-resolution CDP seismic profiles in the Illinois Basin (Pratt et al., 1992; McBride et al., 2003, 2016) (Figure 1). Together, the new profiles describe part of a deep basinward trend of dipping Precambrian basal reflections (Figure 1), interpreted as mafic igneous sills but with distinct seismic reflectivity signatures above them.

The variation in the pattern of reflectivity for the uppermost Precambrian crust on the two profiles may support previous geochemical arguments for a major suture corresponding to the terrane boundary; however, the deeper, basal Precambrian reflector on both sides of the boundary may also suggest that the location of suturing requires revision below the Illinois Basin. Since the exact age of the Precambrian reflectivity is unknown, it could be either coeval with the formation of the Granite-Rhyolite Province (1.55-1.35 Ga) or post-date it. For example, an episode of Keweenawan mafic igneous intrusive volcanism that is circa 1.1 Ga old (Freiburg et al., 2020) could be responsible for some of the strong reflectivity and overprint both sides of the proposed terrane boundary.

Acknowledgments

Analysis of the seismic data was made possible in part by software grants from the Landmark (Halliburton) University Grant Program, the IHS Markit Kingdom Educational Grant Program, and the Schlumberger Worldwide University Software Program. We gratefully acknowledge these software grants in making this research possible.

References

Bear, G. W., J. A. Rupp, and A. J. Rudman, 1997, Seismic interpretation of the deep structure of the Wabash Valley Fault System: Seismological Research Letters, 68, 624-640.

Buschbach, T. C., and D. R. Kolata, 1991, Regional setting of Illinois Basin, in M. W. Leighton, D. R. Kolata, D. F. Oltz, and J. J. Eidel, eds., Interior cratonic basins: AAPG Memoir 51, 29-55.

Drahovzal, J. A., 1997, Proterozoic sequences and their implications for Precambrian and Cambrian geologic evolution of western Kentucky: Evidence from seismic-reflection data: Seismological Research Letters, 68, 553–566.

Freiburg, J. T., McBride, J. H., Malone, D. H., and Leetaru, H. E., 2020, Petrology, geochronology, and geophysical characterization of Mesoproterozoic rocks in central Illinois, USA: Geoscience Frontiers, 11, 581-596, doi.org/10.1016/j.gsf.2019.07.004.

Greenberg, S. E., 2013, Creating a sequestration capacity building and knowledge sharing program: Energy Procedia, 37, 7291–7298.

Kisvarsanyi, E. B., and G. Kisvarsanyi, 1990, Alkaline granite ring complexes and metallogeny in the Middle Proterozoic St. Francois Terrane, southeastern Missouri, U.S.A., in C. Gower, T. Rivers, B. Ryan, eds., Mid-Proterozoic Laurentia-Baltica: Geological Association of Canada Special Paper 38, 433–446.

McBride, J. H., D. R. Kolata, and T. G. Hildenbrand, 2003, Geophysical constraints on understanding the origin of the Paleozoic Illinois basin and the Proterozoic Eastern Granite-Rhyolite Province, USA: Tectonophysics, 363, 45-78.

McBride, J. H., H. E. Leetaru, R. W. Keach, II, and E. I. McBride, 2016, Fine-Scale Structure of the Precambrian beneath the Illinois Basin: Geosphere, 12, 585-606,

doi:10.1130/GES01286.1.
Potter, C. J., J. A. Drahovzal, M. L. Sargent, and J. H. McBride, 1997, Proterozoic structure, Cambrian rifting, and younger faulting as revealed by a regional seismic reflection network in the Southern Illinois Basin: Seismological Research Letters, 68, 537-552.
Pratt, T. L., E. C. Hauser, and K. D. Nelson, 1992, Widespread buried Precambrian layered sequences in the U.S. Mid-continent: Evidence for large Proterozoic depositional basins: AAPG Bulletin, 76, 1384-1401.
Van Schmus, W. R., M. E. Bickford, and A. Turek, 1996, Proterozoic geology of the east-central Midcontinent basement, in B. A. van der Pluijm, and P. A. Catacosinos, eds., Basement and basins of eastern North America: Geological Society of America Special Paper 308, 7-32.
Whitmeyer, S. J., and K. E. Karlstrom, 2007, Tectonic model for the Proterozoic growth of North America: Geosphere, 3, 220–259; doi: 10.1130/GES00055.1.

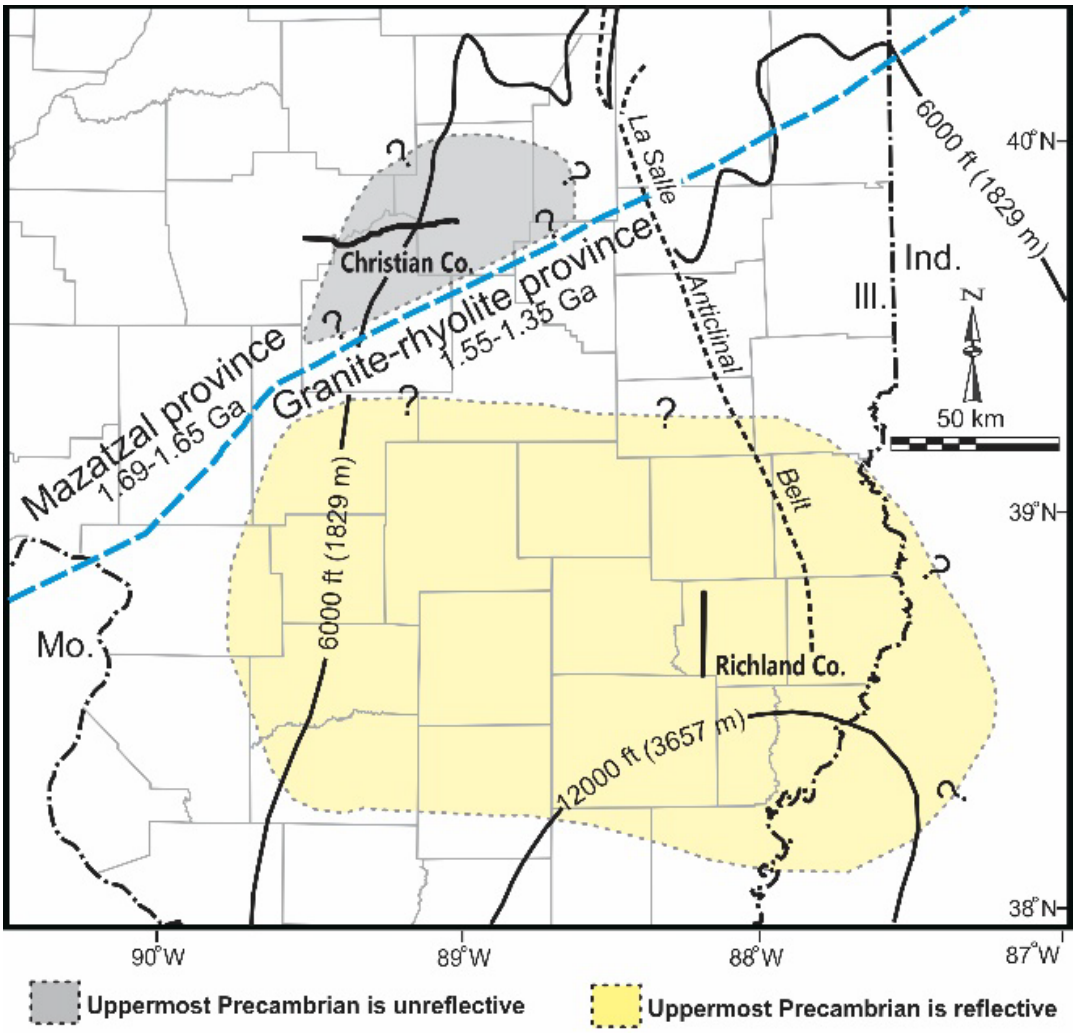

Figure 1. Location map for two seismic profiles in Christian and Richland Counties, Illinois. Two structural contours for top of Precambrian (Buschbach and Kolata, 1991) are selected for reference. The blue dashed line is a geochemically defined terrane boundary (Van Schmus et al., 1996). The shaded areas show reflection character of uppermost Precambrian, based on the present study and on previous compilations of long-record seismic data (Pratt et al., 1992; Bear et al., 1997; Drahovzal, 1997; Potter et al., 1997; McBride et al., 2013; McBride et al., 2016; Freiburg et al., 2020).

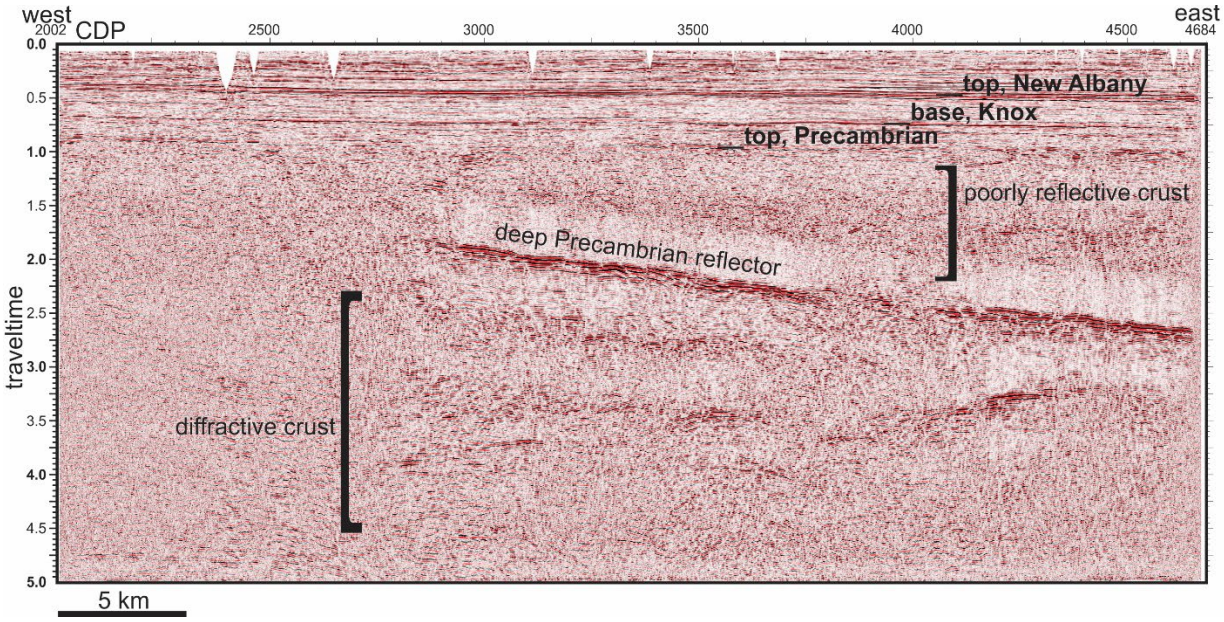

Figure 2. Christian County CDP seismic profile (Figure 1). Stratigraphic markers are based on a vertical seismic profile and on regional correlations. The section is displayed with a vertical exaggeration of about 1.4:1, assuming an average velocity of 6 km/s. Note that the dimmed zone above the deep reflector is a shadowing artifact of the automatic gain control.

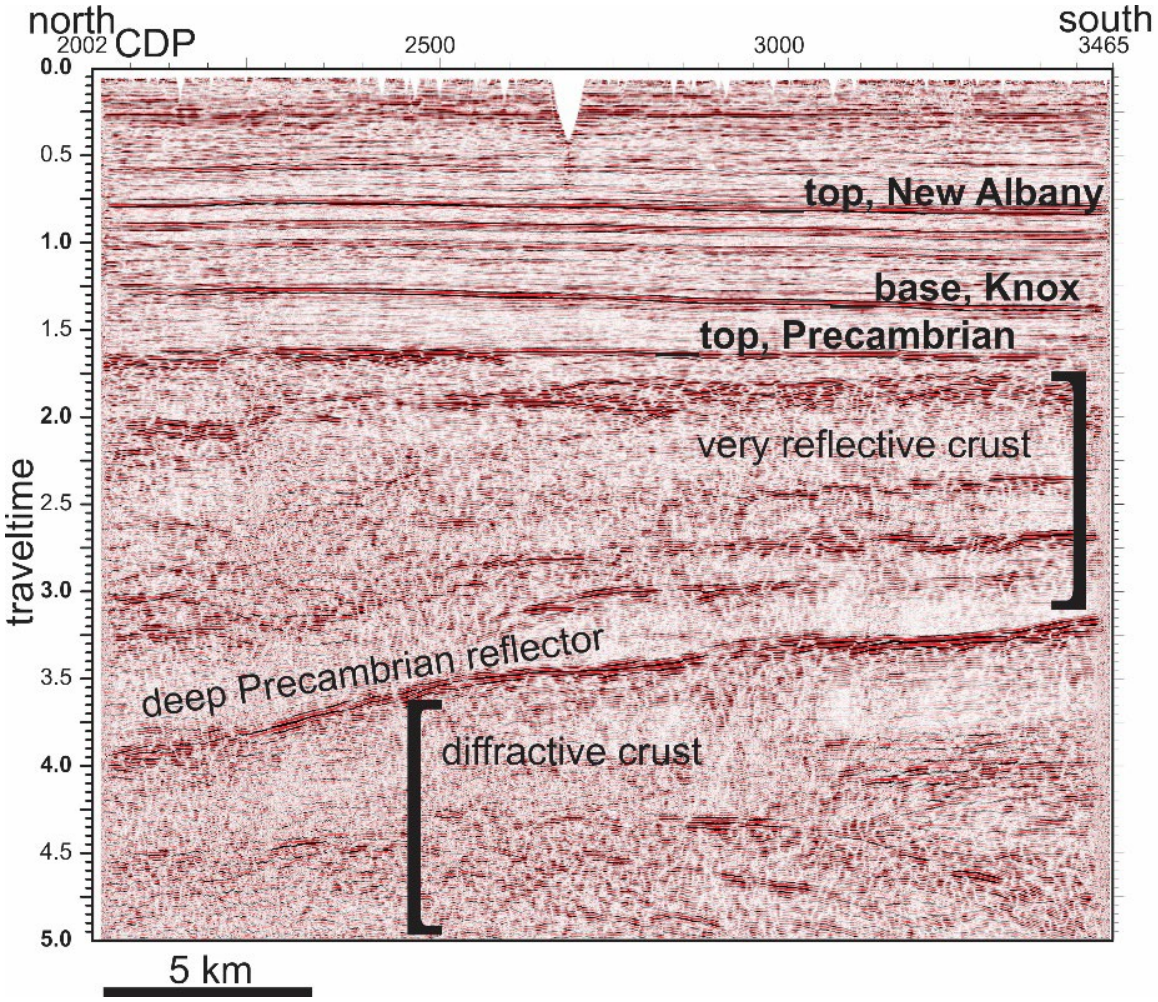

Figure 3. Richland County CDP seismic profile (Figure 1). The stratigraphic markers are based on regional correlations. The section is displayed with a vertical exaggeration of about 1.4:1, assuming an average velocity of 6 km/s.

Chapter 3
Sediment Provenance

By: Jared Freiburg[1] and Dave Malone[2]

[1]Illinois State Geological Survey
[2]Illinois State University, Normal, Illinois

Introduction

The Precambrian basement of the Illinois Basin has recently gained the attention of both researchers and industry as a result of investigations into geologic storage of CO_2 through CarbonSAFE, the Illinois Basin-Decatur Project, and the Illinois Carbon Capture and Storage Project (Freiburg et al., 2014). These projects were designed to evaluate and conduct CO_2 injection to store industrially sourced CO_2 in basal Cambrian strata.

We present 960 detrital zircon ages from five Lower Mt. Simon and Argenta Sandstone samples extracted from three cores that were obtained as part of the greater CarbonSAFE efforts with a focus on the CarbonSAFE Macon County project. These new data are compared with detrital zircon age spectra from younger Cambrian sandstones present to the north on the far flank of the Illinois Basin to provide an understanding of the evolution of sedimentary provenance during the Sauk transgression and the early development of the Illinois Basin. Our results show that the Mt. Simon and Argenta Sandstones were derived from Late Paleoproterozoic to Early Cambrian crust. We interpret the 530, 1,370, 1,460, and 1,650 Ma detrital zircon populations to be locally derived from Paleo- to Mesoproterozoic basement beneath the Illinois Basin and Cambrian igneous rocks associated with the development of a northern arm of the Reelfoot Rift.

Background

The Illinois Basin is an intracratonic basin that extends across most of Illinois and into parts of Kentucky and Indiana and contains more than 5 km of Paleozoic strata (Buschbach and Kolata, 1990; Kolata and Nelson, 1990; Kissock et al., 2018). Basement rocks of the Illinois Basin consist of a voluminous Mesoproterozoic magmatic province referred to as the Eastern Granite-Rhyolite Province (EGRP; Thomas et al., 1984; Van Schmus et al., 1993). The EGRP is bisected by a southwest–northeast trending isotopic discontinuity dubbed the "Nd line" (Figure 1; Van Schmus et al., 1996). The Nd line separates Mesoproterozoic igneous rocks with Nd model ages > 1.55 Ga to the northwest from those with < 1.55 Ga model ages to the southeast and is generally interpreted to be a continental-scale Proterozoic terrane boundary. Mesoproterozoic rocks to the southeast are thought to represent 1.55–1.4 Ga juvenile crust that accreted to Laurentia as part of a long-lived arc system, whereas rocks to the northwest were derived from melting of Paleoproterozoic crust during Granite-Rhyolite magmatism (Van Schmus et al., 1996; Whitmeyer and Karlstrom, 2007; Bickford et al., 2015). Thus far, isotopic ages for Illinois basement granite and rhyolite are known from only five deep boreholes, four of

which were drilled along the northern and western margins of the Illinois Basin (Bickford et al., 2015 and references therein). The fifth is from VW #1 (Freiburg et al., 2019), from which we analyzed the overlying Cambrian sandstone as part of this study. All five published core samples reveal rocks that are 1,450–1,500 Ma in age.

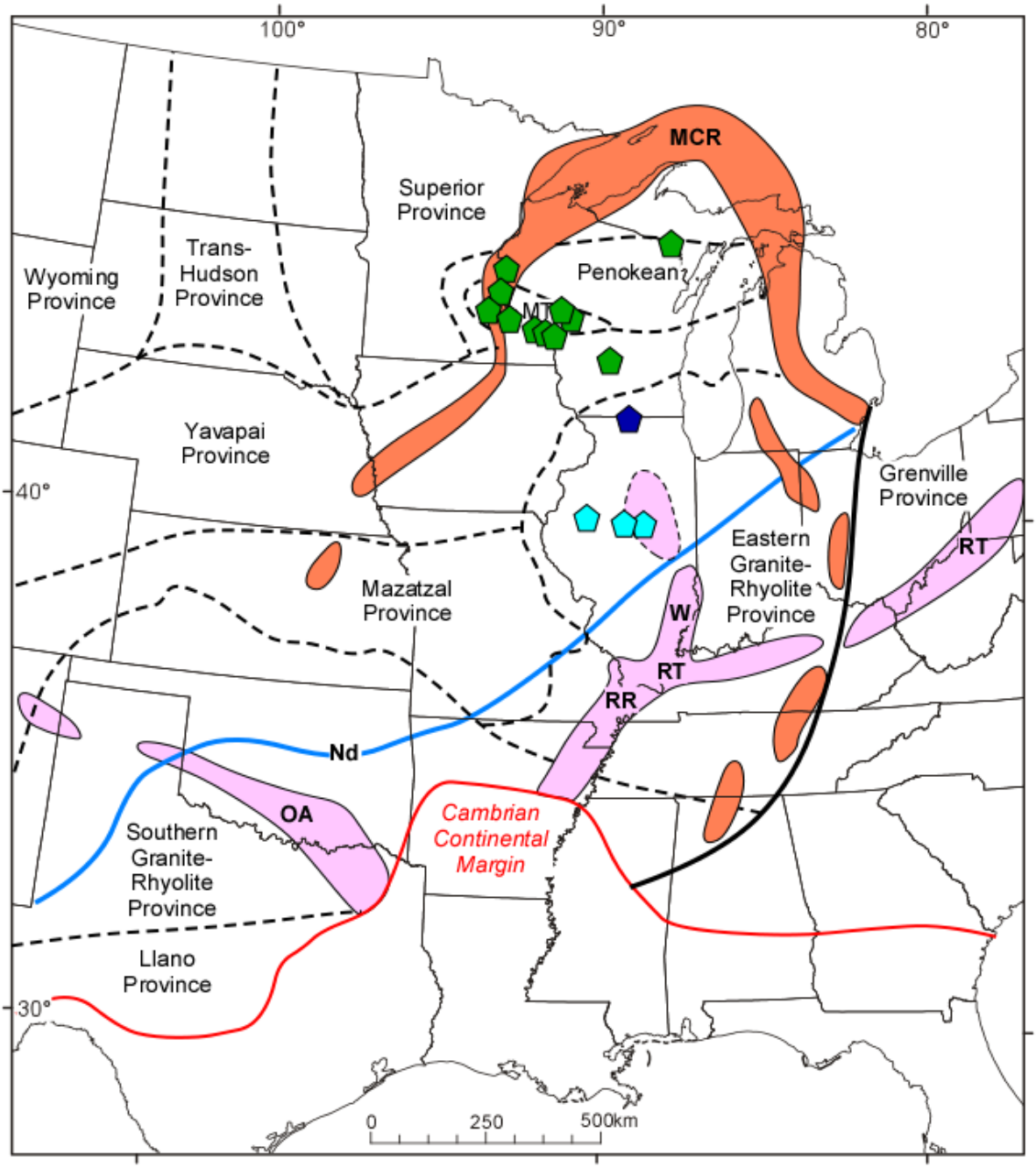

Figure 1. Map of basement terranes of the Laurentian Midcontinent (modified from Bickford et al., 2015). The locations of the Oklahoma Aulocogen (OA), Reelfoot Rift (RR), Rome Trough (RT), and Wabash (W) and LaSalle (L) deformational belts are indicated in pink. The northern arm of the Reelfoot Rift (Figure 2) is indicated by the pink area enclosed by the dashed line. The 1.1 Ga Midcontinent rift (MCR) is indicated in orange. Light blue pentagons indicate Illinois Basin sample locations for this study. Green pentagons indicate sampling sites for Late Cambrian arenites reported in Konstantinou et al. (2014). Dark blue pentagons indicate Mt. Simon drill core sampling locality

reported in Lovell and Bowen (2013). The blue line is the “Nd line” of Bickford et al. (2015), which separates crust yielding Nd model ages greater than 1.55 Ga to the north and less than 1.55 Ga to the south. Modified from Bickford et al. (2015) and Stein et al. (2018).

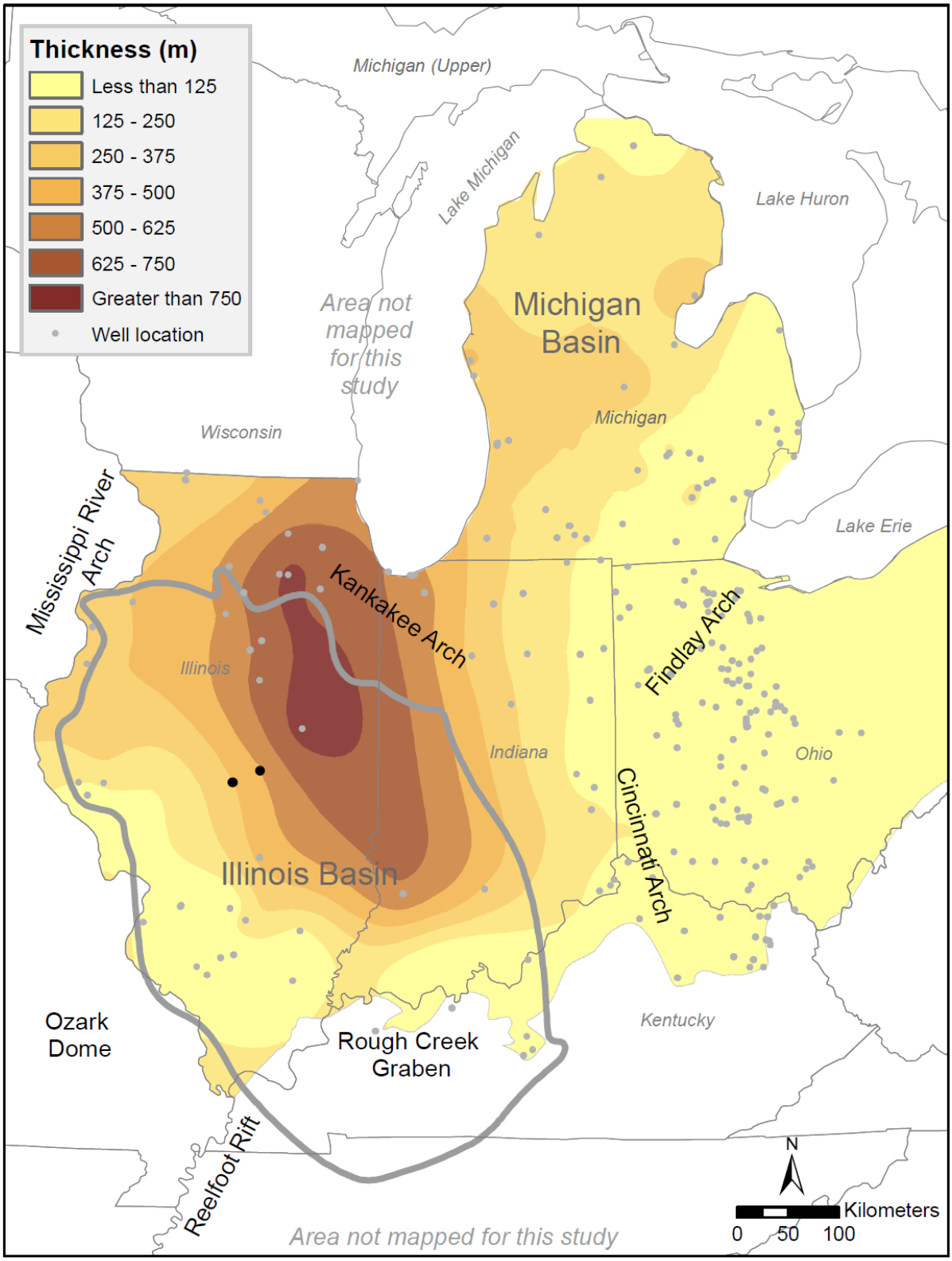

Figure 2. Isopach map of the combined Mt. Simon and Argenta Sandstones that indicates the depocenter in east-central Illinois. The locations of the well cores analyzed in this study are indicated.

The Cambrian Mt. Simon Sandstone unconformably overlies Precambrian basement rocks (Figure 2). Through seismic studies and deep drilling, Leetaru and Freiburg (2014) discovered an Early Paleozoic depocenter located several hundred kilometers north of the Late Paleozoic Illinois Basin depocenter (Freiburg et al., 2016). The axis of this Early Paleozoic depocenter roughly corresponds to the north–south geometry of the La Salle Anticlinal Belt (Craddock et al., 2017 and references therein). Drilling also revealed a previously unknown sandstone unit referred to as the pre-Mt. Simon (Freiburg et al., 2014) and more recently as the Argenta Sandstone (Freiburg et al., 2016). The Lower Mt. Simon and Argenta Sandstones overlie a layered Precambrian sedimentary or volcanic succession thus far known only on seismic reflection data and referred to as the Centralia Sequence (McBride et al., 2003).

The Cambrian Mt. Simon Sandstone in central Illinois is divided into three informal lithostratigraphic units referred to as the Upper, Middle, and Lower Mt. Simon (Figure 3; Freiburg et al., 2014). The Argenta Sandstone is an informal basal Cambrian unit that nonconformably overlies the Precambrian basement and disconformably underlies the Lower Mt. Simon Sandstone. Together, the Argenta and Mt. Simon Sandstones compose a thick (nearly 800 m) succession of sandstone and conglomerate that form the lowermost part of the Sauk sequence in the Illinois Basin (Sloss, 1963; Collinson et al., 1988). This interval represents the thickest succession of Cambrian strata in the Laurentian Midcontinent. The Argenta and Lower Mt. Simon Sandstones were deposited in a rift basin (Kolata and Nelson, 1990) located in north-central Illinois, several hundred kilometers north of the Illinois Basin depocenter.

Deposition of the Argenta Sandstone occurred in a rift basin setting where it is known to be as thick as 180 m (591 ft) near the depocenter and thins toward the margin of the basin. The depositional setting along the rift margin includes a transition from a fan-delta into a marine environment. Conglomeratic alluvial-fan facies occur along steeply dipping normal faults. Fluvial-deltaic, fining-upward succession of coarse sandstone overlain by red mudstone occurs above conglomerate. Fine-grained sandstone and mudstone are bioturbated with abundant *Skolithos*-, *Diplocraterion*-, and *Arencolites*-type burrows. The contact between the Argenta and the Lower Mt. Simon Sandstones is marked by a heavily bioturbated mudstone surface that includes pebble-sized, subangular, crystalline rock clasts. The Argenta Sandstone is texturally immature with abundant pore-filling clays.

In its depocenter in east-central Illinois, the Mt. Simon Sandstone is more than 700 m (2,297 ft) thick. The Lower Mt. Simon Sandstone comprises sandstone and conglomerate deposited in nearshore eolian and fluvial environments. Fine to coarse sandstone and conglomerate are tan to maroon in color and arkosic to subarkosic in composition. Some maroon mudstone and gray siltstone interbedded with fine, lenticular-bedded, and bioturbated sandstone is also present. These are interpreted as floodplain or lagoon deposits (Freiburg et al., 2014). Compared with the underlying Argenta, the Lower Mt. Simon is texturally mature with minor pore-filling clays.

Detrital zircon provenance studies of Cambrian strata in Laurentia are numerous (e.g., Gaudette et al., 1981; Gehrels et al., 1995; Stewart et al., 2001; Amato et al., 2012; May et al., 2013; Link et al., 2017; Malone et al., 2017a; Matthews et al., 2017; Karlstrom et al., 2018). Studies

show that Late Cambrian arenites of the Laurentian Midcontinent, which have well-established ages based on fossils (e.g., Berg, 1952; Nelson, 1956; Byers and Dott, 1995), are dominated by zircons recycled from the Proterozoic Huron, Animike, and Midcontinent Rift Basins (Lovell and Bowen, 2013; Konstantinou et al., 2014), and they reflect greater sediment dispersal and sediment recycling as the Sauk Seas transgressed and local basement rocks were buried.

Methods

We sampled the Lower Mt. Simon and the underlying Argenta Sandstones from core from two deep wells ~30 km apart in central Illinois: the CarbonSAFE T.R. McMillen #2 well (API 120212565000) located in Christian County and the Illinois Basin-Decatur Project VW #1 (API 121152346000) located in Macon County (Figure 4). We also sampled the Lower Mt. Simon from the FutureGen Industrial Alliance well #1 (API 121372213100) in Morgan County, ~100 km to the west, where the Argenta Sandstone is absent and only a thin Lower Mt. Simon Sandstone is present. Zircon crystals were extracted from core samples by traditional methods of crushing and grinding, followed by separation by panning, heavy liquids, and a Frantz magnetic separator. About 1 ft of drill core (~5 kg) was processed for each sample.

The mounts were sanded down to a depth of ~20 mm, polished, imaged, and cleaned before isotopic analysis. U-Pb geochronology of zircons was conducted by laser ablation inductively coupled plasma mass spectrometry at the Arizona LaserChron Center (Gehrels et al., 2006, 2008; Gehrels and Pecha, 2014). The analyses involved ablation of zircon with a Photon Machines Analyte G2 excimer laser equipped with HelEx ablation cell using a spot diameter of 20 mm. The ablated material was carried in helium into the plasma source of an Element2 HR inductively coupled plasma mass spectrometer, which sequences rapidly through U, Th, and Pb isotopes.

The ages are shown on relative age-probability diagrams, using the routines in Isoplot (Ludwig, 2008). The age-probability diagrams show each age and its uncertainty (for measurement error only) as a normal distribution and sum all ages from a sample into a single curve. Composite age-probability plots were made from an in-house Excel program that normalizes each curve according to the number of constituent analyses, such that each curve contains the same area, and then stacks the probability curves. The maximum depositional age (MDA) for each sample was calculated by taking the weighted mean age of the youngest subset of grains (at least four) with overlapping age errors. The zircon data tables are provided in the supplementary data.

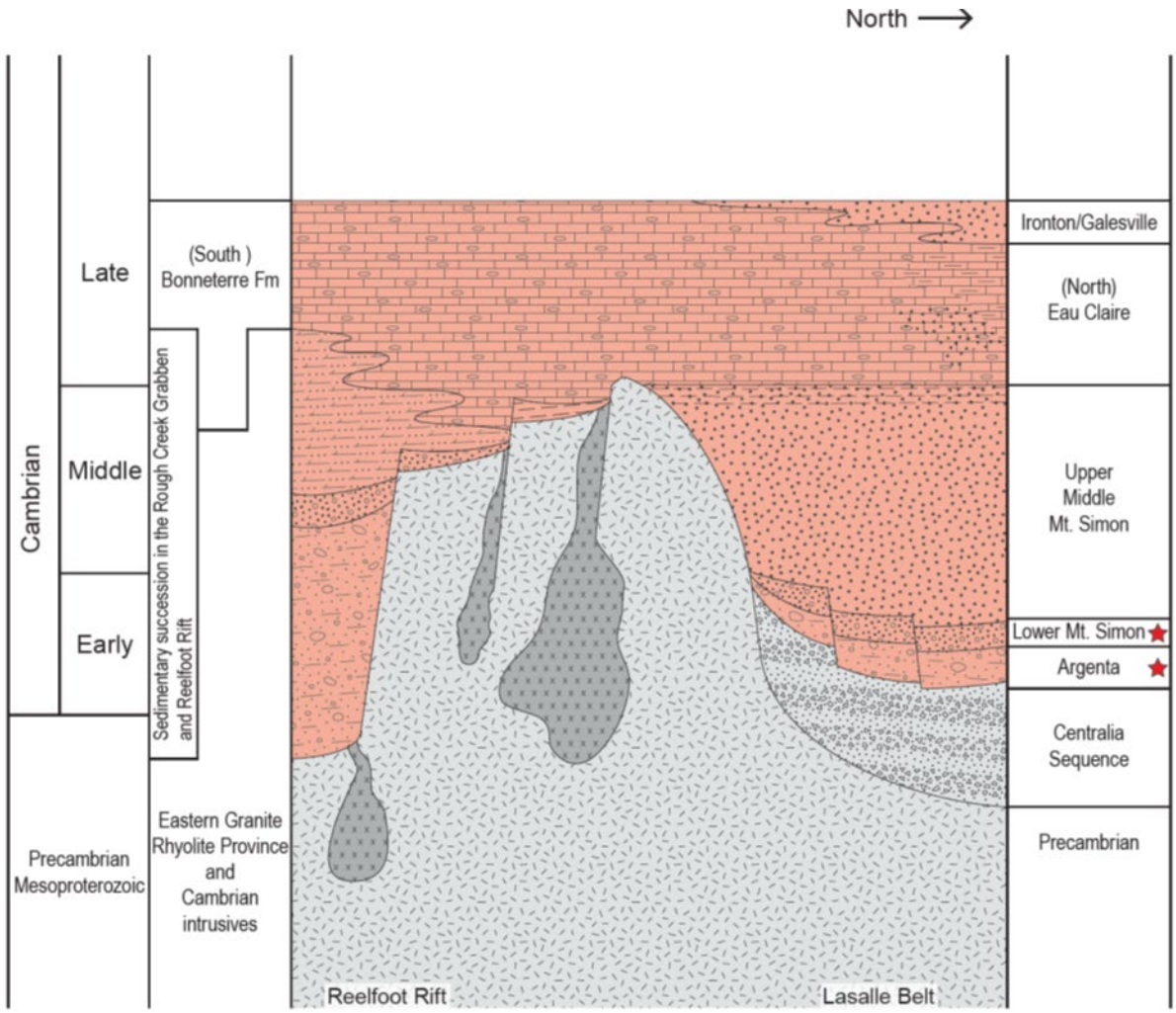

Figure 3. Correlation diagram of Cambrian strata and Proterozoic basement rocks present in the Illinois Basin. Our sampling localities are indicated by the red stars.

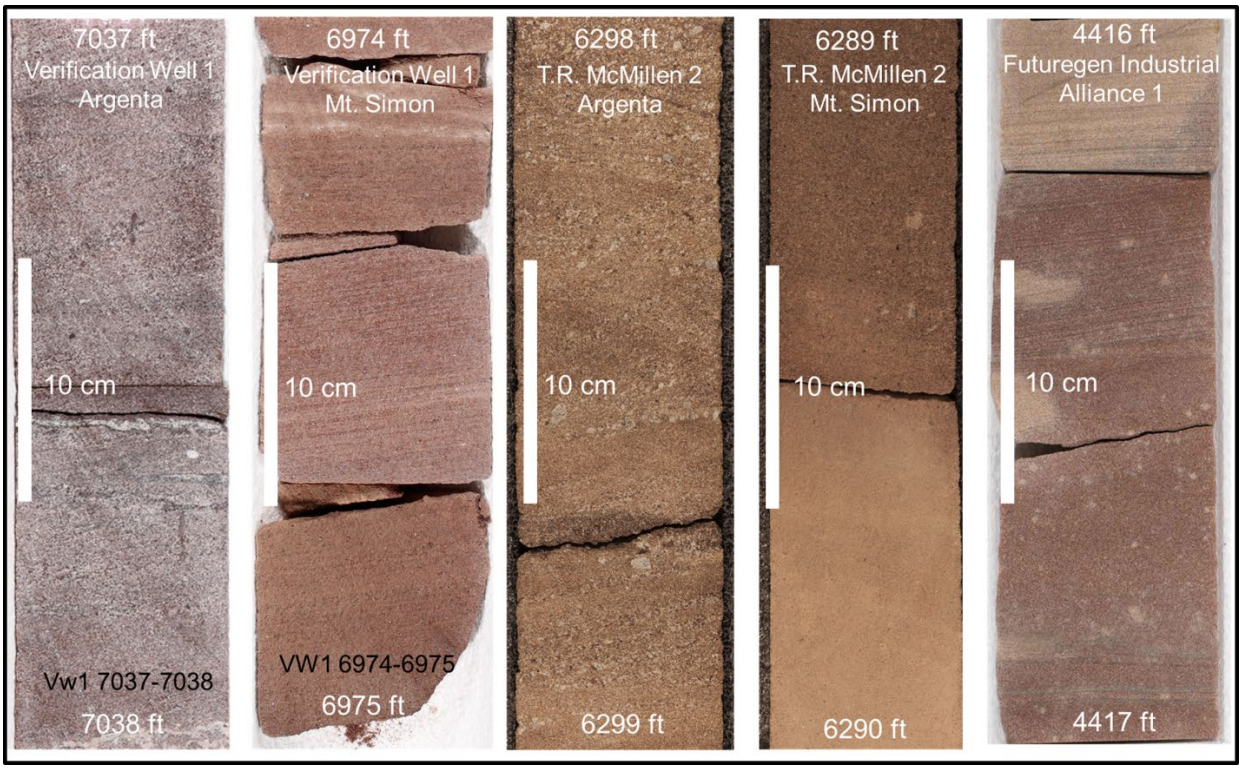

Figure 4. Photographs of core from five samples of the Lower Mt. Simon and Argenta Sandstones analyzed here.

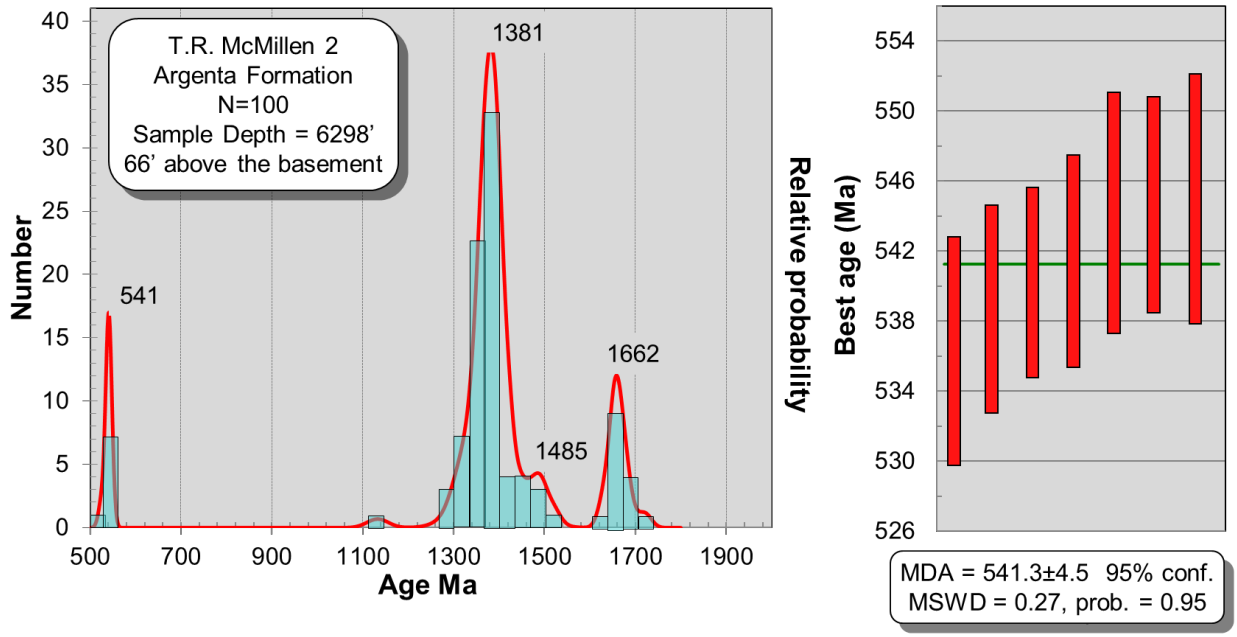

Figure 5. Probability density plot, histogram, and maximum depositional age of the Argenta Sandstone in T.R. McMillen #2.

Results

The probability density plots and the MDAs for each sample are provided in Figures 5–9. The Argenta Sandstone in VW #1 was sampled from a depth of 2,144.8–2,145.1 m (7,037–7,038 ft), which is 6.4 m (21 ft) above the underlying basement. The basement here has a U-Pb age of 1,467 ±10 Ma (Freiburg et al., 2019). A total of 192 detrital zircon ages are presented. The dominant age peak is ~1,372 Ma with lesser peaks at 1,650; 534; and 1,460 Ma. The MDA is 534 ± 4.7 Ma (Figure 5).

The Argenta Sandstone from the T. R. McMillen #2 was sampled at a depth of 1,919.6–1,919.9 m (6,298–6,299 ft), which is 20.1 m (66 ft) above the underlying basement. An isotopic age determination for basement rock here is in progress. The zircon age peaks are 1,381; 1,662; 541; and 1,485 Ma. The MDA is 541 ± 4.5 (Figure 6).

The Lower Mt. Simon Sandstone in VW #1 was sampled from a depth of 2,125.6–2,125.9 m (6,974–6,975 ft), which is 25.2 m (83 ft) above the underlying basement. A total of 180 detrital zircon ages are presented. The dominant age peak is ~1,381 Ma with lesser peaks at 1,650; 530; and 1,452 Ma. The MDA is 5,295 ± 5.6 Ma (Figure 7).

The Lower Mt. Simon Sandstone in T.R. McMillen #2 was sampled from a depth of 1,916.8–1,917.1 m (6,289–6,290 ft), which is 22.8 m (75 ft) above the underlying basement. A total of 183 detrital zircon ages are presented. The dominant age peak is ~1,381 Ma with lesser peaks at 527; 1,653; and 1,132 Ma. The MDA is 5,275 ± 4.1 Ma (Figure 8).

The Lower Mt. Simon Sandstone for the FutureGen Industrial Alliance well #1 was sampled from a depth of 1,406.6–1,406.9 m (4,615–4,616 ft), which is 4.2 m (14 ft) above the underlying basement. This well was drilled ~100 km west of and more than 600 m (2,000 ft) above the Argenta trough penetrated by the other two wells. An isotopic age determination for basement rock here is in progress. A total of 305 detrital zircon ages are presented. The dominant age peak is ~1,380 Ma with lesser peaks at 2,600; 1,652; 1,453; 1,652; and 1,140 Ma. This sample is the only one of the five samples to have notable concentrations of Archean and Grenville grains. The MDA is 5,345 ± 4.6 Ma (Figure 9).

Kolmogorov-Smirnov analysis (supplementary data) indicates a statistical relationship between the lower samples in each well, between each upper sample and each lower sample in each well, but not between the two upper samples. When treated as a whole (i.e., all 960 grains; Figure 10), the youngest age group (~5% of the total) ranges in age from 524 to 547 Ma and has a peak age of 533 Ma. For the stratigraphically deeper Argenta Sandstone, the respective age peaks are slightly older at 535 and 542 Ma.

For the shallower Lower Mt. Simon sample in each well, the respective peak ages are younger at 531 and 528 Ma. The largest age peak of 1,375 Ma, with a secondary age peak of 1,460 Ma, accounts for nearly 80% of the detrital zircon age spectrum. Paleoproterozoic zircons, with a peak age of 1,655 Ma, account for ~10% of the zircon age spectrum. Grenville-age grains with a peak of 1,130 Ma account for ~5% of the composite age spectrum.

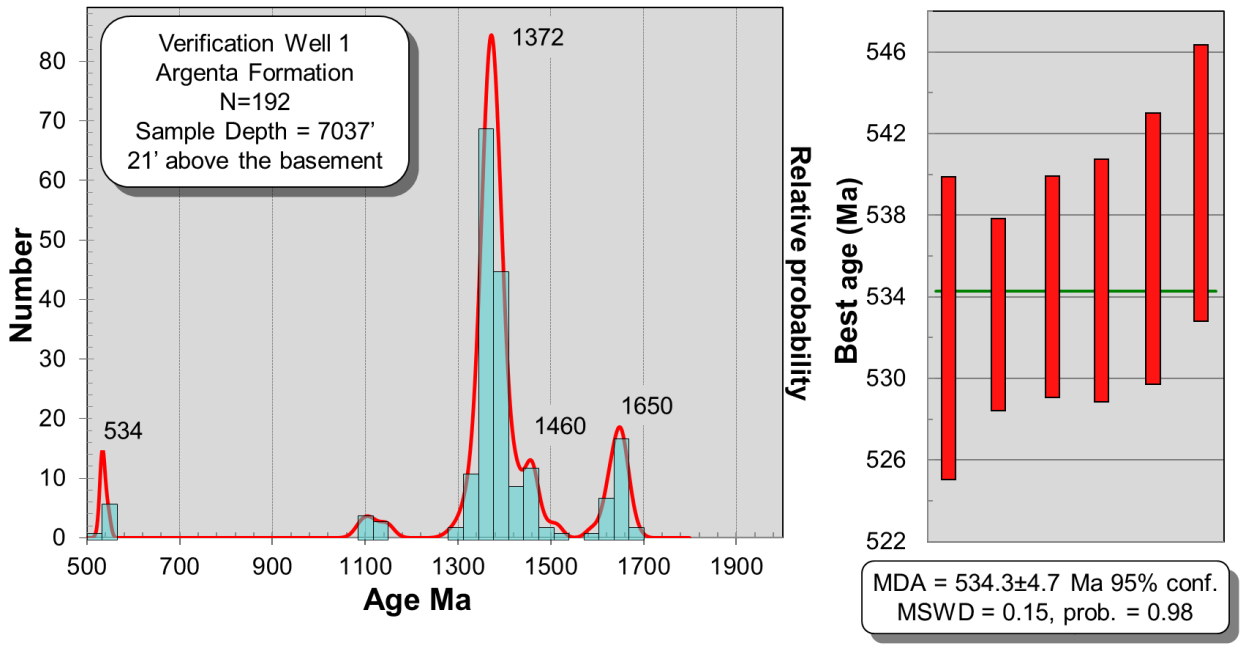

Figure 6. Probability density plot, histogram, and maximum depositional age of the Argenta Sandstone in VW #1. Freiburg et al. (2019) report an age of 1,467 Ma from the underlying rhyolite penetrated by this well.

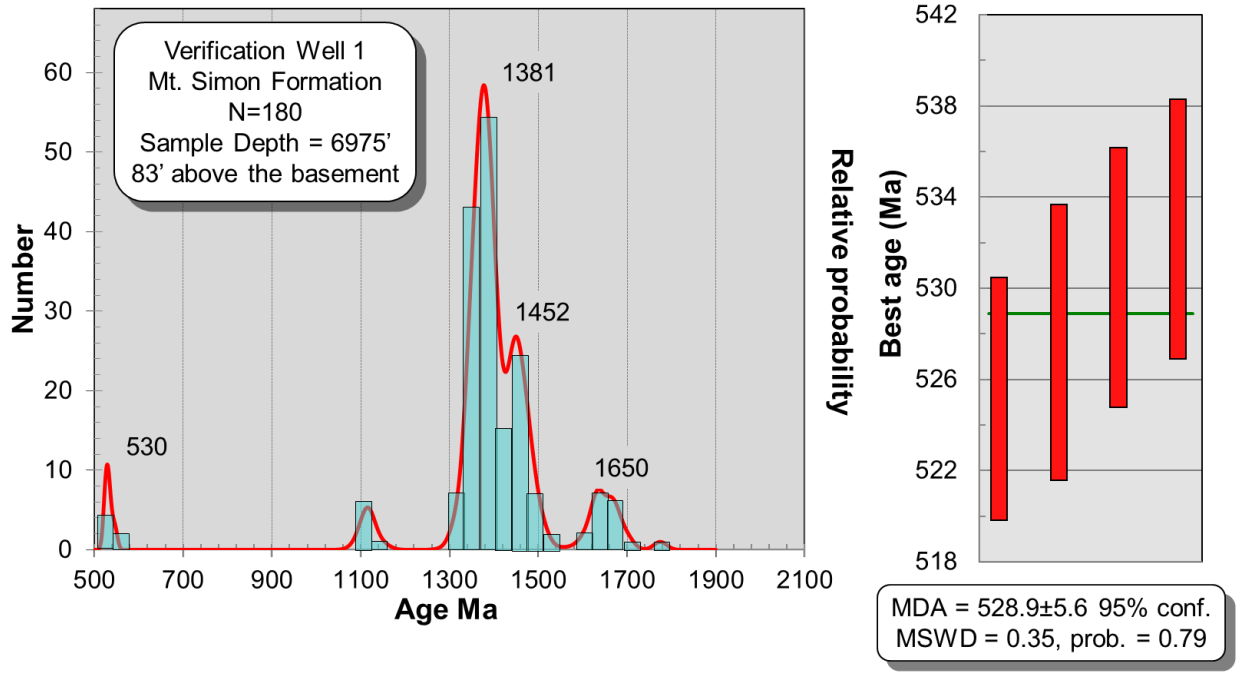

Figure 7. Probability density plot, histogram, and maximum depositional age of the Lower Mt. Simon Sandstone in VW #1.

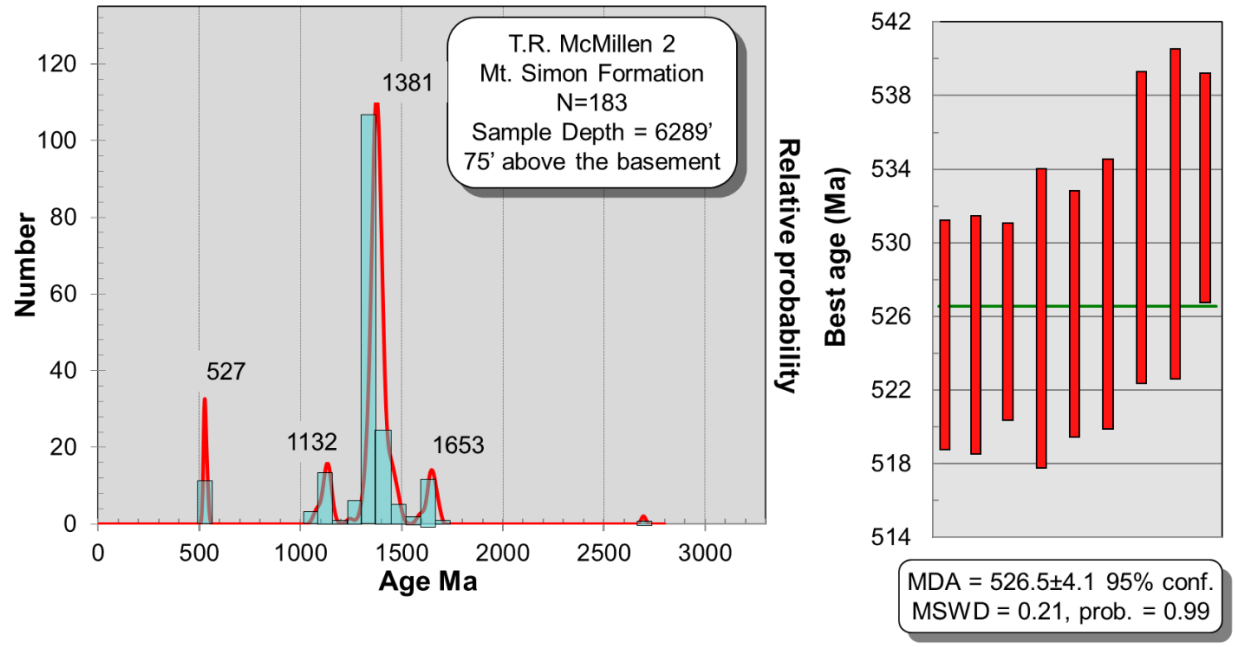

Figure 8. Probability density plot, histogram, and maximum depositional age of the Lower Mt. Simon Sandstone in T.R. McMillen #2.

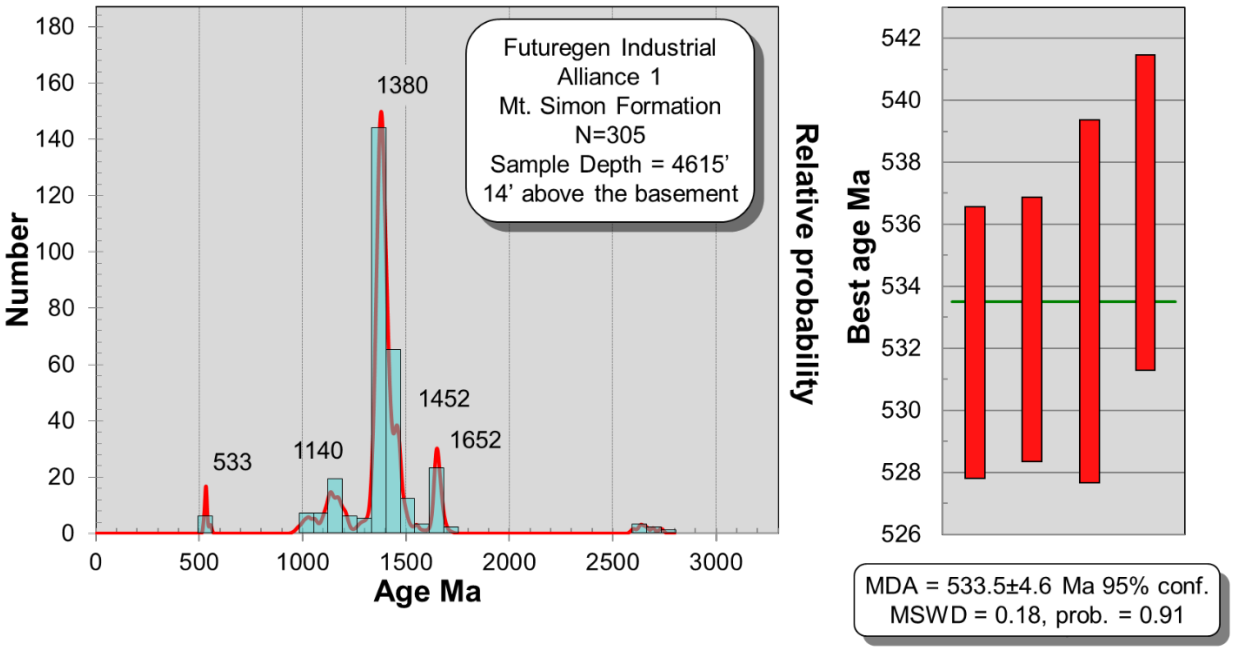

Figure 9. Probability density plot, histogram, and maximum depositional age of the Lower Mt. Simon Sandstone in FutureGen Industrial Alliance well #1.

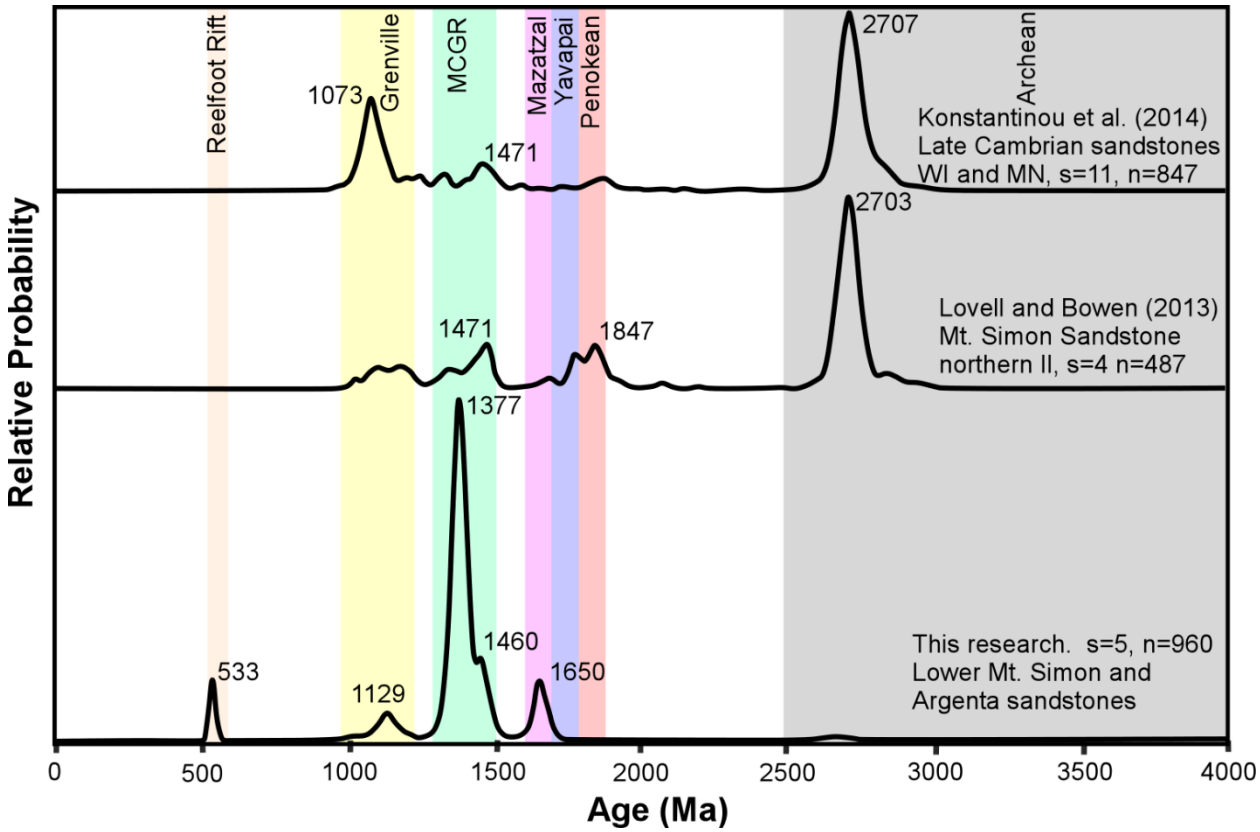

Figure 10. Stacked probability plots comparing the combined Mt. Simon and Argenta Sandstones detrital zircon ages analyzed here to the Upper Mt. Simon core from northern Illinois (Lovell and Bowen, 2013) and the Cambrian arenites in Minnesota and Wisconsin (Konstantinou et al., 2014).

Discussion

Age and provenance of the Lower Mt. Simon and Argenta Sandstones

Cambrian strata in Wisconsin and Missouri are interpreted to be Late Cambrian in age (Ojakangas, 1963; Houseknecht and Ethridge, 1978). These same strata overlie the Argenta and Lower Mt. Simon by more than 500 m (1,640 ft). The maximum depositional age for the Argenta and Lower Mt. Simon Sandstones ranges from 527-541 Ma, which we interpret to reflect a local Early Cambrian rifting event. Unfortunately, the cores that we analyzed do not provide biostratigraphic control for the age, and these rocks are most likely Middle Cambrian in age. The middle Cambrian interpretation is supported by the presence of nearly 1,000 m (3,281 ft) of demonstrably Late Cambrian strata that overlie the lower Mt. Simon and Argenta Sandstones and by the range of MDAs from 527 to 541 Ma determined in this study.

Detrital zircon geochronologic data indicate that the Mt. Simon and Argenta Sandstones sampled in this study have a provenance distinct from the overlying ubiquitous Late Cambrian arenites present in the Laurentian Midcontinent (Figure 11). Following is a summary of the major detrital zircon populations present in the Mt. Simon and Argenta Sandstones and their possible sources, with important implications for the Paleoproterozoic to Cambrian evolution of the Laurentian Midcontinent.

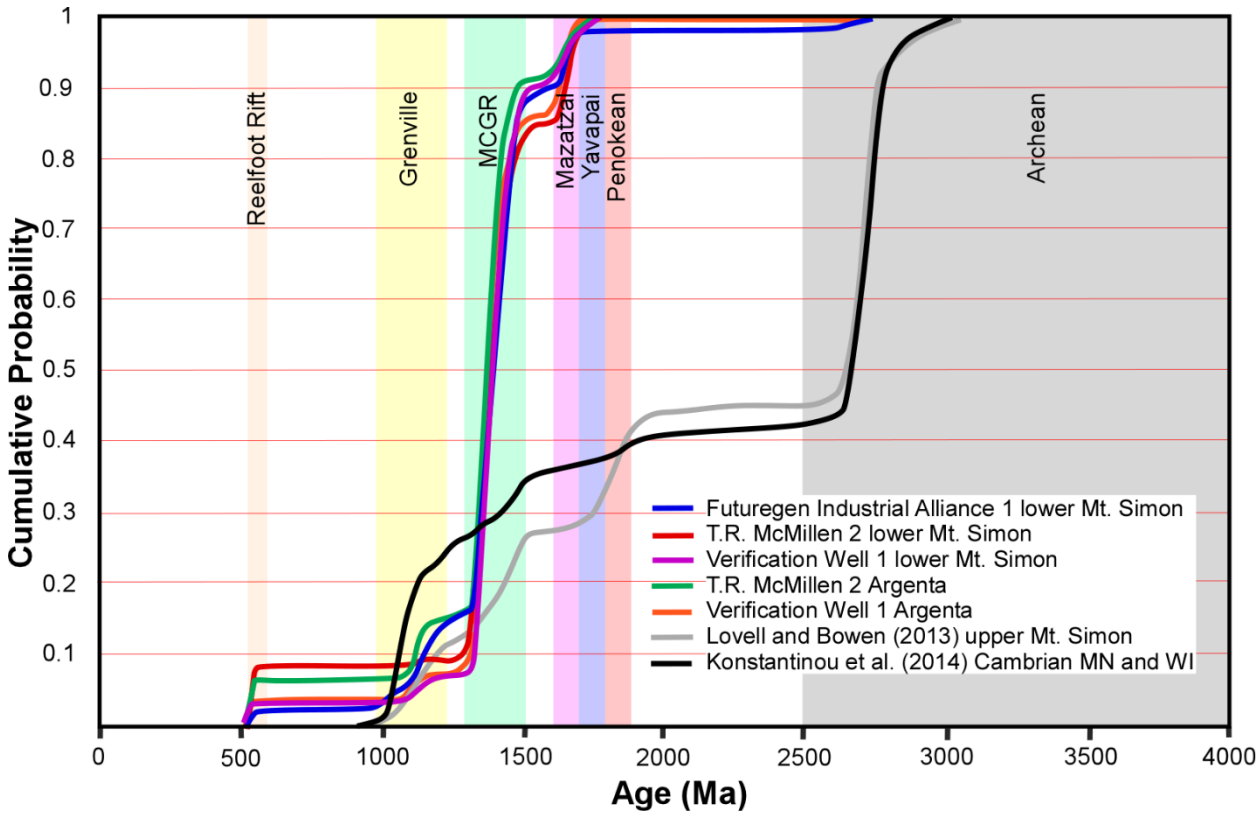

Figure 11. Cumulative probability plots comparing the combined Mt. Simon and Argenta Sandstones detrital zircon ages analyzed here to the Upper Mt. Simon core from northern Illinois (Lovell and Bowen, 2013) and the Cambrian arenites in Minnesota and Wisconsin (Konstantinou et al., 2014).

Paleoproterozoic Ages

The oldest detrital zircon population present in all samples is ~1,650 Ma. This age is characteristic of the Mazatzal Province of Whitmeyer and Karlstrom (2007), known to be exposed in the southwestern United States and present in the subsurface in the midcontinent region. The 1,650 Ma detritus in the Mt. Simon and Argenta Sandstones could have been derived from the Mazatzal crustal province to the west of the Illinois Basin, where crust of that age is known to be present in the subsurface. Alternatively, 1,650 Ma detrital zircons may have been locally derived. Proterozoic basement beneath the Illinois Basin is significantly under-sampled compared with regions to the southwest and northeast (Bickford et al., 2015). Therefore, although the presence of 11.55 Ga Paleoproterozoic crust is inferred northwest of the Nd line, its true extent is unknown because of uncertainties about the location and tectonic significance of the Nd line itself (e.g., Petersson et al., 2015).

EGRP Basement Ages

All five samples of the Mt. Simon and Argenta Sandstones display a prominent 1,380–1,370 Ma age peak and a subsidiary 1,485–1,450 Ma peak. These ages are consistent with the magmatic record of the EGRP. The EGRP is defined by rocks exposed in the St. Francois Mountains in eastern Missouri and data from deep drill cores in Missouri, Arkansas, Tennessee, Kentucky, Indiana, and Illinois, although the data set is heavily biased toward Missouri (Lidiak et al., 1993; Bickford et al., 2015). Rocks of the St. Francois Mountains record at least two episodes of magmatism: (1) silicic volcanic rocks and epizonal granitic plutons have been interpreted as a caldera complex that was emplaced at ~1.47 Ga (Sides et al., 1981; Van Schmus et al., 1996) and

(2) a relatively minor episode of granitic magmatism at ~1.37 Ga (Van Schmus et al., 1996). Both ages are represented in samples from drill cores throughout the EGRP, although the 1.47 Ga mode is more common, and 1.37 Ga magmatism is more typical of the Southern Granite-Rhyolite Province (SGRP; Van Schmus et al., 1996; Bickford et al., 2015). The only available basement data indicate that the Illinois Basin is underlain by 1,500–1,460 Ma crust (Hoppe et al., 1983; Van Schmus et al., 1987; Freiburg et al., 2019). Thus, the prominence of the 1,380–1,370 Ma age peak over the 1,460 Ma peak may be interpreted to indicate either that rocks of this age are present throughout more of the EGRP than is currently recognized or that the Mt. Simon and Argenta Sandstones received detritus from the SGRP.

Cambrian Ages

A population of 540–525 Ma detrital zircons is present in all five samples from the Argenta and Lower Mt. Simon Sandstones. This age range is characteristic of the Wichita igneous province exposed in the Wichita and Arbuckle Mountains of southern Oklahoma (Hanson et al., 2013), and their presence could indicate that the Lower Mt. Simon and Argenta Sandstones were derived from sediment supplied from the southwest. A southwestern source would be consistent with the predominance of ~1,370 Ma over 1,460 Ma detrital zircons in the Lower Mt. Simon and Argenta samples.

A Northern Arm of the Reelfoot Rift

Despite the apparent match between distal sources discussed above and the detrital zircon populations observed in our samples, we favor an alternative interpretation. We propose that the Lower Mt. Simon and Argenta Sandstones were deposited in a trough located north of (or perhaps a northern extension of) the Reelfoot Rift, an extensional arm of the New Madrid Rift system associated with the breakup of the supercontinent Rodinia. In our interpretation, the Lower Mt. Simon and Argenta Sandstones were deposited before and during rifting and were derived primarily from local Proterozoic basement rocks exposed along rift shoulders and Cambrian igneous rocks associated with the Reelfoot Rift itself.

Ample geophysical evidence shows intrusive bodies along the margins of the Reelfoot Rift. Large igneous bodies have been interpreted from gravity and magnetic data (Ervin and McGinnis, 1975; Hildenbrand, 1982, 1985). Rift strata below the Paleozoic section are not observed at the VW #1 site, but seismic study reveals a bowl-shaped feature in the Precambrian rocks with apparent layering (McBride et al., 2016). A drill core in the basement is rhyolitic and yields an age of 1,467 Ma, and a gabbro intrusion in the rhyolite yields an age of 1,073 Ma (Freiburg et al., 2019). Freiburg et al. (2019) proposed that the bowl-shaped feature emplaced younger EGRP on older crust, herein proposed as 1,650 Ma crust (Figure 12). The margin of the Proterozoic basement appears faulted with a series of normal faults accommodating thicker sections of Argenta and Lower Mt. Simon Sandstones eastward. Cawood et al. (2012) report that syndepositional sandstones in active rift basins tend to have the youngest subset of grains approximate the age of deposition. Most zircons present in sandstones deposited in rift-related successions, such as this setting, tend to derive from proximal rather than distal source areas. This accounts for the disparity between detrital zircon populations of the Lower Mt. Simon and Argenta and younger Cambrian sandstones regionally (Figure 10). Grenville zircons are rare in the Argenta and occur only in small numbers in the Lower Mt. Simon, which indicates the first appearance of distal sediment that becomes dominant in Late Cambrian sandstones to the north. Archean and Paleoproterozoic grains that dominate the Late Cambrian succession to the north are not observed in the samples of this study (Lovell and Bowen, 2013; Konstantinou et al., 2014). If these zircons were indeed far

traveled, significant concentrations of the ubiquitous Superior and Grenville Province grains could also be expected in the Lower Mt. Simon and Argenta Sandstones, as they are in the overlying strata. The fertility bias for Grenville-age zircons is well known, and if such rocks were supplying sediment to the Lower Mt. Simon and Argenta, zircons of this age would be present in quantity (Moecher and Samson, 2006). Moreover, paleocurrent data for Cambrian strata to the north indicate that sediment was transported to the southwest (Michelson and Dott, 1973). Westerly rather than easterly sediment transport of Laurentian sediment is evident for the entire Late Neoproterozoic-Cambrian strata deposited along the Cordilleran continental margin from California to Idaho (Yonkee et al., 2014; Malone et al., 2017b). Finally, the presence of ~1,650 Ma basement beneath the Illinois Basin is supported by the presence of similarly aged (1,660 Ma) detrital zircons in the Waterloo quartzite of Wisconsin, which records north-directed paleocurrent indicators (Medaris et al., 2019).

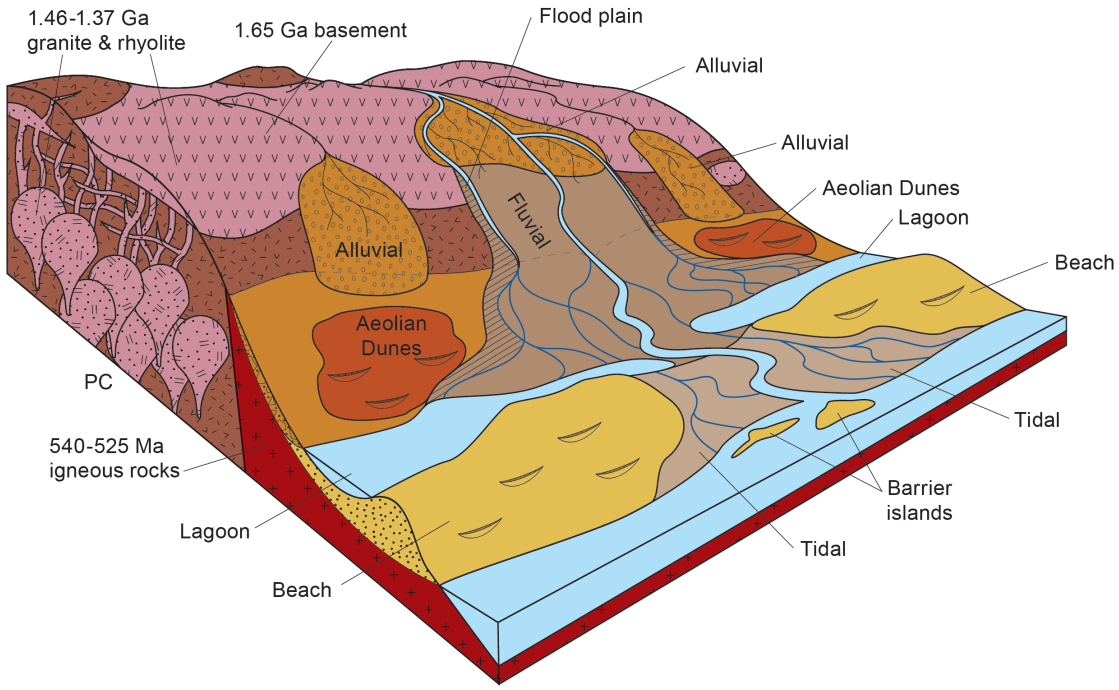

Figure 12. Depositional model for the Mt. Simon and Argenta Sandstones in east-central Illinois. The Argenta and lower Mt. Simon Sandstones were deposited in an isolated basin north of and perhaps an arm of the Reelfoot Rift. Sediment was derived from the rift shoulders, which include EGRP and Late Paleoproterozoic crust, and from Cambrian rocks in the rift itself.

The Rifting of Rodinia

During the breakup of Rodinia (~780–530 Ma), major rift systems developed along the margins of Laurentia. The thickest, best exposed, and most studied occur along the Cordilleran continental margin (Yonkee et al., 2014), where almost 5 km of siliciclastic strata of the Uinta Mountain Group dated at 770–740 Ma are overlain by more than 1 km of the Pocatello Formation, representing the main phase of rifting from 720 to 680 Ma (Fanning and Link, 2004). The Neoproterozoic- Cambrian Brigham Group consists of mature siliciclastic rocks that are as much as 4 km thick and were deposited along the Cordilleran continental margin following the earlier rifting. Late Neoproterozoic to Cambrian passive margin strata are also present along the

Appalachian continental margin. The timing of rifting there ranged from ~770 to 570 Ma (Walsh and Aleinikoff, 1999; Smoot and Southworth, 2014). The Oklahoma aulacogen developed, and associated 540–530 Ma rift-related volcanic and plutonic rocks were also emplaced (Thomas, 1991; Thomas et al., 2012; Hanson et al., 2013). Thomas et al. (2004) provide a detrital zircon age spectrum for the Early-Middle Cambrian Rome Formation in Alabama, but only long-transported cratonic rather than rift-related zircons are present. The timing of the opening of the northern arm of the Reelfoot Rift in Illinois is now proposed to be 540–525 Ma based on the new detrital zircon ages. This age is identical to that of igneous rocks that occur in the Oklahoma aulacogen, which indicates that the timing of the rifting of the Iapetan rifted margin of southeast Laurentia occurred coevally rather than sequentially. Our data support the model of Thomas et al. (2004), showing that the Oklahoma aulacogen and Reelfoot Rift were failed arms of the fragmentation of the Argentine Precordillera. As rifting ceased and the transgression of the Sauk Seas commenced, the basement paleotopography was buried and the supply of local sediment to the Cambrian depositional systems waned. By Late Cambrian time, much of the Reelfoot Rift, EGRP, and Paleo- to Mesoproterozoic basement crust of the Laurentian Midcontinent were buried, and mature sediment recycled from older Proterozoic Basins in the Lake Superior area and the Grenville Province was deposited in the Midcontinent (Konstantinou et al., 2014; Malone et al., 2016). It is evident that these Neoproterozoic-Cambrian Rift Basins in Illinois do not coincide with the presumed location of Proterozoic lithospheric boundaries (e.g., the Nd line).

Conclusions

The detrital zircon age spectra for the Lower Mt. Simon and Argenta Sandstones help constrain the age of Illinois basement rocks and Early Cambrian rifting associated with the breakup of Rodinia (Figure 11). Both the Argenta and Lower Mt. Simon were derived locally and eroded from Paleo- and Mesoproterozoic crust present on the northern extension of the Reelfoot Rift. Magmatic rocks associated with rifting from ~540 to 525 Ma also supplied sediment to the terrestrial and marginal marine depositional systems. As the Sauk Seas transgressed and sea level rose, the deeper troughs were filled and the sediment supply from local basement sources waned. By Late Cambrian time, sediment was derived from more distal source areas in the Grenville and Superior Provinces. At this time, Lower Mt. Simon and Argenta Sandstones and underlying basement rocks were buried, and thus the availability of locally derived sediment into the Late Cambrian arenites was not possible.

References

Amato, J.M. and Mack, G.H., 2012, Detrital zircon geochronology from the Cambrian-Ordovician Bliss Sandstone, New Mexico: Evidence for contrasting Grenville-age and Cambrian sources on opposite sides of the Transcontinental Arch: Geological Society of America Bulletin, v. 124, p. 1826-1840.

Berg, R.R. 1952, Feldspathized sandstone: Minnesota and Wisconsin. Journal of Sedimentary Petrology, v. 22, p. 221–223.

Bickford, M.E. and Van Schmus, and W.R., Zietz, I., 1986, Proterozoic history of the midcontinent region of North America: Geology v. 14, p. 492–496.

Bickford, M.E., Van Schmus, W.R., Karlstrom, K.E., Mueller, P.A. and Kamenov, G.D., 2015, Mesoproterozoic-trans-Laurentian magmatism: A synthesis of continent-wide age distributions, new SIMS U–Pb ages, zircon saturation temperatures, and Hf and Nd isotopic compositions. Precambrian Research, v. 265, p. 286-312.

Buschbach, T.C., and Kolata, D.R., 1990, Regional Setting of Illinois Basin: Chapter 1: Part I. Illinois Basin: Regional Setting, in Leighton, M. W., Kolata, D. R., Oltz, D. T., and Eidel, J. J. eds., Memoir 51: Interior Cratonic Basins: American Association of Petroleum Geologists, p. 29-55.

Byers, C. W., and Dott, R. H. 1995. Sedimentology and depositional sequences of the Jordan Formation (Upper Cambrian) northern Mississippi Valley: Journal of Sedimentary Research, v. 65, p. 1073–1318.

Cawood, P.A., Hawkesworth, C.J. and Dhuime, B., 2012, Detrital zircon record and tectonic setting. Geology, v. 40, p. 875-878.

Collinson, C., Sargent, M.L. and Jennings, J.R., 1988. Illinois basin region. Sedimentary Cover—North American Craton, US: Geological Society of America, The Geology of North America, 2, p . 383-426.

Craddock, J.P., Malone, D.H., Porter, R., Compton, J., Luczaj, J., Konstantinou, A., Day, J.E. and Johnston, S.T., 2017, Paleozoic reactivation structures in the Appalachian-Ouachita-Marathon foreland: Far-field deformation across Pangea: Earth-Science Reviews, v. 169, p. 1-34.

Ervin, C.P. and McGinnis, L.D., 1975, Reelfoot rift: Reactivated precursor to the Mississippi embayment. Geological Society of America Bulletin, v. 86, p. 1287-1295.

Fanning, C.M. and Link, P.K., 2004, U-Pb SHRIMP ages of Neoproterozoic (Sturtian) glaciogenic Pocatello Formation, southeastern Idaho: Geology, v. 32, p. 881-884.

Freiburg, J.T., D., Morse, H., Leetaru, R.P., Hoss and Q., Yan, 2014, A Depositional and Diagenetic Characterization of the Mt. Simon Sandstone at the Illinois Basin-Decatur Project Carbon Capture and Storage Site, Decatur, Illinois, USA: Illinois State Geological Survey Circular 583, 59 p.

Freiburg, J.T., R.W., Ritzi and K.S., Kehoe, 2016, Depositional and diagenetic controls on anomalously high porosity within a deeply buried CO2 storage reservoir—The Cambrian Mt. Simon Sandstone, Illinois Basin, USA: International Journal of Greenhouse Gas Control, v. 55, 42-54.

Freiburg, J.T., McBride, J.H., Malone, D.H., and Leetaru, H.E., 2019, Petrology, geochronology and geophysical characterization of Mesoproterozoic rocks in central Illinois, USA: Manuscript in press at Geoscience Frontiers.

Gaudette, H.E., Vitrac-Michard, A. and Allegre, C.J., 1981, North American Precambrian history recorded in a single sample: high-resolution U-Pb systematics of the Potsdam sandstone detrital zircons, New York State: Earth and Planetary Science Letters, 54, p. 248-260.

Gehrels, G.E., Dickinson, W.R., Ross, G.M., Stewart, J.H. and Howell, D.G., 1995, Detrital zircon reference for Cambrian to Triassic miogeoclinal strata of western North America. Geology, v. 23, p. 831-834.

Gehrels, G.E., Valencia, V., Ruiz, J., 2008, Enhanced precision, accuracy, efficiency, and spatial resolution of U-Pb ages by laser ablation–multicollector–inductively coupled plasma–mass spectrometry. Geochemistry, Geophysics, Geosystems 9, Q03017, doi:10.1029/2007GC001805.

Gehrels, G.E., Valencia, V., Pullen, A., 2006. Detrital zircon geochronology by Laser-Ablation Multicollector ICPMS at the Arizona LaserChron Center, in Loszewski, T., and Huff, W., eds., Geochronology: Emerging Opportunities, Paleontology Society Short Course: Paleontology Society Paper, v. 11, p. 1-10.

Hanson, R.E., Puckett, R.E., Jr., Keller, G.R., Brueseke, M.E., Bulen, C.L., Mertzman, S.A., Finegan, S.A., and McCleery, D.A., 2013, Intraplate magmatism related to opening of the southern Iapetus Ocean: Cambrian Wichita igneous province in the Southern Oklahoma rift zone: Lithos, v. 174, p. 57–70.

Hildenbrand, T.G., 1982, Model of the southeastern margin of the Mississippi Valley graben near Memphis, Tennessee, from interpretation of truck-magnetometer data. Geology, v. 10. p. 476-480.

Hildenbrand, T.G., 1985, Rift structure of the northern Mississippi embayment from the analysis of gravity and magnetic data: Journal of Geophysical Research Solid Earth, v. 90 (B14), p. 12607-12622.

Hoppe, W.J., Montgomery, C.W., Van Schmus, W.R., 1983, Age and significance of Precambrian Basement samples from northern Illinois and adjacent states: Journal of Geophysical Research (Red.) v. 88, p. 7276–7286.

Houseknecht, D.W. and Ethridge, F.G., 1978, Depositional history of the Lamotte Sandstone of southeastern Missouri. Journal of Sedimentary Research, v. 48, p. 575-586.

Karlstrom, K., Hagadorn, J., Gehrels, G., Matthews, W., Schmitz, M., Madronich, L., Mulder, J., Pecha, M., Giesler, D. and Crossey, L., 2018, Cambrian Sauk transgression in the Grand Canyon region redefined by detrital zircons: Nature Geoscience, v. 11, p. 438.

Kissock, J.K., Finzel, E.S., Malone, D.H., and Craddock, J.P., 2018, Lower–Middle Pennsylvanian strata in the North American midcontinent record the interplay between erosional unroofing of the Appalachians and eustatic sea-level rise: Geosphere, v. 15, p. 1-21.

Kolata, D.R., Nelson, W.J., 1990.Tectonic history of the Illinois basin. In: Leighton, M.W., Kolata, D.R., Oltz, D.E, Eidel, J.J., (Eds.), Interior Cratonic Basins. American Association of Petroleum Geologists, Memoir 51, 263-285.

Konstantinou, A., Wirth, K., Craddock, J.P., Malone, D.H., Vervoort, J.D., and Davidson, C., 2014, Provenance of Early Paleozoic Quartz Arenites, Midcontinent, USA: Journal of Geology, v. 122, p. 201-216.

Leetaru, H.E. and Freiburg, J.T., 2014, Litho-facies and reservoir characterization of the Mt Simon Sandstone at the Illinois Basin – Decatur Project: Greenhouse Gases: Science and Technology, v. 4, p. 580-595.

Lidiak, E.G., Bickford, M.E., Kisvarsanyi, E.B., 1993, Proterozoic geology of the eastern midcontinent basement. In: Van Schmus, W.R., Bickford, M.E. (Eds.), Chapter 4, Transcontinental Proterozoic Provinces, Precambrian Volume, Decade of North American Geology (DNAG). Geological Society of America, p. 259–270.

Link, P.K., Todt, M.K., Pearson, D.M. and Thomas, R.C., 2017, 500–490 Ma detrital zircons in Upper Cambrian Worm Creek and correlative sandstones, Idaho, Montana, and Wyoming: Magmatism and tectonism within the passive margin: Lithosphere, v. 9, p. 910-926.

Lovell, T.R. and Bowen, B.B., 2013, Fluctuations in sedimentary provenance of the Upper Cambrian Mt. Simon Sandstone, Illinois Basin, United States. The Journal of Geology, v. 121, p. 129-154.

Ludwig, K. R. 2012. User's manual for ISOPLOT 3.75: a geochronological toolkit for Microsoft Excel. Spec. Publ. 5. Berkeley, CA, Berkeley Geochronology Center, 75 p.

Malone, D.H., Stein, C.A., Craddock, J.P., Kley, J., Stein, S. and Malone, J.E., 2016, Maximum depositional age of the Neoproterozoic Jacobsville Sandstone, Michigan: Implications for the evolution of the Midcontinent Rift: Geosphere, v. 12, p. 1271-1282.

Malone D.H., Craddock, J.P., and Kenderes, S., 2017, Detrital Zircon Geochronology of the Cambrian Flathead Sandstone, Park County, WY: Mountain Geologist, v. 54, p. 86-103. DOI:10.31582/rmag.mg.54.2.86

Malone, D.H., Craddock, J.P., Link, P.K., Foreman, B.Z., Scroggins, M.A. and Rappe, J., 2017, Detrital zircon geochronology of quartzite clasts, northwest Wyoming: Implications for Cordilleran Neoproterozoic stratigraphy and depositional patterns: Precambrian Research, v. 289, p. 116-128.

May, S.R., Gray, G.G., Summa, L.L., Stewart, N.R., Gehrels, G.E., and Pecha, M.E.,2013, Detrital zircon geochronology from the Bighorn Basin, Wyoming, USA: Implications for tectonostratigraphic evolution and paleogeography: Geological Society of America Bulletin, v. 125, p. 1403-1422.

Matthews, W., Guest, B. and Madronich, L., 2017, Latest Neoproterozoic to Cambrian detrital zircon facies of western Laurentia: Geosphere, v. 14, p. 243-264.

McBride, J.H., Kolata, D.R. and Hildenbrand, T.G., 2003, Geophysical constraints on understanding the origin of the Illinois basin and its underlying crust: Tectonophysics, p. 45-78.

McBride, J.H., Leetaru, H.E., Keach, R.W. and McBride, E.I., 2016, Fine-scale structure of the Precambrian beneath the Illinois Basin: Geosphere, v. 12, p. 585-606.

Medaris, L.G., Jr.; Singer, B. S.; Jicha, B. R.; Malone, D. H.; Schwartz, J. J.; Stewart, E. K.; Van Lankvelt, A.; Williams, M. L.; and Reiners, P. 2019. The geon 14 WolfRiver tectonomagmatic event: a midcontinental link between the Picuris and Pinwarian orogenies. Geol. Soc. Am. Abstr. Program 51(5). https://doi.org/10.1130 /abs/2019AM-332516.

Michelson, P.C. and Dott Jr, R.H., 1973, Orientation analysis of trough cross stratification in upper Cambrian sandstones of western Wisconsin: Journal of Sedimentary Research, v. 43, p. 784-794

Moecher, D.P. and Samson, S.D., 2006, Differential zircon fertility of source terranes and natural bias in the detrital zircon record: Implications for sedimentary provenance analysis: Earth and Planetary Science Letters, v. 247, p. 252-266.

Nelson, C.A. 1956. Upper Croixan stratigraphy, upper Mississippi valley: Geological Society of America Bulletin. v. 67, v. 165–183.

Ojakangas, R.W., 1963. Petrology and sedimentation of the upper Cambrian Lamotte Sandstone in Missouri. Journal of Sedimentary Research, v. 33, p. 860-873.

Petersson, A., Scherstén, A., Andersson, J., Whitehouse, M.J. and Baranoski, M.T., 2015, Zircon U-Pb, Hf and O isotope constraints on growth versus reworking of continental crust in the subsurface Grenville orogen, Ohio, USA: Precambrian Research, v. 265, p. 313-327.

Sides, J. R., Bickford, M. E., Shuster, R. D., & Nusbaum, R. L., 1981, Calderas in the Precambrian terrane of the St. Francois Mountains, southeastern Missouri: Journal of Geophysical Research, v. 86, p. 10349–10364.

Sloss, L.L., 1963, Sequences in the Cratonic Interior of North America: Geological Society of America Bulletin, v. 74, p. 93-114.

Stein, C.A., Stein, S., Elling, R., Keller, G.R. and Kley, J., 2018. Is the “Grenville Front” in the central United States really the Midcontinent Rift?: GSA Today, v. 28, p. 4-10.

Stewart, J.H., Gehrels, G.E., Barth, A.P., Link, P.K., Christie-Blick, N. and Wrucke, C.T., 2001, Detrital zircon provenance of Mesoproterozoic to Cambrian arenites in the western United States and northwestern Mexico. Geological Society of America Bulletin, v. 113, p. 1343-1356.

Thomas, J.J., Shuster, R.D., Bickford, M.E., 1984, A terrane of 1,350- to 1,400-my-old silicic volcanic and plutonic rocks in the buried Proterozoic of the mid-continent and in the Wet Mountains, Colorado: Geological Society of America Bulletin, v. 95, p. 1150–1157.

Thomas, W.A., 1991, The Appalachian-Ouachita rifted margin of southeastern North America. Geological Society of America Bulletin, v. 103, p. 415-431.

Thomas, W.A., Astini, R.A., Mueller, P.A., Gehrels, G.E. and Wooden, J.L., 2004, Transfer of the Argentine Precordillera terrane from Laurentia: Constraints from detrital-zircon geochronology: Geology, v. 32, p. 965-968.

Thomas, W.A., Tucker, R.D., Astini, R.A., and Denison, R.E., 2012, Ages of pre-rift basement and synrift rocks along the conjugate rift and transform margins of the Argentine Precordilleraand Laurentia: Geosphere, v. 8, p. 1366–1383.

Van Schmus, W.R., Bickford, M.E., Sims, P.K., Anderson, R.R., Shearer, C.K. and Treves, S.B., 1993, Proterozoic geology of the western midcontinent basement. Precambrian: Conterminous USA Geological Society of America, Boulder, Colo., Geology of North America, 2, pp.239-258.

Van Schmus, W.R., Bickford, M.E., Turek, A., Van der Pluijm, B.A. and Catacosinos, P.A., 1996. Proterozoic geology of the east-central Midcontinent basement. SPECIAL PAPERS-GEOLOGICAL SOCIETY OF AMERICA, p. 7-32.

Walsh, G.J. and Aleinikoff, J.N., 1999, U-Pb zircon age of metafelsite from the Pinney Hollow Formation; implications for the development of the Vermont Appalachians: American Journal of Science, v. 299, p.157-170.

Whitmeyer, S.J. and Karlstrom, K.E., 2007, Tectonic model for the Proterozoic growth of North America: Geosphere, v. 3, p. 220-259.

Yonkee, W.A., Dehler, C.D., Link, P.K, Balgord, E.A., Keeley, J.A., Hayes, D.S., Wells, M.L., Fanning, C.M., and Johnson, S.M., 2014, Tectono-stratigraphic framework of Neoproterozoic to Cambrian strata, west-central U.S.: Protracted rifting, glaciation, and evolution of the North American Cordilleran margin: Earth-Science Reviews, v. 136, p. 59-95.

Chapter 3 Addendum
Precambrian Basement Geochronology

Introduction

In addition to the four wells that penetrate the Precambrian basement at the IBDP, as reported in Freiburg et al. (2019), core samples were acquired for two new wells that penetrate the basement (Figure A-1). The first well is the T.R. McMillen #2 well (TRM2), located approximately 18 mi southwest of the IBDP wells (Figure A-1). This well was drilled as part of the CarbonSAFE Macon County project, a carbon storage feasibility study. The well is located on the southwest flank of the positive magnetic anomaly identified in Freiburg et al. (2019). The second well is the FutureGen Industrial Alliance #1 (FutureGen1) well located approximately 100 miles due west of the IBDP wells and approximately 45 miles west of the T.R. McMillen #2 well (Figure A-1). It was drilled as part of the FutureGen 2.0 Project, a carbon storage demonstration project. The T.R. McMillen #2 well is located on the east side of the proposed Nd line (Van Schmus et al., 1996) and the FutureGen Industrial Alliance #1 is on the west side (Figure 1). The Precambrian rocks from both wells are described as meta-rhyolite, or altered rhyolites. One core sample from each well was selected for geochronology, and zircons were mechanically separated for U-Pb dating following the methods outlined in Freiburg et al. (2019).

Results

Zircons were separated from approximately 1 kg (TRM2) and 0.5 kg (FutureGen1) of rhyolite. The U-Pb geochronology results are provided in Tables A-1 and A-2. Twenty-three zircons from T.R. McMillen #2 rhyolite where analyzed, and twelve zircons were used in the age calculation. Rejected zircons were either more than 20% discordant, 3% reverse discordant, had high internal error, or had more than 1,000 ppm ^{204} Pb. Uranium concentrations are moderate to high and range from 63 ppm to 613 ppm. The U/Th ratio ranges from 0.8 to 3.8. Zircon ages range from 1,352.2 Ma to 1,468.5 Ma. The Concordia age is 1,372 ± 13 Ma with an MSWD (mean square weighted deviation) of 0.95 (2s; Figure 2A). The WMA (weighted mean average) of these same zircons is 1,376.0 ± 8.9 Ma with an MSWD of 0.89 (Figure 6-2B). Twenty-two zircons were analyzed from the FutureGen Industrial Alliance #1 rhyolite. Ten passed the filters indicated above. Uranium concentrations are moderate to high and range from 58 ppm to 667 ppm. The U/Th ratio ranges from 1.5 to 2.0. Zircon ages range from 1,350.7 Ma to 1,730.8 Ma. The majority of zircons range from 1,630.6 Ma to 1,673.2 Ma. The Concordia age is 1,653 ± 20 Ma with an MSWD of 0.22 (2s; Figure 6-2C). The WMA of these zircons is 1,649 ± 13 (95% confidence interval) with an MSWD of 1.17 (Figure 6-2D).

Discussion

This study provides an opportunity to compare geochronological data to a high-resolution 2D seismic profile across a major North American Precambrian terrane boundary beneath the Paleozoic in the Illinois Basin. This boundary separates the proposed Mazatzal Province from the Granite-Rhyolite Province, which have different isotopic ages and tectono-magmatic origins (Whitmeyer and Karlstrom, 2007). The significant variation in the pattern of reflectivity for the upper Precambrian crust on the profile (McBride et al., 2020) supports previous geochemical arguments for a major suture corresponding to the terrane boundary (Van Schmus et al., 1996).

Such a suture may present the convergence of a juvenile crustal block (with a model age younger than 1.55 Ga) against the older, south-east facing Laurentian continental margin (southeastern edge of the Mazatzal Province) (Whitmeyer and Karlstrom, 2007; Freiburg et al., 2020). New evidence provide here supports the emplacement or intrusion of Granite-Rhyolite Province rock onto older Mazatzal Province crust.

As discussed in Freiburg et al. (2020), seismic reflection data suggest that the IBDP wells as well as the T.R. McMillen #2 well are located on an Upper Precambrian sequence that is defined by poor reflectivity and separated by a deeper, and likely older, Precambrian sequence with strong reflectivity at the top (green line; Figure 3). The U-Pb geochronology of zircons extracted from rhyolite penetrated within this Upper Precambrian sequence, which forms a dish shape visible on 2D seismic reflection (Figure A-3), indicates that this sequence is comprised of Granite-Rhyolite Province crust. Two events of magmatism are recorded in this sequence: (1) 1.46 Ga at the IBDP VW #1. This age correlates to the Eastern Granite-Rhyolite Province (Bickford et al., 2015); (2) 1.37 Ga at the CarbonSAFE Macon County T.R. McMillen #2 well. This age correlates to the Southern Granite-Rhyolite Province (Bickford et al., 2015) and is the first record of crust of this age in Illinois as the most northern record of this province. This bimodal record of magmatism, where early events of magmatism ~1.45 Ga have been re-intruded by later events of magmatism ~1.35 Ga, has been observed in other locations. For example: (1) in Colorado, the ca. 1.37 Ga San Isabel Batholith intrudes older crust consisting of ca. 1.65 and 1.44 Ga granitoids (Bickford et al., 1989), and (2) in the St. Francois Mountains of southeast Missouri, the ca. 1.36 Ga Graniteville granite intrudes ca. 1.48 Ga rhyolites (Bickford and Mose, 1975). Below this magmatic intrusion of Granite-Rhyolite-age rock, marked by strong reflectivity in the 2D seismic (green line; Figure 3), is likely older crust that the Granite-Rhyolite intruded through. This older crust appears to be the top of the Precambrian west of the Granite-Rhyolite intrusion. On this surface, approximately 100 miles west of the IBDP site is the FutureGen Industrial Alliance #1 well. The seismic reflection signal near FutureGen appears similar to the deep seismic reflection signal beneath the dish-shaped structure filled with Granite-Rhyolite Province rocks. Isotopic ages for zircons extracted from the FutureGen Alliance #1 well yielded two general age groups (Table A-2: [1] 1,350.7 Ma to 1,455.3 Ma, and [2] 1,630.5 Ma to 1,730.8 Ma). Three points yielded Granite-Rhyolite ages in the 1,350.7 Ma to 1,455.3 Ma range. These dates may be the true age of the rhyolite, and it is possible that the older age group are all xenocrysts. This older age group comprises the bulk of the zircons dated and, thus a Concordia age was assigned to this group of 1,653 ± 20 Ma and a WMA of these zircons of 1,649 ± 13 Ma, which can be classified as Mazatzal Province in age. The complete lack of Mazatzal-age zircons in the T.R. McMillen #2 and IBDP rhyolites imply Mazatzal-age crust is shallower and closer to the Precambrian surface west of the major Granite-Rhyolite Province intrusion viewed on seismic (Figure 6-3). Based on zircon data from the FutureGen1 rhyolite, it is most likely part of the Granite-Rhyolite Province, occurring as a thin intrusion of magmatic layer over a thick Mazatzal Province-age juvenile crust.

Understanding the Precambrian geology and sediment provenance is critical for predicting sediment distribution across the Precambrian surface and reservoir development. The Lower Mt. Simon Sandstone, the storage reservoir for the IBDP, is made up of detrital sediment from five major sources: (1) Southern Granite-Rhyolite Province (ca. 1,377 Ma), (2) Eastern Granite-Rhyolite Province (ca. 1,460 Ma), (3) Mazatzal Province (ca. 1,650 Ma), (4) Grenville Province (ca. 1,129 Ma), and (5) Cambrian Rift Intrusives (ca. 533 Ma). Sources 1, 2, and 3 can be accounted for proximally. Sources 4 and 5 are predicted to be more prominent eastward towards the rift or along the Mt. Simon depocenter. On the far northern flanks of the Illinois Basin and Mt. Simon

depocenter, the Mt. Simon detritus shows a nearly complete distal source comprised of Archaean-age sediments (Lovell and Bowen, 2013). The porous Lower Mt. Simon is partly attributed to this proximal source comprised dominantly of Granite-Rhyolite Province sediments, particularly Southern Granite-Rhyolite Province sediments. It is proposed here that a zone of long-lived weakness in which magmatic rocks were emplaced onto older juvenile crust acts as a zone of reactivation (failed rifting) and caused the development of a series of normal faults or localized depocenters. Along these zones of magmatism and reactivation, arkose accumulates, and the thickest Lower Mt. Simon occurs.

References

Bickford, M.E. and Mose, D.G., 1975. Geochronology of Precambrian rocks in the St. Francois Mountains, southeastern Missouri (Vol. 165). Geological Society of America.

Bickford, M.E., Cullers, R.L., Shuster, R.D., Premo, W.R. and Van Schmus, W.R., 1989. U-Pb geochronology of Proterozoic and Cambrian plutons in the Wet Mountains and southem Front Range, Colorado. Grarnbling, JA, and Tewksbury, BJ, Proterozoic geology of the southem Rocky Mountains: Boulder, Colorado. Geological Society of America Special Paper, 235.

Bickford, M.E., Van Schmus, W.R., Karlstrom, K.E., Mueller, P.A. and Kamenov, G.D., 2015. Mesoproterozoic-trans-Laurentian magmatism: A synthesis of continent-wide age distributions, new SIMS U–Pb ages, zircon saturation temperatures, and Hf and Nd isotopic compositions. Precambrian Research, 265, pp.286-312.

McBride, J.H., Leetaru, H.E., Freiburg, J.T., and Whittaker, S.G., 2020. Variations in Precambrian structure revealed by CCS seismic profiles from the Illinois Basin, Society for Economic Geophysics

Van Schmus, W.R., Bickford, M.E., Turek, A., Van der Pluijm, B.A. and Catacosinos, P.A., 1996. Proterozoic geology of the east-central Midcontinent basement. SPECIAL PAPERS-GEOLOGICAL SOCIETY OF AMERICA, pp.7-32.

Whitmeyer, S.J. and Karlstrom, K.E., 2007. Tectonic model for the Proterozoic growth of North America. Geosphere, 3(4), pp.220-259.

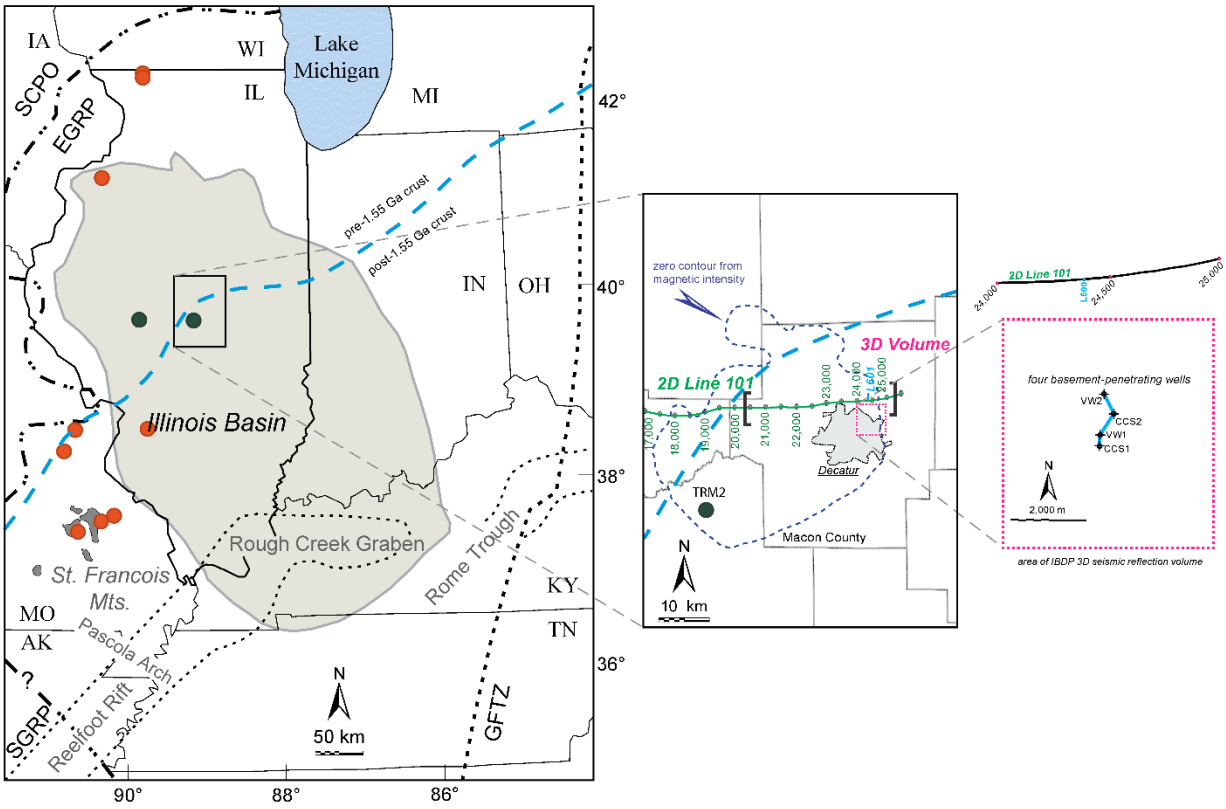

Figure A-1. (Left to right) Location map showing the outline of the extent of Pennsylvanian strata in the Illinois Basin and selected tectonic elements and boundaries. The dashed blue line is the geochemically defined boundary delineating model ages for the Precambrian basement crust (modified from Van Schmus et al., 1996). Eastern Granite-Rhyolite Province (EGRP) rocks with approximately 1.47 Ga ages in Missouri and Illinois are marked with red circles (from Bickford et al., 2015). Two wells are marked in black circles: the T.R. McMillan #2 well (east side of dashed blue line) and the FutureGen Industrial Alliance #1 well (west side). Detailed map of the L101 2D seismic reflection profile and 3D IBDP–ICCS seismic data volume, along with the zero-contour outline for a positive magnetic anomaly. The black brackets delineate limits of the high-amplitude reflection on the L101 seismic profile. Detailed map showing the locations of four drill holes within the area of the 3D seismic volume. Southern Central Plains Orogen (SCPO); Southern Granite-Rhyolite Province (SGRP); Grenville Front Tectonic Zone (GFTZ). Figure modified from Freiburg et al., 2019.

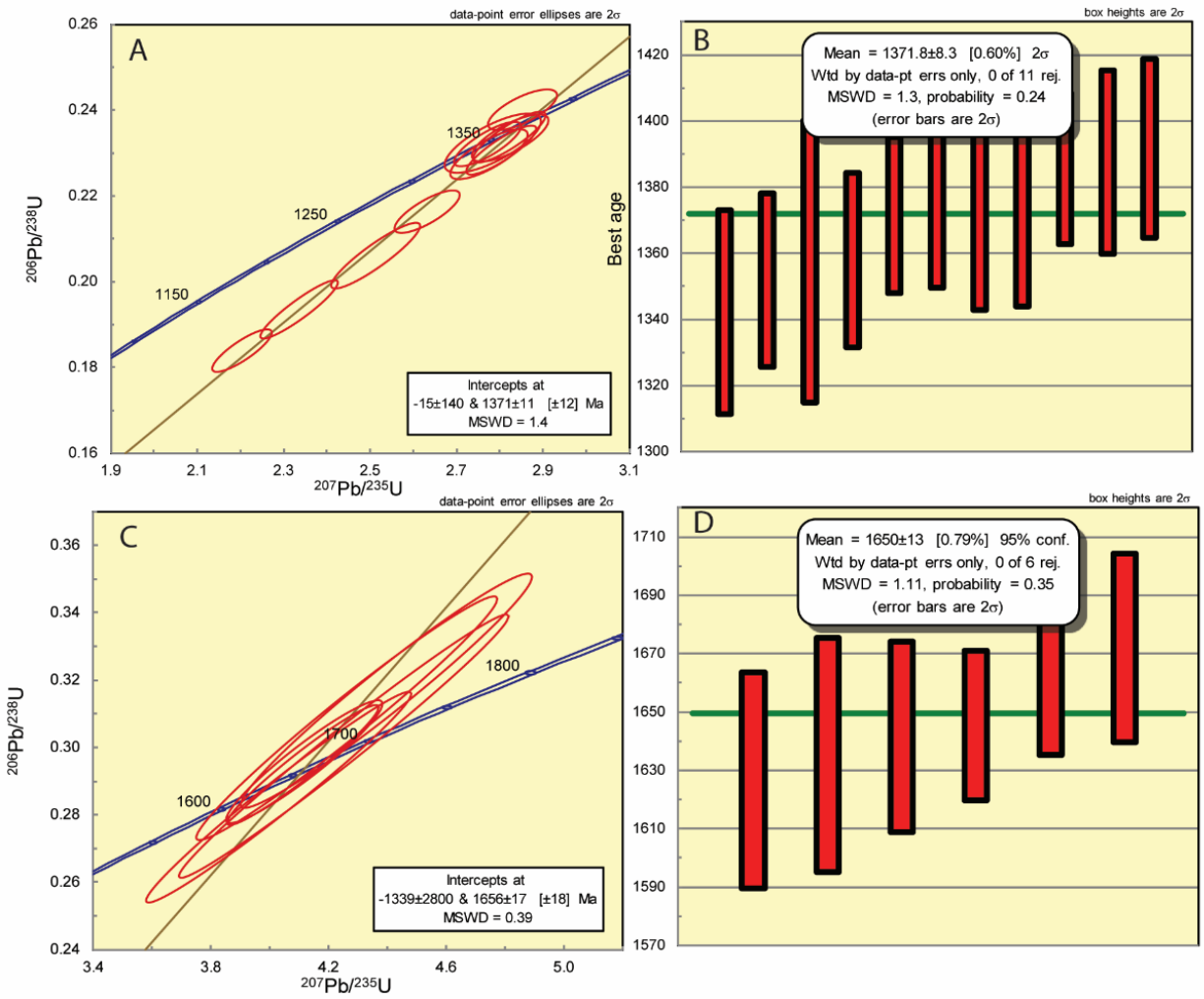

Figure A-2. Concordia (A) and weighted mean (B) determinations for the CarbonSAFE Macon Co. Project TRM2 basement rhyolite. Concordia (C) and weighted mean (B) determinations for the FutureGen1 basement rhyolite. Well locations are shown on Figure A-1.

Table A-1. U-Pb geochronological data for the basement rhyolite in the T.R. McMillen #2 well

Well analysis	Isotope ratio									
	U (ppm)	$^{206}Pb/^{204}Pb$	U/Th	$^{206}Pb/^{207}Pb$*	± (%)	$^{207}Pb/^{235}U$ *	± (%)	$^{206}Pb/^{238}U$	± (%)	Error correction
TRM2_1_25	112	37727	2.6	11.5387	0.7	2.8024	1.1	0.2346	0.9	0.79
TRM2_1_9	107	33890	1.8	11.5052	1.1	2.7348	1.6	0.2283	1.2	0.73
TRM2_1_17	396	30326	0.8	11.4215	0.6	2.3738	1.5	0.1967	1.4	0.91
TRM2_ 1_3	87	23550	3.2	11.4099	0.6	2.7782	1.2	0.2300	1.0	0.86
TRM2_1_10	69	21054	2.1	11.4033	0.8	2.7777	1.3	0.2298	1.0	0.77
TRM2_1_16	63	18955	2.8	11.3930	0.8	2.8009	1.3	0.2315	0.9	0.74
TRM2_1_11	97	40262	1.9	11.3387	0.6	2.7398	1.2	0.2254	1.0	0.86
TRM2_1_5	379	303209	1.0	11.3265	0.7	2.6687	1.1	0.2193	0.9	0.78
TRM2_1_23	613	20034	1.0	11.3027	0.7	2.5861	1.6	0.2121	1.4	0.90
TRM2_1_6	232	28986	2.8	10.9971	0.6	3.1612	1.2	0.2522	1.0	0.87
TRM2_1_19	261	300158	3.8	10.8585	0.7	3.0869	1.3	0.2432	1.1	0.82

	Apparent ages (Ma)								
	$^{206}Pb/^{238}U$	± (Ma)	$^{207}Pb/^{235}U$	± (Ma)	$^{206}Pb/^{207}Pb$	± (Ma)	Best age (Ma)	± (Ma)	Concordance (%)
TRM2_1_25	1358.7	10.8	1356.2	8.3	1352.2	13.1	1352.2	13.1	100.5
TRM2_1_9	1325.6	14.4	1338.0	12.1	1357.8	21.4	1357.8	21.4	97.6
TRM2_1_17	1157.7	14.7	1234.7	10.8	1371.9	11.8	1371.9	11.8	84.4
TRM2_ 1_3	1334.5	12.4	1349.7	9.0	1373.8	11.9	1373.8	11.9	97.1
TRM2_1_10	1333.6	12.1	1349.6	9.7	1374.9	15.9	1374.9	15.9	97.0
TRM2_1_16	1342.6	11.4	1355.8	9.4	1376.7	16.2	1376.7	16.2	97.5
TRM2_1_11	1310.4	12.0	1339.3	8.7	1385.9	11.4	1385.9	11.4	94.6
TRM2_1_5	1278.3	10.3	1319.8	8.4	1387.9	13.8	1387.9	13.8	92.1
TRM2_1_23	1239.9	16.2	1296.7	11.7	1392.0	13.5	1392.0	13.5	89.1
TRM2_1_6	1450.0	13.3	1447.7	9.0	1444.3	11.0	1444.3	11.0	100.4
TRM2_1_19	1403.4	13.4	1429.4	9.9	1468.5	14.0	1468.5	14.0	95.6

Table A-2. Geochronological data for the basement rhyolite in the FutureGen Industrial Alliance #1 well

Well analysis	Isotope ratio									
	U (ppm)	$^{206}Pb/^{204}Pb$	U/Th	$^{206}Pb/^{207}Pb$*	± (%)	$^{207}Pb/^{235}U$ *	± (%)	$^{206}Pb/^{238}U$	± (%)	Error correction
FutureGen1_1	114	12382	2.2	11.5474	1.1	2.8181	2.9	0.2361	2.7	0.93
FutureGen1_9	333	58206	1.4	11.2250	0.8	2.8207	3.5	0.2297	3.5	0.98
FutureGen1_11	132	12618	2.0	10.9342	1.0	2.9270	3.1	0.2322	2.9	0.94
FutureGen1_20	69	21913	2.1	9.9612	1.0	4.1487	4.8	0.2999	4.7	0.98
FutureGen1_16	62	39870	1.6	9.9270	1.1	4.2675	4.5	0.3074	4.4	0.97
FutureGen1_3	162	46109	1.6	9.9110	0.9	4.0911	2.6	0.2942	2.5	0.94
FutureGen1_2	134	135054	2.0	9.9004	0.7	4.0717	2.5	0.2925	2.4	0.96
FutureGen1_18	667	41669	1.1	9.7525	0.9	4.0453	4.5	0.2863	4.4	0.98
FutureGen1_15	82	49802	1.8	9.7345	0.9	4.1529	5.2	0.2933	5.1	0.99
FutureGen1_22	58	8033	2.0	9.4346	1.3	4.1883	5.6	0.2867	5.4	0.97

	Apparent ages (Ma)								
	$^{206}Pb/^{238}U$	± (Ma)	$^{207}Pb/^{235}U$	± (Ma)	$^{206}Pb/^{207}Pb$	± (Ma)	Best age (Ma)	± (Ma)	Concordance (%)
FutureGen1_1	1366.5	33.5	1360.4	21.9	1350.7	20.9	1350.7	20.9	101.2
FutureGen1_9	1333.1	41.6	1361.1	26.5	1405.2	14.8	1405.2	14.8	94.9
FutureGen1_11	1346.1	34.9	1388.9	23.1	1455.3	19.6	1455.3	19.6	92.5
FutureGen1_20	1690.6	69.9	1663.9	39.3	1630.5	18.2	1630.5	18.2	103.7
FutureGen1_16	1727.8	66.2	1687.1	37.0	1636.9	20.0	1636.9	20.0	104.6
FutureGen1_3	1662.5	36.3	1652.5	21.4	1639.9	16.3	1639.9	16.3	101.4
FutureGen1_2	1654.0	35.6	1648.6	20.7	1641.9	12.8	1641.9	12.8	100.7
FutureGen1_18	1622.8	63.1	1643.4	36.5	1669.7	16.3	1669.7	16.3	97.2
FutureGen1_15	1658.1	75.3	1664.8	42.8	1673.2	16.2	1673.2	16.2	99.1
FutureGen1_22	1625.1	77.5	1671.7	45.6	1730.8	24.4	1730.8	24.4	93.9

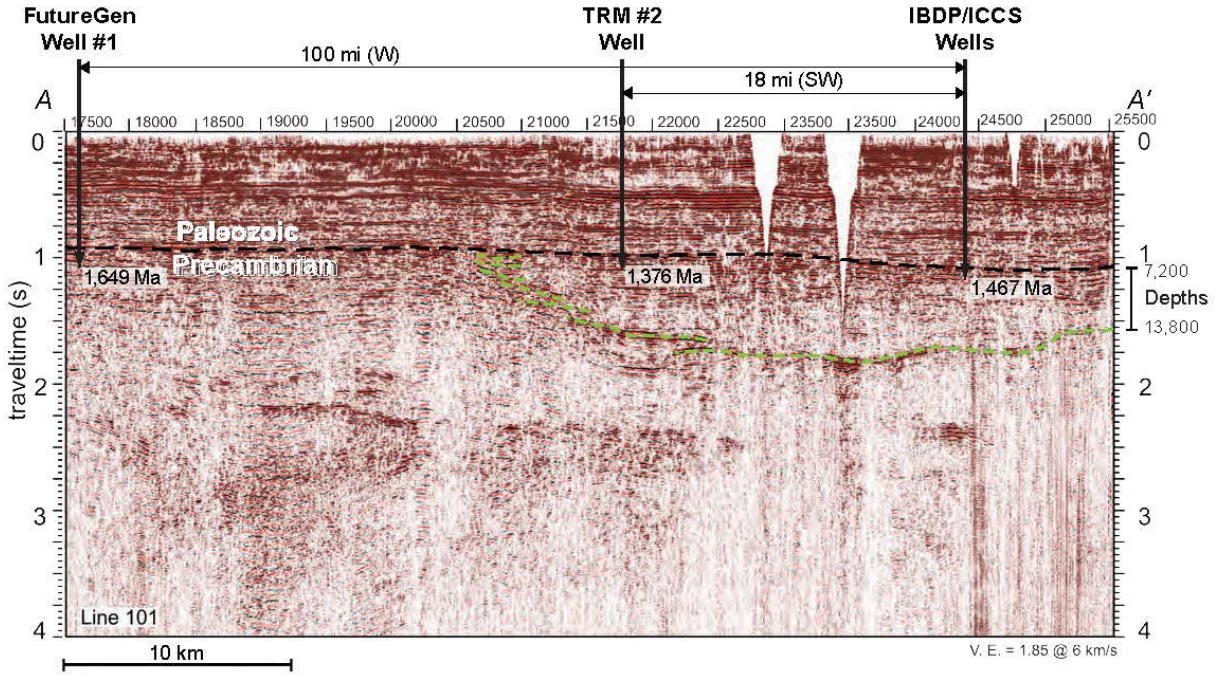

Figure 3. Section of the L101 2D seismic profile A-A (Figure A-1) through Macon County, Illinois. The approximate locations of the TRM2 and FutureGen1 in respect to the IBDP/ICCS wells are not to scale on the seismic profile, but rather show the distance and direction from the IBDP/ICCS wells. The age dates of the Precambrian rocks penetrated in each well are annotated just below the Precambrian surface (dashed line).

Chapter 4
Petrophysics

By: James Damico
Illinois State Geological Survey

Seal

The primary seal, the Eau Claire, is broken into two sections: the Eau Claire and the Eau Claire Shale. The Eau Claire Shale is considered a "true" shale, while the upper part of the Eau Claire fluctuates in lithology. Figure 1 has a graphical display of logs of the Eau Claire. The Eau Claire is in total 523 ft thick, while the Eau Claire Shale is 85 ft thick. The elemental capture spectroscopy (ECS) and photo electric (PE) log indicate the Eau Claire transitions from a carbonate-dominated lithology near the top to a mixture of QFM (quartz, feldspar, and mica) and clay with clay increasing towards the base. The gamma ray and PE indicate the base is mostly composed of shale. A total of nine rotary sidewall core samples were taken from the Eau Claire with four of those taken from the Eau Claire Shale (see Tables 1 and 2 below). The average porosity of 9.8% for the Eau Claire and 12.5% for the Eau Claire Shale and the median permeability of the Eau Claire of 2.08 mD fall within expected values. The median permeability of the Eau Claire Shale of 11.2 mD is higher than expected; it is probably a product of sampling bias/low sample numbers.

Table 1. Rotary sidewall core porosity statistics for the seal

Unit	n	Avg	St. Dev	Median	Max	Min
Eau Claire shale	4	0.125	0.0413	0.135	0.171	0.0615
Eau Claire	**9**	**0.0980**	**0.0571**	**0.106**	**0.177**	**0.0204**

Table 2. Rotary sidewall core permeability statistics for the seal

	Permeability (mD)						Log_{10} (Permeability)				
Unit	**n**	**Avg**	**St. Dev**	**Median**	**Max**	**Min**	**Avg**	**St. Dev**	**Median**	**Max**	**Min**
Eau Claire shale	4	26.3	32.9	11.2	82.5	0.390	0.886	0.841	1.02	1.92	-0.409
Eau Claire	**9**	**12.5**	**25.2**	**2.08**	**82.5**	**0.00516**	**0.184**	**1.1**	**0.318**	**1.92**	**-2.29**

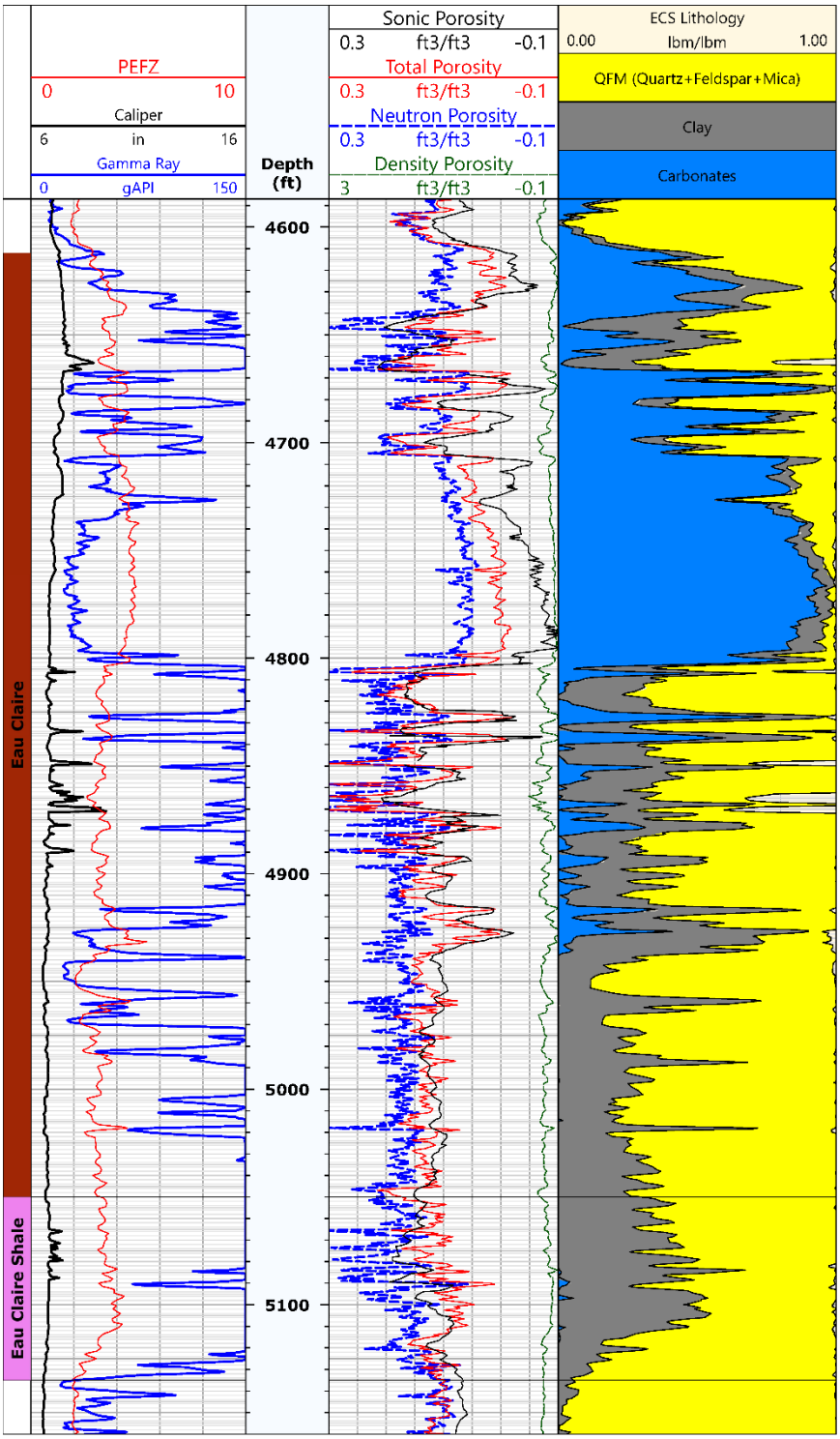

Figure 1. Porosity and lithology geophysical logs of the Eau Claire

Reservoir

The Mt. Simon is broken into three major subunits (Upper, Middle, and Lower) and five smaller subunits (E, D, C, B, and A), based on the petrography work in Jared et al. (2014). In total, the Mt. Simon is 1,164 ft thick. The thickness of the Upper is 135 ft, the Middle is 575 ft, and the Lower is 454 ft. The thickness of the E is 135 ft, the D is 271 ft, the C is 304 ft, the B is 284 ft, and the A is 170 ft.

Porosity

Core

A total of 64 rotary sidewall core samples were taken and subjected to routine testing. See Table 3 for a summary. The highest average porosity amongst the major division of the Mt. Simon (Upper, Middle, and Lower) is the Lower Mt. Simon at 21.0%, followed by the Middle Mt. Simon at 14.8% and the Upper Mt. Simon at 13.7%. The overall average of the Mt. Simon is 18.6%, while the Argenta is 14.5%.

Table 3. Rotary sidewall core porosity statistics for the reservoir

Unit	n	Avg	St. Dev	Median	Max	Min
UPPER-E	**7**	**0.137**	**0.0278**	**0.149**	**0.163**	**0.0745**
Middle-D	7	0.145	0.0308	0.141	0.206	0.0978
Middle-C	6	0.151	0.0197	0.155	0.168	0.1088
MIDDLE	**13**	**0.148**	**0.0265**	**0.152**	**0.206**	**0.0978**
Lower-B	25	0.218	0.0594	0.224	0.333	0.1090
Lower-A	10	0.188	0.0616	0.196	0.279	0.0374
LOWER	**35**	**0.210**	**0.0616**	**0.210**	**0.333**	**0.0374**
MTSIMON	**55**	**0.186**	**0.0607**	**0.168**	**0.333**	**0.0374**
ARGENTA	**9**	**0.145**	**0.0287**	**0.147**	**0.205**	**0.101**

In addition to sidewall core, 60 feet of whole core was taken from depths of 6,246 to 6,306 ft, with most of the samples taken predominantly from the Lower Mt. Simon Unit A and a small portion from the Argenta. The core was sampled at regular intervals, resulting in 24 total measurements, which were subjected to routine testing. See Table 4 for a summary. The Lower Mt. Simon Unit A average porosity is 22.5%, while the Argenta is 16.7%.

Table 4. Whole core porosity statistics

Unit	n	Avg	St. Dev	Median	Max	Min
LOWER MT. SIMON A	21	0.225	0.0218	0.227	0.254	0.160
ARGENTA	3	0.167	0.0295	0.145	0.202	0.138

Geophysical Logs

After comparing the different versions of the neutron porosity, the enhanced thermal neutron porosity (curve mnemonic: NPOR) from the platform express tool was selected and used with the standard resolution density porosity (curve mnemonic: DPHZ) to create the cross-plot porosity (PHIT), which is representative of the formation's total porosity. The porosity logs are displayed graphically in Figure 2, with core measurements overlain, and Table 5 contains a summary. The highest average porosity amongst the major division of the Mt. Simon (Upper, Middle, and Lower) is the Lower Mt. Simon at 19.8%, followed by the Middle Mt. Simon at 13.8% and the Upper Mt. Simon at 12.8%. The overall average of the Mt. Simon is 15.4%, while the average of the Argenta is 13.3%. Overall, comparing the cross-plot porosity to the rotary sidewall core samples, the log values are lower than the sidewall core samples, but the agreement between the log values and rotary sidewall core sample measurements is acceptable, given sampling bias that exists in coring. The average of the whole core samples for the Mt. Simon Unit A and the Argenta are higher than both the log and the sidewall core samples.

Table 5. Geophysical log porosity statistics

	Density Porosity				**Neutron Porosity**				**Cross-Plot Porosity**			
Unit	**Avg**	**St Dev**	**Max**	**Min**	**Avg**	**St Dev**	**Max**	**Min**	**Avg**	**St Dev**	**Max**	**Min**
UPPER-E	**0.126**	**0.0232**	**0.169**	**0.0516**	**0.130**	**0.0306**	**0.287**	**0.0714**	**0.128**	**0.0207**	**0.195**	**0.0770**
Middle-D	0.138	0.0251	0.210	0.0818	0.139	0.0291	0.229	0.0808	0.139	0.0263	0.216	0.0813
Middle-C	0.130	0.0217	0.197	0.0649	0.146	0.0259	0.278	0.0910	0.138	0.0207	0.212	0.0824
MIDDLE	**0.132**	**0.0231**	**0.210**	**0.0649**	**0.144**	**0.0271**	**0.278**	**0.0808**	**0.138**	**0.0227**	**0.216**	**0.0813**
Lower-B	0.188	0.0276	0.262	0.0971	0.199	0.0292	0.273	0.1173	0.194	0.0273	0.267	0.1116
Lower-A	0.192	0.0392	0.268	0.0595	0.211	0.0413	0.338	0.1238	0.202	0.0387	0.294	0.1096
LOWER	**0.190**	**0.0339**	**0.268**	**0.0595**	**0.205**	**0.0362**	**0.338**	**0.1173**	**0.198**	**0.0337**	**0.294**	**0.1096**
MTSIMON	**0.149**	**0.0380**	**0.268**	**0.0516**	**0.160**	**0.0422**	**0.338**	**0.0714**	**0.154**	**0.0384**	**0.294**	**0.0770**
ARGENTA	**0.095**	**0.0540**	**0.200**	**-0.0403**	**0.172**	**0.0341**	**0.295**	**0.1023**	**0.133**	**0.0331**	**0.209**	**0.0702**

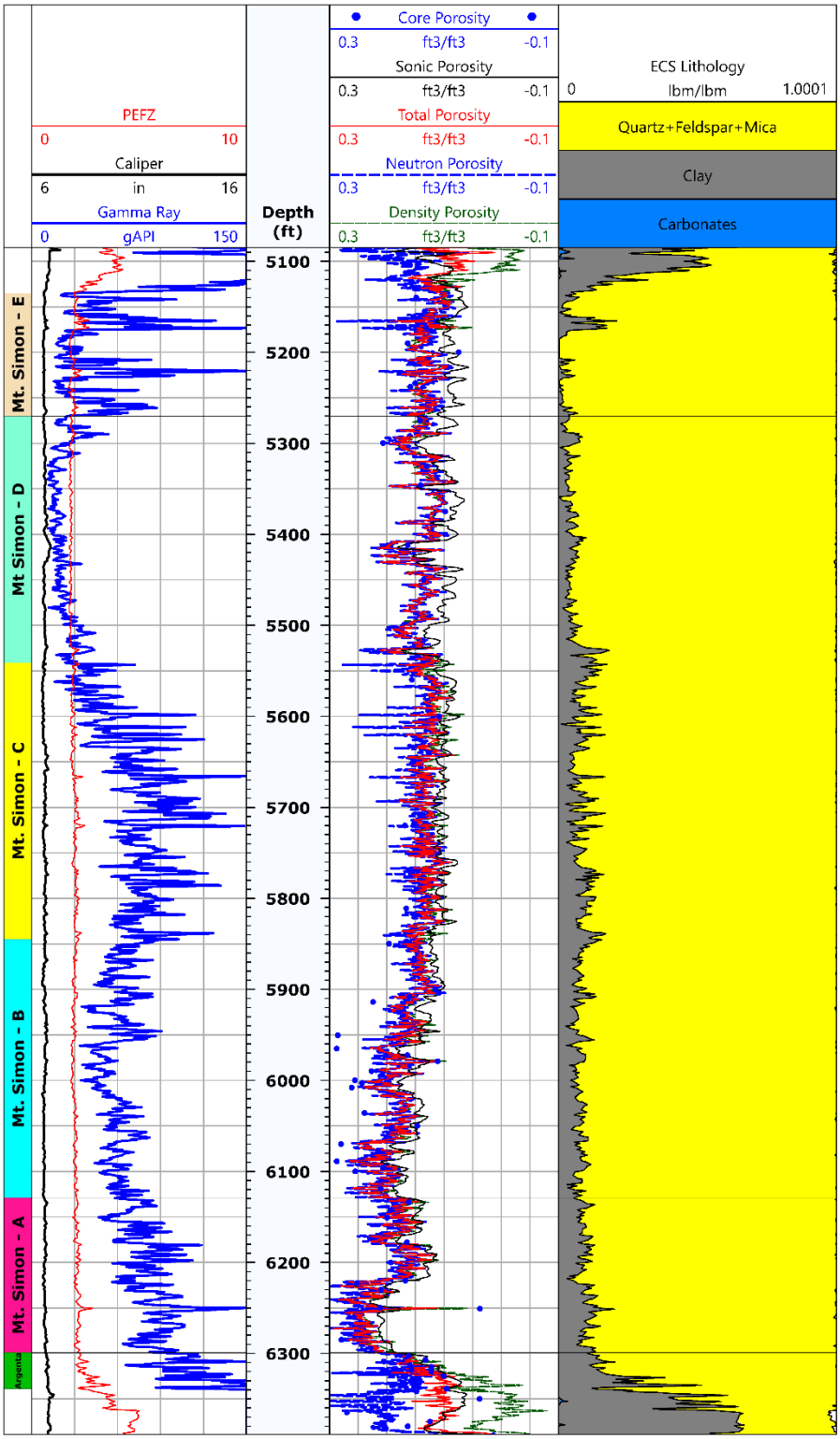

Figure 2. Porosity and lithology geophysical logs with core measurements superimposed of the Mt. Simon and Argenta

Permeability

Core

Permeability was measured on the 64 samples from the sidewall rotary core using standard lab methods, the summary of which is presented in Table 6. Amongst the major divisions of the Mt. Simon, average permeability was highest in the Upper Mt. Simon (Unit E) at 349 mD, compared to 92.7 mD and 90.8 mD for the Middle and Lower Mt. Simon, respectively. However, these relationships are a product of sampling bias. The portion of the Lower Mt. Simon with the best reservoir quality, and also the highest reservoir properties at IBDP, was sparsely sampled during the rotary sidewall coring since that portion was sampled during the whole core sampling. The Middle Mt. Simon, which was represented by a total of 13 samples, is overly affected by a single sample that had a value of 750 mD. Although there is no indication of error in the sample, removing the sample reduces the average from 92.7 to 38.0 mD, which is more in line with expectations. The discrepancy between the average permeability of the Middle Mt. Simon and the median, 3.03 mD, likewise demonstrates that the average is biased by the sample. The Upper Mt. Simon does contain one sample that is marked as chipped, but removing that sample does not significantly change the overall average (reduction to 298 mD). There are three samples out of seven taken from the Upper Mt. Simon that have permeabilities over 500 mD, leading to the conclusion that there do exist portions of high-quality reservoir in the Upper Mt. Simon. However, the average is strongly affected by low sampling numbers as seven samples are being used to represent 135 ft. The Upper Mt. Simon is characterized as being highly heterogenous, owing to thin, interbedded layers of sandstone and shale. Still, the data suggest that portions of the Upper Mt. Simon, although probably compartmentalized and not well connected due to the reservoir architecture, have high reservoir qualities.

Table 6. Rotary sidewall core permeability statistics

	Permeability (mD)						**Log_{10} (Permeability)**					
Unit	**n**	**Avg**	**St. Dev**	**Median**	**Max**	**Min**	**n**	**Avg**	**St. Dev**	**Median**	**Max**	**Min**
UPPER-E	**7**	**348**	**334**	**173**	**955**	**5.00**	**7**	**2.09**	**0.832**	**2.24**	**2.98**	**0.699**
Middle-D	7	161	252	9.52	750	1.10	7	1.31	1.05	0.978	2.87	0.0410
Middle-C	6	13.3	17.2	2.33	45.5	0.604	6	0.628	0.684	0.357	1.66	-0.219
MIDDLE	**13**	**92.7**	**200**	**3.03**	**750**	**0.604**	**13**	**0.996**	**0.960**	**0.481**	**2.87**	**-0.219**
Lower-B	25	39.7	73.0	4.38	230	0.0530	25	0.723	0.961	0.642	2.36	-1.28
Lower-A	9	233	362	17.3	1121	0.256	9	1.34	1.19	1.24	3.05	-0.592

LOWER	**34**	**90.8**	**214**	**5.83**	**1121**	**0.0530**	**34**	**0.886**	**1.06**	**0.753**	**3.05**	**-1.28**
MTSIMON	**54**	**125**	**246**	**9.25**	**1121**	**0.0530**	**54**	**1.07**	**1.09**	**0.966**	**3.05**	**-1.28**
ARGENTA	**9**	**2.81**	**5.86**	**0.535**	**19.3**	**0.0630**	**9**	**-0.173**	**0.683**	**-0.271**	**1.28**	**-1.20**

Permeability was also measured from the whole core samples, a summary of which is in Table 7. The whole core presents a more complete picture of the petrophysical properties of the Lower Mt. Simon versus the rotary sidewall core. The whole core average of the Lower Mt. Simon Unit A is 2,050 mD and has some of the highest permeability recorded for the Mt. Simon (Medina et al., 2008), the highest at 5,530 mD. Based on these results, the reservoir quality at the well in the Lower Mt. Simon is excellent and some of the highest in the basin. A cursory search of permeability measurements from core analysis data of the Mt. Simon from Illinois, Indiana, Kentucky, Ohio, and Michigan reveals that these core specimens are in the upper 0.4%. Only two other samples have higher values.

Table 7. Whole core permeability statistics

	Horizontal Permeability (mD)						**Log_{10}(Horizontal Permeability)**					
Unit	**n**	**Avg**	**St. Dev**	**Median**	**Max**	**Min**	**n**	**Avg**	**St. Dev**	**Median**	**Max**	**Min**
LOWER MT. SIMON A	21	2050	1660	1570	5530	4.68	21	3.01	0.716	3.19	3.74	0.670
ARGENTA	3	124	156	9.40	365	5.42	3	1.51	0.780	0.973	2.56	0.734
	Vertical Permeability (mD)						**Log_{10}(Vertical Permeability)**					
Unit	**n**	**Avg**	**St. Dev**	**Median**	**Max**	**Min**	**n**	**Avg**	**St. Dev**	**Median**	**Max**	**Min**
LOWER MT. SIMON A	21	726	932	396	3490	1.25	21	2.37	0.871	2.60	3.54	0.0969
ARGENTA	3	21.7	31.4	0.714	71.3	0.361	3	0.485	0.957	-0.146	1.85	-0.442

Geophysical Log Estimates

Permeability was estimated from the geophysical logs through different methods. Permeability was estimated from the Combinable Magnetic Resonance (CMR) log, a nuclear magnetic resonance-type log, which estimates permeability by analyzing the rate of decay of polarized hydrogen nuclei. This type of tool has become standard in the industry for estimating permeability. Permeability was also estimated from porosity using the standard equations, Wylie-Rose (Wylie and Rose, 1950) and Timur (Timur, 1968). A final method employed was developed

at the ISGS to estimate permeability from porosity using different regression models selected via the cementation exponent from Archies Equation (Archie, 1942). Figure 3 has a graphical display of the permeability estimates from logs with the core measurements overlain, and Table 8 is a summary of the results.

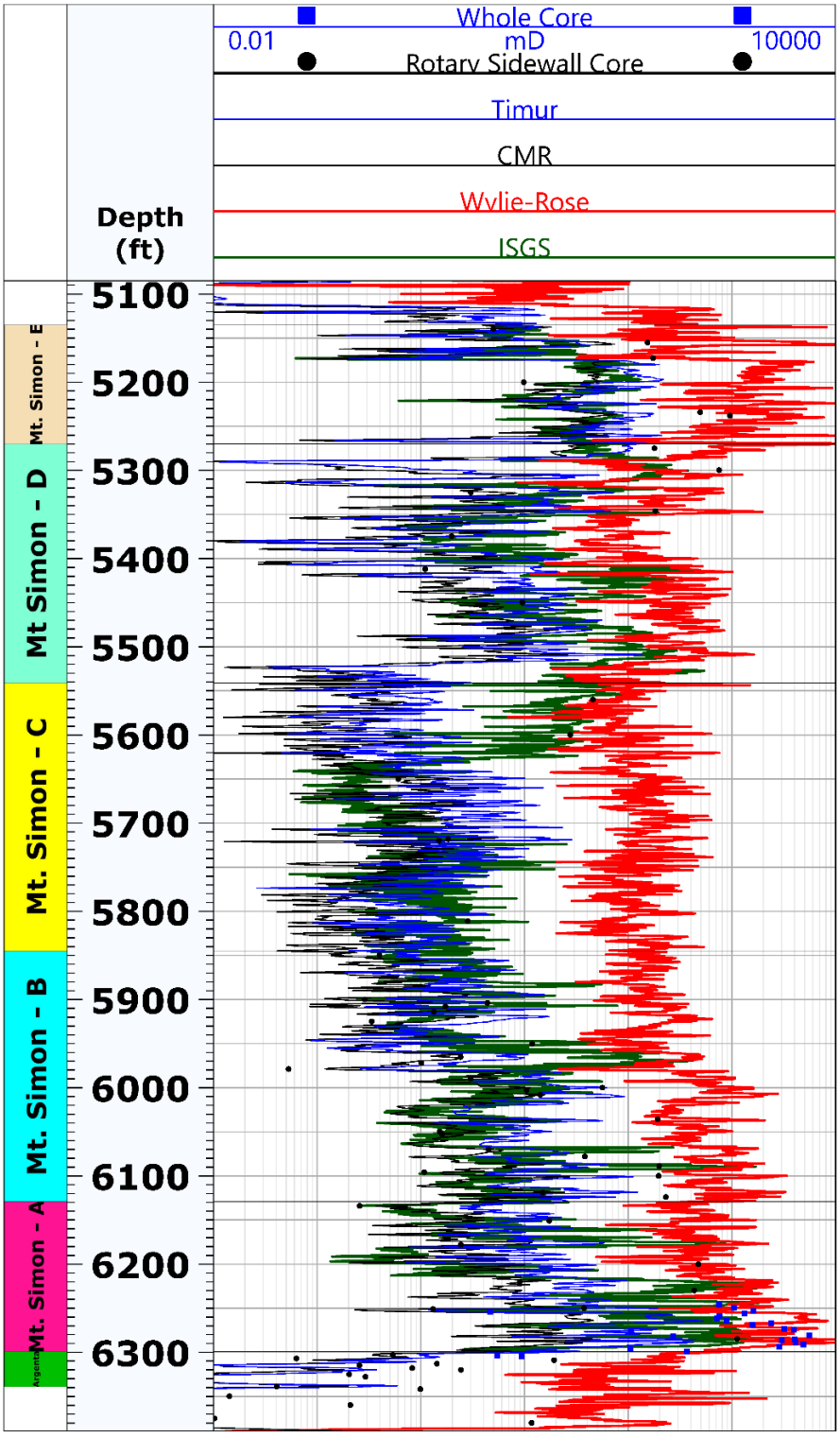

Figure 3. Permeability estimates from geophysical logs with core measurements superimposed for the Mt. Simon and Argenta

Table 8. Permeability estimates from geophysical log statistics

	CMR (mD)					Log_{10}(CMR)				
Unit	**Avg**	**St Dev**	**Median**	**Max**	**Min**	**Avg**	**St Dev**	**Median**	**Max**	**Min**
UPPER-E	**25.3**	**21.0**	**20.4**	**80.7**	**0.0674**	**1.08**	**0.715**	**1.31**	**1.91**	**-1.17**
Middle-D	4.13	6.82	1.83	51.2	0.0073	0.0835	0.811	0.264	1.71	-2.14
Middle-C	0.534	0.697	0.291	5.49	0.0100	-0.546	0.503	-0.536	0.739	-2.00
MIDDLE	**2.23**	**5.04**	**0.516**	**51.2**	**0.00730**	**-0.249**	**0.736**	**-0.288**	**1.71**	**-2.14**
Lower-B	2.59	3.74	1.38	27.1	0.0409	0.0835	0.558	0.139	1.43	-1.39
Lower-A	7.81	9.76	3.74	52.9	0.208	0.598	0.528	0.573	1.72	-0.683
LOWER	**4.55**	**7.12**	**1.97**	**52.9**	**0.0409**	**0.276**	**0.601**	**0.294**	**1.72**	**-1.39**
MTSIMON	**5.80**	**11.6**	**1.34**	**80.7**	**0.00730**	**0.110**	**0.807**	**0.127**	**1.91**	**-2.14**
ARGENTA	**0.456**	**1.44**	**0.0515**	**7.44**	**0.000100**	**-1.61**	**1.33**	**-1.29**	**0.871**	**-4.00**
	Timur (mD)					**Log_{10}(Timur)**				
Unit	**Avg**	**St Dev**	**Median**	**Max**	**Min**	**Avg**	**St Dev**	**Median**	**Max**	**Min**
UPPER-E	**59.3**	**56.0**	**37.9**	**225**	**0.146**	**1.44**	**0.689**	**1.58**	**2.35**	**-0.835**
Middle-D	15.0	23.4	7.18	150	0.0114	0.637	0.851	0.856	2.18	-1.94
Middle-C	2.07	3.12	1.08	28.5	0.0262	0.0147	0.518	0.0327	1.46	-1.58
MIDDLE	**8.18**	**17.5**	**1.81**	**150**	**0.0114**	**0.308**	**0.762**	**0.258**	**2.18**	**-1.94**
Lower-B	11.0	17.1	5.02	123	0.0887	0.645	0.630	0.701	2.09	-1.05
Lower-A	50.3	83.4	17.4	526	0.710	1.29	0.604	1.24	2.72	-0.149
LOWER	**25.7**	**56.1**	**8.21**	**526**	**0.0887**	**0.887**	**0.695**	**0.915**	**2.72**	**-1.05**

MTSIMON	**20.9**	**44.7**	**4.92**	**526**	**0.0114**	**0.665**	**0.826**	**0.692**	**2.72**	**-1.94**
ARGENTA	**1.76**	**6.55**	**0.154**	**34.2**	**0.000500**	**-1.13**	**1.23**	**-0.811**	**1.53**	**-3.30**
	Wylie-Rose (mD)					**Log$_{10}$(Wylie-Rose)**				
Unit	**Avg**	**St Dev**	**Median**	**Max**	**Min**	**Avg**	**St Dev**	**Median**	**Max**	**Min**
UPPER-E	**1800**	**2310**	**1140**	**17000**	**17.1**	**2.94**	**0.578**	**3.06**	**4.23**	**1.23**
Middle-D	323	627	188	8750	8.56	2.24	0.477	2.27	3.94	0.932
Middle-C	143	124	107	1490	6.85	2.04	0.321	2.03	3.17	0.836
MIDDLE	**228**	**449**	**128**	**8750**	**6.85**	**2.13**	**0.415**	**2.11**	**3.94**	**0.836**
Lower-B	469	520	277	3360	21.0	2.47	0.417	2.44	3.53	1.32
Lower-A	1480	1830	813	12800	49.1	2.92	0.466	2.91	4.11	1.69
LOWER	**848**	**1290**	**415**	**12800**	**21.0**	**2.64**	**0.488**	**2.62**	**4.11**	**1.32**
MTSIMON	**652**	**1270**	**239**	**17000**	**6.85**	**2.43**	**0.554**	**2.38**	**4.23**	**0.836**
ARGENTA	**180**	**221**	**76.6**	**1100**	**6.48**	**1.98**	**0.508**	**1.88**	**3.04**	**0.812**
	ISGS (mD)					**Log$_{10}$(ISGS)**				
Unit	**Avg**	**St Dev**	**Median**	**Max**	**Min**	**Avg**	**St Dev**	**Median**	**Max**	**Min**
UPPER-E	**35.8**	**29.9**	**29.9**	**137**	**0.0623**	**1.33**	**0.550**	**1.48**	**2.14**	**-1.21**
Middle-D	51.8	71.3	21.9	463	0.230	1.27	0.714	1.34	2.67	-0.639
Middle-C	8.08	50.4	2.17	539	0.0542	0.281	0.769	0.223	2.01	-1.27
MIDDLE	**29.4**	**59.9**	**4.03**	**539**	**0.0542**	**0.717**	**0.888**	**0.605**	**2.73**	**-1.27**
Lower-B	41.6	147	5.20	1680	0.380	0.846	0.704	0.716	3.23	-0.420
Lower-A	260	451	26.4	2130	0.134	1.40	1.18	1.42	3.33	-0.872

LOWER	**150**	**351**	**8.25**	**2130**	**0.134**	**1.12**	**1.01**	**0.917**	**3.33**	**-0.872**
MTSIMON	**65.7**	**204**	**7.33**	**2130**	**0.0542**	**0.907**	**0.924**	**0.865**	**3.33**	**-1.27**
ARGENTA	**3.08**	**8.11**	**0.478**	**57.3**	**0.0141**	**-0.327**	**0.846**	**-0.320**	**1.76**	**-1.85**

Trends are observable in the permeability estimates. The CMR and Timur estimates tend to average lower, while the Wylie-Rose tends to average higher. The ISGS estimate tends to be more variable than all the other estimates and fluctuates between the CMR/Timur estimates and the Wylie-Rose estimates. Intuitively, it would make sense to compare the estimates of permeability for logs to data provided by the core samples. However, log estimates and core measurements are not equivalent. Core measurements are direct measurements made on a small, controlled volume in a controlled laboratory setting, while geophysical log data are recorded in situ as an indirect measurement over a semi-controlled volume with several sources of potential error (borehole conditions, incorrect lithology, etc). The result is that the agreement between core measurements of permeability and estimates based on log data is typically low; thus, comparing the two may not be reflective of the log estimate's ability to predict permeability. However, despite the flaw in the comparison, it is one of the only methods available for evaluating the performance of estimates from log data. Cross plots of the log estimates versus the core measurements of permeability are presented in Figures 4 and 5, while Table 9 contains the statistical evaluation of the estimates and the core measurements.

Table 9. Statistical analysis of performance of permeability estimates from geophysical logs

Rotary Sidewall Core Samples				
Estimate	CMR	ISGS	Timur	Wylie-Rose
Number of core samples	63	63	63	63
r^2	0.355	0.325	0.457	0.413
RMSE (mD)	222	185	193	1080
Average of absolute difference of residuals (mD)	101	106	96.6	779
Median of absolute difference of residuals (mD)	2.37	12.2	9.95	355
(Number) Percentage of residuals >10 mD	(24) 38.1%	(34) 54.0%	(31) 49.2%	(62) 100%
(Number) Percentage of residuals >100 mD	(15) 23.8%	(17) 27.0%	(15) 23.8%	(51) 81.0%
(Number) Percentage of residuals >500 mD	(4) 6.35%	(3) 4.76%	(4) 6.35%	(27) 42.9%

(Number) Percentage of residuals >1,000 mD	(1) 1.59%	(0) 0.00%	(0) 0.00%	(16) 25.4%
Whole Core Samples				
Estimate	CMR	ISGS	Timur	Wylie-Rose
Number of core samples	24	24	24	24
r^2	0.202	0.218	0.0958	0.0947
RMSE (mD)	1680	1340	1640	1400
Average of absolute difference of residuals (mD)	1790	1440	1730	1730
Median of absolute difference of residuals (mD)	1160	858	1090	1140
(Number) Percentage of residuals >10 mD	(21) 87.5%	(22) 91.7%	(22) 91.7%	(24) 100%
(Number) Percentage of residuals >100 mD	(20) 83.3%	(21) 87.5%	(20) 83.3%	(24) 81.0%
(Number) Percentage of residuals >500 mD	(17) 70.8%	(17) 70.8%	(17) 70.8%	(21) 42.9%
(Number) Percentage of residuals >1,000 mD	(13) 54,2%	(10) 41.7%	(13) 0.00%	(13) 25.4%

The cross plot in Figure 4 indicates that the CMR and Timur estimates tend to underestimate permeability relative to the measurements from rotary sidewall core, particularly for higher values, while Wylie-Rose overestimates permeability relative to core. The ISGS estimate has relatively even distribution scatter both above and below the measurements from sidewall core. However, all the estimates have obvious points where the estimate failed by several orders of magnitude. Figure 5 compares the performance of the estimates to the measurements from whole core samples. The ISGS, CMR, and Timur all underestimate the values relative to the measurements, while the Wylie-Rose is a closer match. The Wylie-Rose excels in the high reservoir-quality portion of the Lower Mt. Simon, but it does so at the expense of grossly overpredicting the permeability in all the other proportions of the Mt. Simon. The underprediction from the ISGS, CMR, and Timur methods is expected since the whole core shows the extreme relationship between permeability and porosity that is not captured in the datasets from which these estimates were developed. Ideally, the ISGS estimate, which was built specific to Mt. Simon data, should be adjusted to match the new data. But this was not done because there was considerable debate whether there was experiment error in the measurements, which was not resolved until much later in the project and required significant modification to the method and would likely hurt the overall performance of the method. For input into the geocellular static model, the Wylie-Rose estimate was used instead for this portion of the Mt. Simon when whole core data was absent. The ISGS estimate was used for the other portions of the Mt. Simon.

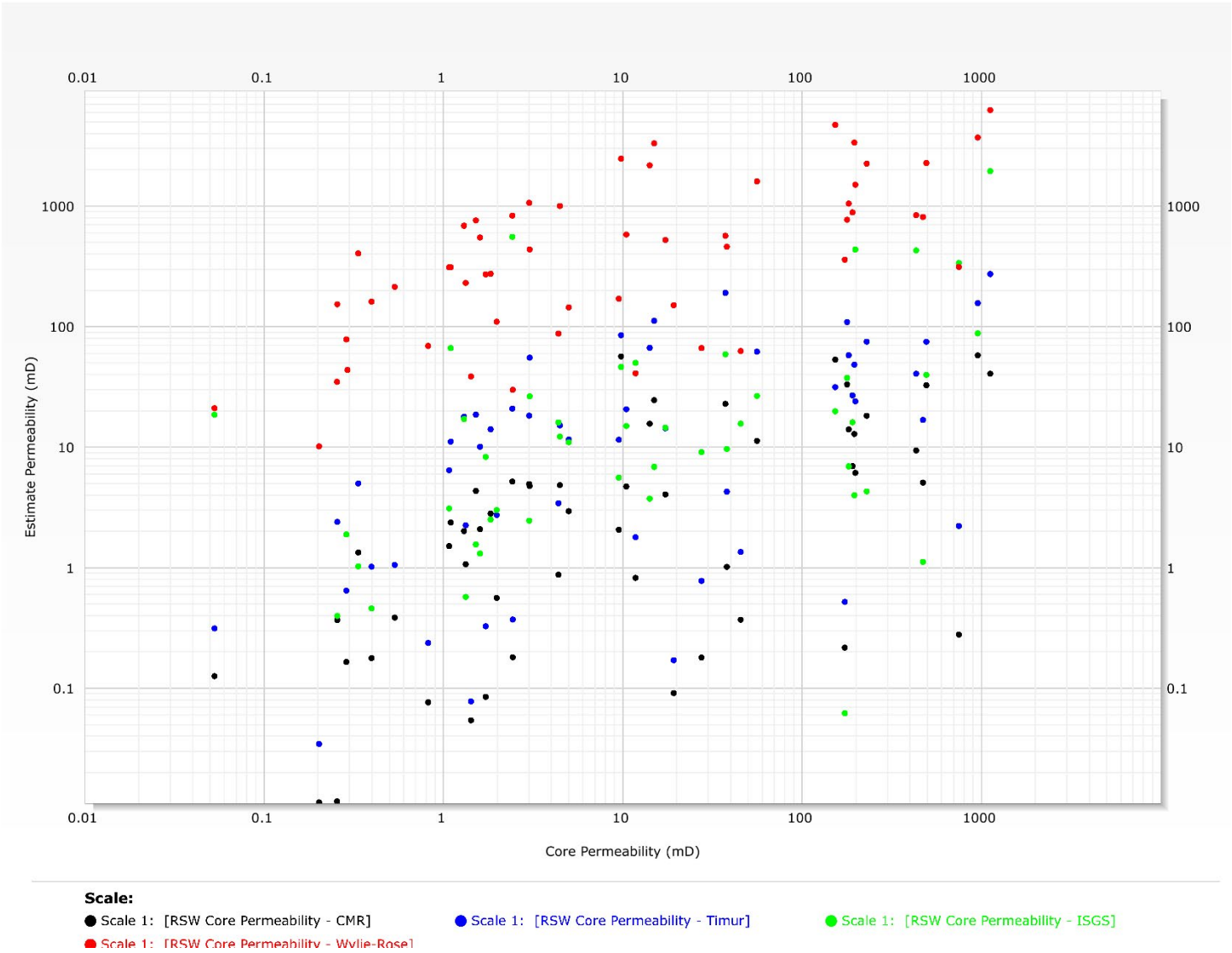

Figure 4. Cross plot of permeability measurements from rotary side wall core samples versus various estimates of permeability from geophysical logs

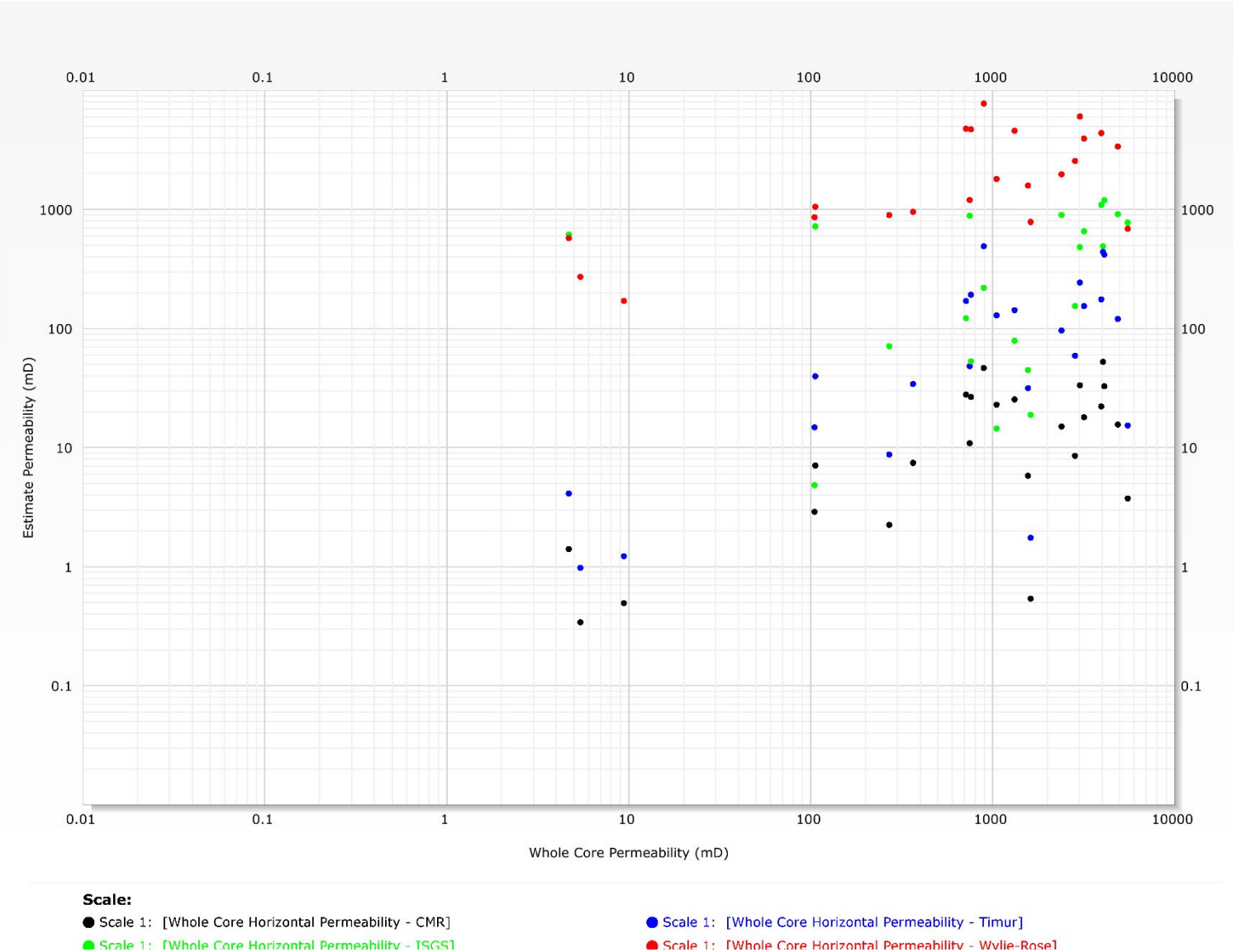

Figure 5. Cross plot of permeability measurements from whole core samples versus various estimates of permeability from geophysical logs

Lithology

Lithology was evaluated in three different geophysical logs: the photoelectric (PE) log, the elemental capture spectroscopy (ECS) log, and the spectral gamma ray log. The PE measures photoelectric absorption factor and is independent of fluid volume and content, thus making it an ideal lithology indicator. A value of 2 is indicative of sandstone (quartz) lithology, which is reflected throughout the Mt. Simon. The log is displayed graphically in Figure 2, and Table 10 contains the statistics.

Table 10. PE geophysical log statistics

	PE			
Unit	**Avg**	**St Dev**	**Max**	**Min**
UPPER-E	**1.96**	**0.193**	**2.74**	**1.70**
Middle-D	1.82	0.0523	2.06	1.70
Middle-C	1.98	0.115	2.55	1.76
MIDDLE	**1.93**	**0.123**	**2.55**	**1.70**
Lower-B	1.98	0.0824	2.20	1.79
Lower-A	2.13	0.115	2.86	1.90
LOWER	**2.05**	**0.124**	**2.86**	**1.79**
MTSIMON	**1.97**	**0.145**	**2.86**	**1.70**
ARGENTA	**2.48**	**0.380**	**3.72**	**2.02**

Figures 6 through 9 contain cross plots of PE versus bulk density (RHOB) and are color coded by Gamma Ray (GR) for the Upper, Middle, and Lower Mt. Simon and the Argenta. The cross plots also demonstrate the dominance of quartz sandstone in the formation. The Argenta clearly represents a shift in mineralogy, although the values may be a product of borehole conditions. The ECS is a pulsed neutron tool that processes gamma ray spectra and produces an estimate of relative proportion of mineral content. Quartz, feldspar, and mica are grouped together as QFM. Other minerals displayed are clays and carbonates, while minor minerals (Anhydrite, siderite, etc.) are not included. The log is displayed graphically in Figure 2, and Table 11 contains the statistics.

Table 11. ECS lithology statistics

	ECS Carbonates				ECS Clay				Cross-Plot Porosity			
Unit	**Avg**	**St Dev**	**Max**	**Min**	**Avg**	**St Dev**	**Max**	**Min**	**Avg**	**St Dev**	**Max**	**Min**
UPPER-E	**0.00**	**0.00**	**0.00**	**0.00**	**0.0316**	**0.0406**	**0.210**	**0.00**	**0.968**	**0.0410**	**1.00**	**0.790**
Middle-D	0.00	0.00	0.00	0.00	0.0493	0.0288	0.188	0.000900	0.950	0.0292	0.999	0.805

Middle-C	0.00	0.00	0.00	0.00	0.0858	0.0339	0.183	0.00850	0.914	0.0338	0.992	0.817
MIDDLE	**0.00**	**0.00**	**0.00**	**0.00**	**0.0686**	**0.0365**	**0.188**	**0.000900**	**0.931**	**0.0364**	**0.999**	**0.805**
Lower-B	0.00	0.00	0.00	0.00	0.0755	0.0215	0.156	0.0169	0.924	0.0215	0.983	0.844
Lower-A	0.00	0.00	0.00	0.00	0.0983	0.0254	0.201	0.0249	0.901	0.0254	0.975	0.799
LOWER	**0.00**	**0.00**	**0.00**	**0.00**	**0.0841**	**0.0255**	**0.201**	**0.0169**	**0.916**	**0.0256**	**0.983**	**0.799**
MTSIMON	**0.00**	**0.00**	**0.00**	**0.00**	**0.0703**	**0.0368**	**0.210**	**0.00**	**0.929**	**0.0368**	**1.00**	**0.790**
ARGENTA	**0.00**	**0.00**	**0.00**	**0.00**	**0.192**	**0.0955**	**0.525**	**0.103**	**0.808**	**0.0954**	**0.897**	**0.475**

According to the ECS, QFM is the dominant lithology, reflective of the high amount of quartz in the formation, but there is a noticeable amount clay throughout the formation. This is likely reflective of the clay coating noted in the thin-section analysis. Likewise, the ECS indicates a shift in mineralogy in the Argenta. However, this is reflective of an increase of clay content versus an increase in carbonates, indicated by the analysis from the PE log. The spectral gamma ray indicates the type of clay minerals present in the formation by measuring the signal from thorium, uranium, and potassium. Cross plots in Figures 9 through 13 show the clay mineralogy breakdown according to the spectral gamma ray in the Upper, Middle, and Lower Mt. Simon and the Argenta. The illite and mixed layer clays tend to dominate the Lower and Upper, with the Lower also including minor amounts of micas. The Middle Mt. Simon exhibits the most diverse distribution of clay content, ranging in type from mixed layer clays, montmorillonite, thorium-bearing minerals, small amounts of illite, and possibly chlorite.

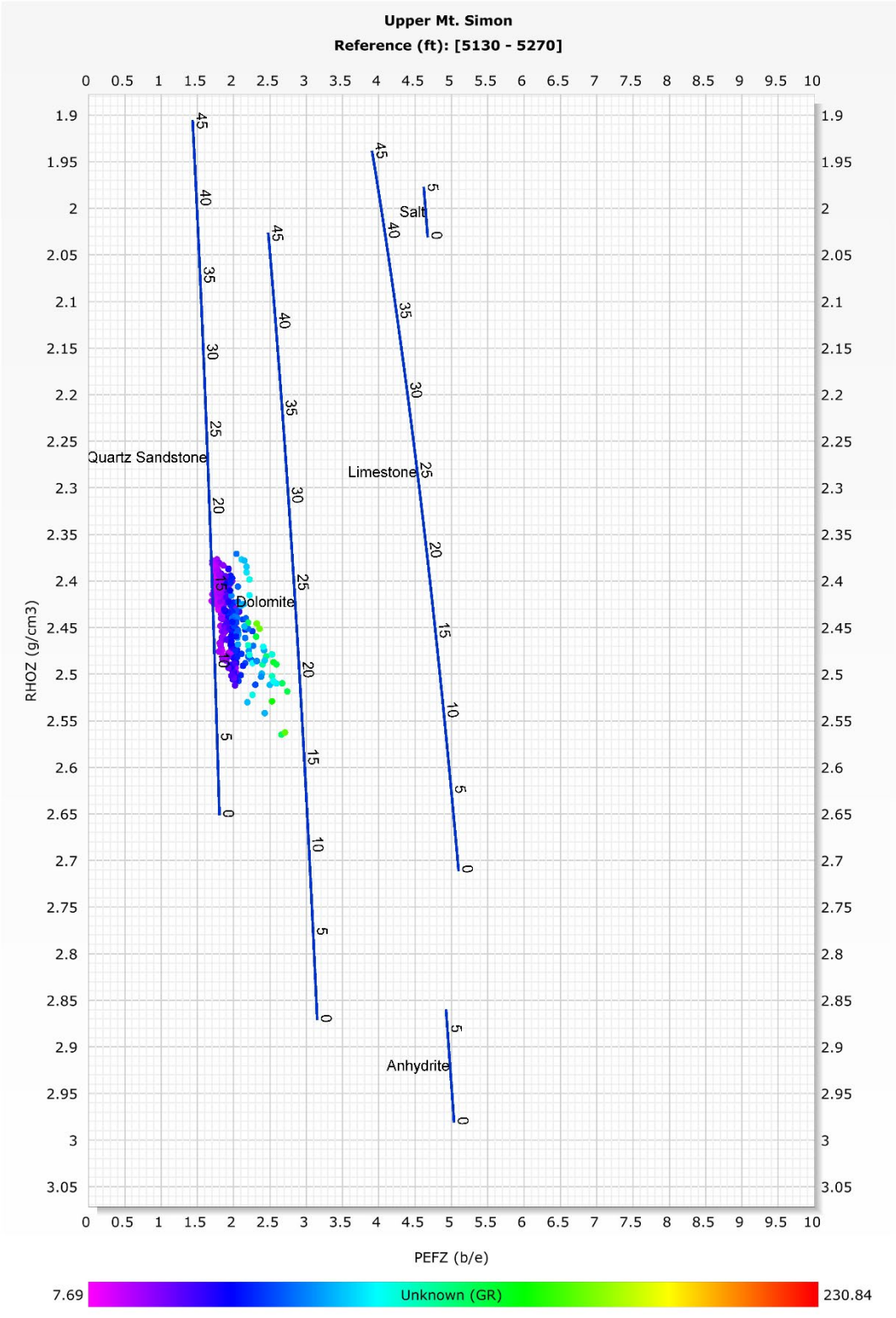

Figure 6. PE versus bulk density for the Upper Mt. Simon

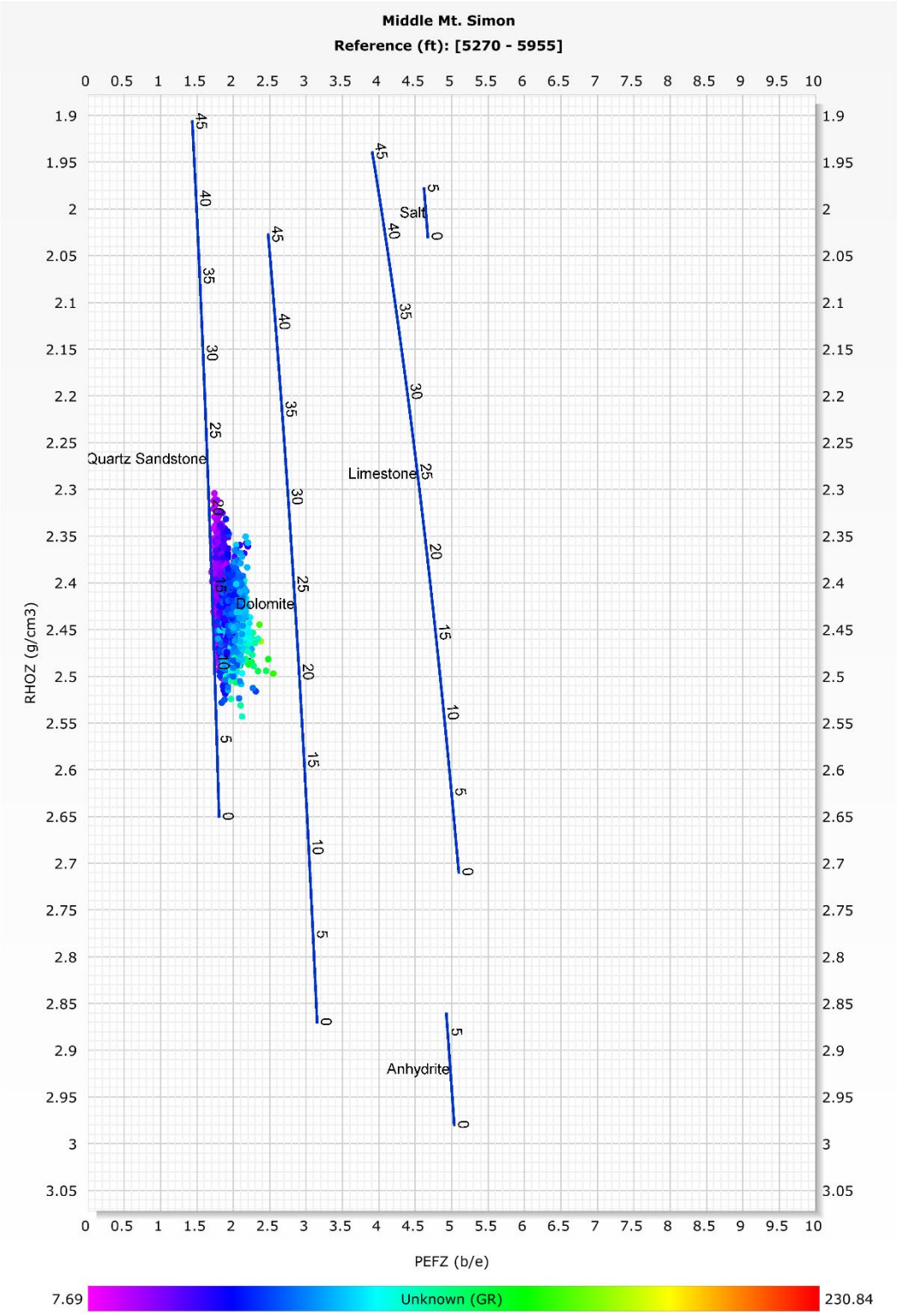

Figure 7. PE versus bulk density for the Middle Mt. Simon

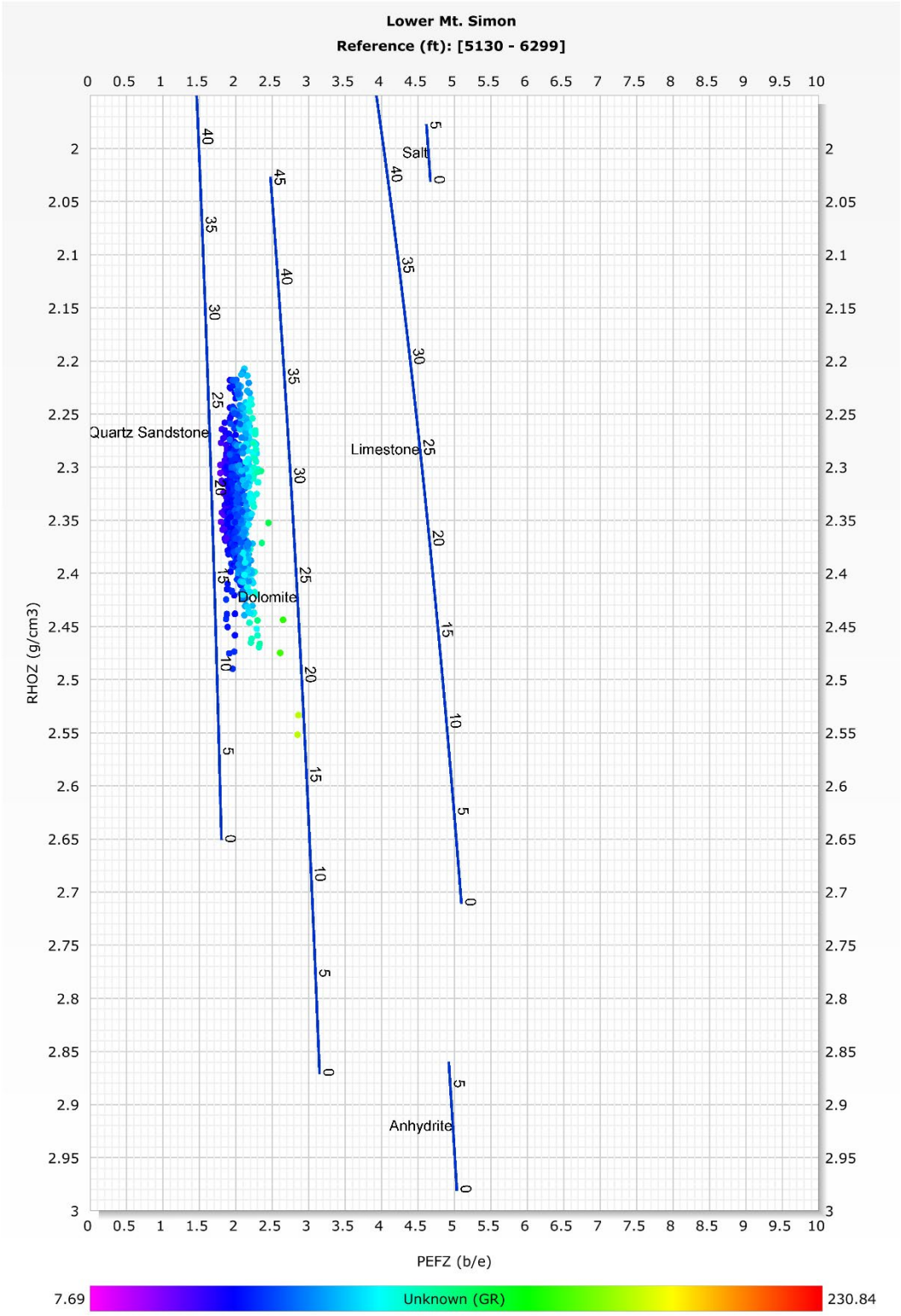

Figure 8. PE versus bulk density for the Lower Mt. Simon

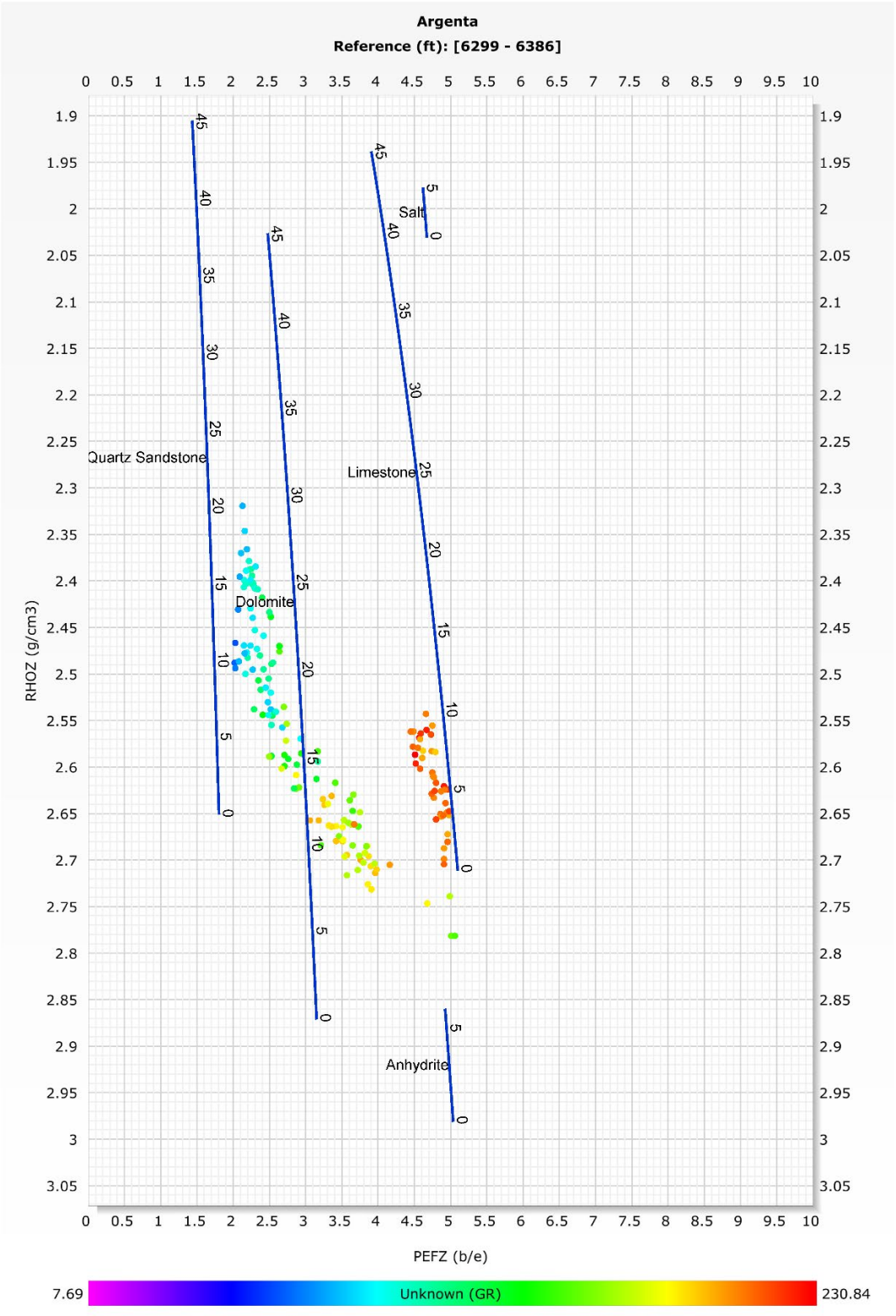

Figure 9. PE versus bulk density for the Argenta

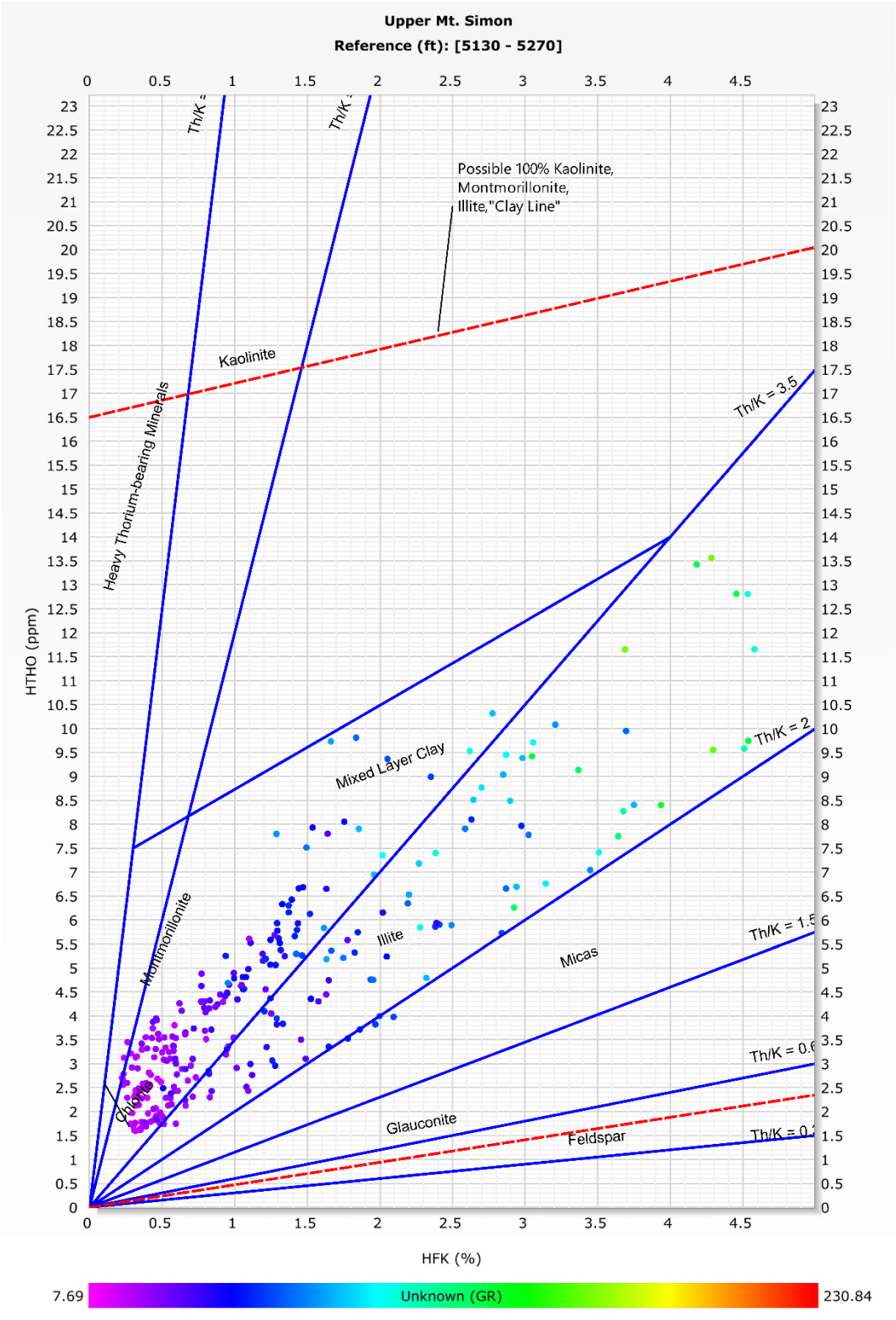

Figure 10. Clay mineralogy cross plot from spectral gamma ray log for the Upper Mt. Simon

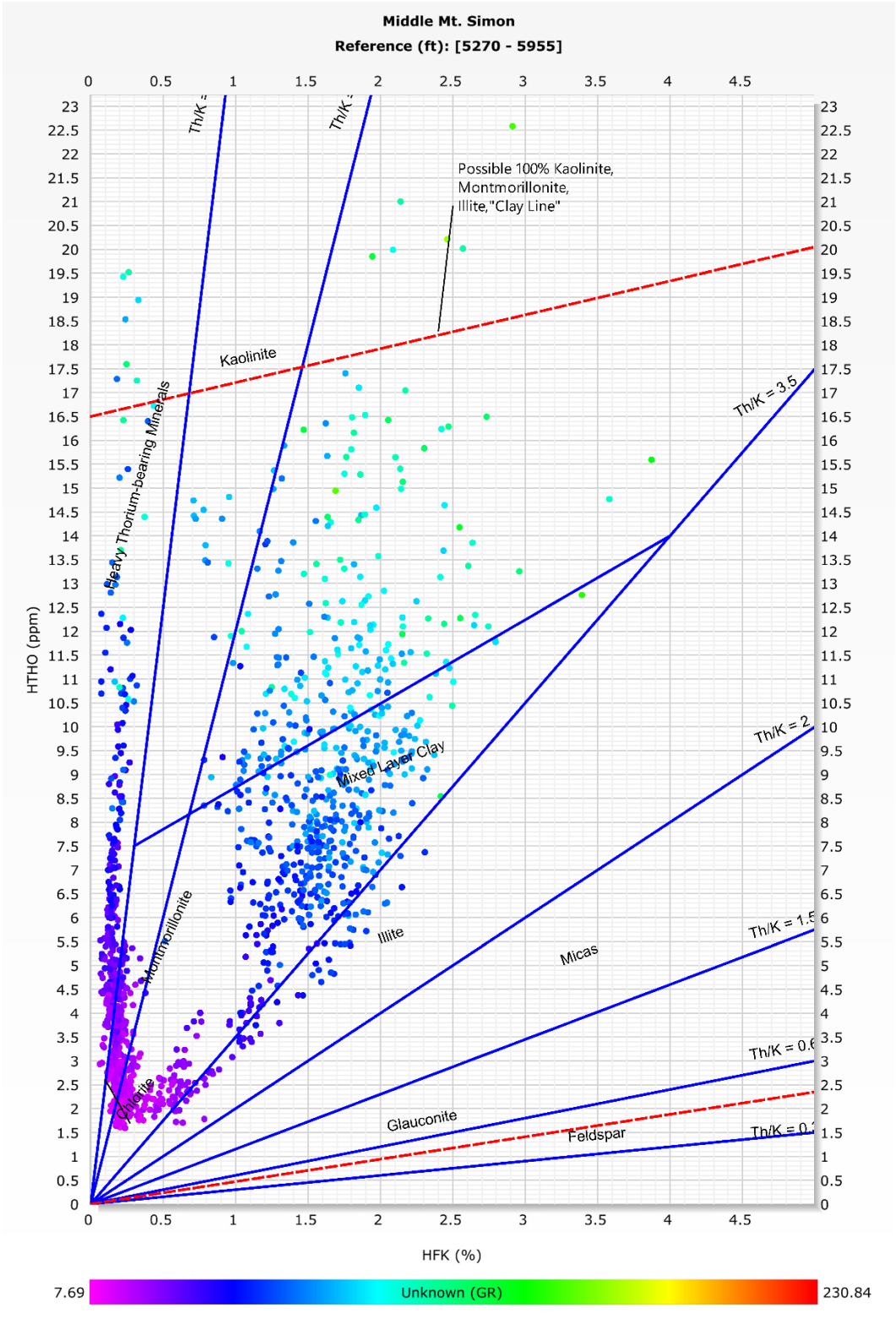

Figure 11. Clay mineralogy cross plot from spectral gamma ray log for the Middle Mt. Simon

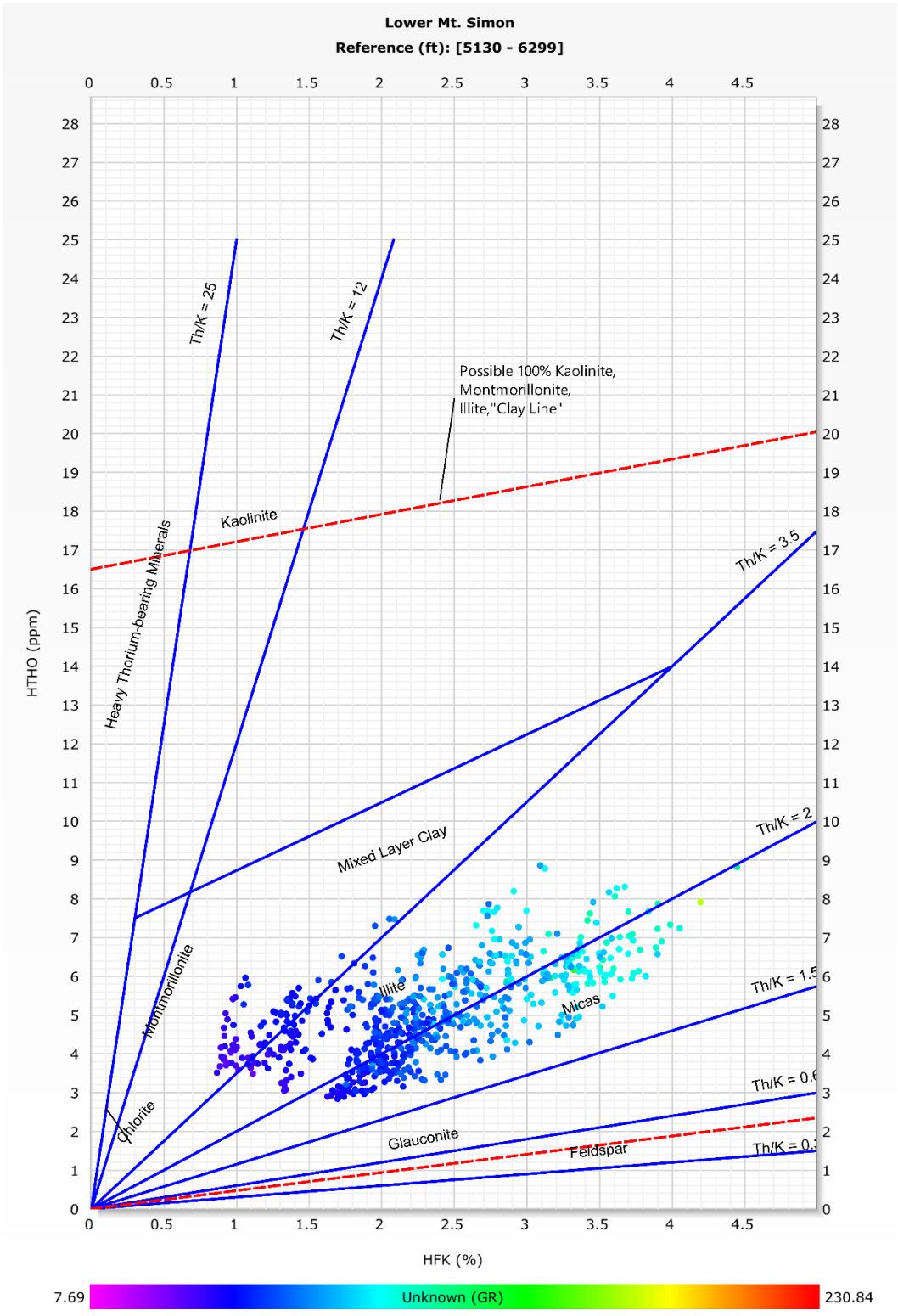

Figure 12. Clay mineralogy cross plot from spectral gamma ray log for the Lower Mt. Simon

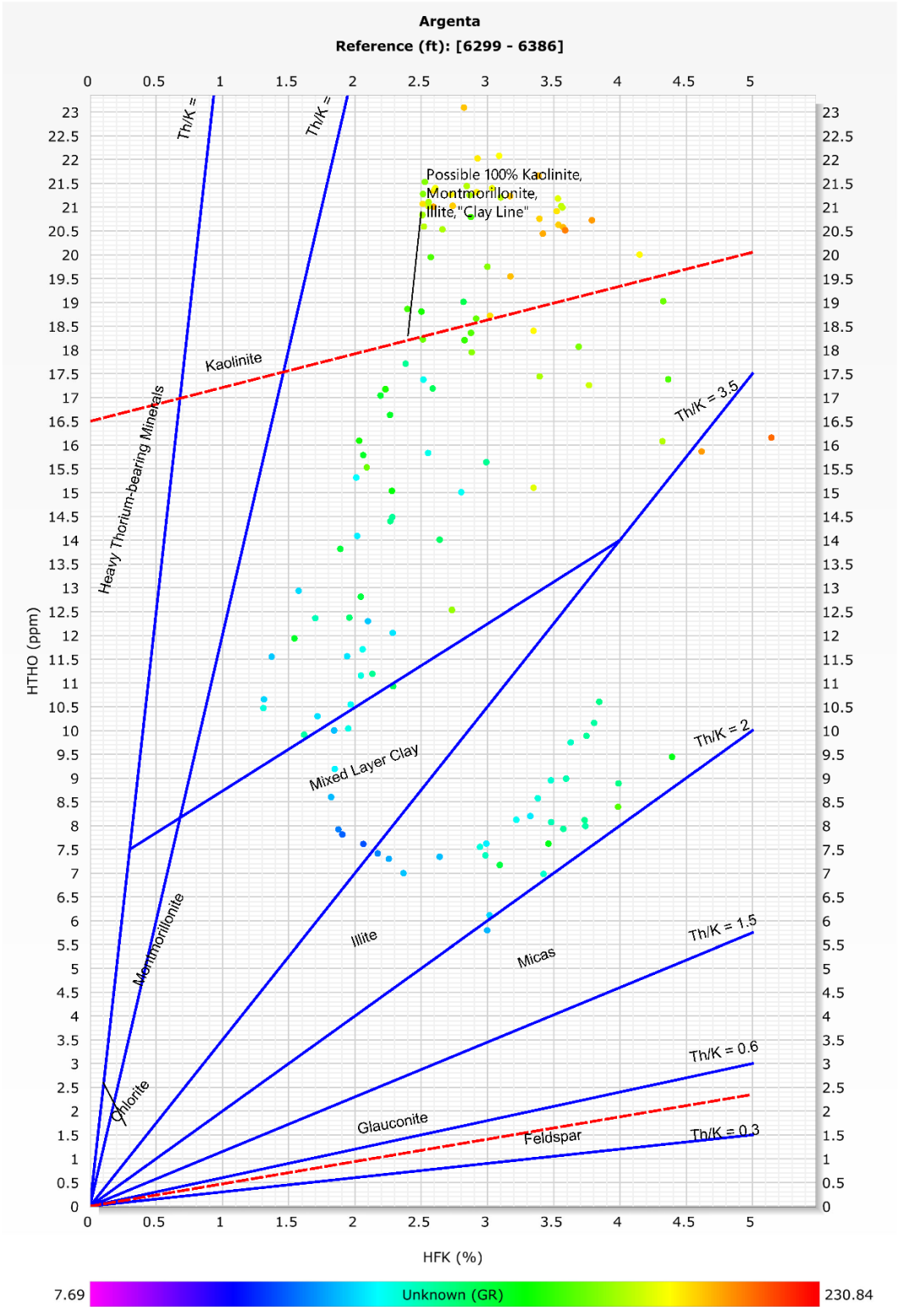

Figure 13. Clay mineralogy cross plot from spectral gamma ray log for the Argenta

Refences

Archie, G. E., 1942, The Electrical Resistivity Log as an Aid in Determining Some Reservoir Characteristics, Petroleum Transactions of the AIME, *Transactions of AIME*, 146, pp. 54-62.

Freiburg, J.T., Morse, D.G., Leetaru, H.E., Hoss, R.P,, and Q. Yan, 2014, A Depositional and diagenetic characterization of the Mt. Simon Sandstone at the Illinois Basin - Decatur Project Carbon Capture and Storage Site, Decatur, Illinois, USA, *Illinois State Geological Survey Circular, 583*, Urbana, IL, Illinois State Geological Survey, University of Illinois at Urbana-Champaign, p. 65.

Timur, A., 1968, An Investigation of Permeability, Porosity, & Residual Water Saturation Relationships For Sandstone Reservoirs, *The Log Analys*t, 9, pp. 8-17.

Wyllie, M.R.J. and W.D. Rose, 1950, Some Theoretical Considerations Related to the Quantitative Evaluation of the Physical Characteristics of Reservoir Rock From Electrical Log Data*, Journal of Petroleum Technology,* 189, pp. 105-110, SPE-950105-G, doi:10.2118/950105-G.

Chapter 5
Reservoir Properties and Petrographic Characterization

By: Mingyue Yue
Illinois State Geological Survey

Introduction

The T.R. McMillen #2 well was drilled to a depth of 6,478 ft through unconsolidated Quaternary sediments and down into the bedrock of Pennsylvanian to Cambrian units and into the Precambrian crystalline basement. Approximately 62 ft of 4-in-core was cut in the base of the New Albany Shale seal and into the Racine dolomite, 61 ft in the Lower Mt. Simon and into the Argenta Sandstone, 27 ft in the Precambrian basement, and 108 1-in diameter rotary sidewall cores from the Potosi through Precambrian units.

This report details the core analysis completed, including thin section point count analysis that includes mineralogical (detrital and diagenetic) and pore space quantification (including grain size analysis, annotated thin section photomicrographs, scanning electron microscopy [SEM] with energy dispersive X-ray spectroscopy [EDS], X-ray powder diffraction [XRD] analysis, and routine analysis of full diameter core and rotary sidewall core for porosity and permeability calculations).

Eau Claire Formation

Table 1. (From top to bottom) Petrographic point count analysis from thin sections prepared from rotary sidewall cores cut in the Eau Claire Formation, including detrital grains, authigenic cements, and matrix analysis.

RSWC	Detrital								
Eau Claire			Lithics		Feldspar			Quartz	
Depth	Glauconite	Dolomite2	Granitic	Rhyolite	Anorthite	Orthoclase	agioclas	Monocrystalline	Polycrystalline
4638.12	0.00%	0.75%	0.00%	0.00%	0.25%	2.75%	0.00%	1.50%	0.00%
4661.98	0.00%	27.82%	1.00%	0.25%	0.25%	0.00%	0.00%	16.29%	0.00%
4750.01	0.00%	11.25%	0.00%	0.00%	0.00%	0.00%	0.00%	0.25%	0.00%
4830.07	0.00%	14.00%	0.00%	3.00%	3.25%	30.25%	0.00%	14.25%	0.00%
4930.00	0.50%	5.50%	0.00%	0.00%	0.00%	2.50%	0.00%	36.25%	0.00%
5000.05	0.00%	8.00%	0.00%	3.75%	36.00%	3.25%	0.00%	20.50%	0.00%
5049.87	3.25%	3.25%	0.00%	0.00%	25.75%	0.50%	0.00%	27.50%	0.00%
5062.05	0.00%	13.16%	0.00%	0.00%	13.42%	2.03%	0.00%	12.41%	0.00%
5100.92	0.00%	1.50%	0.00%	0.00%	0.50%	0.00%	0.00%	8.25%	0.00%
5118.97	0.00%	0.00%	0.25%	2.02%	1.26%	18.69%	0.00%	27.78%	0.00%

RSWC Eau Claire	Authigenic Mineral						
		Illite					
Depth	Dolomite	Pore Filling	Grain Lining w/ quartz	Grain Lining	Iron rich	Kaolinite	Quartz
4638.12	19.75%	2.25%	0.00%	0.00%	0.00%	0.00%	0.00%
4661.98	45.36%	1.75%	0.00%	0.75%	0.00%	0.00%	2.51%
4750.01	76.50%	3.00%	0.00%	0.00%	0.00%	0.00%	0.00%
4830.07	11.25%	0.75%	0.00%	0.50%	0.00%	0.00%	4.00%
4930.00	34.00%	6.00%	0.25%	12.00%	0.00%	0.00%	0.00%
5000.05	7.25%	4.75%	0.00%	2.00%	0.00%	0.00%	7.75%
5049.87	6.75%	1.50%	0.00%	0.00%	0.00%	0.00%	8.00%
5062.05	38.73%	19.75%	0.00%	0.00%	0.00%	0.00%	0.51%
5100.92	11.75%	5.50%	0.00%	0.00%	0.00%	0.00%	0.00%
5118.97	0.00%	24.49%	0.51%	1.01%	0.00%	0.00%	11.62%

RSWC Eau Claire	Matrix			Porosity
				Intergranular
Depth	Illitic	Terrigenous	Clay lamina	Clay lined
4638.12	0.00%	72.75%	0.00%	0.00%
4661.98	0.00%	0.00%	0.00%	4.01%
4750.01	0.00%	9.00%	0.00%	0.00%
4830.07	0.00%	0.00%	0.00%	18.75%
4930.00	0.00%	0.25%	0.00%	2.75%
5000.05	0.00%	0.00%	0.00%	6.75%
5049.87	0.00%	0.00%	0.00%	23.50%
5062.05	0.00%	0.00%	0.00%	0.00%
5100.92	0.00%	72.50%	0.00%	0.00%
5118.97	0.00%	0.00%	0.00%	12.37%

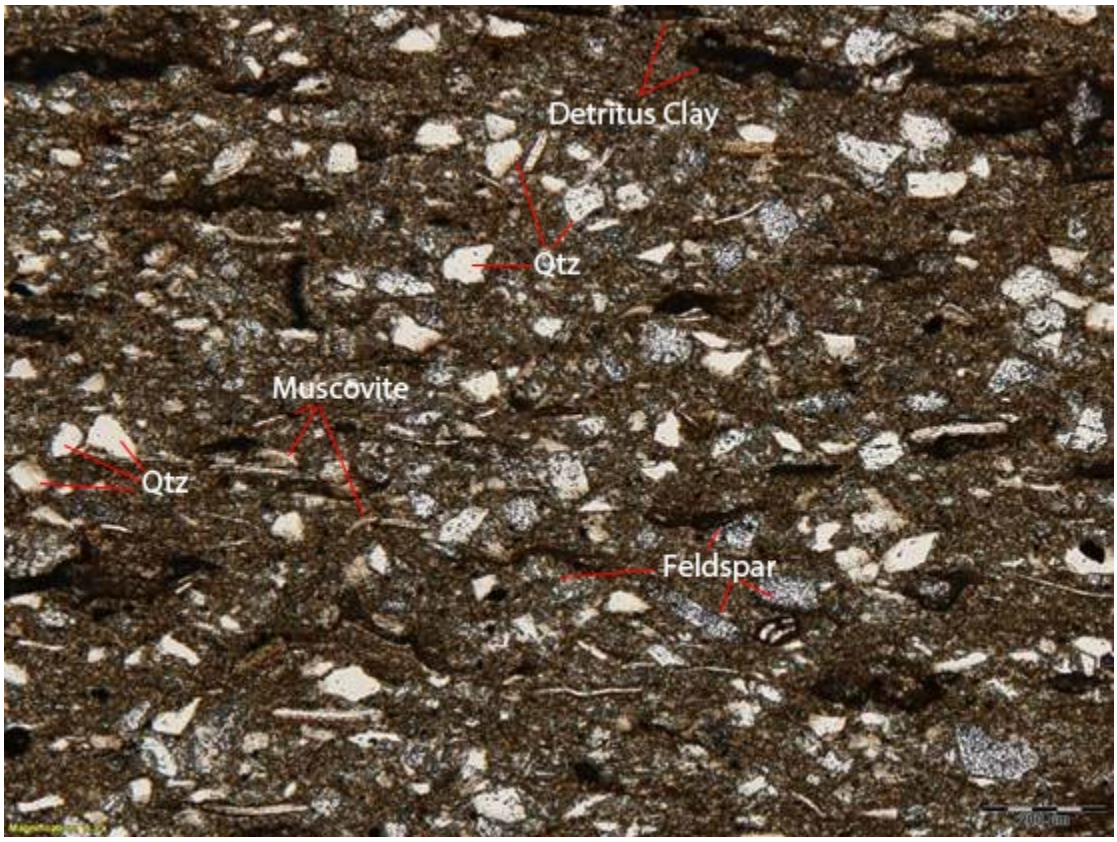

Figure 1. Thin section photomicrograph of an Eau Claire Formation shale sample at depth of 5,100.92 ft. Scale bar is 200 μm.

Mt. Simon

Table 2. (From top to bottom) Petrographic point count analysis from thin sections prepared from rotary sidewall cores cut in the Upper and Middle Mt. Simon Sandstone, including detrital grains, authigenic cements, and matrix/porosity analysis.

RSWC Upper/Middle Mt. Simon	Detrital								
			Lithics		Feldspar			Quartz	
Depth	Glauconite	Dolomite2	Granitic	Rhyolite	Anorthite	Orthoclase	Plagioclase	Monocrystalline	Polycrystalline
5140.02	0.00%	0.00%	0.00%	0.00%	8.75%	0.25%	0.00%	62.75%	1.50%
5155.04	0.00%	0.00%	1.00%	1.50%	0.00%	3.00%	0.00%	67.75%	0.75%
5172.97	0.00%	0.00%	0.00%	0.00%	0.75%	0.00%	0.00%	85.50%	1.25%
5190.04	0.00%	0.00%	0.00%	0.00%	0.00%	0.75%	0.00%	68.75%	0.50%
5200.01	0.00%	0.00%	0.00%	0.00%	0.00%	0.00%	0.00%	77.25%	10.00%
5234.05	0.00%	0.00%	0.00%	0.00%	0.00%	0.00%	0.00%	74.75%	0.75%
5238.06	0.00%	0.00%	0.00%	0.50%	0.00%	0.25%	0.00%	82.25%	0.50%
5275.03	0.00%	0.00%	2.75%	0.25%	0.00%	3.00%	0.00%	68.50%	0.25%
5299.93	0.00%	0.00%	0.00%	0.00%	0.50%	0.50%	0.00%	81.00%	0.25%
5325.03	0.00%	0.00%	0.00%	0.00%	0.00%	0.00%	0.00%	77.00%	0.75%
5346.09	0.00%	0.00%	0.00%	0.00%	0.00%	0.00%	0.00%	68.00%	0.75%
5374.99	0.00%	0.00%	0.00%	0.00%	0.00%	0.00%	0.00%	70.00%	0.75%
5412.02	0.00%	0.00%	0.00%	0.00%	0.00%	0.00%	0.00%	88.25%	0.25%
5412.07	0.00%	0.00%	0.00%	0.00%	0.00%	0.00%	0.00%	72.50%	0.25%
5450.05	0.00%	0.00%	0.00%	0.00%	0.00%	0.00%	0.00%	76.25%	0.25%
5499.93	0.00%	0.00%	0.00%	0.00%	0.00%	0.00%	0.00%	61.50%	0.75%
5559.97	0.00%	0.00%	0.00%	0.00%	0.00%	0.00%	0.00%	68.25%	1.00%
5599.99	0.00%	0.00%	0.00%	0.00%	0.00%	0.00%	0.00%	67.00%	2.00%
5650.12	0.00%	0.00%	0.00%	0.00%	0.25%	7.50%	0.00%	63.75%	9.75%
5718.08	0.00%	0.00%	1.25%	0.75%	0.75%	0.75%	0.00%	65.25%	5.50%
5720.11	0.00%	0.00%	0.00%	0.00%	2.75%	11.25%	0.00%	62.50%	3.75%
5778.08	0.00%	0.00%	0.00%	0.75%	2.75%	2.75%	0.00%	61.25%	9.75%
5811.11	0.00%	0.00%	3.52%	6.28%	0.00%	11.06%	2.26%	60.05%	9.80%

RSWC Upper/Middle Mt. Simon Depth	Authigenic Mineral						
		Illite					
	Dolomite	Pore Filling	Grain Lining w/ quartz	Grain Lining	Iron rich	Kaolinite	Quartz
5140.02	0.00%	2.75%	0.00%	0.00%	0.00%	0.00%	6.00%
5155.04	0.00%	0.25%	0.00%	2.00%	0.00%	0.00%	14.00%
5172.97	0.00%	1.50%	0.00%	0.50%	0.00%	0.00%	2.25%
5190.04	0.00%	0.00%	0.00%	7.00%	0.00%	0.00%	13.00%
5200.01	0.00%	0.00%	0.00%	0.00%	0.00%	0.00%	9.50%
5234.05	0.00%	0.25%	0.00%	6.00%	0.00%	0.00%	10.50%
5238.06	0.00%	0.00%	0.00%	1.00%	0.00%	0.25%	6.75%
5275.03	0.00%	1.00%	0.00%	1.50%	0.00%	0.00%	12.00%
5299.93	0.00%	0.75%	2.00%	0.75%	0.00%	0.00%	3.50%
5325.03	0.00%	0.75%	2.75%	5.75%	0.00%	0.00%	5.25%
5346.09	0.00%	1.00%	0.50%	2.50%	0.00%	0.00%	17.00%
5374.99	0.00%	0.50%	0.00%	10.25%	0.00%	0.00%	16.25%
5412.02	0.00%	3.00%	0.00%	1.00%	0.00%	0.00%	4.00%
5412.07	0.00%	1.75%	3.50%	0.75%	0.00%	0.00%	12.75%
5450.05	0.00%	1.50%	0.00%	0.75%	0.00%	0.00%	9.00%
5499.93	0.00%	7.00%	7.25%	5.00%	0.00%	0.00%	8.00%
5559.97	0.00%	2.75%	0.00%	1.00%	0.00%	0.00%	13.00%
5599.99	0.00%	5.50%	0.00%	1.00%	0.00%	0.75%	9.50%
5650.12	0.00%	0.75%	0.00%	0.00%	0.00%	0.00%	1.25%
5718.08	0.00%	7.75%	0.00%	1.50%	0.00%	0.00%	3.25%
5720.11	0.00%	0.25%	0.00%	0.00%	0.00%	0.00%	4.75%
5778.08	0.00%	0.25%	2.00%	0.00%	0.00%	0.00%	5.25%
5811.11	0.00%	0.25%	0.00%	0.00%	0.00%	0.25%	4.27%

RSWC Upper/Middle Mt. Simon	Matrix			Porosity
				Intergranular
Depth	Illitic	Terrigenous	Clay lamina	Clay lined
5140.02	0.00%	0.00%	0.00%	18.00%
5155.04	0.00%	0.00%	0.00%	9.75%
5172.97	0.00%	0.00%	0.00%	8.25%
5190.04	0.00%	0.00%	0.00%	10.00%
5200.01	0.00%	0.00%	0.00%	3.25%
5234.05	0.00%	0.00%	0.00%	7.75%
5238.06	0.00%	0.00%	0.00%	8.50%
5275.03	0.00%	0.00%	0.00%	10.75%
5299.93	0.00%	0.00%	0.00%	10.75%
5325.03	0.00%	0.00%	0.00%	7.75%
5346.09	0.00%	0.00%	0.00%	10.25%
5374.99	0.00%	0.00%	0.00%	2.25%
5412.02	0.00%	0.00%	0.00%	3.50%
5412.07	0.00%	0.00%	0.00%	8.50%
5450.05	0.00%	0.00%	0.00%	12.25%
5499.93	0.00%	0.00%	0.00%	10.50%
5559.97	0.00%	0.00%	0.00%	14.00%
5599.99	0.00%	0.00%	0.00%	14.25%
5650.12	0.00%	0.00%	0.00%	16.75%
5718.08	0.00%	0.00%	0.00%	13.25%
5720.11	0.00%	0.00%	0.00%	14.75%
5778.08	0.00%	0.25%	0.00%	15.00%
5811.11	0.00%	0.00%	0.00%	2.26%

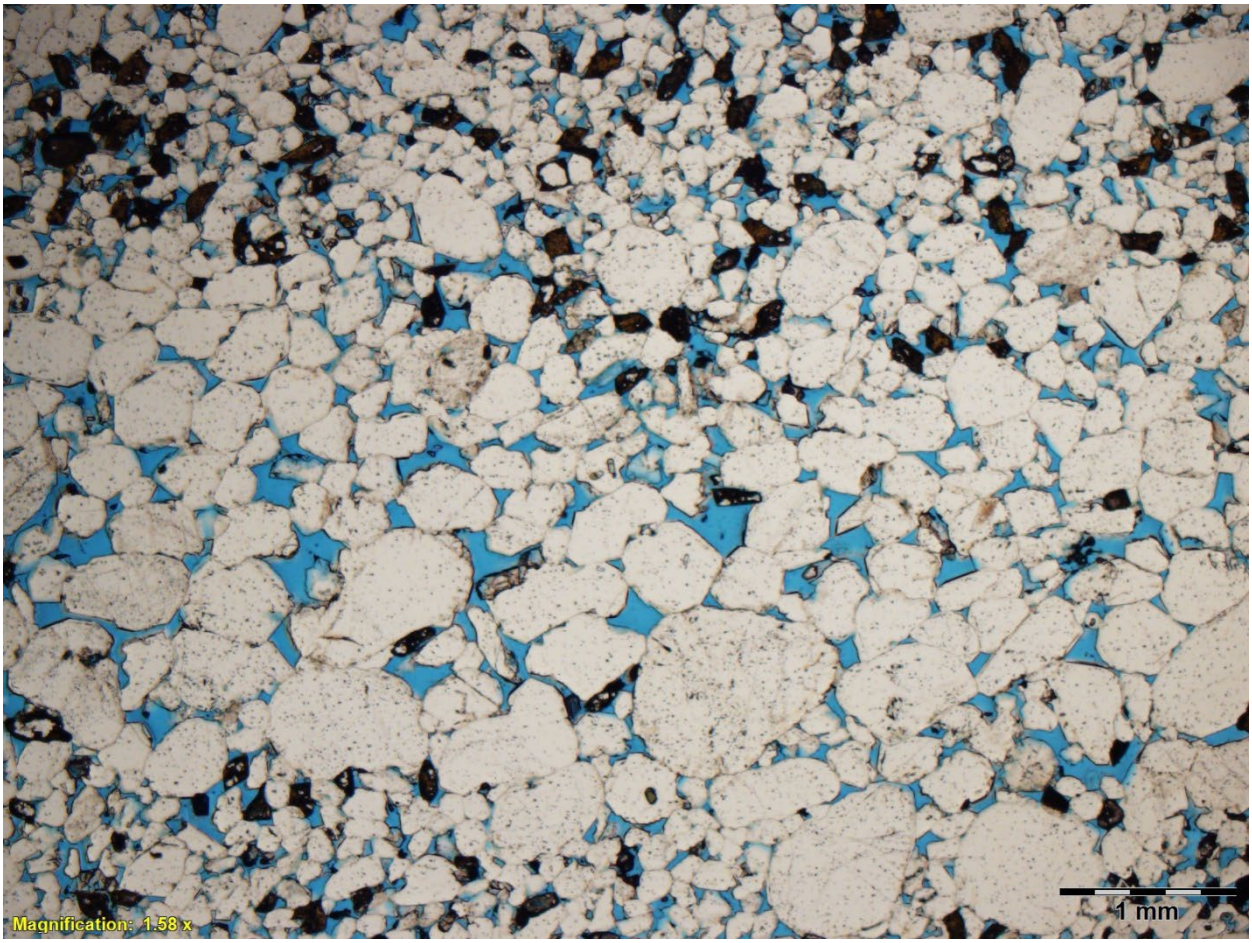

Figure 2. Thin section photomicrograph in the Upper Mt. Simon Sandstone at depth of 5,155.04 ft. Note the graded bedding and accumulation of feldspar (orthoclase) in the finer-grained laminae. Scale bar at 1 mm.

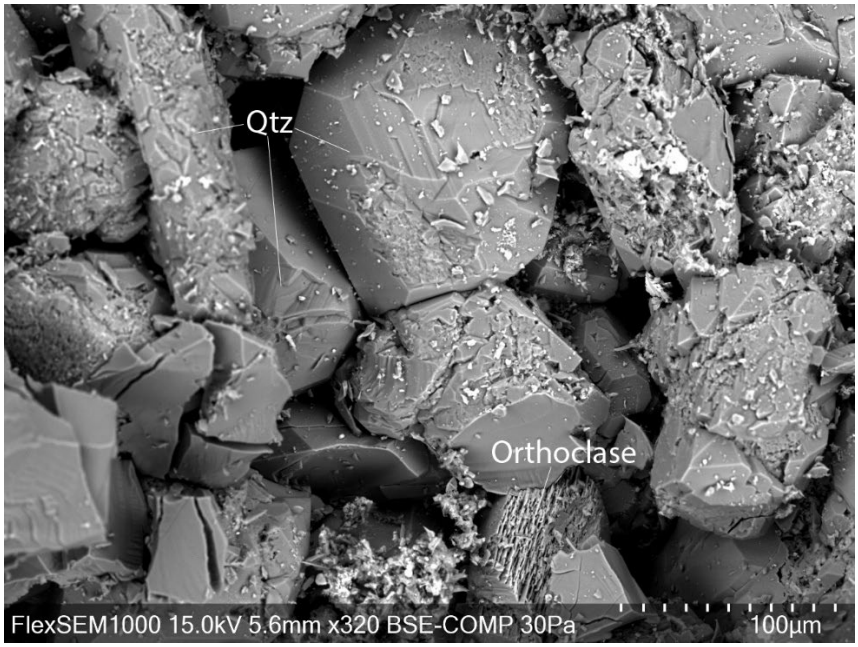

Figure 3A. SEM photomicrograph of Upper Mt. Simon Sandstone at depth of 5,155.04 ft. Note the large pore throats between grains.

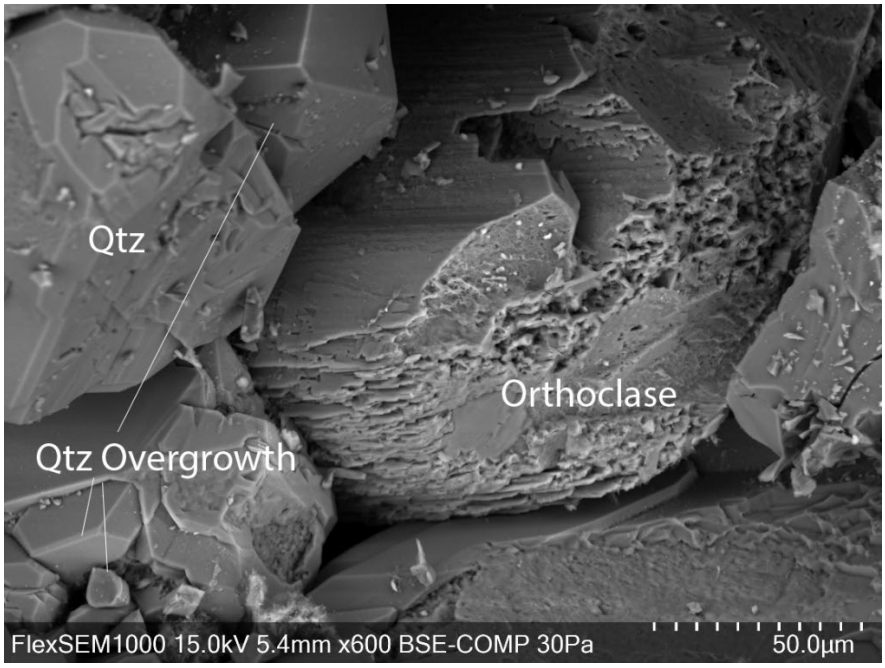

Figure 3B. SEM photomicrograph of Upper Mt. Simon Sandstone at depth of 5,155.04 ft. Note the euhedral crystal faces on both the quartz and feldspar (orthoclase) grains. Nearly every grain in the Upper Mt. Simon has authigenic overgrowths.

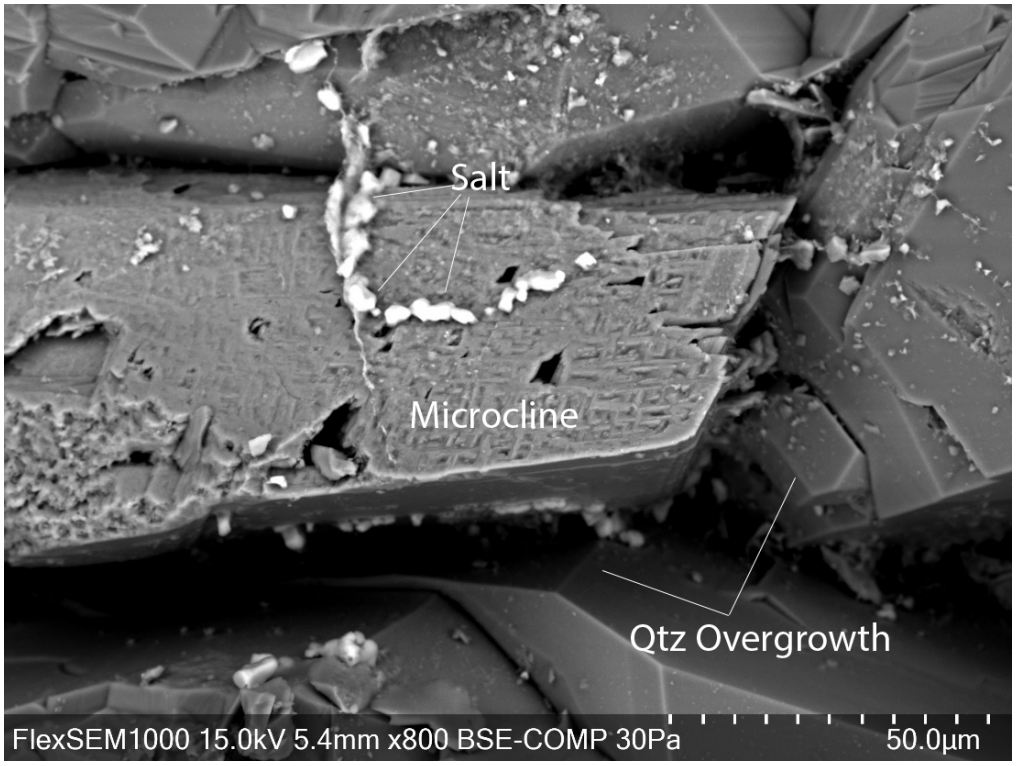

Figure 3C. SEM photomicrograph of Upper Mt. Simon Sandstone at depth of 5,155.04 ft. Note the euhedral crystal faces on the quartz and feldspar (microcline) grains. The microcline is partially dissolved with salt crystals along fractures and dissolution surface. Salt is a common occurrence in samples due to the drying of the pore brine fluids.

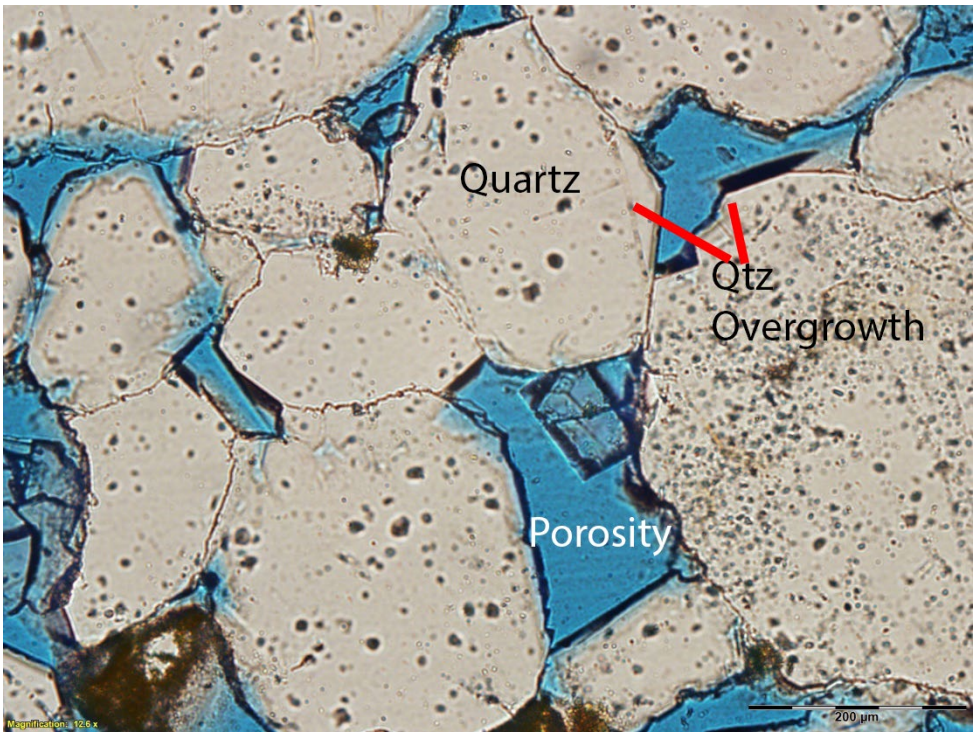

Figure 4. Thin section photomicrograph of the Upper Mt. Simon Sandstone at depth of 5,172.97 ft. Clay-lined pore space. All quartz grains have partial authigenic quartz overgrowth. Feldspars have common authigenic overgrowth. Both detrital and authigenic feldspar phases are partially dissolved, producing secondary moldic porosity. Clay coatings coat partially dissolved feldspar grains and intergranular pore space.

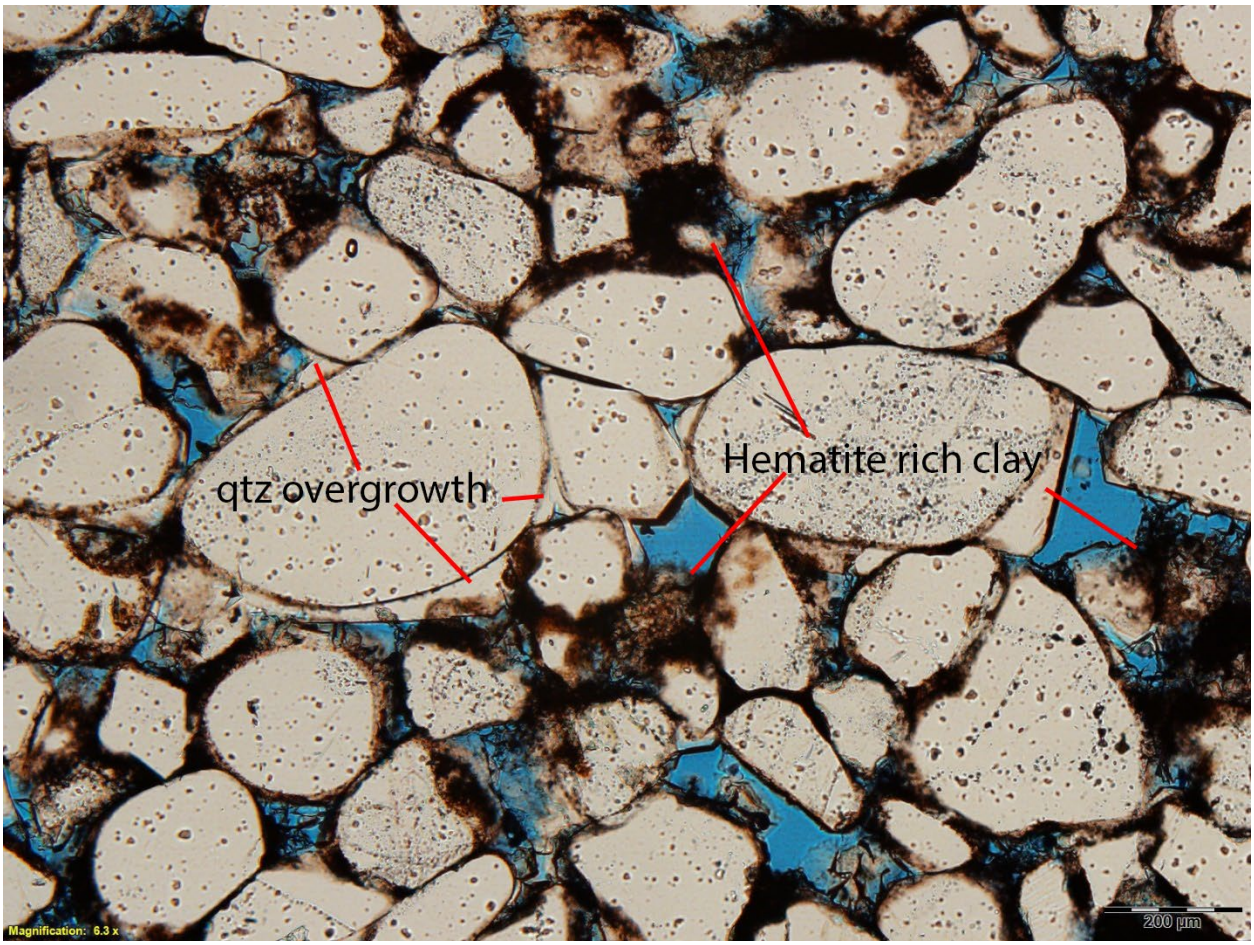

Figure 5. Thin section photomicrograph of the Upper Mt. Simon Sandstone at depth of 5,412.07 ft. Note the abundant hematite, or iron-rich clay, coating grains. Clay is observed as both grain and pore lining. Clay coatings occur over both detrital grains and authigenic cements, suggesting multiple generations of clay. In general, samples with more clay coatings contain less authigenic quartz cements.

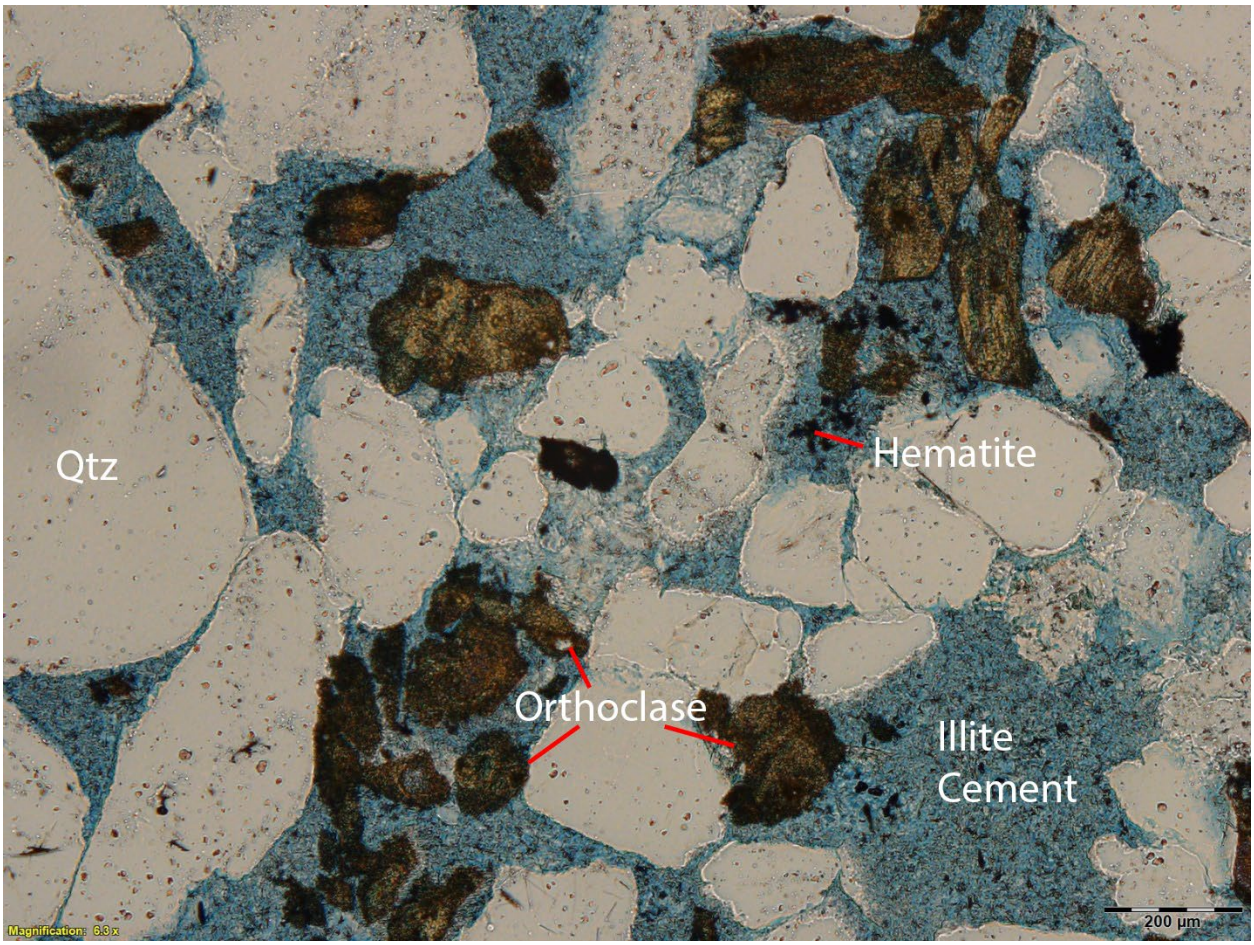

Figure 6. Thin section photomicrograph of the Middle Mt. Simon Sandstone at depth of 5,650.12 ft. The sample has high intergranular porosity, but all pore space is partially filled with illite and kaolinite. Authigenic quartz overgrowths are interrupted by intergranular clay with rough and serrated edges.

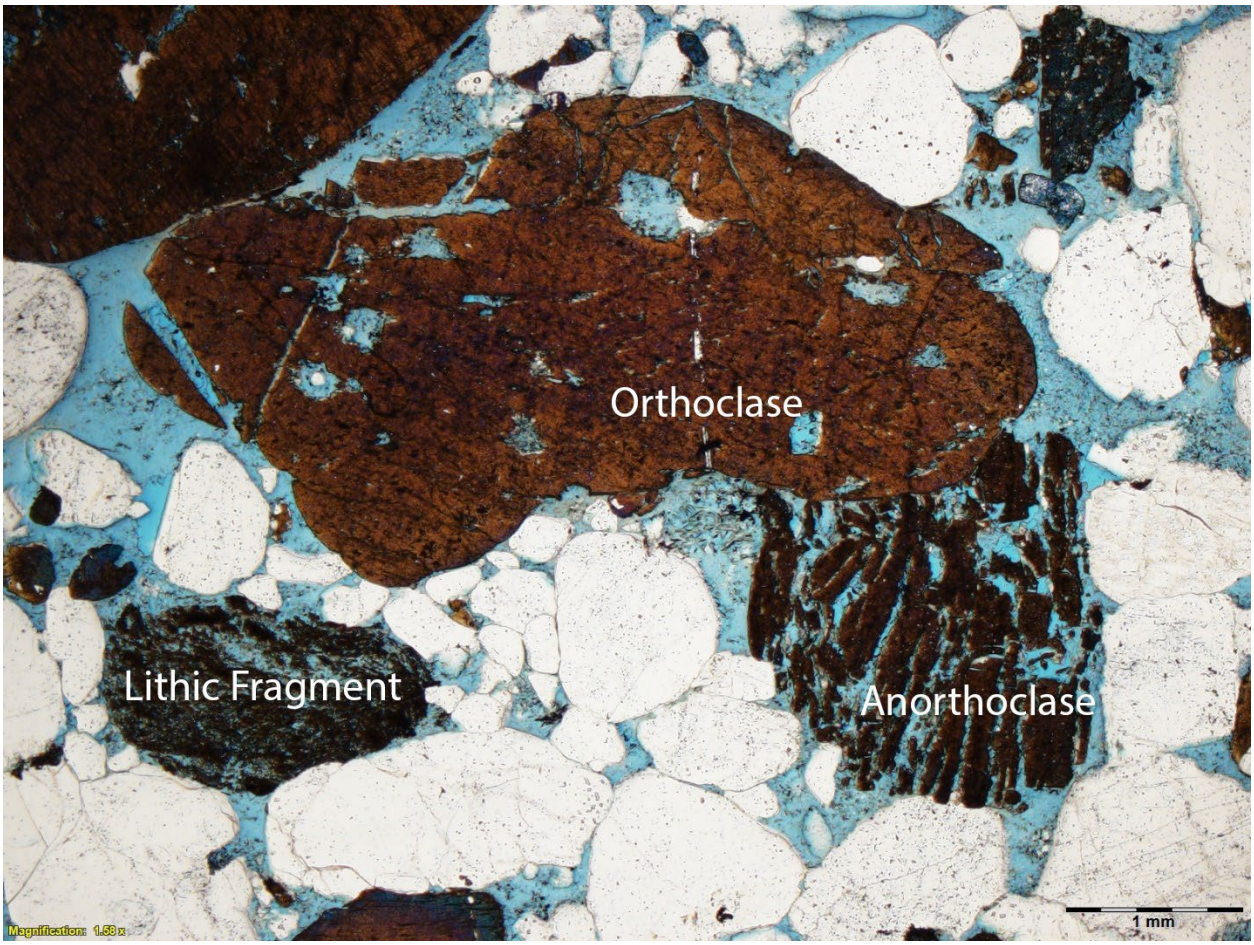

Figure 7. Thin section photomicrograph of the Middle Mt. Simon Sandstone at depth of 5,811.11 ft. Note the partially dissolved feldspar (orthoclase/anorthoclase) grains and lithic fragments.

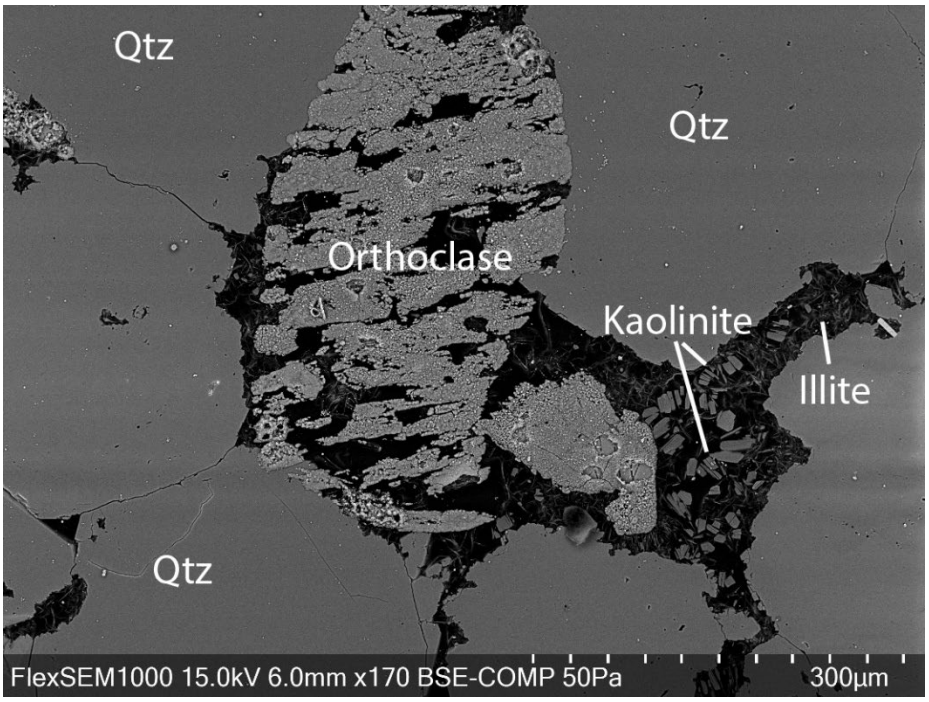

Figure 8A. SEM photomicrograph of the Middle Mt. Simon Sandstone at depth of 5,811.11 ft. Note the partially dissolved feldspar (orthoclase), relatively isolated pore space (closed throats), and the pore-filling clay (kaolinite and illite).

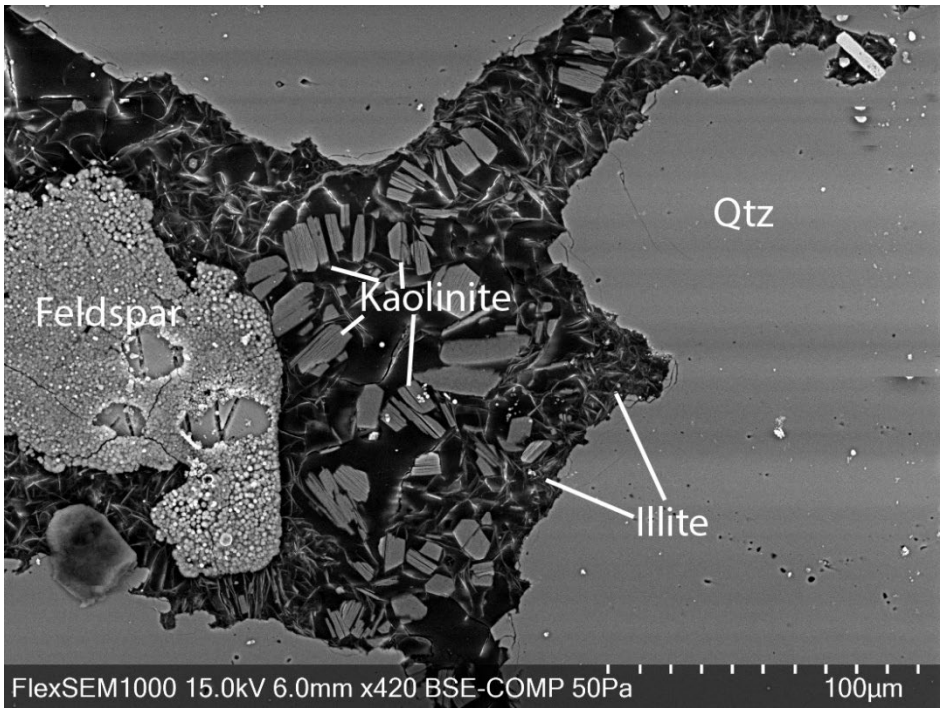

Figure 8B. SEM photomicrograph of the Middle Mt. Simon Sandstone at depth of 5,811.11 ft. Abundant clay (kaolinite and illite) fills the pore space.

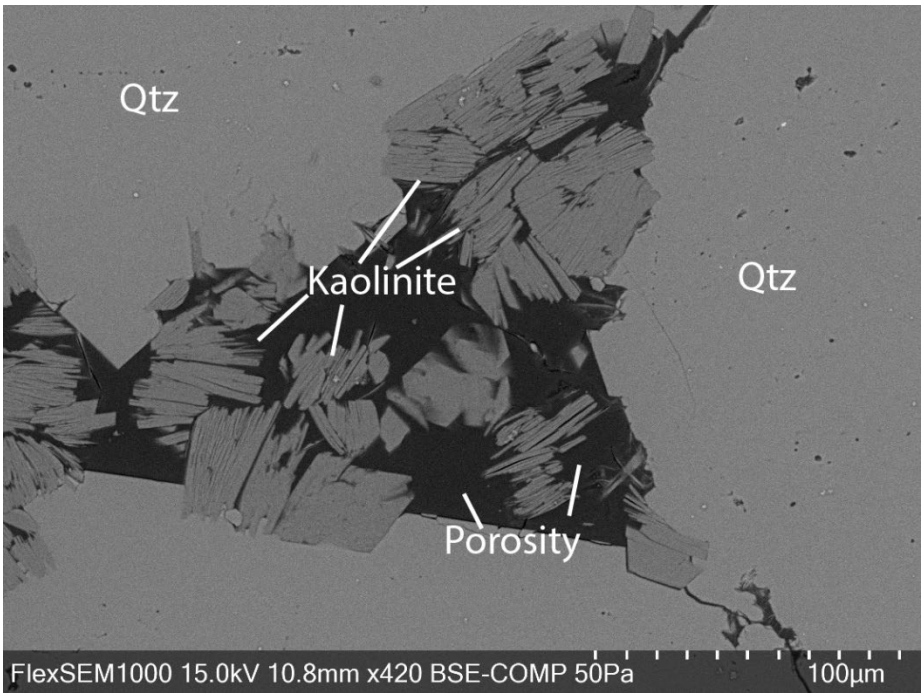

Figure 8C. SEM photomicrograph of the Middle Mt. Simon Sandstone at depth of 5,811.11 ft. Abundant clay fills pore space and interrupts authigenic quartz overgrowths.

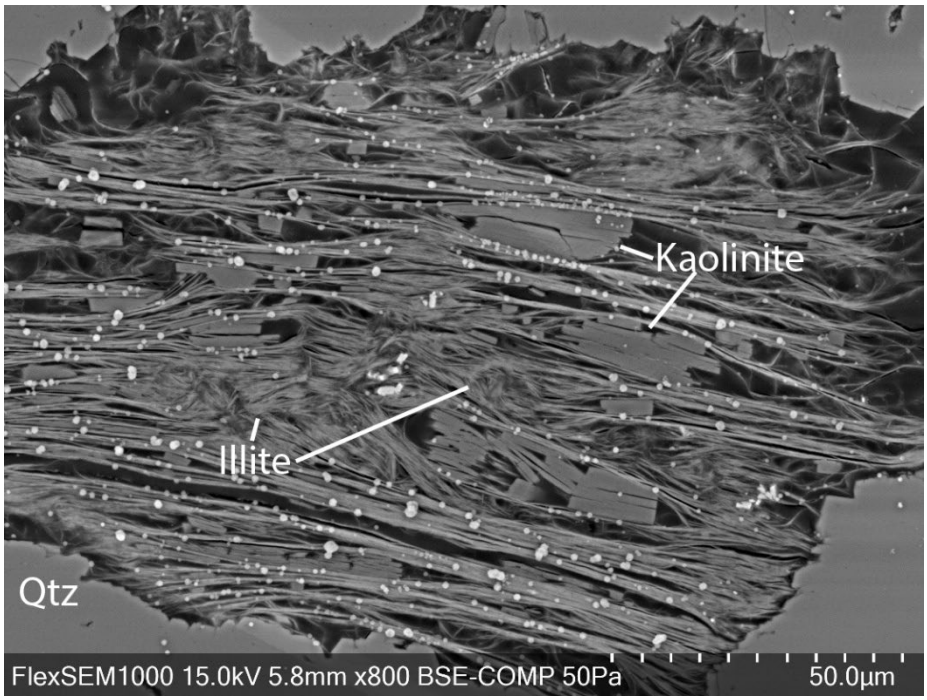

Figure 8D. SEM photomicrograph of the Middle Mt. Simon Sandstone at depth of 5,811.11 ft. Altered feldspar at this depth might be the source material for the clays forming in the pore spaces. Abundant fibrous and hairy illite interlayered with kaolinite interrupts authigenic quartz overgrowth, causing a serrated-appearing nucleation.

Table 3. (From top to bottom) Petrographic point count analysis from thin sections prepared from rotary sidewall cores cut in the Lower Mt. Simon Sandstone, including detrital grains, authigenic cements, and matrix/porosity analysis.

RSWC	Detrital								
Lower Mt. Simon			Lithics		Feldspar			Quartz	
Depth	Glauconite	Dolomite2	Granitic	Rhyolite	Anorthite	Orthoclase	Plagioclase	Monocrystalline	Polycrystalline
5903.98	0.00%	0.00%	0.00%	2.00%	0.25%	2.00%	0.00%	76.50%	5.50%
5907.99	0.00%	0.00%	0.00%	0.25%	0.00%	3.25%	0.00%	62.50%	0.50%
5914.01	0.00%	0.00%	2.25%	2.75%	0.00%	1.00%	1.25%	51.75%	0.00%
5918.97	0.00%	0.00%	0.00%	1.25%	0.50%	8.00%	0.50%	49.75%	0.25%
5925.05	0.00%	0.00%	2.75%	3.00%	0.00%	0.25%	0.50%	56.25%	0.00%
5950.49	0.00%	0.00%	0.00%	1.75%	1.00%	4.75%	0.00%	70.25%	0.25%
5965.07	0.00%	0.00%	3.01%	2.51%	0.00%	0.25%	0.00%	56.14%	0.75%
5965.33	0.00%	0.00%	0.00%	1.25%	1.25%	5.00%	0.00%	66.75%	0.00%
5972.38	0.00%	0.00%	1.69%	1.45%	1.20%	0.48%	0.00%	61.20%	0.24%
5979.03	0.00%	0.00%	0.00%	0.75%	0.75%	4.98%	0.50%	62.69%	0.50%
5982.39	0.00%	0.00%	2.00%	1.50%	0.25%	1.00%	0.00%	60.10%	0.00%
5990.03	0.00%	0.00%	0.00%	1.00%	0.50%	5.75%	0.25%	48.50%	0.00%
5995.10	0.00%	0.00%	5.00%	2.00%	0.00%	0.00%	0.25%	57.50%	0.00%
6000.08	0.00%	0.00%	0.00%	0.50%	1.75%	3.00%	0.00%	56.50%	0.50%
6003.08	0.00%	0.00%	2.98%	4.47%	0.00%	2.48%	0.74%	62.78%	0.00%
6008.03	0.00%	0.00%	0.00%	0.50%	1.25%	4.26%	1.25%	48.37%	0.25%
6035.99	0.00%	0.00%	1.75%	5.00%	0.50%	1.25%	1.50%	55.25%	0.50%
6050.00	0.00%	0.00%	0.00%	2.01%	3.27%	7.29%	1.26%	60.80%	0.25%
6053.07	0.00%	0.00%	2.00%	3.75%	1.00%	3.00%	0.25%	66.50%	0.00%
6070.04	0.00%	0.00%	0.00%	3.00%	6.50%	7.50%	0.00%	60.00%	0.50%
6078.01	0.00%	0.00%	2.26%	3.26%	1.75%	1.75%	1.25%	67.42%	0.25%
6089.07	0.00%	0.00%	0.00%	2.26%	3.27%	5.03%	0.00%	48.49%	0.25%
6096.03	0.00%	0.00%	3.04%	4.81%	1.77%	1.77%	0.51%	55.19%	0.25%
6100.08	0.00%	0.00%	0.00%	2.01%	2.76%	6.02%	0.00%	53.88%	1.50%
6119.06	0.00%	0.00%	2.51%	6.53%	0.00%	3.02%	0.25%	57.54%	0.50%
6124.07	0.00%	0.00%	0.00%	0.25%	6.25%	6.50%	1.75%	53.00%	1.00%
6133.97	0.00%	0.00%	5.51%	3.76%	1.50%	6.52%	0.75%	52.88%	0.00%
6151.02	0.00%	0.00%	0.00%	0.75%	3.00%	6.75%	0.50%	58.25%	2.50%
6178.08	0.00%	0.00%	4.24%	5.24%	2.00%	1.75%	0.25%	70.07%	0.25%
6200.09	0.00%	0.00%	0.00%	1.75%	0.00%	9.52%	4.01%	58.90%	0.00%
6220.13	0.00%	0.00%	0.00%	0.00%	9.25%	8.50%	0.00%	48.25%	2.25%
6222.99	0.00%	0.00%	0.00%	3.00%	1.00%	4.25%	7.25%	50.00%	3.75%
6230.08	0.00%	0.00%	8.25%	9.75%	0.50%	2.50%	0.00%	55.25%	1.00%
6249.99	0.00%	0.00%	2.50%	8.00%	1.00%	7.00%	2.50%	39.25%	1.25%
6251.09	0.00%	0.00%	0.00%	0.00%	0.00%	13.25%	0.00%	21.75%	0.00%
6285.02	0.00%	0.00%	3.03%	2.27%	0.51%	5.05%	4.80%	47.22%	2.02%

RSWC Lower Mt. Simon Depth	Authigenic Mineral						
		Illite					
	Dolomite	Pore Filling	Grain Lining w/ quartz	Grain Lining	Iron rich	Kaolinite	Quartz
5903.98	0.00%	0.50%	0.00%	0.00%	0.00%	0.00%	7.25%
5907.99	0.00%	0.50%	0.75%	0.50%	0.00%	0.00%	13.25%
5914.01	0.00%	1.00%	1.00%	3.75%	0.00%	1.25%	10.25%
5918.97	0.00%	13.25%	0.00%	1.25%	0.00%	0.25%	5.50%
5925.05	0.00%	2.50%	3.75%	3.50%	0.00%	0.00%	8.50%
5950.49	0.00%	0.75%	1.50%	2.50%	0.00%	0.00%	8.50%
5965.07	0.00%	1.00%	2.51%	2.01%	0.00%	0.00%	10.28%
5965.33	0.00%	0.50%	2.50%	2.75%	0.00%	0.00%	11.50%
5972.38	0.00%	6.51%	5.78%	3.13%	9.16%	0.00%	2.17%
5979.03	0.00%	7.71%	4.23%	3.23%	0.00%	0.00%	7.46%
5982.39	0.00%	1.00%	4.74%	3.99%	0.00%	0.00%	8.98%
5990.03	0.00%	2.50%	10.75%	3.75%	0.00%	0.00%	10.50%
5995.10	0.00%	2.25%	3.75%	3.00%	0.00%	0.00%	8.50%
6000.08	0.00%	1.75%	4.25%	1.50%	0.00%	0.00%	6.00%
6003.08	0.00%	2.23%	1.49%	2.73%	0.00%	0.00%	4.71%
6008.03	0.00%	2.51%	5.01%	5.76%	0.00%	0.00%	10.03%
6035.99	0.00%	0.50%	0.00%	0.00%	0.00%	0.00%	4.75%
6050.00	0.00%	1.51%	1.01%	3.02%	0.00%	0.00%	8.04%
6053.07	0.00%	0.50%	1.25%	4.00%	0.00%	0.00%	2.25%
6070.04	0.00%	0.25%	1.00%	1.50%	0.00%	0.25%	4.50%
6078.01	0.00%	0.50%	2.01%	1.50%	0.00%	0.25%	0.50%
6089.07	0.00%	3.52%	2.51%	8.79%	0.00%	0.25%	4.77%
6096.03	0.00%	1.52%	1.52%	5.82%	0.00%	0.00%	3.04%
6100.08	0.00%	4.76%	2.51%	3.51%	0.00%	0.00%	3.76%
6119.06	0.00%	1.51%	0.75%	0.50%	0.00%	0.00%	4.52%
6124.07	0.00%	1.50%	0.00%	5.50%	0.00%	0.00%	1.75%
6133.97	0.00%	3.01%	3.76%	6.52%	0.00%	0.00%	5.76%
6151.02	0.00%	1.75%	1.75%	7.25%	0.00%	0.00%	3.25%
6178.08	0.00%	0.75%	0.00%	0.00%	0.00%	0.25%	1.50%
6200.09	0.00%	0.25%	0.50%	0.50%	0.00%	0.00%	9.02%
6220.13	0.00%	0.25%	2.00%	0.75%	0.00%	0.00%	5.00%
6222.99	0.00%	1.25%	2.50%	5.75%	0.00%	0.00%	6.25%
6230.08	0.00%	2.00%	1.00%	0.75%	0.00%	0.00%	3.50%
6249.99	0.00%	2.75%	0.00%	0.00%	0.00%	0.00%	6.00%
6251.09	0.00%	56.50%	1.00%	0.25%	0.00%	0.00%	7.00%
6285.02	0.00%	2.27%	1.77%	2.02%	0.00%	0.00%	2.78%

RSWC Lower Mt. Simon	Matrix			Porosity
				Intergranular
Depth	Illitic	Terrigenous	Clay lamina	Clay lined
5903.98	0.00%	0.25%	0.00%	5.75%
5907.99	0.00%	3.00%	0.00%	15.50%
5914.01	0.00%	0.50%	0.00%	23.25%
5918.97	0.00%	2.50%	0.00%	17.00%
5925.05	0.00%	2.25%	0.00%	16.75%
5950.49	0.00%	1.75%	0.00%	7.00%
5965.07	0.00%	1.50%	0.00%	20.05%
5965.33	0.00%	3.00%	0.00%	5.50%
5972.38	0.00%	0.00%	0.00%	6.99%
5979.03	0.00%	0.00%	0.00%	7.21%
5982.39	0.00%	0.00%	0.00%	16.46%
5990.03	0.00%	0.00%	0.00%	16.50%
5995.10	0.00%	0.00%	0.00%	17.75%
6000.08	0.00%	0.00%	0.00%	24.25%
6003.08	0.00%	0.00%	0.00%	15.38%
6008.03	0.00%	0.00%	0.00%	20.80%
6035.99	0.00%	0.00%	0.00%	29.00%
6050.00	0.00%	0.00%	0.00%	11.56%
6053.07	0.00%	0.00%	0.00%	15.50%
6070.04	0.00%	0.00%	0.00%	15.00%
6078.01	0.00%	0.00%	0.00%	17.29%
6089.07	0.00%	0.00%	0.00%	20.85%
6096.03	0.00%	0.00%	0.00%	20.76%
6100.08	0.00%	0.00%	0.00%	19.30%
6119.06	0.00%	0.00%	0.00%	22.36%
6124.07	0.00%	0.00%	0.00%	22.50%
6133.97	0.00%	0.00%	0.00%	10.03%
6151.02	0.25%	0.00%	0.00%	14.00%
6178.08	0.00%	1.50%	0.00%	12.22%
6200.09	2.01%	0.00%	0.00%	13.53%
6220.13	0.00%	0.00%	0.00%	23.75%
6222.99	0.50%	0.00%	0.00%	14.50%
6230.08	0.00%	0.25%	0.00%	15.25%
6249.99	0.00%	0.00%	0.00%	29.75%
6251.09	0.00%	0.00%	0.00%	0.25%
6285.02	0.00%	0.00%	0.00%	26.26%

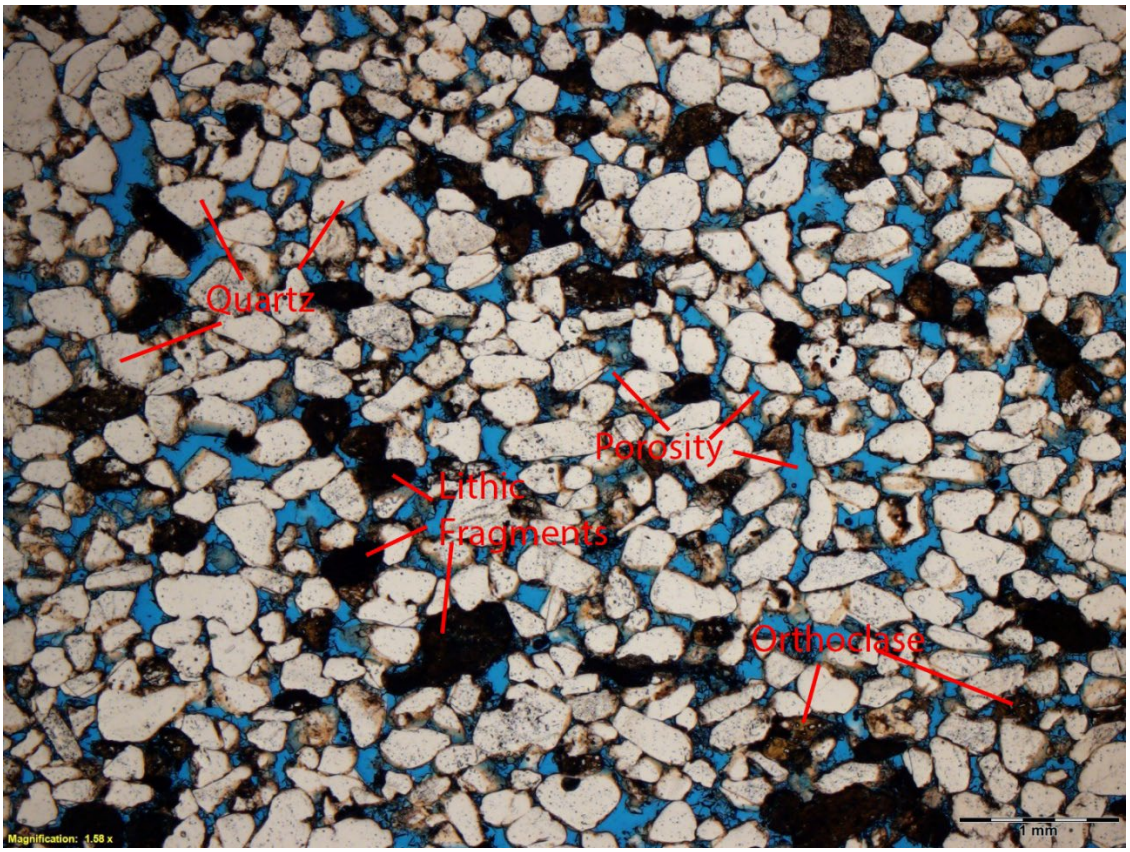

Figure 9. Thin section photomicrograph of the Lower Mt. Simon Sandstone at depth of 6,008.03 ft. Note the abundant intergranular pore space with well-connected pore throats. Most pore space is lined with clay.

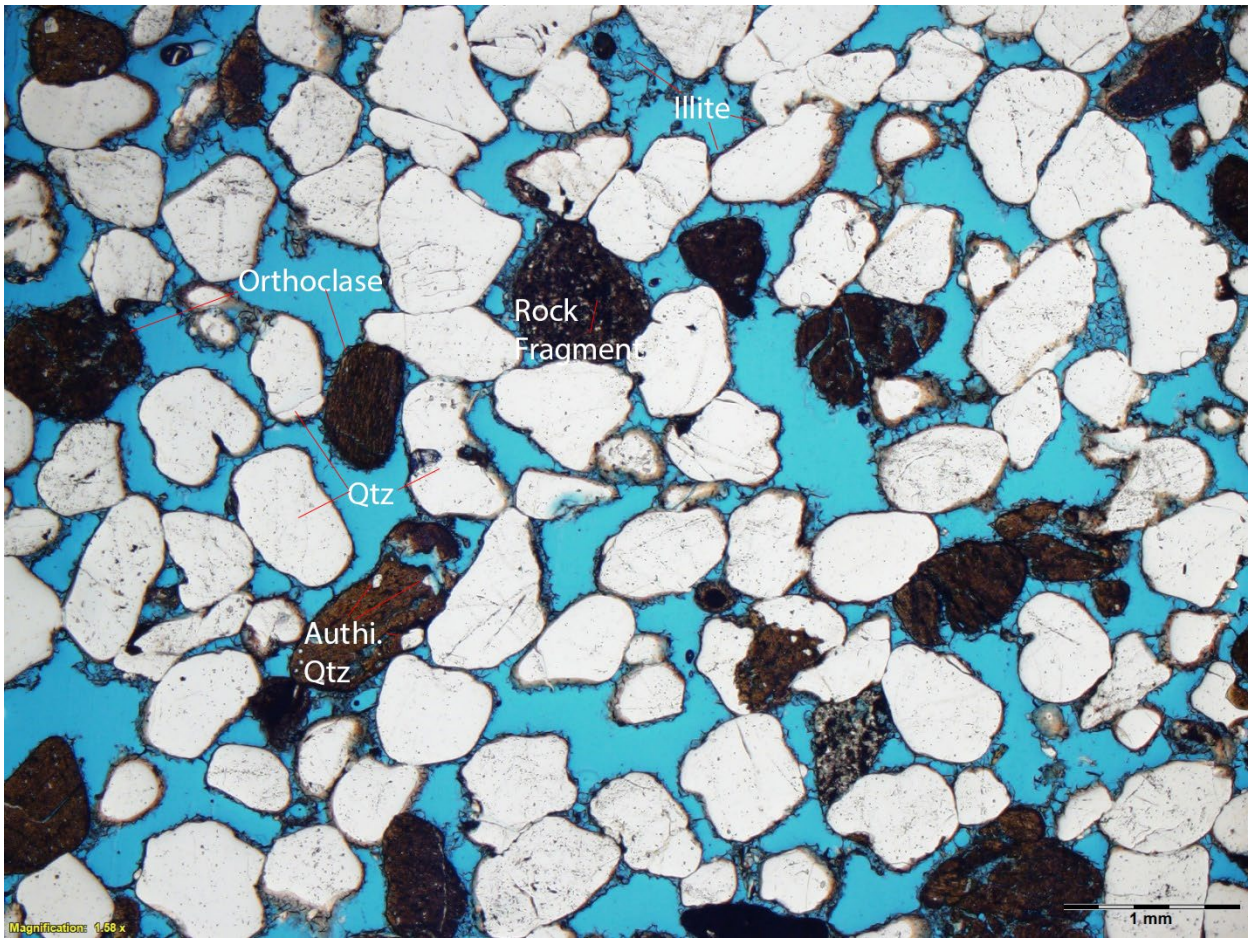

Figure 10. Thin section photomicrograph of the Lower Mt. Simon Sandstone at depth of 6,124.07 ft. Note the pore and grain lining illite and the spherical pore shape, implying possible complete grain dissolution porosity. Numerous curved illite bridges also imply secondary porosity from complete grain dissolution.

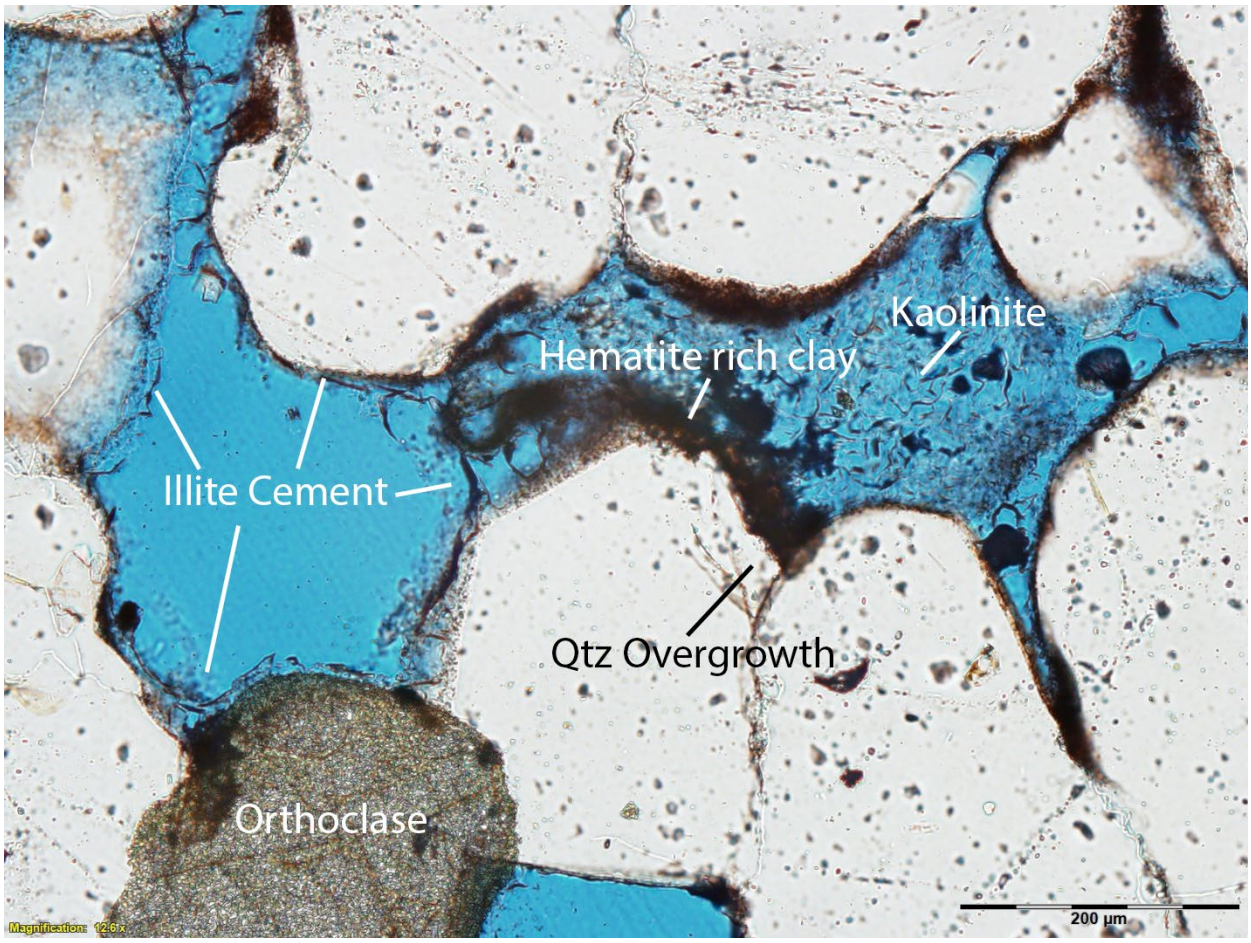

Figure 11. Thin section photomicrograph of the Lower Mt. Simon Sandstone at depth of 6,222.99 ft. Pore-lining clays in the outline of the grain boundary imply secondary porosity from grain dissolution. Illite and kaolinite in pore space may be the result of grain replacement/alteration.

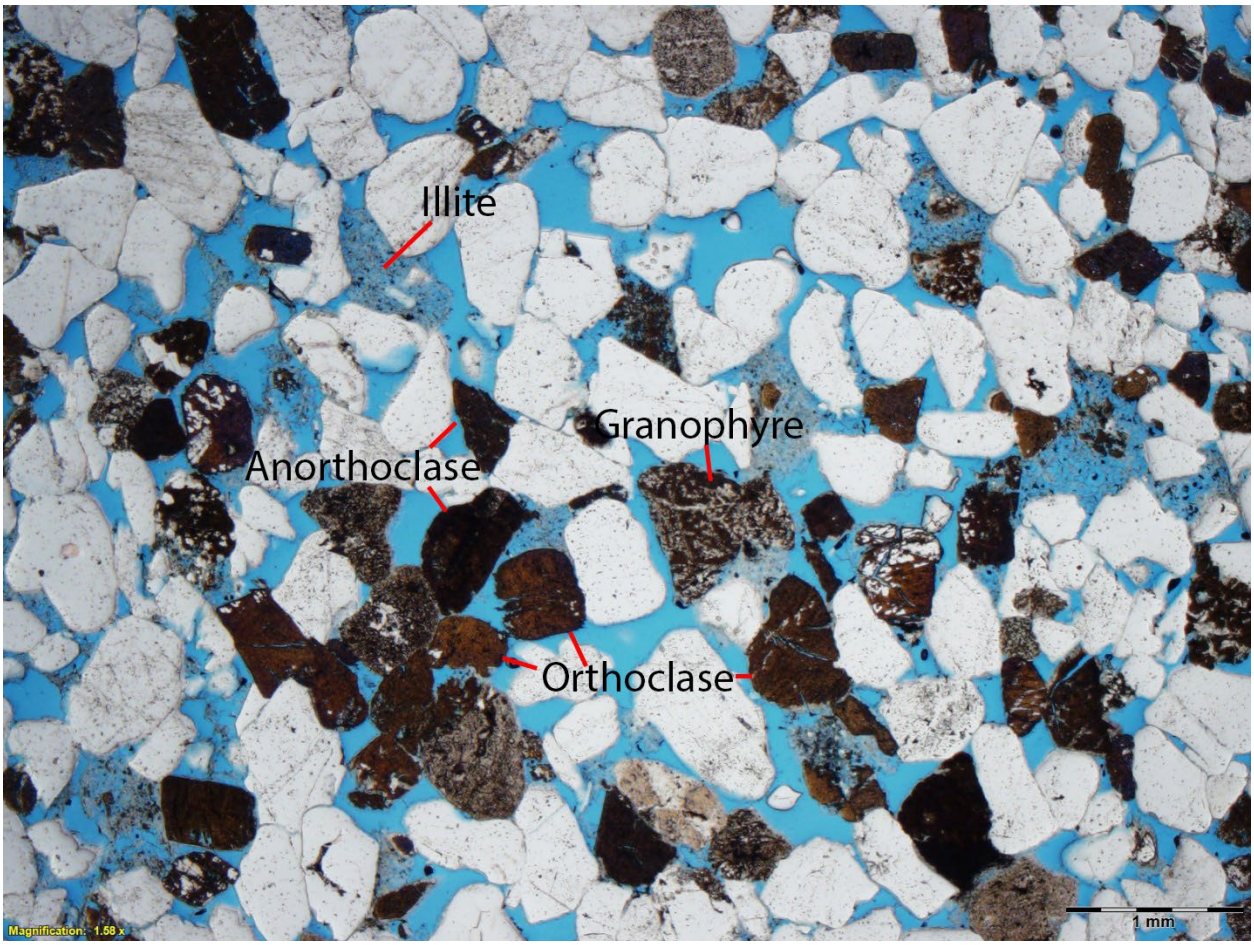

Figure 12. Thin section photomicrograph of the Lower Mt. Simon Sandstone at depth of 6,249.99 ft. Note the abundant lithics (rhyolite/granite or granophyre). Clay occurs as both pore filling and grain replacement.

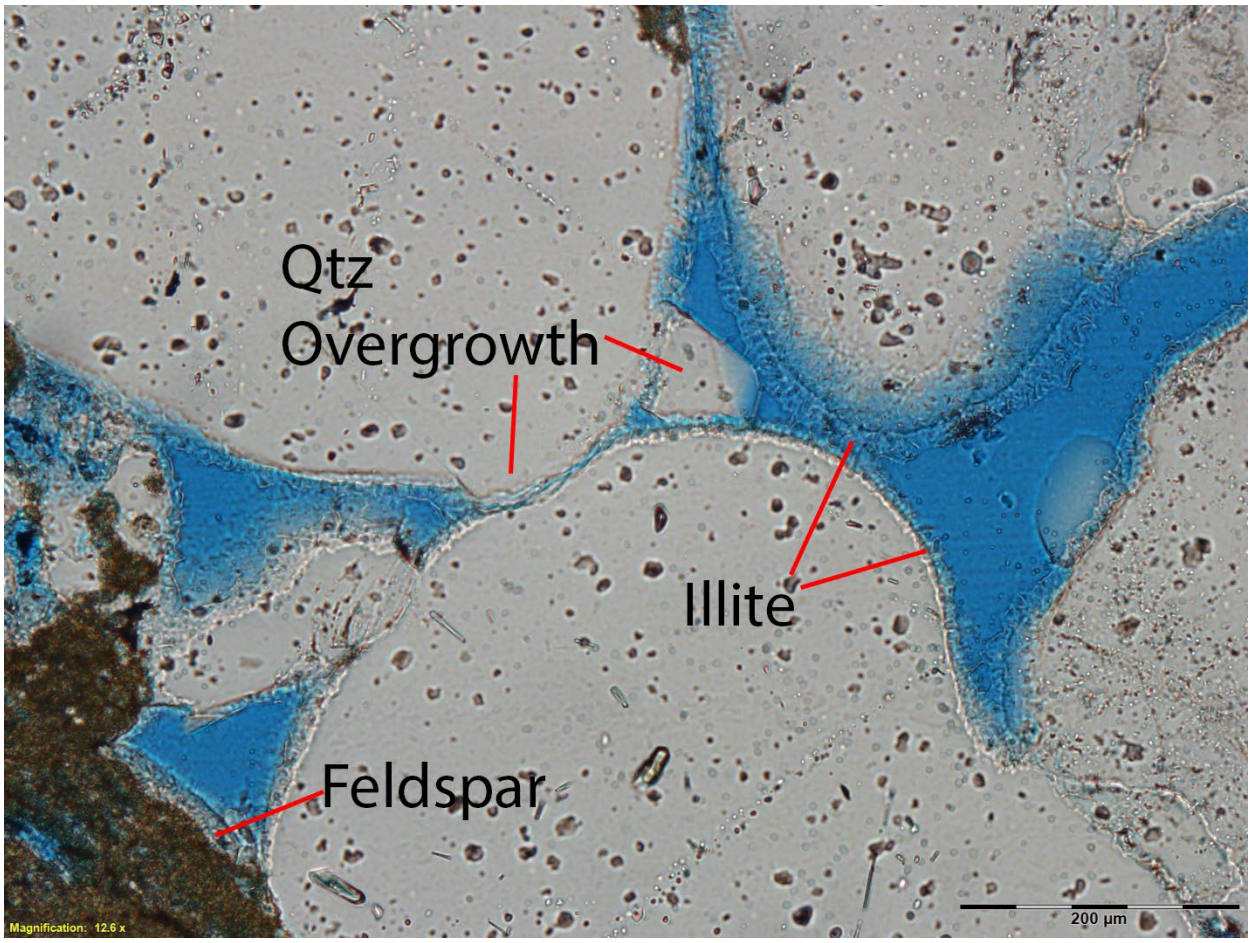

Figure 13. Thin section photomicrograph of the Lower Mt. Simon Sandstone at depth of 6,249.99 ft. Abundant illite grain coating prevents pervasive authigenic quartz overgrowths.

Figure 14. SEM photomicrograph of the Lower Mt. Simon Sandstone at depth of 6,249.99 ft. Abundant hairy illite lines grains, preventing pervasive authigenic quartz nucleation. Authigenic quartz is localized on small openings to the quartz grain surface between hairy illite.

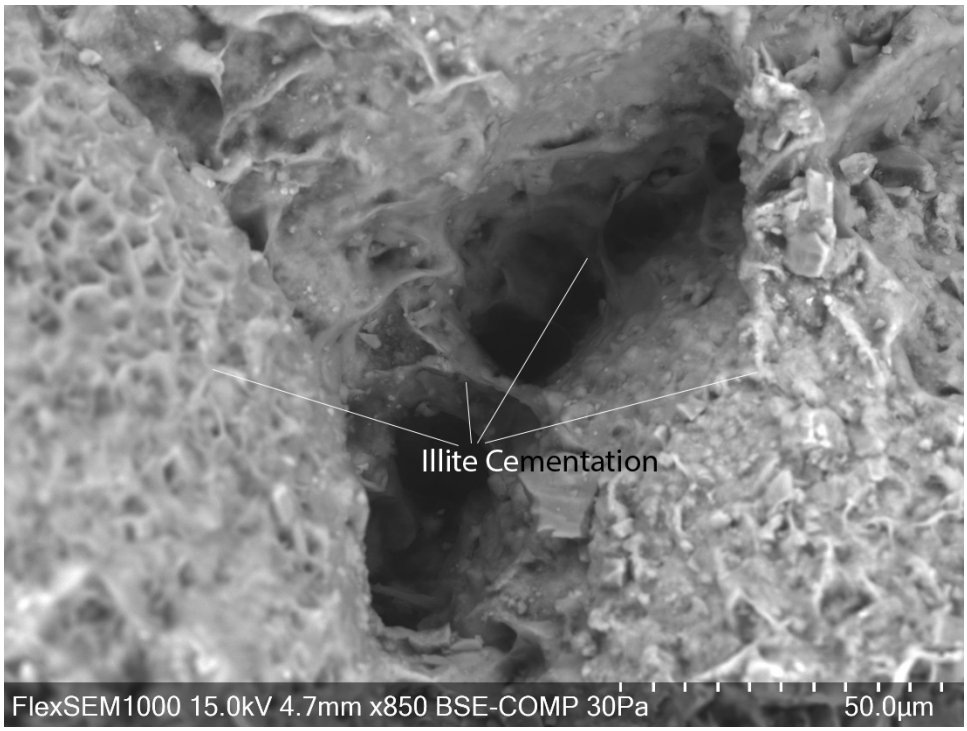

Figure 15. SEM photomicrograph of the Lower Mt. Simon Sandstone at depth of 6,285.70 ft. Clays often form pore bridges between grains.

Table 4. Lower Mt. Simon full diameter sample analysis of sorting ranking, average grain size, initial porosity, intergranular volume (IGV), compaction porosity loss (COPL), cementation porosity loss (CEPL), and index of compaction, all based on methodology from Freiburg et al. (2016).

Sample	Sorting	Grain Size	Initial Porosity (Pi)	IGV	Cement Volume(C)	COPL	CEPL	Index of Compaction
6243.2	3	Um	38.1	29.5	5.5	12.19858156	4.829078014	0.716398017
6247.4	4	Um	34.2	30	6	6	5.64	0.515463918
6252.3	4	Um	34.2	28	3.75	8.611111111	3.427083333	0.715315835
6255.5	4	Lm	34.9	27.75	4.75	9.896193772	4.279930796	0.698088799
6258	3	Um	38.1	29.75	4.25	11.886121	3.744839858	0.760421647
6260.8	5	Um	31.5	29.75	5.25	2.491103203	5.119217082	0.327332242
6262.58	5	Lm	31.3	29.25	6	2.897526502	5.82614841	0.332145172
6267.17	5	Um	31.5	30.75	3.75	1.083032491	3.709386282	0.225988701
6268.56	4	Um	34.2	30.75	3.5	4.981949458	3.325631769	0.59968712
6270.46	5	Uf	30.4	20.5	5.75	12.45283019	5.033962264	0.712127751
6274.8	4	Lm	34.9	30.75	3	5.992779783	2.820216606	0.679993446
6276	4	Uf	33.9	21.5	4.25	15.79617834	3.57866242	0.815293325
6279.25	4	Um	34.2	30	2	6	1.88	0.76142132
6282.96	5	Lm	31.3	28.75	3.5	3.578947368	3.374736842	0.514683621
6287.27	5	Um	31.5	25	0.75	8.666666667	0.685	0.926751025
6290.4	4	Lm	34.9	19.75	3.5	18.87850467	2.839252336	0.869265858
6293.28	4	Um	34.2	29.25	4.75	6.996466431	4.417667845	0.612965141
6294.6	5	Lc	29.8	4.75	0.5	26.2992126	0.368503937	0.986181646
6294.8	5	Um	31.5	6	2.25	27.12765957	1.63962766	0.943003744
6295.5	5	Lc	29.8	27	9.75	3.835616438	9.376027397	0.290320908

Legend for colors
Green: Controlled by compaction
Yellow: Equal amount of effect from compaction and cementation
Red: Controlled by cementation

Argenta

Table 5. (From top to bottom) Petrographic point count analysis from thin sections prepared from rotary sidewall cores cut in the Lower Mt. Simon Sandstone, including detrital grains, authigenic cements, and matrix/porosity analysis.

RSWC	Detrital								
Argenta			Lithics		Feldspar			Quartz	
Depth	Glauconite	Dolomite2	Granitic	Rhyolite	Anorthite	Orthoclase	Plagioclase	Monocrystalline	Polycrystalline
6303.07	0.00%	0.00%	0.00%	0.00%	22.00%	7.50%	0.00%	39.50%	0.75%
6307.17	0.00%	0.00%	0.75%	12.75%	2.25%	1.25%	0.50%	33.25%	0.75%
6309.02	0.00%	0.00%	0.00%	0.00%	10.30%	2.76%	0.00%	38.94%	24.87%
6313.07	0.00%	0.00%	3.01%	4.01%	0.50%	0.50%	1.00%	47.37%	11.53%
6314.95	0.00%	0.00%	0.00%	0.00%	4.50%	1.25%	0.00%	68.50%	4.00%
6318.00	0.00%	0.00%	1.50%	10.00%	3.75%	2.00%	0.00%	42.00%	5.75%
6320.07	0.00%	0.00%	0.00%	0.00%	4.50%	1.50%	0.00%	63.75%	2.00%
6325.03	0.00%	0.00%	1.75%	6.25%	0.00%	0.75%	0.25%	53.50%	0.50%
6327.92	0.00%	0.00%	0.75%	0.00%	1.00%	1.50%	0.00%	65.16%	4.01%
6339.01	0.00%	0.00%	3.75%	14.25%	2.00%	3.00%	0.00%	46.50%	0.50%
6341.93	0.00%	0.00%	0.50%	0.00%	16.62%	2.77%	0.00%	46.85%	0.00%
6350.07	0.00%	0.00%	0.00%	0.00%	0.00%	1.00%	0.00%	9.50%	0.00%
6359.98	0.00%	0.00%	0.00%	0.00%	0.00%	3.00%	0.00%	2.50%	32.75%

RSWC	Authigenic Mineral						
Argenta		Illite					
Depth	Dolomite	Pore Filling	Grain Lining w/ quartz	Grain Lining	Iron rich	Kaolinite	Quartz
6303.07	0.00%	3.75%	0.00%	0.00%	0.00%	0.00%	9.25%
6307.17	0.00%	9.75%	1.50%	0.50%	0.00%	0.00%	9.75%
6309.02	0.00%	10.30%	0.00%	0.00%	0.00%	0.00%	7.54%
6313.07	0.00%	8.77%	0.00%	0.25%	0.00%	0.00%	3.51%
6314.95	0.00%	12.75%	0.00%	0.00%	0.00%	0.00%	3.25%
6318.00	0.00%	5.75%	0.00%	0.00%	0.00%	0.00%	10.00%
6320.07	0.00%	1.25%	0.00%	0.00%	0.00%	0.00%	17.75%
6325.03	0.00%	7.00%	0.00%	0.00%	0.00%	0.00%	22.00%
6327.92	0.00%	22.31%	0.00%	0.00%	0.00%	0.00%	4.76%
6339.01	0.00%	21.50%	0.00%	0.00%	0.00%	0.00%	8.50%
6341.93	0.00%	5.54%	0.00%	0.00%	0.00%	0.00%	10.08%
6350.07	0.00%	87.50%	0.00%	0.00%	0.00%	0.00%	2.00%
6359.98	0.00%	61.00%	0.00%	0.00%	0.00%	0.00%	0.75%

RSWC Argenta Depth	Matrix			Porosity Intergranular
	Illitic	Terrigenous	Clay lamina	Clay lined
6303.07	0.00%	0.00%	0.00%	17.25%
6307.17	4.25%	0.00%	17.50%	5.25%
6309.02	0.00%	0.00%	0.00%	5.28%
6313.07	0.75%	0.00%	0.00%	18.80%
6314.95	0.00%	0.00%	0.00%	5.75%
6318.00	0.00%	0.00%	0.00%	19.25%
6320.07	0.00%	0.00%	0.00%	9.25%
6325.03	0.00%	0.00%	0.00%	8.00%
6327.92	0.00%	0.00%	0.00%	0.50%
6339.01	0.00%	0.00%	0.00%	0.00%
6341.93	0.00%	0.00%	0.00%	17.63%
6350.07	0.00%	0.00%	0.00%	0.00%
6359.98	0.00%	0.00%	0.00%	0.00%

XRD Analysis

Table 6. (From top to bottom) XRD bulk mineralogy and clay mineral results from rotary sidewall core samples.

	Results: Semi-Quantitative X-Ray Powder Diffraction Analysis, MBP									
	Bulk mineral data									
Depth	%clay	%Quartz	%K-feldsp	%P-feldsp	%Calcite	%Dolomit	%Siderite	rite/Marc	%Magneti	Total %
5000.05	4%	47%	22%	2%	1%	11%	6%	1%	4%	100%
5118.97	5%	52%	23%	2%	3%	3%	8%	1%	4%	100%
5172.97	2%	93%	2%	1%	0%	0%	1%	0%	0%	100%
5200.01	3%	93%	1%	2%	0%	0%	0%	1%	0%	100%
5275.03	2%	92%	3%	1%	0%	0%	1%	0%	0%	100%
5325.03	2%	94%	1%	1%	0%	0%	1%	1%	0%	100%
5374.99	2%	95%	1%	1%	0%	0%	1%	0%	0%	100%
5450.05	2%	95%	1%	1%	0%	0%	0%	0%	0%	100%
5559.97	2%	93%	1%	1%	0%	0%	1%	1%	1%	100%
5650.12	3%	87%	6%	1%	0%	1%	1%	1%	1%	100%
5750.11	3%	81%	10%	1%	1%	1%	1%	0%	2%	100%
5850.08	3%	83%	8%	1%	1%	1%	2%	1%	1%	100%
5907.99	3%	82%	8%	1%	1%	1%	1%	1%	2%	100%
5925.05	3%	90%	3%	1%	0%	1%	1%	0%	1%	100%
5979.03	3%	87%	6%	1%	0%	0%	0%	1%	1%	100%
5990.03	3%	86%	6%	1%	1%	1%	2%	1%	1%	100%
6000.08	3%	89%	5%	1%	0%	0%	1%	0%	1%	100%
6008.03	3%	88%	5%	1%	0%	1%	1%	1%	1%	100%
6050.00	2%	84%	8%	1%	0%	1%	1%	1%	2%	100%
6070.05	3%	83%	9%	1%	1%	1%	1%	1%	1%	100%
6089.07	3%	85%	7%	1%	1%	1%	2%	1%	1%	100%
6100.08	3%	84%	7%	1%	0%	1%	1%	1%	2%	100%
6124.07	2%	82%	9%	0%	1%	1%	2%	1%	2%	100%
6151.02	3%	86%	7%	1%	1%	1%	1%	1%	1%	100%
6200.09	2%	81%	11%	1%	0%	1%	1%	0%	2%	100%
6230.08	3%	81%	9%	1%	1%	1%	1%	1%	2%	100%
6285.02	3%	81%	10%	1%	1%	1%	2%	1%	1%	100%
6303.07	4%	71%	17%	1%	1%	1%	2%	1%	3%	100%
6314.95	3%	87%	5%	1%	0%	1%	1%	1%	1%	100%
6318.00	3%	80%	10%	1%	1%	1%	2%	1%	2%	100%
6325.03	3%	88%	4%	1%	0%	1%	2%	1%	1%	100%
6341.93	3%	72%	15%	1%	1%	1%	3%	2%	2%	100%
6359.98	9%	63%	7%	1%	1%	2%	4%	9%	3%	100%
6375.08	9%	38%	22%	2%	3%	3%	10%	11%	3%	100%
6390.11	7%	31%	14%	25%	2%	2%	8%	6%	5%	100%
6416.02	7%	32%	17%	24%	2%	2%	6%	4%	6%	100%
6424.22	5%	30%	19%	25%	1%	3%	5%	6%	8%	100%
6445.01	7%	31%	16%	27%	3%	3%	5%	4%	6%	100%

Depth	Results: Semi-Quantitative X-Ray Powder Diffraction Analysis, < 2 CLAY					
	Clay mineral percentages					
	%Smectite	%Illite	%Kaolinite	%Chlorite	%Corrensite	Total %
5000.05	3%	39%	15%	44%		100%
5118.97	3%	79%	6%	12%		100%
5172.97	31%	58%	4%	7%		100%
5200.01	25%	63%	4%	7%		100%
5275.03	14%	62%	8%	15%		100%
5325.03	8%	84%	4%	4%		100%
5374.99	11%	50%	16%	23%		100%
5450.05	6%	52%	36%	6%		100%
5559.97	5%	16%	75%	4%		100%
5650.12	1%	56%	42%	1%		100%
5750.11	2%	96%	1%	0%		100%
5850.08	2%	91%	6%	1%		100%
5907.99	1%	62%	30%	7%		100%
5925.05	3%	92%	5%	1%		100%
5979.03	2%	86%	9%	3%		100%
5990.03	2%	80%	18%	1%		100%
6000.08	8%	75%	16%	1%		100%
6008.03	3%	79%	16%	2%		100%
6050.00	4%	85%	9%	2%		100%
6070.05	3%	86%	7%	4%		100%
6089.07	29%	65%	3%	3%		100%
6100.08	6%	93%	1%	0%		100%
6124.07	12%	87%	0%	0%		100%
6151.02	6%	93%	0%	0%		100%
6200.09	5%	92%	1%	2%		100%
6230.08	4%	93%	2%	1%		100%
6285.02	17%	81%	1%	1%		100%
6303.07	1%	97%	2%	0%		100%
6314.95	3%	94%	2%	1%		100%
6318.00	2%	96%	1%	1%		100%
6325.03	9%	85%	3%	2%		100%
6341.93	2%	77%	16%	5%		100%
6359.98	2%	48%	42%	8%		100%
6375.08	2%	97%	1%	0%		100%
6390.11	11%	46%	24%	19%		100%
6416.02	4%	21%	9%	41%	24%	100%
6424.22	6%	7%	12%	6%	69%	100%
6445.01	7%	34%	12%	46%		100%

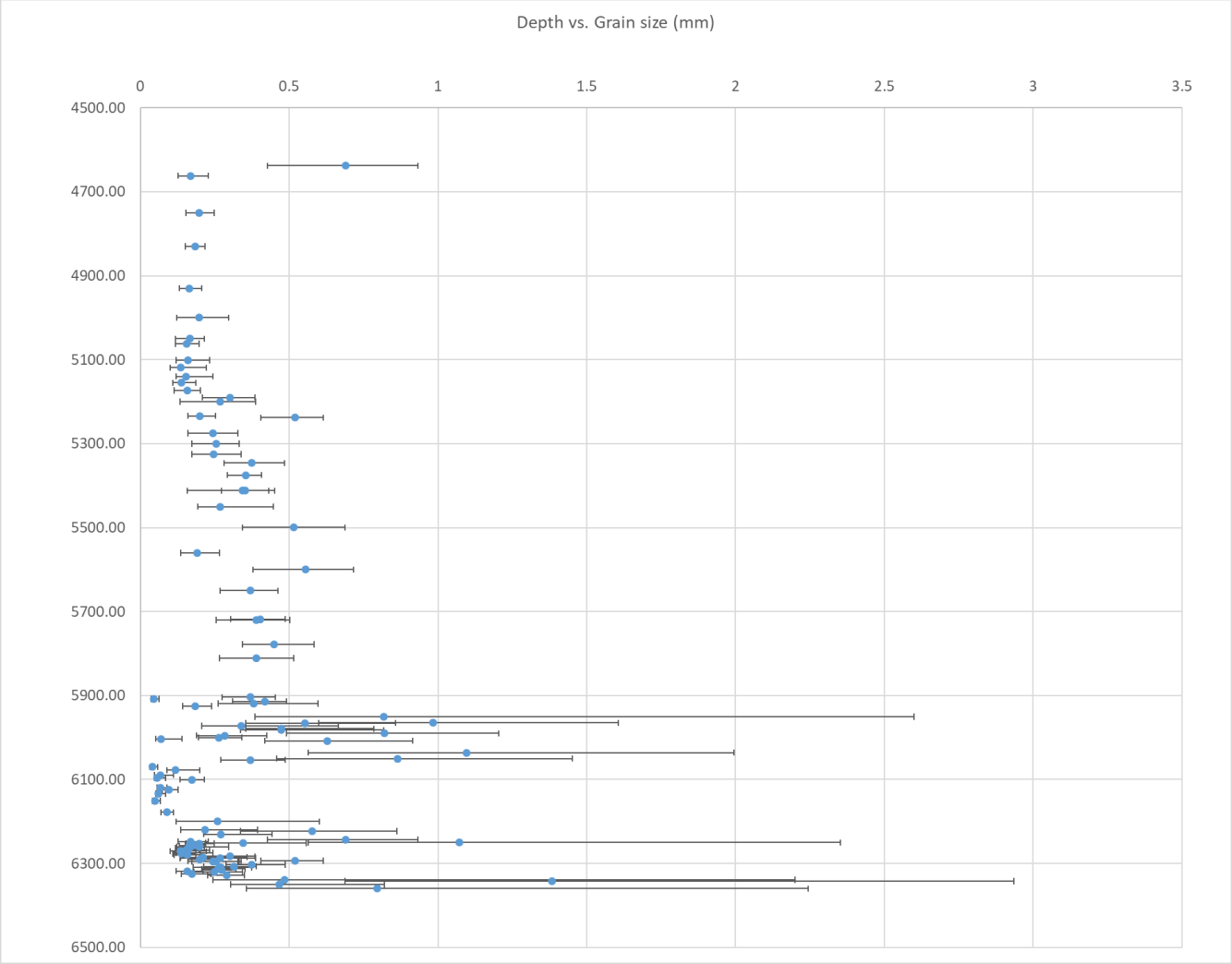

Figure 16. Graph of textural data with the average grain size (blue points) and range of grain size.

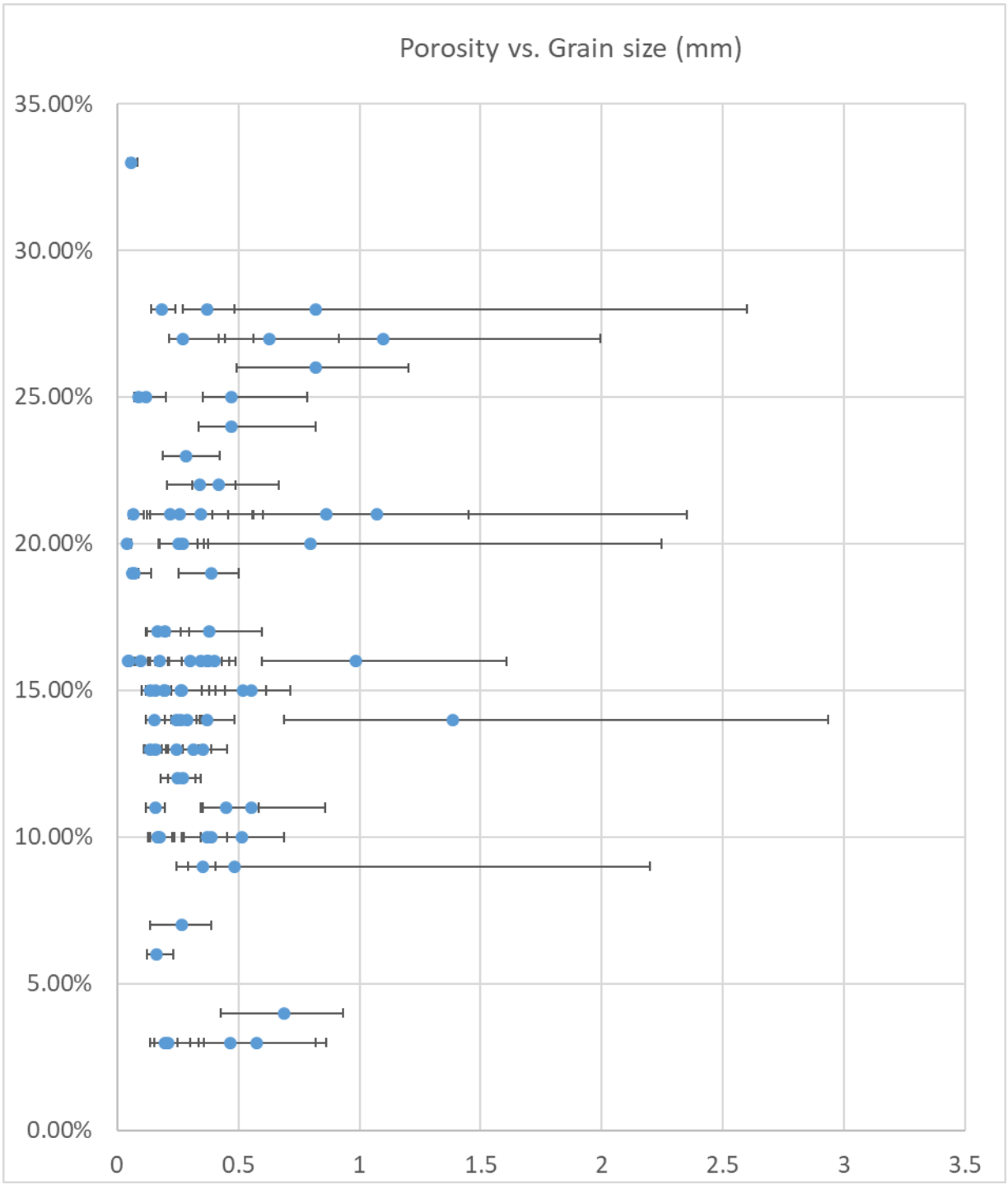

Figure 17. Graph showing porosity and grain size (average and range). Note there is little correlation between grain size and total porosity.

Routine Analysis

Rotary Sidewall Core Analysis

Depth	Porosity	Confining_Press_psig	Kgas_mD	Avg_Single_point_empirical_KL_mD	KL_Count	Multi_points_KL_mD	Water_Extracted; Comment
4450.13	4.00%	300	0.032	0.02	1		0 mL, scoring marks
4510.08	3.00%	300	0.036	0.02	1		0 mL
4520.13	13.00%	300	16.284	12.93	6	15.04	0.5 mL
4560.03	9.00%	300	73.984	56.65	2	0.00	0 mL, one face of the sample is not squared off
4597.95	15.00%	300	51.346	44.64	6	47.01	0.9 mL
4626.05	2.00%	300	0.591	0.39	1		0 mL
4638.12	4.00%	300	2.904	2.08	1		0.3 mL
4661.98	10.00%	300	3.951	2.67	6	3.60	0 mL
4750.01	3.00%	300	0.01	0.01	1		0.05 mL
5000.05	17.00%	300	1.246	0.86	1		1 mL
5049.87	17.00%	300	19.968	15.98	6	15.26	1.2 mL
5062.05	11.00%	300	85.536	74.31	6	82.51	0 mL, sample is chipped
5100.92	6.00%	300	0.592	0.39	1		0.1 mL
5118.97	15.00%	300	8.096	5.95	6	7.15	0 mL, sample is chipped
5140.02	14.00%	300	6.582	4.73	6	5.00	0 mL
5155.04	13.00%	300	160.333	146.52	6	153.37	0.5 mL
5172.97	13.00%	300	180.567	165.09	6	173.33	1.1 mL
5190.04	16.00%	300	658.816	624.67	6	649.48	0.8 mL, plug is chipped
5200.01	7.00%	300	10.295	7.84	6	9.80	0 mL
5234.05	15.00%	300	509.075	482.54	6	493.58	1.05 mL
5238.06	15.00%	300	1019.02	982.48	6	954.64	1 mL
5275.03	14.00%	300	186.436	170.84	6	178.33	1.05 mL
5299.98	20.00%	300	772.141	739.41	6	749.75	1 mL
5325.03	13.00%	300	3.57	2.54	6	3.03	NA
5346.09	14.00%	300	223.689	185.68	6	182.05	.3 mL
5374.99	9.00%	300	2.864	1.98	1		.1 mL
5412.07	16.00%	300	1.573	1.10	1		0.6 mL
5450.05	13.00%	300	10.365	7.88	6	9.52	0 mL
5559.97	15.00%	300	48.724	41.63	6	45.52	.5 mL
5599.99	10.00%	300	32.482	26.97	6	27.52	0.4 mL
5650.12	15.00%	300	0.894	0.60	1		.5 mL
5718.08	15.00%	300	2.64	1.83	1		0 mL, Fracture Potential, plane of weakness
5720.11	16.00%	300	2.137	1.49	1		.9 mL
5811.11	16.00%	300	3.778	2.61	6	2.82	.1 mL
5850.08	19.00%	300	0.603	0.40	1		1.2 mL
5899.98	11.00%	300	0.444	0.29	1		0 mL, sample is chipped
5903.98	10.00%				0	0.00	NA
5903.98		300	5.065	3.74	6	4.38	NA
5907.99	16.00%	300	5.252	3.24	6	1.72	.65 mL
5914.01	22.00%	300	1.885	1.33	1		2 mL, Already broken, more cracks visible
5925.05	17.00%	300	0.513	0.34	1		.8 mL
5950.49	28.00%	300	20.539	13.09	6	11.79	0.05 mL
5965.33	28.00%	300	6.849	4.68	6	2.41	0.3 mL
5972.38	16.00%	300	1.453	1.01	1		1 mL
5979.03	11.00%	300	0.09	0.05	1		.3 mL
5990.03	22.00%	300	4.118	2.87	6	3.01	2 mL, VERTICALLY CRACKED

Depth	Porosity	Confining_Press_psig	Kgas_mD	Avg_Single_point_empirical_KL_mD	KL_Count	Multi_points_KL_mD	Water_Extracted; Comment
6000.08	25.00%	300	87.408	76.12	6	56.05	1.65 mL
6003.08	24.00%	300	13.969	10.66	6	10.48	0 mL, sample is chipped
6008.03	26.00%	300	14.207	10.85	6	14.14	1.9 mL
6035.99	23.00%	300	208.221	189.22	6	191.16	.25 mL
6050	14.00%	300	2.166	1.52	1		1.15 mL
6053.07	19.00%	300	2.417	1.60	1		.2 mL
6070.04	27.00%	300	17.356	12.94	6	7.20	1.8 mL
6070.04	27.00%	300	9.645	7.10	6	4.46	1.8 mL
6078.01	21.00%	300	48.09	40.85	6	38.08	0 mL
6089.07	28.00%	300	242.039	218.26	6	198.28	2.3 mL
6096.03	20.00%	300	4.995	3.26	6	1.08	.9 mL
6100.08	25.00%	300	239.684	212.96	6	195.92	3.0 mL
6119.06	21.00%	300	23.47	14.35	6	14.98	1.4 mL
6124.07	33.00%	300	270.823	243.21	6	229.67	2.6 mL
6133.97	16.00%	300	0.398	0.26	1		1 mL
6151.02	19.00%	300	50.773	42.58	6	17.31	2 mL
6178.08	16.00%	300	8.939	2.77	6	2.43	.9 mL
6200.09	19.00%	300	522.2	478.22	6	472.58	1.9 mL
6220.13	16.00%	300	11.333	8.58	6	8.98	1.6 mL
6222.99	25.00%				0		1.1 Ml, bulk volume may be inaccurate, end is chipped
6230.08	21.00%	300	453.993	426.58	6	432.96	2 mL
6249.99	21.00%	300	47.643	40.52	6	37.38	2.3 mL
6251.09	3.00%	300	1.848	1.30	1		NA
6285.02	27.00%	300	1768.435	1237.87	6	1121.24	1.9 mL
6303.07	16.00%	300	0.798	0.54	1		.4 mL
6307.17	13.00%	300	0.106	0.06	1		0 mL
6309.02	20.00%	300	23.046	15.01	6	19.25	0 mL
6313.07	15.00%	300	2.175	1.42	1		0 mL
6314.95	12.00%	300	0.397	0.26	1		.35 mL
6318	15.00%	300	1.196	0.82	1		1 mL
6320.07	12.00%	300	3.439	2.44	1		.4 mL
6325.03	10.00%	300	0.319	0.20	1		.2 mL
6327.92	14.00%	300	0.45	0.29	1		0 mL
6339.01	9.00%	300	0.07	0.04	1		0 mL
6341.93	14.00%	300	1.424	0.99	1		1.1 mL
6350.07	3.00%	300	0.026	0.01	1		0 mL
6359.98	20.00%	300	0.446	0.25	6	0.21	.2 mL
6365.06	26.00%				0		.60 mL; visible vertical crack
6375.08	12.00%	300	0.019	0.01	1		0.05 mL
6380.11	16.00%	300	13.434	10.32	6	11.65	0 mL, sample is chipped
6390.11	1.00%	300	0.006	0.00	1		0 mL
6414.27	18.00%	300	1.404	0.97	1		0.1 mL
6415.06	9.00%	300	0.002	0.00	1		0 mL, one face of the sample is not squared off
6416.02	1.00%	300	0.004	0.00	1		0 mL
6419.96	10.00%	300	0.004	0.00	1		0 mL
6424.03	8.00%	300	0.011	0.01	1		0 mL, Chip on edge
6424.22	3.00%	300	0.005	0.00	1		0 mL
6438.96	1.00%	300	0.004	0.00	1		0 mL
6445.01	0.00%	300	0.005	0.00	1		0 mL

Table 7. Routine analysis of the rotary sidewall cores. Analysis was completed at the Illinois State Geological Survey.

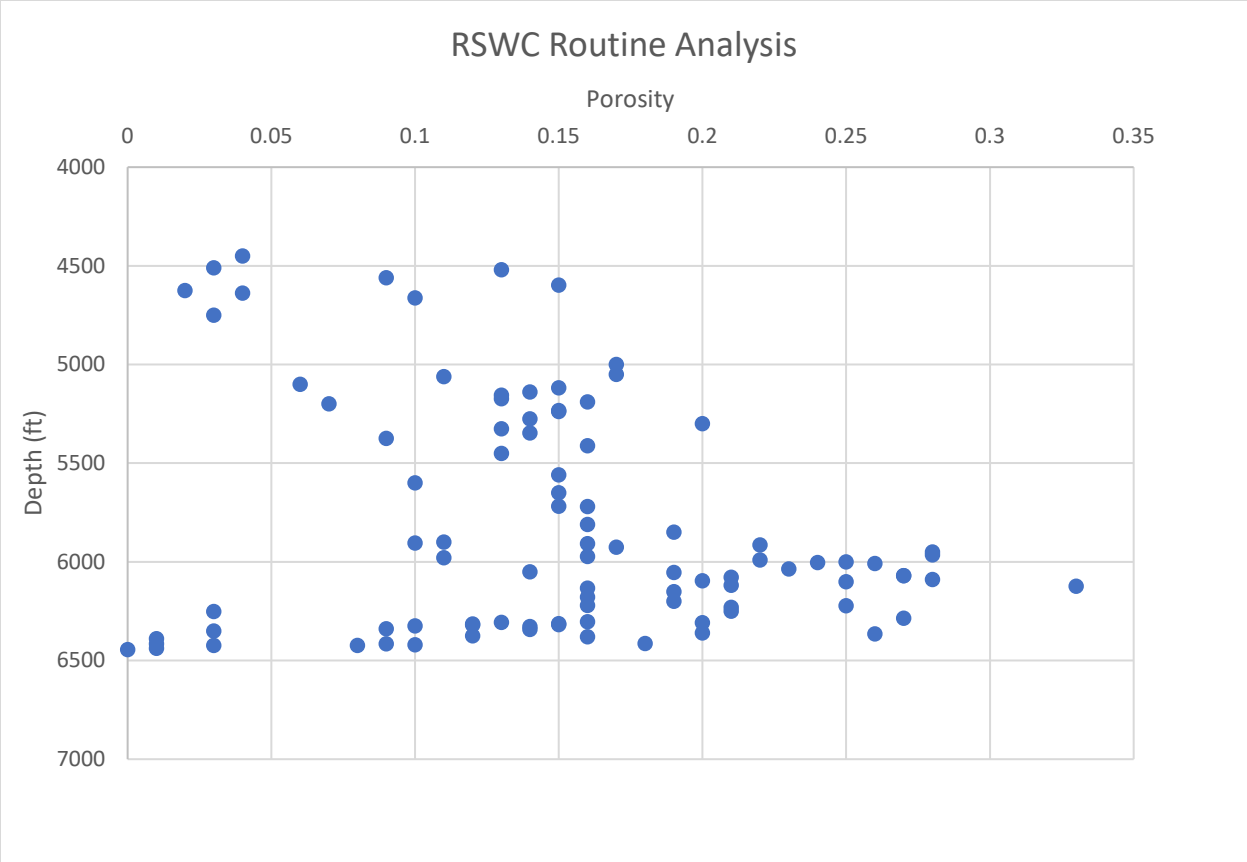

Figure 18. Graph of porosity and depth.

Whole Core Analysis

Top Depth (ft)	Bottom Depth (ft)	K_{MAX} Air (md)	$K_{MAX\ ESTIMATED}$ Klinkenberg (md)	K_{MIN} Air (md)	$K_{MIN\ ESTIMATED}$ Klinkenberg (md)	K_{VERT} Air (md)	$K_{VERT\ ESTIMATED}$ Klinkenberg (md)	POR (He) (% of BV)	GD (gm/cc)
6240	6241	802	771	802	771	446	424	21.8	2.63
6248	6249	6.95	5.60	5.70	4.44	2.10	1.48	16.0	2.63
6250	6251	1,370	1319	1,370	1319	578	554	25.0	2.64
6243	6244	1066	1050	998	962	341	312	22.2	2.64
6247	6248	1691	1617	1691	1617	284	265	22.9	2.65
6252	6253	786	760	762	722	408	396	22.7	2.64
6256	6256	728	714	706	652	217	200	21.5	2.65
6258	6258	933	893	933	893	614	580	23.2	2.67
6261	6261	2420	2389	2015	1925	182	174	23.6	2.64
6263	6263	1652	1565	1524	1442	98.8	87.6	24.4	2.64
6267	6268	3216	3175	3216	3175	416	386	24.7	2.65
6269	6269	4099	3953	3903	3822	1119	1089	23.9	2.65
6270	6271	117	106	87.8	79.1	9.05	7.35	19.4	2.65
6275	6275	5599	5532	4547	4439	561	534	24.7	2.64
6276	6276	285	270	205	191	32.4	27.2	20.9	2.64
6279	6280	4132	4042	4132	4042	3581	3488	25.1	2.64
6280	6280	3052	3015	2774	2694	2001	1966	24.5	2.63
6283	6283	4291	4108	4291	4108	1566	1535	22.3	2.64
6285	6286	4983	4873	4599	4402	2902	2815	22.0	2.64
6287	6288	2887	2837	2726	2616	464	444	22.0	2.65
6290	6291	112	105	99.4	89.9	9.26	7.35	19.8	2.65
6293	6294	685	365	364	337	80.2	71.3	20.2	2.65
6297	6298	6.8	5.42	6.21	4.76	0.604	0.361	13.8	2.64
6298	6299	11.4	9.4	9.91	8.03	1.05	0.714	14.5	2.64

Table 8. Full diameter (3 in) core analysis. Analysis was completed by CoreLAB.

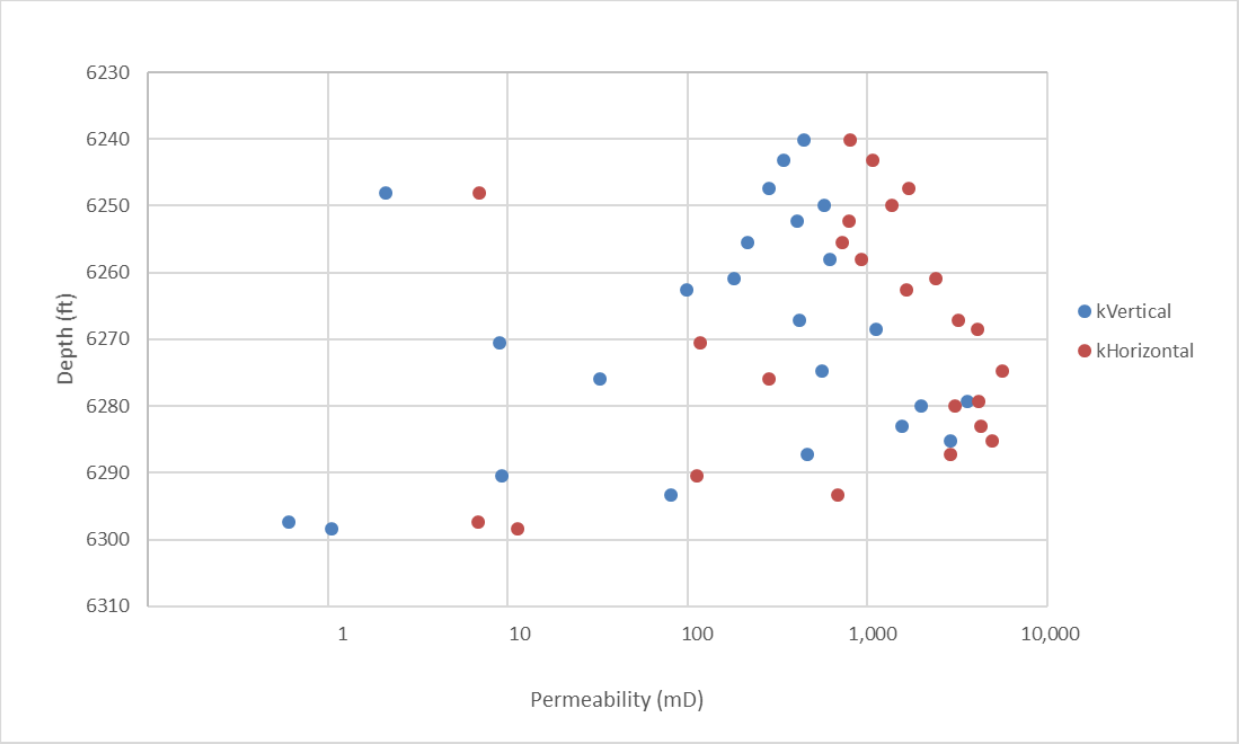

Figure 19. Graph of full diameter core permeability vs depth.

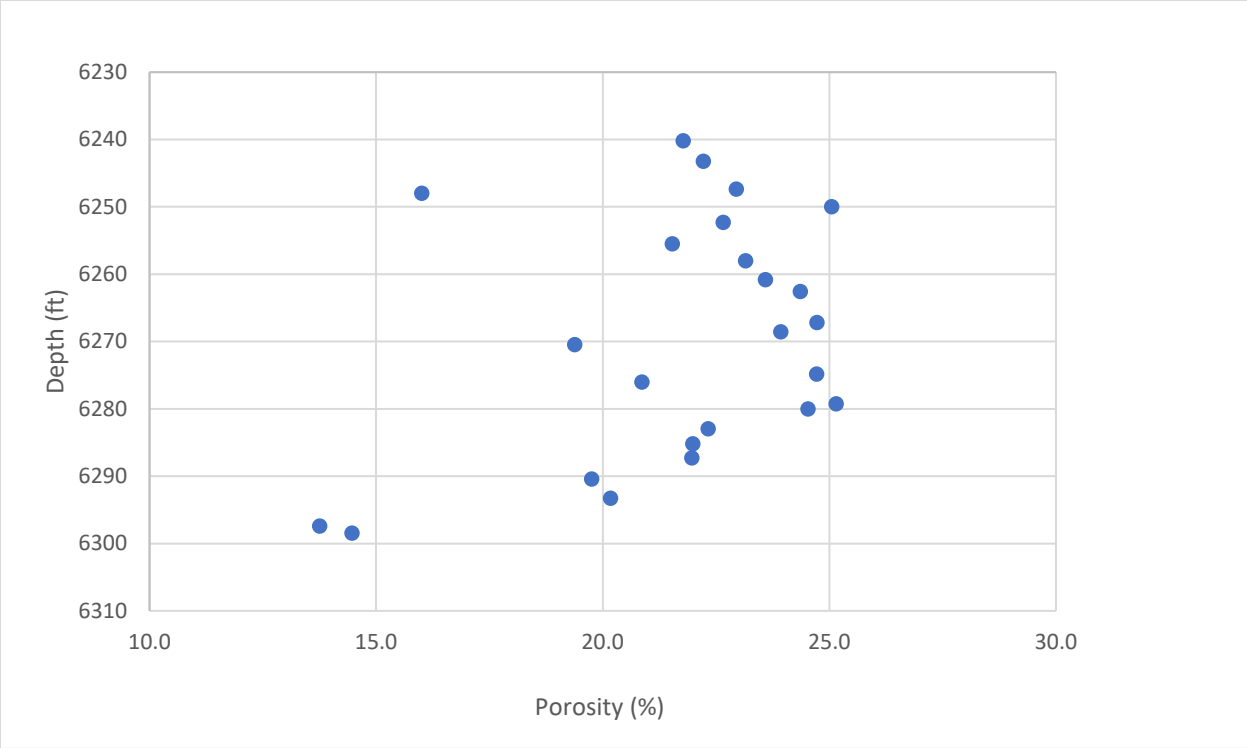

Figure 20. Graph of full diameter core porosity vs depth.

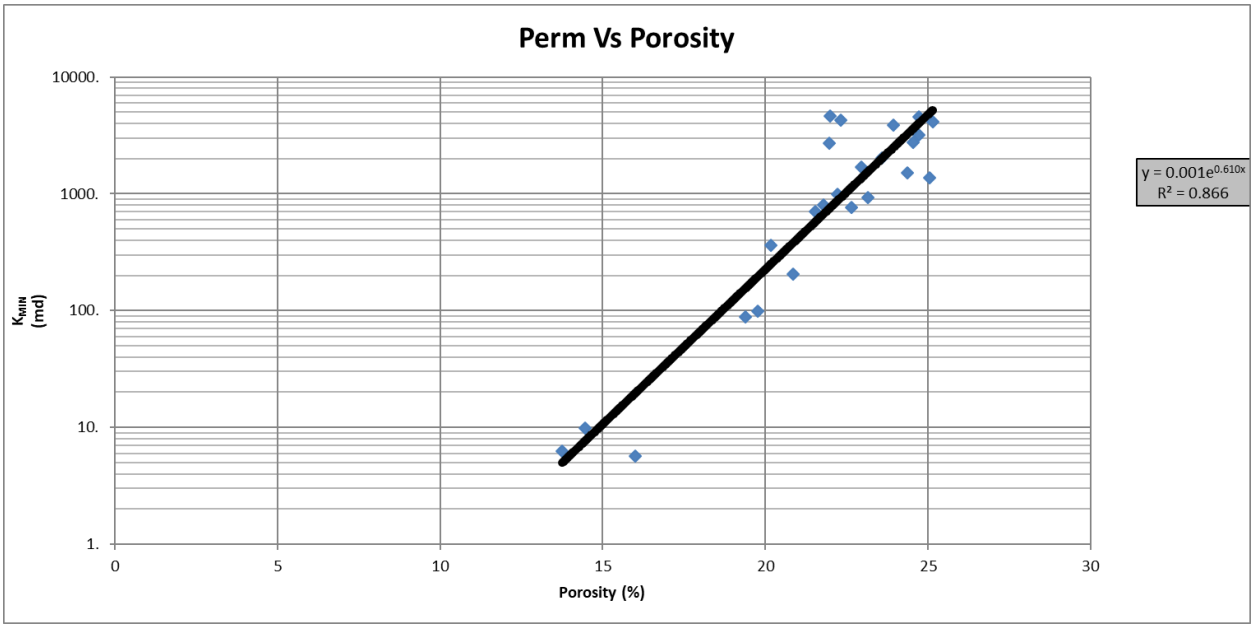

Figure 21. Graph of full diameter core porosity vs permeability.

Top Depth ft	Bottom Depth ft	X Position ft	Y Position	Ka PDPK md Air Perm	Kl PDPK md Klinkenberg	Beta	Repeat X Position	Repeat Y Position	Repeat Ka PDPK md Air Perm	Repeat Kl PDPK md Klinkenberg	Repeat Beta	Kmaximum	Kminimum	Comment
6280	6280.47	6280.049	0	1220	1180	1.36E+07	6280.049	0.56	985	951	2.05E+07	1220	985	
6280	6280.47	6280.127	0	1200	1160	1.33E+07	6280.128	0.56	1880	1830	8.99E+06	1880	1200	
6280	6280.47	6280.184	0	584	559	2.76E+07	6280.184	0.56	996	963	1.48E+07	996	584	
6280	6280.47	6280.24	0	873	842	1.29E+07	6280.239	0.56	706	679	1.91E+07	873	706	
6280	6280.47	6280.283	0	775	747	1.84E+07	6280.281	0.56	656	630	2.93E+07	775	656	
6280	6280.47	6280.327	0	935	902	1.59E+07	6280.327	0.56	1110	1070	1.28E+07	1110	935	
6280	6280.47	6280.369	0	1620	1580	7.29E+06	6280.369	0.56	1160	1120	1.37E+07	1620	1160	
6280	6280.47	6280.417	0	1720	1670	5.16E+06	6280.417	0.25	1610	1560	6.64E+06	1720	1610	
6285.19	625.68	6285.242	0	5860	5760	2.21E+06	6285.243	-0.04	3410	3340	5.07E+06	5860	3410	rough surface
6285.19	625.68	6285.231	0	3410	3340	3.06E+06	6285.332	-0.61	3890	3810	2.04E+06	3890	3410	
6285.19	625.68	6285.372	0	1290	1250	8.61E+06	6285.332	-0.05	2790	2730	3.45E+06	2790	1290	repeat depth shift smoother surface
6285.19	625.68	6285.413	-0.6	1440	1390	7.65E+06	6285.415	-0.6	1510	1460	7.37E+06	1510	1440	third attempt at smooth surface
6285.19	625.68	6285.452	0	1950	1900	5.31E+06	6285.459	0.29	2360	2300	3.50E+06	2360	1950	third attempt at smooth surface
6285.19	625.68	6285.55	0.79	2240	2180	6.00E+06	6285.561	-0.6	5690	5590	1.43E+06	5690	2240	
6285.19	625.68	6285.585	0	3100	3030	3.82E+06	6285.585	0.39	2220	2170	7.93E+06	3380	2220	third attempt at smooth surface
6285.19	625.68	6285.64	0	1950	1900	8.17E+06	6285.63	1.03	2110	2060	4.64E+06	2110	1950	

Table 9. Full diameter (slabbed) core pressure decay profile permeameter (PDPK) analysis. Data in red indicate potential error due to slab surface variability.

Top Depth (ft)	Bottom Depth (ft)	K_{MAX} Air (md)	KMAX ESTIMATED Klinkenberg (md)	K_{MIN} Air (md)	KMIN ESTIMATED Klinkenberg (md)	K_{VERT} Air (md)	KVERT ESTIMATED Klinkenberg (md)	POR (He) (% of BV)	GD (gm/cc)	So (% of PV)	Sw (% of PV)
6256	6257	1,922	1,862	1,922	1,862	1,648	1,571	21.4	2.62	0.0	94.2
6273	6274	2,156	2,139	2,156	2,139	180	165	22.1	2.61	0.0	89.1

Table 10. Full diameter core analysis after 40-45% humidity dry 140-145°F.

Chapter 6
Characterization of Precambrian Rhyolite and Argenta Formations in the Illinois Basin

By: Roman Y. Makhnenko and Nikita B. Bondarenko
Department of Civil and Environmental Engineering
University of Illinois at Urbana-Champaign

Introduction

Injection of CO_2 into the lower part of reservoir formations for geologic carbon storage has the potential to induce seismicity or reactivate pre-existing faults in the underlying crystalline basement. Monitoring of seismicity during the Illinois Basin Decatur Project (IBDP) showed that induced microseismicity is mainly concentrated in the crystalline basement (Goertz-Allmann et al., 2017; Bauer et al., 2019). Analysis of microseismic events registered during IBDP conducted by Williams-Stroud et al. (2020) revealed that the presence of an intermediate layer between reservoir and basement rock (Mt. Simon sandstone and Precambrian rhyolite, respectively) might prevent downward migration of fluid and reactivation of pre-existing faults in the basement. It was noticed that most microseismic events are located in the area where the intermediate layer (called Argenta) is thin or missing. Therefore, geomechanical characterization of Argenta and Precambrian rhyolite was conducted to evaluate the role of these formations in induced microseismicity during CO_2 injection in the Illinois Basin.

Material and testing

In the framework of the CarbonSAFE Macon Co. project, the Argenta cores (77-114 mm in length and 59.4 mm in horizontal size) were extracted from the CarbonSAFE well at depths between 6,296-6,299 ft and are used for the characterization of the geomechanical properties of the intermediate layer (Figure 1a). Cores (150 mm in length and 88 mm in diameter) of Precambrian rhyolite used for the study are from depths between 6,399-6,464 ft (Figure 1b). Geomechanical testing includes measurements of index properties, ultrasonic velocities, strength characteristics, and poromechanical and flow properties for involved formations.

Figure 1. a) Cores of Argenta from depths between 6,296-6,299 ft. b) Cores of Precambrian rhyolite (basement rock) from depths between 6,399-6,464 ft.

Index properties

Index properties (e.g., density, porosity, pore size distribution, and permeability) are parameters that identify and classify rock. Density is defined as mass per unit volume denoted by the symbol ρ. Dry density is solid mass per unit bulk volume that can be calculated using a micrometer caliper if the rock is in the form of a prism or a cylinder. The porosity ϕ is defined as the volume of the interconnected pore space divided by the bulk volume. Interconnected porosity and pore size distribution of a tight rock can be accurately measured from mercury intrusion porosimetry and nitrogen adsorption tests on a low porous rock.

The results of the nitrogen adsorption test on the Precambrian rhyolite specimen are presented in Figure 2 and indicate that pore widths in intact basement rock specimen span the range of 0.007-0.1 μm (micron) with the dominant pore size of d = 0.02 μm.

The results of mercury intrusion porosimetry on Argenta specimen are presented in Figure 3 and indicate that pore widths in Argenta specimen span the range of 0.03-10 μm (micron) with the dominant pore size of d = 0.25 μm.

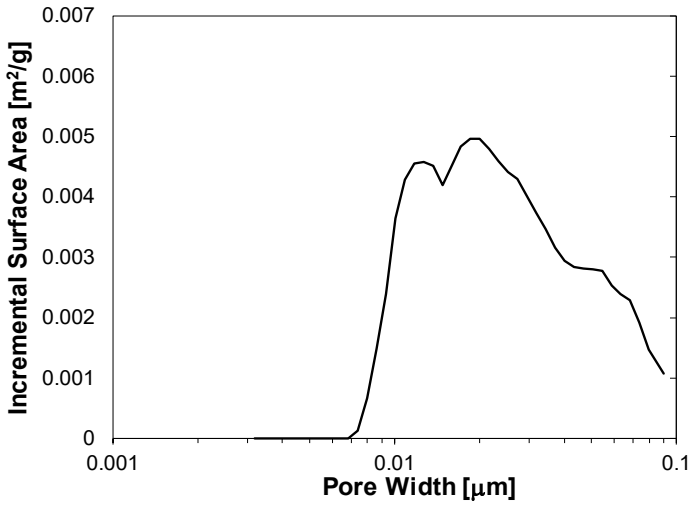

Figure 2. Pore width distribution in intact basement rock specimen from nitrogen adsorption test. The dominant pore width is 0.02 μm.

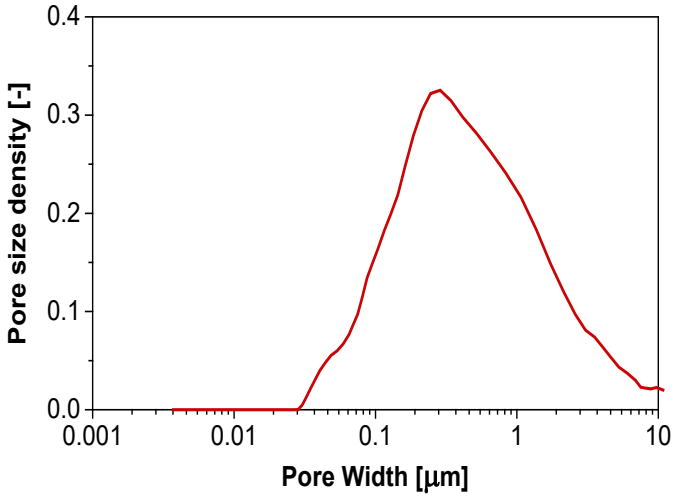

Figure 3. Pore width distribution in Argenta specimen from mercury intrusion porosimetry. The dominant pore size is 0.25 μm.

Grain size distribution analysis was conducted to characterize the heterogeneity of the Argenta formation. The specimen with mass of approximately 100 grams was carefully remolded without crushing the grains. The sieve test was performed for the grains of a size larger than 0.15 mm (ASTM International, 2017, D6913/D6913M-17). For grains smaller than 0.15 mm, the sedimentation analysis was conducted (ASTM International, 2017, D7928-17). This method is based on density measurement of water-grains suspension and allows estimating grain size from a decrease of suspension's density with time. The combined results of sedimentation analysis and sieve analysis are shown in Figure 4.

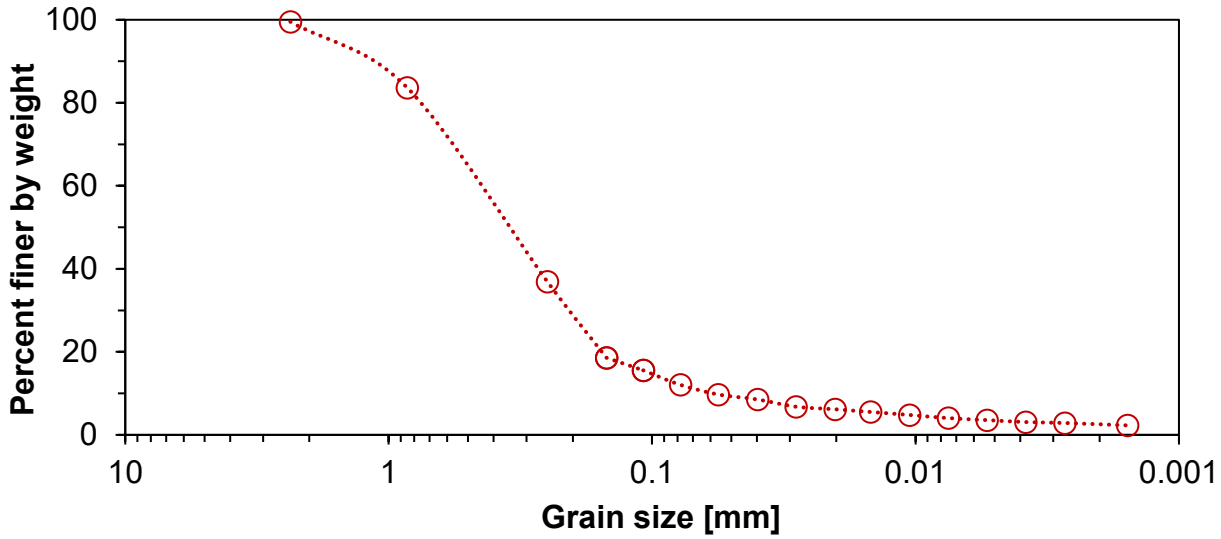

Figure 4. Grain size distribution for Argenta.

Table 1. Index properties of tested specimens

* - mercury intrusion porosimetry test is in progress

Formation	Bulk density ρ_b [g/cm^3]	Dominant pore size d [μm]	Porosity ϕ [-]
Argenta	2.30	0.25	0.14
Precambrian rhyolite	2.74	0.02	*

Dynamic properties

Ultrasonic or "dynamic" elastic constants can be calculated from the measured wave velocities and the bulk density (Brown, 1981). With 2.25 MHz transducers (General Electric Alpha 2.25 MHz & Panametrics V154), both *P*- and *S*-waves (compressional and shear waves) are generated. The data acquisition system for the velocity measurements consists of an ultrasound pulse receiver (Olympus 5077PR), a digital oscilloscope (Tektronix TBS1064), and sets of

ultrasonic transducers. A negative step function excitation (200 V) is applied to the transmitting transducer to generate the ultrasonic pulse. The propagating wave pulse is sensed by the receiving transducer, and then digitized with 8-bit dynamic range resolution, sampling frequency of 10 MHz, and signal duration of 0.25 ms. The signal was then amplified with 20 dB gain. Wave transmission efficiency is improved with the help of a couplant (Vaseline) placed between the transducer face and sample surface. The through transmission measurements are repeated 128 times and time-averaged for improved signal-to-noise ratio (SNR).

By visually and digitally examining the waveform, the departure time and arrival time can be determined for each wave type, and *P*- and *S*-wave velocities, c_p and c_s, can be calculated. Given the material density ρ, the dynamic elastic parameters E_d (Young's modulus) and ν_d (Poisson's ratio) can be obtained using the following relationships:

$$E_d = \frac{\rho c_s^{\,2}\left(3c_p^{\,2} - 4c_s^{\,2}\right)}{\left(c_p^{\,2} - c_s^{\,2}\right)} \tag{1}$$

$$\nu_d = \frac{c_p^{\,2} - 2c_s^{\,2}}{2\left(c_p^{\,2} - c_s^{\,2}\right)} \tag{2}$$

Results of measurements for Argenta and Precambrian rhyolite cores (for cores without and with visible cracks) are shown in Table 2.

Table 2. Ultrasonic velocities measurements

Formation		*P*-wave velocity c_p [km/s]	*S*-wave velocity c_s [km/s]	Dynamic Young's modulus E_d [GPa]	Dynamic Poisson's ratio ν_d [-]
Argenta		2.63	1.61	14.3	0.19
Precambrian rhyolite	Intact	5.33	3.28	71.1	0.20
	Fractured	5.52	3.16	68.6	0.25

Strength measurements

A series of uniaxial and conventional triaxial tests were performed on cylindrical specimens of Precambrian rhyolite (Figure 5a) and Argenta (Figure 5b). The specimen ends are lubricated with a stearic acid mixture to promote homogeneous deformation (Labuz and Bridell, 1993), and the specimen is loaded with a displacement rate of 1×10^{-4} mm/s to ensure quasi-static deformation. The axial load, axial and lateral deformation, and peak normal stress at failure are recorded. Triaxial tests were conducted in a Hoek-Franklin cell, with core diameters of 30.5 mm and lengths of 65-75 mm that were put inside rubber membranes and subjected to confining

pressures of σ_3=10, 20, and 30 MPa. It appeared that all the specimens of Precambrian rhyolite fail through pre-existing weak planes that are not visible during the specimen preparation. The low cohesion reported for granitic rock also indicates the influence of weak planes on the material strength. In addition, it can be assumed that cohesion of the specimens with visible weak planes is close to zero since they failed easily during the coring. The results of the tests were interpreted within the framework of a Mohr-Coulomb failure criterion to calculate cohesion C and friction angle φ (Table 3; Figure 6).

Table 3. Results of uniaxial and conventional triaxial compression tests

Formation	Static Young's modulus E [GPa]	Static Poisson's ratio ν [-]	Uniaxial compression strength UCS [MPa]	Cohesion C [MPa]	Friction angle φ [°]
Argenta	10.7	0.22	44	11.2	42
Precambrian rhyolite	44.0	0.22	189	22	61

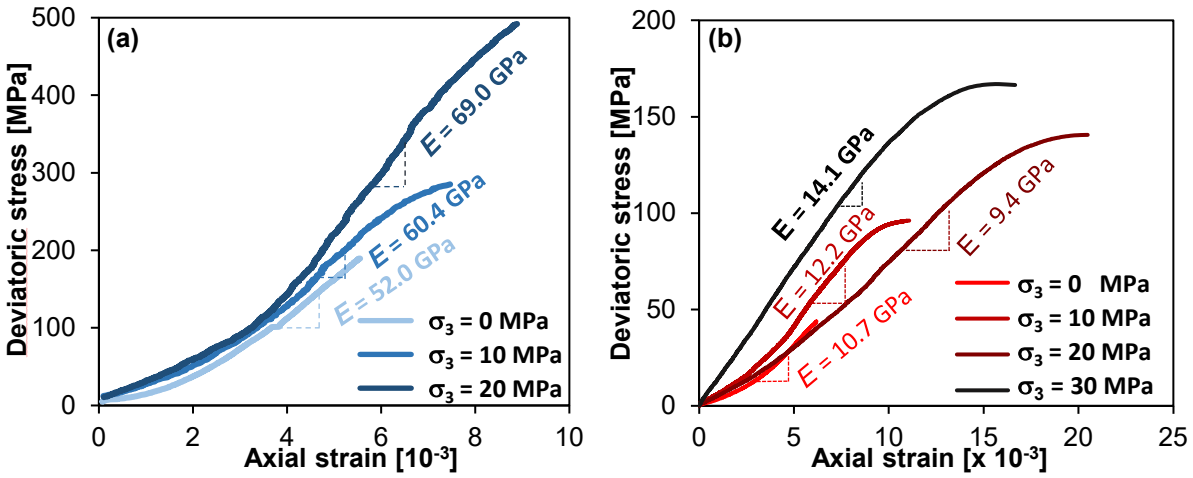

Figure 5. Deviatoric stress – axial strain diagram for triaxial tests on (a) intact basement rock and (b) Argenta

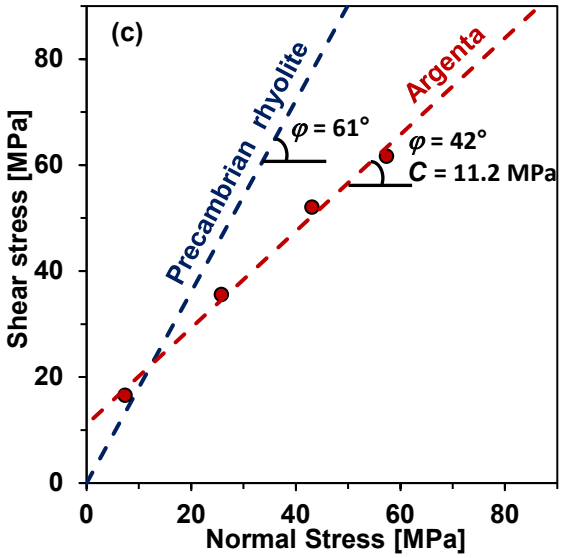

Figure 6. Mohr-Coulomb failure envelope for basement rock (assuming zero cohesion on a pre-existing weak plane) and Argenta

Hydrostatic compression tests

Prismatic specimens of Argenta and Precambrian rhyolite instrumented with strain rosettes in three perpendicular directions were used for hydrostatic compression tests. Then specimens were covered with polyurethane to create a jacket, which prevents the specimen from saturation with hydraulic oil. After that, the specimen is submerged in the hydraulic oil and loaded hydrostatically to measure the material's bulk modulus. The polyurethane jacket is removed for the unjacketed test, and specimens are allowed to saturate at 50 MPa cell pressure. Then, specimens are slowly unloaded with 1-3 MPa step making sure that all excess pore pressure is dissipated and strain gauge readings are in equilibrium. Dissipation time of excess pore pressure could be used to make an order of magnitude estimation of materials' permeability (Precambrian rhyolite – 10^{-21} m^2, Argenta – 10^{-18} m^2).

Measured volume response of specimens under hydrostatic loading is shown in Figures 7a and 7b. Measurements of normal strains during jacketed and unjacketed tests of Argenta specimen result in calculation of drained bulk modulus K = 16.4 GPa and unjacketed bulk modulus K'_s = 40.5 GPa (Figure 7a). For Precambrian rhyolite, measured drained bulk modulus K = 51.6 GPa and unjacketed bulk modulus K'_s = 65.4 GPa (Figure 7b).

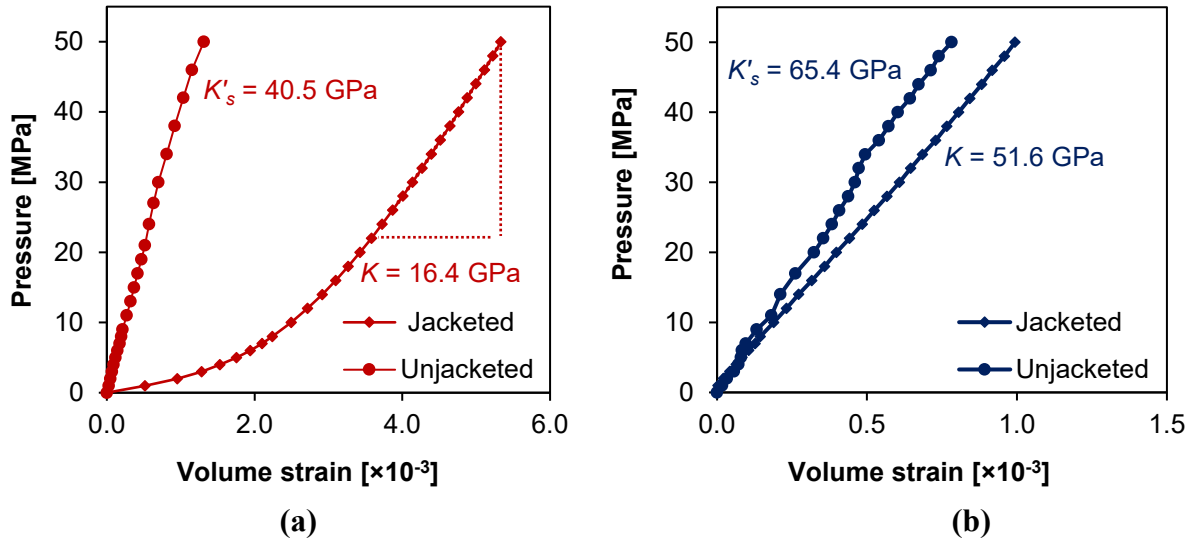

Figure 7. Results of jacketed and unjacketed hydrostatic tests on (a) Argenta (b) Precambrian rhyolite specimens

Assumption that unjacketed bulk modulus K'_s equal to unjacketed pore modulus K''_s allows estimation of other poroelastic properties: Biot coefficient α and Skempton's B coefficient.

$$\alpha = 1 - \frac{K}{K'_s}$$

$$B = \frac{\alpha}{\alpha + \phi K\left(\frac{1}{K_f} - \frac{1}{K''_s}\right)}$$

With the knowledge of poroelastic and flow properties of the involved geomaterials, the simulation of the injection process will be performed to evaluate the factors that may play a role in short- and long-term behavior of a reservoir and adjacent formations.

Table 4. Hydromechanical properties of Argenta and Precambrian rhyolite

Formation	Drained bulk modulus K [GPa]	Unjacketed bulk modulus K'_s [GPa]	Biot coefficient α [-]	Skempton's coefficient B [-]	Permeability (order of magnitude) k [m^2]
Argenta	16.4	40.5	0.6	0.3	10^{-18}
Precambrian rhyolite	51.6	65.4	0.2	0.5	10^{-21}

Conclusions

The geomechanical characterization of Precambrian rhyolite and Argenta specimens indicates that Argenta is significantly softer and has a larger dominant pore size compared to Precambrian rhyolite. This observation supports an assumption that Argenta might be the upper part of the crystalline basement, significantly affected by the weathering process. Preliminary estimation of permeability for the Argenta is four orders of magnitude smaller than the permeability of the reservoir rock (permeability of Mt. Simon sandstone ~ 10^{-14} m^2). This fact supports the assumption that Argenta might act as a bottom seal that prevents the downward migration of fluid into the basement rock. Precise measurements of the flow properties for Argenta and Precambrian rhyolite are in progress. Strength measurements of Precambrian rhyolite indicate the significance of pre-existing weak planes in the basement rock. Cohesion for specimens of Precambrian rhyolite with visible weak planes is close to zero since they failed easily during the coring. The response of the Argenta seems to be more ductile than that of Precambrian rhyolite, which possibly explains the absence of microseismic events in the Argenta formation.

References

ASTM International. 2017. D6913/D6913M-17 Standard Test Methods for Particle-Size Distribution (Gradation) of Soils Using Sieve Analysis. *ASTM International*. West Conshohocken, PA: American Society for Testing and Materials. doi: https://doi.org/10.1520/D6913_D6913M-17.

ASTM International. 2017. D7928-17 Standard Test Method for Particle-Size Distribution (Gradation) of Fine-Grained Soils Using the Sedimentation (Hydrometer) Analysis. *ASTM International*. West Conshohocken, PA: American Society for Testing and Materials. doi: https://doi.org/10.1520/D7928-17.

Bauer, R.A., Will, R., Greenberg, S., Whittaker, S.G. 2019. Illinois Basin-Decatur project. In: Davis, T.M., Landrø, M., Wilson, M. (eds.) *Geophysics and Geosequestration,* chapter 19*,* 339-369, Cambridge University Press.

Goertz-Allmann, B.P., Gibbons, S.J., Oye, V., Bauer, R., Will, R. 2017. Characterization of induced seismicity patterns derived from internal structure in event clusters. *Journal of Geophysical Research: Solid Earth*, 122, 3875–3894.

Labuz, J.F., Bridell, J.M. 1993. Reducing frictional constraint in compression testing through lubrication. *International Journal of Rock Mechanics Mining Sciences & Geomechanical Abstracts,* 30(4), 451–455.

Williams-Stroud, S., Bauer, R., Leetaru, H., Oye, V., Stanek, F., Greenberg, S., Langet, N., 2020. Analysis of microseismicity and reactivated fault size to assess the potential for felt events by CO_2 injection in the Illinois Basin. *Bulletin of the Seismological Society of America,* XX, 1–17.